Een diffusietensor-gebaseerd computationeel model
voor transcraniële magnetische stimulatie:
van macroscopische velden tot neuronale membraanpotentialen

A Diffusion Tensor-Based Computational Model
for Transcranial Magnetic Stimulation:
from Macroscopic Fields to Neuronal Membrane Potentials

Nele De Geeter

Promotoren: prof. dr. ir. L. Dupré, prof. dr. ir. G. Crevecoeur
Proefschrift ingediend tot het behalen van de graad van
Doctor in de Ingenieurswetenschappen

Vakgroep Elektrische Energie, Systemen en Automatisering
Voorzitter: prof. dr. ir. J. Melkebeek
Faculteit Ingenieurswetenschappen en Architectuur
Academiejaar 2014 - 2015

UNIVERSITEIT
GENT

ISBN 978-90-8578-812-6
NUR 954, 981
Wettelijk depot: D/2015/10.500/56

A Diffusion Tensor-Based Computational Model for Transcranial Magnetic Stimulation: from Macroscopic Fields to Neuronal Membrane Potentials

Nele De Geeter

Dissertation submitted to obtain the academic degree of
Doctor of Engineering

Publicly defended at Ghent University on June 15, 2015

Supervisors:

Prof. dr. ir. Luc Dupré
Prof. dr. ir. Guillaume Crevecoeur
Electrical Energy Laboratory
Department of Electrical Energy, Systems and Automation
Faculty of Engineering and Architecture
Ghent University
Technologiepark 913
9052 Zwijnaarde, Belgium
http://www.eesa.ugent.be

Members of the examining board:

Prof. dr. ir. Rik Van de Walle (chairman)	Ghent University, Belgium
Prof. dr. ir. Wout Joseph (secretary)	Ghent University, Belgium
Prof. dr. ir. Luc Dupré (supervisor)	Ghent University, Belgium
Prof. dr. ir. Guillaume Crevecoeur (co-supervisor)	Ghent University, Belgium
Prof. dr. Kristl Vonck	Ghent University Hospital, Belgium
Prof. dr. Alexander Leemans	University Medical Center Utrecht, The Netherlands
Prof. dr. Anton G. Tijhuis	Eindhoven University of Technology, The Netherlands
Dr. ir. Pantelis Lioumis	Helsinki University & Helsinki University Hospital, Finland

INGENIEURSWETENSCHAPPEN ARCHITECTUUR

EELAB

UNIVERSITEIT GENT

The right path in work and life is inherently not unique. This non-uniqueness makes choosing this path unimportant, even though it feels the opposite. The way you outline it will depend on yourself. And - I know - it will always be Nele-wise ... like a walk in the park.

my supervisor and friend, Guillaume Crevecoeur

Prologue

Word of thanks

The right path in work and life is indeed not unique. Along the way you meet many new people who will contribute in this path choice. Also the things you experience, the things that happen to you, both setbacks and good luck, they all have an impact. I wouldn't say this PhD was a walk in the park, but I do was surrounded by many friends, colleagues, family, who helped me to overcome the obstacles and to reach the finish line. To them I want to say... thank you!

I still remember my first day at the department. Actually I was not aware that this would be my first day. I was less than 24 hours back from a round trip through Burkina Faso and Mali. Still in holiday mood, wrapped in a little short and top and with my brightly coloured feet full of henna drawings, I entered the building to quickly sign my contract and then go shopping in Ghent. But this was not as my supervisors Prof. Dupré and Dr. Crevecoeur had planned it. They put me at work all day until I had a fully installed office. I soon got to know them better, along with my entire work environment. Guillaume and Ben, who were happy to finally have a girl in their office. During the past years, they became my two big brothers. Luc, the father figure who takes a lot of care of his people. Nic, our IT Support who is crazy about women and the pictures he can take of them. Annelies, female reinforcement in that men's world, and her beloved Jonathan who in turn reinforces the other team with Hendrik, Frederik and Jasper. I want to thank them all. Mariem for discussing the idea (or is it a myth?) that we as human beings would use only 10 percent of our brain's capacity. Damian, Enrique, Setareh and Ahmed for sharing their traditions and view on Belgium. Ingrid, Marilyn, Tony and Vincent for arranging everything smoothly within our laboratory. Lode, Peter, Bart, Frederik, Kristof, Jeroen, Christof, Jan, Joachim, Louis and all my other colleagues. Thank you all for being there the past years and for creating a pleasant working atmosphere together. It caused me to come to EELAB every day with joy, despite the sometimes long waiting for positive outcomes. Still,

I would like to add some special words of gratitude to a few people individually.

Dear Prof. Dupré, it took me a while to call you Luc. I am very grateful for the fact that you are one of us and not the unreachable professor. If we need you, you are there to help, despite your busy agenda. Thank you for organising meetings for our research team such as the traditional delicious New Year's breakfasts. The start, nor the completion of this work would have been possible without your advice, guidance and support. At the same time I am thankful for the freedom you gave me during this research. It has been an honour to be your PhD student.
Dear Guillaume, even though you are promoted to professor, you stayed available day and night for questions but also for a daily chat. I admire your extensive knowledge and the way you manage it over all the students you guide. Thank you for the many ideas, the endless help, encouragement and patience during all these years. You were there for the pep talks and putting things in perspective, but also for the great beat on the background (or foreground?). Thank you for brainstorming together, for simulation debugging, for proofreading my papers and putting the finishing touches. What I have achieved in this work, I owe to you.
Dear Ben, you were locked up alone with me the last eight months. Thank you for standing my mood, for sharing your cookies, for limiting your Skype sessions and putting some soothing music on when needed. You helped me to keep the level of stress under control and to relativise. As an outsider you could take a fresh look at the things I was simulating and ask out of the box questions. Thank you for being sincerely interested and for supporting me.

With great respect for his dedication to MRI, I would like to thank Prof. Yves De Deene for his help with the gradient echo sequences and the programming on the MR scanner. I am grateful to Dr. Tine Wijckhuys for our cooperation in the TMS project on rats.
A special word of thanks to Prof. Alexander Leemans for the access to his useful toolbox ExploreDTI. Even though your manual is very well explained, I had some questions over the years to which you always responded exceptionally quickly. Thank you for the T1 and DTI data sets and for the information and references regarding DTI and tractography.
Many thanks to Dr. Pantelis Lioumis for our discussions, the positive vibes, introducing me to the practical side of TMS, and in particular for setting up the speech mapping experiment.
Besides Prof. Alexander Leemans and Dr. Pantelis Lioumis, I also would like to thank the other members of my PhD examination board, namely Prof. Anton Tijhuis, Prof. Wout Joseph, Prof. Kristl Vonck and Prof. Rik Van de Walle, for their critical review of this book and their constructive feedback.

A major part of the simulations in this work were carried out using the Stevin Supercomputer Infrastructure at Ghent University. I acknowledge the convenience of this high performance environment. As PhD student of the Agency for Innovation by Science and Technology in Flanders (IWT) SB/101133, I am grateful for their financial support. I'm also thankful for the Research Foundation Flanders (FWO) travel grant, which made my scientific stay at Aalto University, Finland feasible. Thank you, Prof. Risto Ilmoniemi, for inviting me to your research group at the department of Biomedical Engineering and Computational Science (BECS). Performing TMS experiments on sophisticated equipment such as the neuronavigation system was of great value for me. Dear Dr. Julio Hernandez-Pavon, thank you for organising the TMS-EEG summer schools and for introducing me to your friends. Niko Mäkelä and Tuomas Mutanen, thank you for performing some TMS-EEG measurements. Unfortunately, I could not implement these in this work. Johanna Metsomaa, Koos Zevenhoven, Dr. Matti Stenroos and Jaakko Nieminen, thank you all for your help and sharing knowledge.
I am thankful to my master students, Martijn Devrome and Lucas Holvoet, who helped me analysing the speech mapping data, digging through literature, simulations and network analyses. With this I also want to show my appreciation for my own thesis supervisor, Dr. Clara Ionescu, for sharing her research enthusiasm with me.

Further, I want to thank my friends including Karolien, Stijn, Ruben, Bram, Isabel, Caroline, Griet, Koenraad, Lieselot and Bart from secondary school, Ward, Ellen, Gregory, Stef, Dieter, Kevin, Delphine, Els, Charlotte, Matthias, Jan, Bart, Niels, Steven and Steven from university, Freija, Sarah, Farnoosh, Sofie, Greet and Sijntje from the round trip through Burkina Faso and Mali, Valerie, Heleen, Fien and Noortje from the volleyball, the girls from the Gentse Leute and many others. Thank you all for being there and creating a pleasant world besides university.

Of course a special thank you to my family may not be missing here. Mammy and daddy, thanks for your unconditional support and trust, for your advice and care and for the many opportunities you have given me already. You are the very best! Joke, dear sis, you have always been my great role model. Year after year we grow more towards each other, for which I am very happy. I am grateful to life that my four loving grandparents can be here today to experience my promotion. I know they are proud and that makes me more than happy. Thank you for supporting me! Lode and Magda, Jeroen, Ruben, Lien and Mats, thank you for welcoming me so warmly into your family. It means a lot to me. I also appreciate the strong bond with my brother-in-law, nieces and nephews, aunts and uncles. It's wonderful how we all connect and how close we are. I can think of no better family.

Finally, I want to express my passion for the love of my life, Jürgen. (Guillaume, indirectly I must thank you for this as well.) Even though your dad calls us nerds, thank you for brainstorming with me about electromagnetism and numerical problems. Thank you for letting me work until indecent hours the days before the deadline and for letting me chatter about things that were not going smoothly. I think it's marvellous how we cooperate in daily life and work together while creating our own space, our bubble, our family. You give me the energy but also the rest when needed. Thank you for being you. You stimulate my world to a higher level!

Nele De Geeter, June 2015

Contents

Hersenen zijn als pudding, die tussen je oren rijpt. Zeester met koffie, tot je dat begrijpt.

Bart Peeters, *in zijn liedje "Zeester met koffie"*

Samenvatting

Transcraniële magnetische stimulatie, afgekort TMS, is een niet-invasieve techniek die de activiteit van een specifiek deel van de hersenen kan versterken of onderdrukken. Een spoel van koperdraad wordt boven het hoofd gehouden en genereert een tijdsvariërend magnetisch veld. Dit veld wekt elektrische stromen en een elektrisch veld op in het brein. Dit geïnduceerde elektrisch veld interageert met de neurale systemen en kan bepaalde hersengebieden tijdelijk prikkelen of remmen door een verandering van membraanpotentialen teweeg te brengen in de neuronen.

De laatste jaren heeft deze veilige stimulatietechniek zichzelf opgewerkt als een veelbelovende manier voor de diagnose en alternatieve behandeling van verscheidene neurologische en psychiatrische stoornissen zoals oorsuizingen, epilepsie en depressie. Aangezien TMS in staat is om de hersenactiviteit te beïnvloeden, is het bovendien een krachtige tool om de specifieke hersenfuncties te bestuderen. Het kan de normale werking van een bepaald gebied in de cortex tijdelijk verstoren, ook wel een virtueel hersenletsel genoemd. Dit laat toe om bijvoorbeeld de kritische motorische en zintuiglijke gebieden van de cortex te mappen ter voorbereiding van een hersenoperatie.

Hoewel tijdens het laatste decennium TMS op grote schaal gebruikt wordt en zijn werkzaamheid al is gebleken, blijven de onderliggende mechanismen slecht begrepen en is zijn werking moeilijk te voorspellen. Bovendien melden klinische en psychologische studies die TMS gebruiken een hoge variabiliteit van zijn effect op de hersenfunctie. Een beperkte verandering van de parameters in de TMS procedure leidt tot drastische veranderingen in de klinische of psychologische uitkomst. Deze onzekerheid beperkt de grote verscheidenheid aan mogelijke toepassingen en weerhoudt de neurowetenschappers ervan om TMS als routine behandelingsmethode te beschouwen. Om meer inzicht te krijgen, is onderzoek nodig met betrekking tot computationele methoden, waaronder bio-elektromagnetische modellering die nauwkeurig en zowel kwalitatief als kwantitatief de impact van de geïnduceerde velden op het menselijk brein kan bepalen. Deze simulaties zijn cruciaal omdat *in vivo* metingen meestal duur zijn. Bovendien zijn grote homogene patiëntengroepen moeilijk te verzamelen en beperkt als gevolg van ethische kwesties. Tenslotte hebben experimentele studies voordeel bij modellering door hun

voorspelling, betere planning en controle en dus vermindering van het aantal experimenten.
Tijdens dit doctoraat werd een computationeel model voor TMS ontwikkeld. Aangezien TMS niet steeds hetzelfde effect teweegbrengt, maar varieert tussen de proefpersonen, zijn we overtuigd van het belang om persoonsspecifieke informatie te implementeren. Zeker omdat de 21e eeuw ons toegang geeft tot individuele MRI, zoals de T1-gewogen anatomische hersenscans en diffusie-gewogen beelden, beter bekend als diffusietensor beelden of DTI. Deze data geeft ons de mogelijkheid om om te gaan met de grote variabiliteit tussen de hersenen en hun anatomische structuren. Bovendien stellen neuronavigatiesystemen ons in staat om het stimulatiedoelgebied in kaart te brengen op de MRI van het hoofd van de proefpersoon en de TMS spoel te positioneren en oriënteren met grotere nauwkeurigheid en reproduceerbaarheid. Hoewel dit een belangrijke verbetering is vergeleken met de handmatige spoelplaatsing, wordt de schatting van het stimulatiedoelgebied nog steeds berekend op bolvormige hoofdmodellen. In tegenstelling tot deze werkwijze, richten wij ons op het invoeren van zowel patiënt- als casespecifieke karakteristieken in ons model.
De onafhankelijke impedantiemethode is ontwikkeld om de elektromagnetische verschijnselen te modelleren. Het is gebaseerd op de conventionele impedantiemethode, maar elimineert op basis van grafentheorie de afhankelijke lussen en bijgevolg de overbodige vergelijkingen in het lineair stelsel. Dit resulteert in een betere conditionering en een versnelling van de numerieke convergentie. Een 3D netwerk van impedanties wordt opgesteld en opgelost om de wervelstromen die TMS induceert in de hersenen te bepalen. De bijhorende geïnduceerde elektrische veldverdeling kan dan worden berekend.
De elektrische geleidbaarheidswaarden van de verschillende hersenweefsels dienen ingevoerd te worden in de elektromagnetische berekeningen. Deze waarden kunnen worden beschreven door het frequentieafhankelijke parametrische 4-Cole-Cole-model. Dit model biedt echter een optimale schatting op basis van een bestaand materiaaldatabank, maar heeft een grote onzekerheid bij lage frequenties. Bovendien hebben de diëlektrische weefseleigenschappen een grote variabiliteit tussen individuen. Daarom stellen we een techniek voor die op een niet-invasieve manier de geleidbaarheidswaarden schat door geavanceerde MRI-sequenties toe te passen. Twee fasebeelden worden opgemeten: een keer met een gradiënt geschakeld die wervelstromen induceert en een keer zonder. Het verschil tussen beide fasebeelden bevat de nodige informatie om de geleidbaarheidsdistributie te reconstrueren. We zijn erin geslaagd om de geleidbaarheidsprofielen van de weefsels huid, bot, grijze en witte stof numeriek te reconstrueren. Dit bevestigt het potentieel en de haalbaarheid van de techniek. Verder onderzoek met echte klinische metingen is echter een nodige voorwaarde om de robuustheid te beoordelen en de

techniek klinisch toepasbaar te maken.
Doorheen het doctoraat wordt naar klinisch relevante simulaties toegewerkt. Aanvankelijk zijn eenvoudige bolvormige hoofdmodellen beschouwd, maar naarmate we evolueren, worden meer geavanceerde gepersonaliseerde hoofdmodellen gebouwd. Een realistische geometrie en de frequentie-afhankelijke anisotrope weefseleigenschappen worden opgenomen op basis van T1- en diffusie-gewogen MRI. Onze ontwikkelde solver gebruikt eerst cirkelvormige spoelen, maar wordt dan uitgebreid voor elk spoelontwerp, met inbegrip van de meestal toegepaste en commercieel beschikbare cijfer-acht spoelen. Het kan de positie en oriëntatie van de spoel uit het neuronavigatiesysteem direct in het model invoeren.
De vorm van de spoel is belangrijk aangezien het de geïnduceerde veldverdeling beïnvloedt en daarmee de plaats van stimulatie. Desalniettemin blijkt uit onze simulaties dat deze verdeling ook sterk afhankelijk is van de locatie en oriëntatie van de spoel met betrekking tot het hoofd van de proefpersoon en van de inhomogene en anisotrope geleidbaarheidsstructuur van het hoofd.
De geïnduceerde elektrische velden interageren met het zenuwstelsel - meer bepaald met de spanningsafhankelijke ionenkanalen in het plasmamembraan van neuronen - en kunnen bepaalde hersengebieden prikkelen of remmen door de membraanpotentialen te wijzigen. Om het precieze mechanisme van stimulatie te bestuderen, breiden we onze elektromagnetische solver uit naar de neurofysiologie om de spatio-temporele verdeling van membraanpotentialen langs de neuronen in de hersenen te berekenen. Aanvankelijk gaan we uit van rechte en radiaal-gerichte neuronenbundels, daarna worden realistische 3D reconstructies gegenereerd met behulp van DTI-gebaseerde tractografie. Dicht bij het hersengebied waarop de TMS spoel gericht is, worden bundels van gegroepeerde witte stof geselecteerd, tractussen genaamd. Het geïnduceerde elektrische veld wordt uitgezet langsheen de banen van deze tractussen en dient als de basis voor de beschouwde stimulatiemechanismen. We beschrijven de reactie van deze mechanismen op de membraanpotentiaal aan de hand van een kabelvergelijking bestaande uit verschillende componenten. Alle tractussen worden verondersteld gemyeliniseerde neuronen te zijn, met secties die dendrieten, soma, axon hillock, eerste segment, knopen van Ranvier en gemyeliniseerde internoden voorstellen, en worden gemodelleerd met passieve en actieve membraaneigenschappen.
Ondanks het feit dat de elektrische velden maximaal zijn in het corticale oppervlak dichtbij de spoel en slechts beperkt doordringen in de subcorticale structuren, tonen experimenten aan dat standaard TMS spoelen ook effect kunnen hebben op de diepere hersengebieden. Wij geloven dat dit veroorzaakt wordt door de neurale verbindingen tussen corticale en subcorticale structuren. TMS kan de membraanpotentialen depolariseren en actiepotentialen initiëren in het neuraal weefsel onder de spoel, die zich op hun beurt

kunnen voortzetten langs de tractussen naar diepere regionen.
De elektromagnetische modellering is gevalideerd door vergelijking met analytische en standaard eindige-elementenmethoden. De neurofysiologische berekeningen, namelijk de spatio-temporele variaties van de membraanpotentialen, zijn moeilijker te valideren, omdat het onmogelijk is om de membraanpotentialen direct in de hersenen te meten. Als alternatief verklaren we numeriek de waargenomen variabiliteit van TMS bij taalmapping tijdens een benoemtaak.
De ontwikkelde flexibele en gepersonaliseerde toolbox modelleert TMS van de macroscopische velden in de hersenen tot de potentialen op microscopisch neuronaal niveau. Voor zover wij weten is deze manier van simuleren nieuw en een belangrijke stap naar volledig geval- en persoonsspecifieke resultaten. De simulaties bevestigen dat een nauwkeurige bepaling van het stimulatiedoel in combinatie met een neuronavigatiesysteem noodzakelijk is om betrouwbare TMS studies te verrichten.
Deze toolbox biedt vele mogelijkheden. Zo kan het de gevoeligheid van de spoelpositionering onderzoeken, net zoals de variabiliteit van de TMS effecten bij verschillende proefpersonen. Het kan het mechanisme en de locatie van stimulatie voorspellen en inschatten welke tractussen effectief bijdragen. Bovendien is het geschikt om te combineren met TMS experimenten en hun elektrofysiologische respons opgenomen met EEG en/of EMG.
"Hersenen zijn als pudding, die tussen je oren rijpt. Zeester met koffie, tot je dat begrijpt." Wat Bart Peeters er precies mee bedoelt, begrijp ik nog steeds niet helemaal. Maar ik ben overtuigd dat hersenonderzoek iets is wat lang moet rijpen. Verder onderzoek moet het aantal veronderstellingen verminderen en vooral synapsen bevatten voor verdere communicatie met andere neuronen in het hersennetwerk, zodat we een breder beeld van de neurale respons op TMS verkrijgen. Een mogelijke validatie is volgens ons haalbaar door de spatio-temporele variatie van de membraanpotentialen te vergelijken met de verspreiding van hersenactiviteit via het meten van door TMS opgeroepen EEG reacties. Wij benadrukken hier het belang van doordachte, goed voorbereide en nauwkeurig uitgevoerde experimenten.
Uiteindelijk streven we naar computerondersteunde TMS, waarbij persoonsspecifieke informatie optimaal geïntegreerd wordt, zoals structurele MRI, DTI, evenals de gepersonaliseerde geleidbaarheidswaarden van de biologische weefsels. Wanneer een verstoord hersennetwerk van de patiënt wordt geïdentificeerd, zouden dergelijke slimme TMS apparaten de beste plaats voor stimulatie vinden door het detecteren van de bereikbare corticale structuren van dit netwerk. Vervolgens zouden ze de spoelspecificaties optimaliseren, zoals de vorm, positie, oriëntatie en excitatie golfvorm. Hoewel we beseffen dat er nog een lange weg te gaan is, zijn we ervan overtuigd een stap in de goede richting te hebben gezet met dit onderzoek.

"Begin at the beginning," the King said, gravely, "and go on till you come to an end; then stop."

Lewis Carroll, *in his book "Alice in Wonderland"*

Summary

Transcranial magnetic stimulation, or abbreviated TMS, is a non-invasive technique that has the ability to enhance or suppress brain activity. It induces electric currents and an electric field in the brain via a time-varying magnetic field, generated by a coil positioned above the scalp surface. This induced electric field interacts with the neural system and may excite or inhibit certain brain regions by altering the membrane potentials of neurons.

In recent years, this safe and well tolerated brain stimulation technique has established itself as a promising diagnostic tool and alternative treatment for a broad range of neurological and psychiatric disorders including tinnitus, epilepsy and depression. Since TMS has the ability to modify the brain state, it is a powerful tool to explore specific brain functions. It can temporarily disrupt the normal behaviour of a given cortical area, thus creating a 'virtual brain lesion'. This enables, for example, the mapping of critical motor and sensory areas of the cortex prior to neurosurgery.

Although during the last decade TMS has been frequently and widely used and its efficacy has already been demonstrated, the underlying mechanisms remain poorly understood and its working is hard to predict. Moreover, many clinical and psychological studies that employ TMS reported a high variability of its effect on brain functioning. Limited parameter changes in the TMS procedure lead to drastic changes in the clinical or psychological outcome. This uncertainty restricts the wide variety of potential applications and keeps neuroscientists from embracing TMS as a routine treatment method. To gain more insight, research is needed with respect to computational methods for TMS including bio-electromagnetic modelling that can accurately determine the impact of the induced fields on the human brain both qualitatively and quantitatively. These simulations are crucial because *in vivo* measurements are typically expensive and large homogeneous patient groups are difficult to gather and restricted due to ethical issues. Moreover, experimental studies benefit from modelling through prediction, better planning and control and consequently reduction of experiments.

During this PhD, a computational model for TMS was developed. Since the effects of TMS are not fixed, but vary among subjects, we believe that implementing patient-specific information is of great importance. Especially be-

cause the 21st century gives us access to individual MRI, such as T1-weighted anatomical brain scans and diffusion-weighted images, better known as diffusion tensor images or DTI. This data gives us the opportunity to deal with the variability between brains and their anatomical structures. Moreover, neuronavigation systems allow us to map the stimulation target on the MRI of the subject's head, and to position and orientate the TMS coil with increased accuracy and reproducibility. Although it is a major improvement on manual coil positioning, the applied calculations for estimating the stimulated cortical site are still performed on spherical head models. In contrast, we aim at implementing both patient- and case-specific features in our model.

The independent impedance method is developed for modelling the electromagnetic phenomena. It is based on the conventional impedance method, but eliminates the dependent loops and consequently the redundant equations in the linear system using graph theory. This results in improved conditionality and speed-up of numerical convergence. A 3D network of impedances is generated and solved to determine the induced eddy currents. The electric field distribution induced in the brain by TMS can then be calculated.

As input, these electromagnetic calculations require the electric conductivity values of the different brain tissues. These values can be described by the frequency-dependent parametric 4-Cole-Cole model for the Hz-GHz range. However, this model provides a best estimate based on an existing material database, but has large uncertainties at low frequency. Moreover, the dielectric tissue properties have a large inter-subject variability. Therefore, we propose a technique, called the induced current MR phase imaging electrical impedance tomography, to non-invasively estimate the conductivity values by applying advanced MRI sequences. Two phase images are obtained, once with an eddy-current induction gradient switched and once without. The difference between both phase images contains the information necessary to reconstruct the internal conductivity distribution. We succeed in numerically reconstructing the conductivity profiles of the tissues skin, bone, grey and white matter, confirming the potential and feasibility of the technique. Further research with real clinical measurements is a prerequisite for assessing its robustness and making it clinically applicable.

Throughout the PhD, we worked towards clinical relevant simulations. Initially, simple spherical head models are considered, but as we progress more sophisticated personalised head models are constructed. Realistic geometry and frequency-dependent anisotropic tissue properties are included based on T1- and diffusion-weighted MRI. Our developed solver initially uses circular coils, but is extended to allow for any coil design, including the usually applied and commercially available figure-of-eight coils. It can directly retrieve the position and orientation of the coil from the neuronavigation system.

The coil's shape is important, since it influences the induced field distribution

and consequently the site of stimulation. Nevertheless, our simulations reveal that this distribution also depends on the location and orientation of the coil with respect to the subject's head and on the inhomogeneous and anisotropic conductivity structure of the head.
The induced electric fields interact with the neural system - more specifically, with the voltage-gated ion channels at the plasma membrane of neurons - and may excite or inhibit certain brain regions by altering the membrane potentials. To study the precise mechanism of stimulation, we extend our electromagnetic solver towards the neurophysiology so to compute the spatio-temporal distribution of membrane potentials along the neural fibre bundles in the brain. After assuming straight and radially-oriented bundles, realistic 3D fibre reconstructions were generated using DTI-based tractography. Close to the brain region of interest that is targeted with the TMS coil, bundles of grouped neural fibres, called tracts, are selected. The induced electric field is mapped along the trajectories of these tracts and serves as the input for the considered stimulation mechanisms. We describe the response of these mechanisms on the membrane potential by a compartmental cable equation. All tracts are assumed to be myelinated neurons, containing sections representing dendrites, soma, axon hillock, initial segment, Ranvier nodes and myelinated internodes, and are modelled with passive and active membrane properties.
Despite the fact that the electric fields are maximal in the cortical surface close to the coil and penetrate into subcortical structures up to a limited depth, experiments reveal that standard TMS coils can also have effect on deeper brain regions. We believe that this is possible due to the connection via the neural fibre bundles between cortical and subcortical structures. TMS can depolarise the membrane potentials and initiate action potentials in the superficial neural tissue underneath the coil, which in turn can propagate along nerve bundles towards deeper regions.
The electromagnetic modelling has been validated by comparison with analytical and standard finite element methods. The neurophysiologic computations, namely the spatio-temporal variations of the membrane potentials, are more difficult to validate since it is not evident to measure the membrane potential variation directly in the brain. As an alternative, we numerically explain the variability of TMS during a speech mapping experiment.
The developed flexible and personalised toolbox models TMS from the macroscopic fields in the brain to the potentials on microscopic neuronal level. It is, to our knowledge, novel for the simulation of the TMS response and a valuable step towards fully case- and patient-specific results. Our simulations confirm that an accurate determination of the stimulation target in combination with a neuronavigation system is mandatory to perform reliable TMS studies. This toolbox offers many opportunities. It can, for example, investigate the sensitivity of coil positioning and the variability of the TMS effects among

the subjects. It can predict the mechanism and initial location of excitation and estimate which neural pathways contribute effectively to the stimulation. Moreover, it is suitable to be combined with TMS experiments and their electrophysiological responses recorded with EEG and/or EMG.
Unlike the King in "Alice in Wonderland" is saying, research is a never ending story. Further research should decrease the number of assumptions and especially include synapses for further communication to other neurons in the connected brain network, so to obtain a bigger picture of the neural response to TMS. We suggest validation is feasible by comparing the obtained spatio-temporal variation of the membrane potentials and the spreading of neuronal activity by measuring TMS-evoked EEG responses. We emphasise here the importance of well prepared and precisely executed experiments.
In the end we aim at computer-assisted TMS, in which patient-specific information is optimally integrated such as structural MRI, DTI, as well as the personalised conductivity estimation of biological tissues. When the patient's dysfunctioning brain network is identified, such smart TMS devices would find the best site for stimulation by detecting the reachable cortical structures of this network, and would accordingly optimise the coil specifications, such as shape, position, orientation and excitation waveform. Although we realise that there is still a long road ahead, we are confident to have taken a step in the right direction with this research.

List of Abbreviations

2D	Two Dimensional
3D	Three Dimensional
4CC	4-Cole-Cole model
A	Anterior
AC	Alternating Current
ACC	Anterior Cingulate Cortex
BA	Brodmann Area
BEM	Boundary Element Method
BiCG	BiConjugate Gradient method
CNS	Central Nervous System
CSF	CerebroSpinal Fluid
DBS	Deep Brain Stimulation
DC	Direct Current
DCS	Direct Cortical Stimulation
DLPFC	DorsoLateral PreFrontal Cortex
DTI	Diffusion Tensor Imaging
ECI	Eddy-Current Induction
ECT	ElectroConvulsive Therapy
EEG	ElectroEncephaloGraphy
EIT	Electrical Impedance Tomography
EMG	ElectroMyoGraphy
EPI	Echo Planar Imaging
FA	Fractional Anisotropy
FDA	Food and Drug Administration
FDM	Finite-Difference Method
FEM	Finite Element Method
fMRI	functional Magnetic Resonance Imaging
FOV	Field Of View
GABA	Gamma-AminoButyric Acid
GE	Gradient Echo
GM	Grey Matter

I	Inferior
ICMREIT	Induced Current Magnetic Resonance Electrical Impedance Tomography
IIM	Independent Impedance Method
IM	Impedance Method
L	Left
LTD	Long-Term Depression
LTP	Long-Term Potentiation
M1	Primary Motor cortex
MEG	MagnetoEncephaloGraphy
MEP	Motor Evoked Potential
MR	Magnetic Resonance
MRI	Magnetic Resonance Imaging
μSPECT	micro Single Photon Emission Computed Tomography
P	Posterior
PBiCG	Preconditioned BiConjugate Gradient method
PBiCGSTAB	Preconditioned BiConjugate Gradient STABilised method
PhD	Doctor of Philosophy
PET	Positron Emission Tomography
PMC	PreMotor Cortex
PNS	Peripheral Nervous System
PTN	Pyramidal Tract Neuron
R	Right
RF	Radio Frequency
ROI	Region Of Interest
rTMS	repetitive Transcranial Magnetic Stimulation
S	Superior
S1	Primary Somatosensory cortex
sACC	subgenual Anterior Cingulate Cortex
SMA	Supplementary Motor Area
SNR	Signal-to-Noise Ratio
SOR	Successive Over-Relaxation method
SPM	Statistical Parametric Mapping
TBS	Theta Burst Stimulation
tDCS	transcranial Direct Current Stimulation
tES	transcranial Electrical Stimulation
TMS	Transcranial Magnetic Stimulation
VNS	Vagus Nerve Stimulation
WM	White Matter

List of Symbols

Scalars, vectors and matrices

a	scalar
$\mathbf{a}$,$\mathbf{A}$	vectors
$\hat{\mathbf{a}}$,$\hat{\mathbf{A}}$	phasors
$\mathcal{A}$	matrix
$\bar{a}$	mean value of a
$\tilde{a}$	optimal reconstructed value of a
$\breve{a}$	correct value of a
a_i	i-th element of vector $\mathbf{a}$
$\mathcal{A}_{(i,j)}$	i,j-th element of matrix $\mathcal{A}$
$\mathcal{A}^{-1}$	inverse of matrix $\mathcal{A}$
$\mathcal{A}^{\mathrm{H}}$	Hermitian transpose of matrix $\mathcal{A}$
$\mathcal{A}^{\mathrm{T}}$	transpose of matrix $\mathcal{A}$
$\|\cdot\|$	L_2-norm or the Euclidean norm

Mathematical symbols

$\cdot$	dot product
$\times$	cross product
∇	gradient
$\nabla\cdot$	divergence
$\nabla\times$	curl
c_α	cosine of angle α: $\cos(\alpha)$
e	Euler's number: $e \approx 2.718281828$
e^x	natural exponential function
$\mathrm{Im}(a)$	imaginary part of a
j	imaginary number: $\sqrt{-1}$
$\mathrm{Re}(a)$	real part of a
s_α	sine of angle α: $\sin(\alpha)$
t_α	tangent of angle α: $\tan(\alpha)$
$\mathbb{1}$	identity matrix

Greek letters

γ_g	gyromagnetic ratio of hydrogen [rad/sT]
δ	penetration depth [m]
δ_d	loss angle between the total induced and reactive current [rad]
Δt	time step [s]
$\Delta\phi$	simulated phase difference
$\Delta\varphi$	measured phase difference
Δx, Δy, Δz	voxelsize in x-, y- and z-direction [m]
ε	electric permittivity [F/m]
ε_0	electric permittivity of vacuum [F/m]
ε'	real part of the electric permittivity [F/m]
ε''	imaginary part of the electric permittivity [F/m] (defined with a negative sign)
ε_e	total effective permittivity [F/m]
ε_r	electric relative permittivity [-]
ε_∞	electric permittivity in the high-frequency limit [F/m]
κ	over-relaxation parameter of the SOR algorithm [-]
λ	space constant of the neural membrane [m]
μ	magnetic permeability [H/m]
μ_0	magnetic permeability of vacuum [H/m]
μ_r	magnetic relative permeability [-]
ρ_f	free electric volume charge density [C/m^3]
σ	electric conductivity [S/m]
σ_e	total effective conductivity [S/m]
σ_i	frequency-independent ionic electric conductivity [S/m]
τ	rising time [s] time constant of the neural membrane [s]
χ_e	electric susceptibility [-]
χ_m	magnetic susceptibility [-]
ω	angular frequency [rad/s]

Latin letters

A	amplitude
$\mathbf{B}$	magnetic induction, magnetic flux density [Wb/m^2] or [T]
cc	correlation coefficient [-]
c_m	membrane's capacitance per unit length [F/m]
C_m	membrane's capacitance per unit area [F/m^2]
C_m^*	membrane's capacitance [F]

d	diameter [m]
$\mathbf{D}$	electric displacement, electric flux density [C/m^2]
$\partial\mathbf{D}/\partial t$	displacement current density [A/m^2]
$\mathbf{E}$	electric field intensity [V/m]
f	frequency [Hz]
f_L	Larmor frequency [Hz]
g_K, g_L, g_Na	conductance per unit length of the potassium, leakage and sodium channel [S/m]
G_K, G_L, G_Na	conductance per unit area of the potassium, leakage and sodium channel [S/m^2]
G_a^*	axial conductance [S]
h	open probability of the inactivation gate for sodium [-]
$\mathbf{H}$	magnetic field intensity [A/m]
i_K, i_L, i_Na	potassium, leakage and sodium current per unit length [A/m]
i_m	membrane's current per unit length [A/m]
I_a	axial current [A]
I_m	membrane's current [A]
$\mathbf{I}$	branch current [A]
$\mathbf{I}_\mathrm{tot}$	total induced branch current [A]
$\mathbf{J}_\mathrm{c}$	conduction electric current density [A/m^2]
$\mathbf{J}_\mathrm{f}$	free electric current density [A/m^2]
$\mathbf{J}_\mathrm{s}$	source electric current density [A/m^2]
$\mathbf{J}_\mathrm{tot}$	total induced current density [A/m^2]
K	cost function
l	local space parameter along the neural trajectory [m]
L	length of the neural tract [m]
$\mathbf{L}$	loop current [A]
m	open probability of the activation gate for sodium [-]
$\mathbf{m}$	unit vector in the direction of maximal induced currents
$\mathbf{M}$	magnetisation [A/m]
n	open probability of the activation gate for potassium [-]
$\mathbf{n}$	unit vector normal
N_x, N_y, N_z	number of voxels in x-, y- and z-direction [-]
$\mathbf{O}$	origin or centre [m]
$\mathbf{p}$	material parameter vector
$\mathbf{P}$	dielectric polarisation [C/m^2]
Q1, Q3	25th and 75th percentile
r_a	axial resistance per unit length [Ω/m]
r_m	membrane's resistance times unit length [Ωm]
$\mathbf{r}$	location [m]
R_a	resistivity of the axoplasm [Ωm]
std	standard deviation [-]

t	time [s]
T	period [s]
TE	echo time [s]
TR	repetition time [s]
V	electric transmembrane potential [V]
V_{K}, V_{L}, V_{Na}	Nernst equilibrium potential for the potassium, leakage and sodium channel [V]
V_{r}	resting membrane potential [V]
W	energy [J/s] or [W]
Z	impedance [Ω]

List of Publications

Articles in international SCI journals

1. N. De Geeter, G. Crevecoeur, and L. Dupré, "An efficient 3-D eddy-current solver using an independent impedance method for transcranial magnetic stimulation", IEEE *Transactions on Biomedical Engineering*, 58(2):310-320, 2011. DOI:10.1109/TBME.2010.2087758

2. N. De Geeter, G. Crevecoeur, and L. Dupré, "Eddy-current simulations using an independent impedance method in anisotropic biological tissues", *IEEE Transactions on Magnetics*, 47(10):3845-3848, 2011. DOI:10.1109/TMAG.2011.2145361

3. N. De Geeter, G. Crevecoeur, L. Dupré, W. Van Hecke, and A. Leemans, "A DTI-based model for TMS using the independent impedance method with frequency-dependent tissue parameters", *Physics in Medicine and Biology*, 57(8):2169-2188, 2012. DOI:10.1088/0031-9155/57/8/2169.

4. T. Wyckhuys, N. De Geeter, G. Crevecoeur, S. Stroobants, and S. Staelens, "Quantifying the effect of repetitive transcranial magnetic stimulation in the rat brain by SPECT CBF scans", *Brain Stimulation*, 6(4):554-562, 2013. DOI:10.1016/j.brs.2012.10.004.

5. N. De Geeter, G. Crevecoeur, and L. Dupré, "A numerical study on conductivity estimation of the human head in the low frequency domain using induced current MR phase imaging EIT with multiple gradients", *IEEE Transactions on Magnetics*, 49(9):5004-5010, 2013. DOI:10.1109/TMAG.2013.2250985.

6. N. De Geeter, G. Crevecoeur, A. Leemans, and L. Dupré, "Effective electric fields along realistic DTI-based neural trajectories for modelling the stimulation mechanisms of TMS", *Physics in Medicine and Biology*, 60(2):453-471,

2014. DOI:10.1088/0031-9155/60/2/453.

Articles in conference proceedings

1. N. De Geeter, G. Crevecoeur, and L. Dupré, "Low-parametric Induced current-magnetic resonance electrical impedance tomography for quantitative conductivity estimation of brain tissues using a priori information : a simulation study", *Proceedings of the 32nd Annual International Conference of the IEEE Engineering in Medicine and Biology Society (EMBC)*, Buenos Aires, Argentina, August 31 - September 4, 2010.

2. N. De Geeter, G. Crevecoeur, and L. Dupré, "Efficient numerical methods for computer-assisted TMS & conductivity estimation", *Proceedings of the 11th FEA PhD Symposium*, Ghent, Belgium, December 5, 2010.

3. N. De Geeter, G. Crevecoeur, and L. Dupré, "Eddy-current simulations using an Independent Impedance Method in anisotropic biological tissues", *Proceedings of the International Conference on Magnetism (INTERMAG)*, Taipei, Taiwan, April 25-29, 2011.

4. N. De Geeter, G. Crevecoeur, and L. Dupré, "Conductivity estimation of the human brain in the low frequency domain using IC-MREIT with multi gradient echo sequences", *Proceedings of the International Conference on Magnetism (INTERMAG)*, Vancouver, May 7-11, 2012.

5. T. Wyckhuys, N. De Geeter, G. Crevecoeur, S. Stroobants, and S. Staelens, "Use of microSPECT in quantifying the effect of repetitive transcranial magnetic stimulation in the rat", *Proceedings of the Annual Meeting of the Society of Nuclear Medicine (SNM)*, Miami Beach, Florida, USA, June 9-13, 2012.

6. N. De Geeter, G. Crevecoeur, T. Wyckhuys, L. Dupré, and S. Staelens, "A modeling study of the neurophysiological response to transcranial magnetic stimulation in a simple rat head model", *Proceedings of the 18th International Conference on Biomagnetism (BIOMAG)*, Paris, France, August 26-30, 2012.

7. N. De Geeter, G. Crevecoeur, and L. Dupré, "Numerical study on IC-MREIT with multiple gradient echo sequences for the conductivity estimation of brain tissues", *Proceedings of the 12th Workshop on Optimization and Inverse Problems in Electromagnetism (OIPE)*, Ghent, Belgium,

September 19-21, 2012.

8. G. Crevecoeur, N. De Geeter, and L. Dupré, "Optimized small animal transcranial magnetic stimulators using distributed coils", *Proceedings of the 5th International Conference on Non-invasive Brain Stimulation (NBS)*, Leipzig, Germany, March 19-21, 2013.

9. N. De Geeter, G. Crevecoeur, and L. Dupré, "Modeling the active neurodynamic behavior of rTMS in the prefrontal cortex of a realistic human head", *Proceedings of the 5th International Conference on Non-invasive Brain Stimulation (NBS)*, Leipzig, Germany, March 19-21, 2013.

10. N. De Geeter, G. Crevecoeur, and L. Dupré, "The effect of inaccurate targeting of the left dorsolateral prefrontal cortex on TMS response", *Proceedings of the 6th International IEEE EMBS Conference on Neural Engineering (NER)*, San Diego, California, USA, November 6-8, 2013.

11. N. De Geeter, G. Crevecoeur, R. Ilmoniemi, and L. Dupré, "Modeling the active neurodynamics of TMS using realistic neural tracts", *Proceedings of the 19th International Conference on Biomagnetism (BIOMAG)*, Halifax, Canada, August 24-28, 2014.

12. N. De Geeter, G. Crevecoeur, and L. Dupré, "Modeling the response to Transcranial Magnetic brain Stimulation", *Proceedings of the 15th FEA Research Symposium*, Ghent, Belgium, December 5, 2014.

13. N. De Geeter, P. Lioumis, G. Crevecoeur, and L. Dupré, "Simulating the variability of TMS responses in a speech mapping case study", *Proceedings of the 2nd International Conference on Basic and Clinical Multimodal Imaging (BaCI)*, Utrecht, The Netherlands, September 1-5, 2015, submitted.

A Diffusion Tensor-Based Computational Model for Transcranial Magnetic Stimulation: from Macroscopic Fields to Neuronal Membrane Potentials

Introduction to TMS

Basically, they hook up a machine to your head and blast you with low-level electromagnetic pulses in order to alter neural activity.

a woman who was treated with TMS for depression, sharing her experience

1

Introduction to transcranial magnetic stimulation

Transcranial magnetic stimulation (TMS) is a non-invasive technique that has the ability to enhance or suppress brain activity. With minimal discomfort, it induces electric currents and an electric field in the brain via a rapidly changing magnetic field, generated by a coil positioned above the scalp surface. This induced electric field interacts with the neural system and may excite or inhibit certain brain regions by altering the membrane potentials of neurons.

1.1. Historical background

The field of electrophysiology was born in the late eighteenth century with the discovery of bioelectricity by the Italian physician Luigi Galvani. While dissecting dead frogs, he observed that the muscles of their legs twitched when struck by an electrical spark. Galvani's work was continued by his nephew, Giovanni Aldini. He believed that bioelectricity could reanimate dead tissue. To prove this, Aldini travelled extensively throughout Europe with his experiments, inducing muscular contractions in dead animals through the application of direct electric current. However, he did not stop with frogs and dogs, but continued with humans. His most famous public demonstration was per-

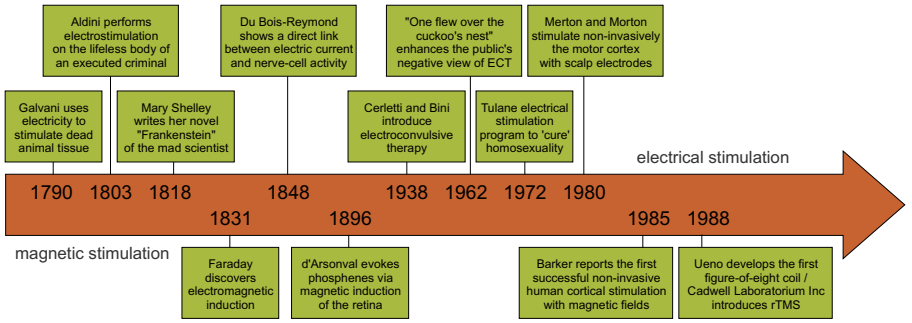

Figure 1.1: Timeline of milestones in electrical and magnetic stimulation leading to the development of TMS.

formed on an executed criminal in London in 1803. With this incident, several important ethical questions began to emerge, first, only in the high levels of education and research, later on also in the non-scientific community through the novel "Frankenstein". Inspired by Galavani's bioelectricity, English writer Mary Shelley wrote this novel in 1818 about the eccentric scientist Victor Frankenstein, who created a monster in an unorthodox experiment. It forever shaped the popular image of the mad scientist.

In 1831, the English physicist Michael Faraday discovered electromagnetic induction, the physical principle of electromagnetic stimulation. He observed the production of an electromotive force across a conductor when it is exposed to a varying magnetic field. Thus, when electric current passes through a TMS coil, it generates a magnetic field and the rate of change of this field determines the induction of a secondary current in a nearby conductor. Faraday's law was generalised in 1861 by the Scottish physicist and mathematician James Clerk Maxwell. He provided the mathematical unifying proof for the reciprocal relation between electricity and magnetism. Nowadays, the four Maxwell's equations underlie many modern technologies.

The German physiologist Emil du Bois-Reymond was the first to prove the electrical nature of nerve signals. He discovered that muscular contraction is accompanied by chemical changes in the muscle, and, in 1843-1848, he demonstrated that ions are formed within a nerve or muscle cell, leading to a negative change in potential from the resting state, when it is stimulated by an electric current.

The first scientific attempts to use magnetic energy to alter brain activity were conducted by Arsenne d'Arsonval in 1896 and Silvanus Thompson in 1910. While human subjects had placed their heads inside a large conduction coil, they stimulated the retina and evoked perception of light flashes, so-called phosphenes, equal to the spots and colours you see when you rub your eyes.

Many years later, this technique would be refined as TMS.
The initial clinical trial of electroconvulsive therapy (ECT), formerly known as electroshock therapy, was performed in 1938 by the Italian neuropsychiatrists Ugo Cerletti and Lucio Bini. ECT uses an electrical current passing through the brain to create a therapeutic seizure, which causes a dramatic reset of the brain. The therapy was intended to treat the manic symptoms of schizophrenic patients. ECT gained widespread popularity among psychiatrists as a form of treatment in the 1940s and 1950s. However, this overuse revealed serious side effects, such as skin burn, prolonged seizures, full-scale convulsion, cardiovascular and pulmonary complications and amnesia, thereby creating a strong negative public attitude towards the therapy. This adverse perception was enhanced by the 1962 novel "One flew over the cuckoo's nest" of Ken Kesey, adapted for a film in 1975, in which ECT was considered as a psychiatric painful tool of punishment. Meanwhile, in 1972, another incident raised ethical concerns. Researchers of the Tulane University attempted to 'cure' a patient of his homosexuality by combining behaviour modification via deep-brain electrical stimulation of the septal area with forced heterosexual interactions provided by a female prostitute. Merton and Morton showed in 1980 that it was possible to stimulate the motor area of the cortex through the intact scalp, via a short high-voltage electric shock (Merton and Morton, 1980). High voltages are needed to overcome the poor conducting properties of scalp and skull, but they cause considerable discomfort and pain, due to the stimulation of nerve endings in the skin and superficial muscles. In current practice, ECT is administered under general anaesthesia with muscle relaxants, overcoming most side effects, and it follows ethical guidelines leading to responsible and transparent practices. Although ECT has shown to be an effective treatment for severe depression and schizophrenia, its use remains impacted by its unfavourable public opinion.
Transcranial magnetic brain stimulation provided a solution. Unlike ECT, TMS does not require anaesthesia and does not produce a seizure, it is much safer and far less painful. Moreover, TMS can be targeted to a specific site in the brain in comparison to the more generalised electrical stimulation. The first reliable TMS stimulator was developed in Sheffield, England, in 1985 by Anthony Barker and colleagues (Barker et al., 1985). They performed TMS over the primary motor cortex, causing muscle contractions in the hand, similar as Merton and Morton did, but with minimal discomfort. Since then, TMS has gone through several major stages of development, always well considered and with great caution, as compared with ECT. Moreover, the application of TMS in research and clinical settings follows safety and ethical guidelines, which are regularly reviewed and updated (Horvath et al., 2011; Rossi et al., 2009; Wassermann, 1998). In 1988 David Cohen and Shoogo Ueno (Ueno et al., 1988) came with the idea and realisation of the figure-of-eight coil, to generate

a more focused electric field in the brain than with the original circular coil. That same year, Cadwell Laboratories Inc. introduced repetitive TMS (rTMS) with water-cooled coils, to deliver trains of stimuli. Newer developments include the addition of stereotactic navigation to existing TMS technology and the integration with other imaging techniques, such as positron emission tomography (PET), electromyography (EMG), electroencephalography (EEG) and functional magnetic resonance imaging (fMRI). The neuronavigation system allows users to map the stimulation target on an anatomy magnetic resonance (MR) image of the patient's or subject's head, and to position the coil with high accuracy and reproducibility. Risto Ilmoniemi was the first to report the mapping and spreading of neuronal TMS activity based on TMS-evoked EEG responses, revealing cortical reactivity and connectivity (Ilmoniemi et al., 1999, 1997). TMS stimulators, whether or not combined with neuronavigation or other imaging techniques, are now commercialised worldwide by companies such as Nexstim Ltd. (Helsinki, Finland), Magstim Inc. (Whitland, United Kingdom) and MagVenture Inc. ® (Atlanta, Georgia USA).
Fig. 1.1 outlines the historical background of TMS with the different milestones. Some of these moments are captured on photo and shown in Fig. 1.2.

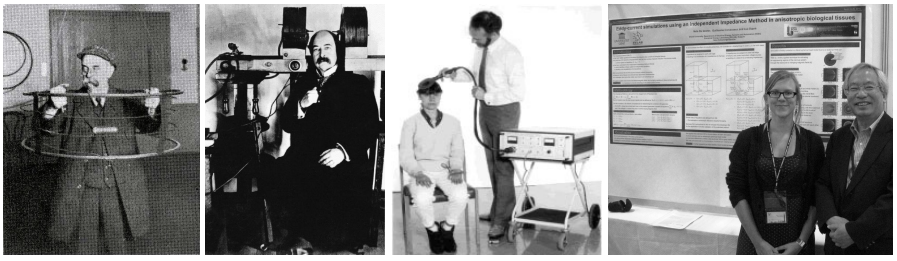

Figure 1.2: From left to right. D'Arsonval demonstrating that the current induced in his arms by a high-frequency solenoid coil will light a lamp, 1893. Thompson showing his primitive magnetic stimulator for phosphene experiments, 1910. Barker demonstrating his TMS device over the primary motor cortex, 1991. Ueno and myself presenting our work at the IEEE International Magnetics Conference, INTERMAG, 2011.

1.2. Basic characteristics

Fig. 1.3 illustrates the basic phenomena that occur in TMS. A magnetic stimulator stores electrical current, and then discharges it in one or more brief pulses through the TMS coil. With the stimulators used nowadays, this excitation current can reach values of more than 5 kA. Such a pulse lasts less than 1 ms and can be repeated up to 50 times per second. According to Biot-Savart's law, each current pulse gives rise to a strong, but also very brief and rapidly changing magnetic field, with a strength directly under the coil up to 4 T, which is

approximately 60 000 times the intensity of the earth's magnetic field. This resultant time-varying magnetic field induces an electric field in the underlying tissue, through Faraday's law of induction. The maximum electric fields and corresponding eddy currents induced in the brain are typically around 100 V/m and 100 A/m^2, respectively.

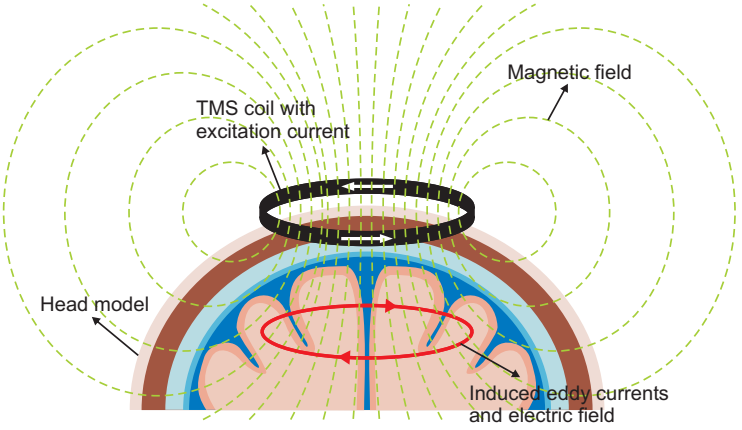

Figure 1.3: Basic principles of TMS. Electrical currents and electric field are induced in the brain through magnetic pulses applied by means of the current-carrying coil positioned above the head.

Transcranial literally means through the skull. Indeed, magnetic fields traverse the scalp and skull without impedance, i.e. the magnetic material properties of biological tissues are the same as those in air. This represents a major advantage over the direct application of electricity due to enhanced comfort of the subject and improved control of localisation and dosage. Even though this magnetic field gave its name to TMS, it is the induced electric field that leads to neuronal stimulation (Roth and Basser, 1990). It may cause depolarisation of the neurons' membrane from its resting potential -84 mV. When enough polarisation accumulates to reach a certain threshold, an action potential (a typical course with a peak of more than 40 mV) can be triggered and propagate along the neuron and to other adjacent neurons, resulting in communication of information.

According to Biot-Savart's law, the magnetic field strength decreases quadratically with distance. As a result, the direct local effects of TMS are confined to the areas that face the skull. However, the brain consists of highly functionally interconnected structures, leading to indirect distant effects of TMS.

The magnetic stimulator consists mainly out of two components: a charge-discharge system and a current carrying excitation coil.

1.2.1 Stimulator circuit

A typical, but simplified biphasic stimulator circuit (Davey and Epstein, 2000) is schematically depicted in Fig. 1.4. Low-voltage alternating current (AC) is transformed into high-voltage direct current (DC), which charges the capacitor C. A trigger-controlled switch, usually a thyristor, which is capable of switching a high current in a short period of time, enables this capacitor to discharge through the TMS coil. A diode is connected in parallel with this thyristor in order to allow current flow in the opposite direction and thus capacitor recharging. A monophasic circuit is similar to the biphasic one, except that the diode of the switch is absent, so that the current through the TMS coil remains positive or zero. For the biphasic and monophasic TMS waveforms, see later Fig. 1.8. Without the switching circuitry and control electronics, the discharge circuit is basically a parallel RLC circuit, characterised by the total resistance R, inductance L and capacitance C. Typical ranges of these parameters are listed in Table 1.1 (Marcolin and Padberg, 2007). Both R and L are mainly determined by the TMS coil windings and are set to the lowest practical values to minimise heating while generating the desired current waveform.

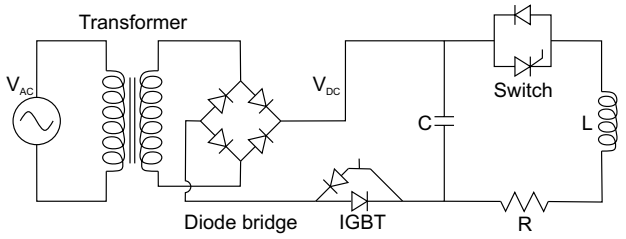

Figure 1.4: Simplified charge-discharge circuit for biphasic TMS pulse generation. The switch consists out of a diode and a thyristor. Figure adapted from (Davey and Epstein, 2000).

Table 1.1: Typical parameter values of the stimulator circuit (Marcolin and Padberg, 2007).

Parameter	Typical range
Resistance R	20-80 mΩ
Inductance L	10-30 μH
Capacitance C	10-250 μF
Peak voltage	0.5-3 kV
Peak current	2-10 kA
Pulse width	60-1000 μs

In the discharging RLC circuit, the following applies:

$$L\frac{\partial^2 I}{\partial t^2} + R\frac{\partial I}{\partial t} + \frac{I}{C} = 0. \tag{1.1}$$

At time t zero, the current I is zero and all the energy W is stored in the capacitor, with V_{DC} the initial voltage across this capacitor.

$$W = \frac{CV_{\mathrm{DC}}^2}{2} \tag{1.2}$$

This initial condition results in a damped sinusoidal current:

$$I(t) = A_{\mathrm{c}}\, e^{-\alpha_{\mathrm{c}} t} \sin(\omega_{\mathrm{c}} t), \tag{1.3}$$

with

$$A_{\mathrm{c}} = \frac{V_{\mathrm{DC}}}{\omega_{\mathrm{c}} L},\ \ \alpha_{\mathrm{c}} = \frac{R}{2L},\ \ \omega_{\mathrm{c}} = \sqrt{\frac{1}{LC} - \alpha_{\mathrm{c}}^2}. \tag{1.4}$$

The duration of one pulse cycle is approximately $2\pi\sqrt{LC}$, since R is much smaller than $\sqrt{4L/C}$ (Peterchev et al., 2008), see Table 1.1.

1.2.2 Coil configuration

Although many researchers have explored unique coil designs for increased focality, efficacy and penetration depth (Crowther et al., 2011; Deng et al., 2013; Roth et al., 2002; Zangen et al., 2005), the most common shapes currently used are the single circular and figure-of-eight coils, both depicted in Fig. 1.5. The latter consists out of two circular coils, located side-by-side, and is in literature also called a double or butterfly coil. TMS coils are usually tightly wound concentric turns of rectangular copper wire, which are adequately insulated and housed in plastic covers.

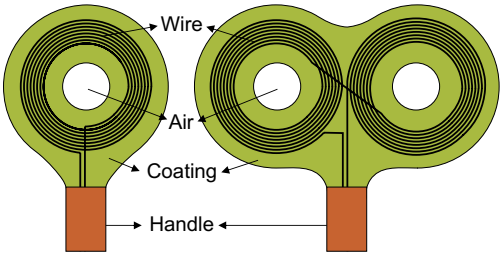

Figure 1.5: (Left) The circular and (right) figure-of-eight coil are the two most common coil configurations. The winding profiles are drawn based on X-ray pictures (Salinas et al., 2007; Thielscher and Kammer, 2004).

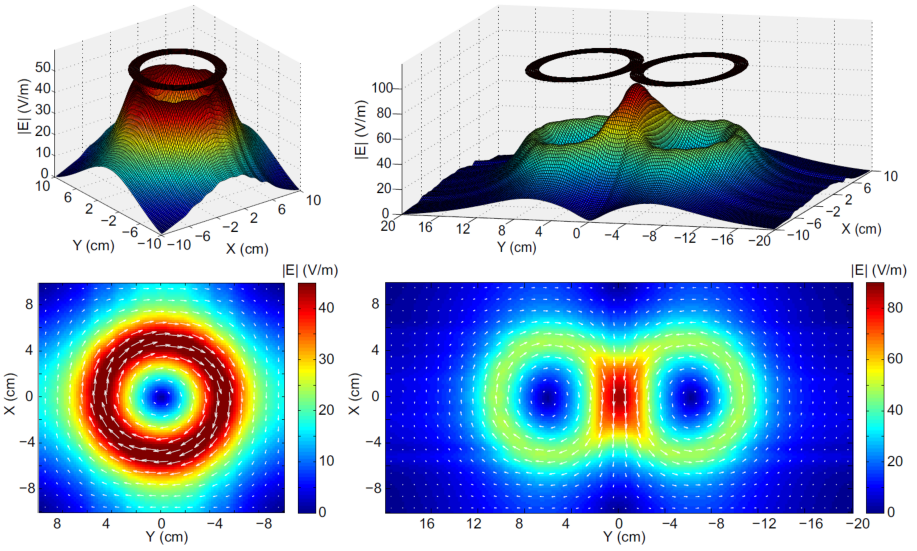

Figure 1.6: Circular and figure-of-eight coils have different induced electric field distributions. The modelled circular coil has a radius of 5 cm and 9 turns and the figure-of-8 coil consists of two such circular coils. A biphasic pulse of 640 A per loop is applied, resulting in 5.76 kA, with a pulse length of 230 μs, and thus a peak excitation current time derivative of approximately 100 A/μs. The strength of the electric field E induced in air in a plane 1 cm below the coils is plotted (in V/m).

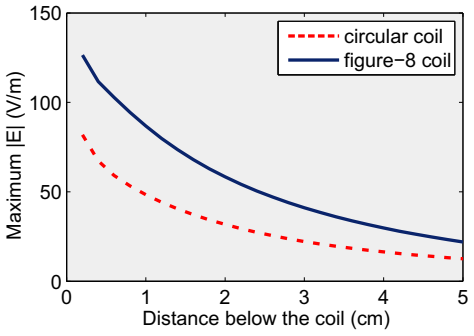

Figure 1.7: The induced electric field decays with increased distance below the coil. The maximum strengths of the electric field E induced in air by the circular and figure-of-eight coils of Fig. 1.6 are plotted.

In Fig. 1.6 the distributions of the electric field induced in air in a plane 1 cm below the coils are compared. Fig. 1.7 shows the decay of both fields with increased distance below the coils. These results were obtained with the in this PhD presented modelling method and are equal to those in literature (Ilmoniemi et al., 1999). The field is strong under the coil windings and drops

to zero in the centre of the winding, and thus in the middle of a circular coil, and for regions far away from the coil. In contrast to that, a figure-of-eight coil induces a maximum electrical field in the middle, under the intersection of its two windings, with a magnitude that amounts almost double the field's maximum under the circular coil. As shown by Heller and van Hulsteyn (1992), the stimulation intensity is always maximum at the cortical surface, for any configuration or superposition of TMS coils. However, it is possible to develop a coil design where the rate of decay from the surface is attenuated compared to Fig. 1.7, such that the percentage of electric field intensity is increased in deeper brain regions, relative to the maximal field at the cortex (Zangen et al., 2005). Researchers have also been investigating the use of conductive shields, placed between the TMS coil and the subject's head (Kim et al., 2006). These shields can inhibit or divert the generated magnetic field, leading to more focussed stimulation. The coil's shape is important, since it directly influences the induced electric field distribution and, thus, the site of stimulation. Nevertheless, this distribution also depends on the location and orientation of the coil with respect to the subject's head and on this head itself, such as the electric conductivity structure. We will emphasise more on these issues in Section 7.2.

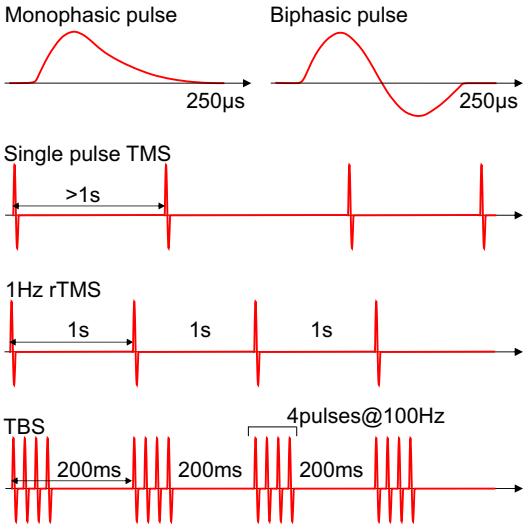

Figure 1.8: Typical monophasic and biphasic TMS waveforms. TMS is commonly applied in single pulses or repetitively (rTMS). Theta burst stimulation (TBS) is a relative new specific type of rTMS at higher frequencies.

The most widely used excitation pulse shapes in TMS are monophasic and biphasic pulses, see Fig. 1.8. For biphasic pulses, a considerable part of the

energy returns to the capacitor at the end of the discharge cycle, thus shortening the time for recharging and saving energy. For example, suppose that at the end of the biphasic pulse V_{DC} remains 60% of its initial value, than the energy needed for recharging is significantly reduced, namely to 64%, see equation (1.2). This makes biphasic current pulses more suitable for repetitive TMS (rTMS), where multiple stimulation pulses are delivered in succession, typically at frequencies in the range [1-100] Hz. Moreover, it was found that the threshold for neuronal activation is generally lower for biphasic compared to monophasic pulses. We will focus on biphasic pulses in this PhD. Initially, we will model this stimulation pulse as a simple sinusoidal current, but in Section 5.2.3 we will investigate the influence of this simplification by comparing it with the damped sinusoidal current wave of equation (1.3).

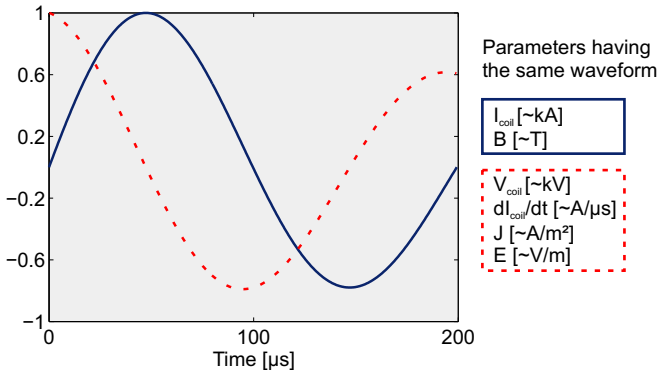

Figure 1.9: Typical waveforms during a biphasic TMS pulse of the excitation current I_{coil}, the magnetic flux density B, the excitation current's time derivative dI_{coil}/dt, the voltage across the stimulation coil V_{coil}, the induced current density J and the induced electric field E and their corresponding order of magnitudes.

Fig. 1.9 illustrates the typical biphasic waveforms. Suppose that we apply a damped sinusoidal excitation current with parameter values V_{DC} = 1.4 kV, R = 50 mΩ, C = 100 μF and L = 10 μH, as in (Wassermann et al., 2008), resulting in an amplitude A_c of 4.441 kA and a working frequency f_c = 5.017 kHz, see equations (1.3-1.4). This current's time derivative is triphasic, with a maximum of 140 A/μs = V_{DC}/L). Remark that the curves in Fig. 1.9 are normalised. The magnetic flux density produced by the coil will exhibit the same waveform as the excitation current, whereas the voltage across the stimulation coil, the induced current density and the induced electric field will exhibit the same waveform as the excitation current's time derivative. Also the induced voltage in the brain follows a similar triphasic curve. When its amplitude is high enough, neural membranes are most likely to depolarise or hyperpolarise, when the voltage is positive or negative, respectively. For the

biphasic TMS pulse of Fig. 1.9, depolarisation will occur first ($\pm$ 0-50 μs), followed by a larger hyperpolarisation ($\pm$ 50-150 μs). Since activation may only occur when the membrane is sufficiently depolarised, the threshold for neuronal activation would thus be lower when the current's polarity would be reversed.
A broad variety of pulse sequences are used in practice, such as single pulse TMS and repetitive TMS (rTMS). One can differentiate between conventional rTMS, when single pulses are repeated at a fixed frequency, and patterned rTMS, when short rTMS trains at a high frequency are interleaved by periods of no stimulation, such as theta burst stimulation (TBS). All of these protocols are illustrated in Fig. 1.8. In contrast to single pulse, rTMS can produce frequency-dependent effects on the neural activity that last much longer than the period of stimulation. A typical 1Hz rTMS session lasts 30 minutes. Generally, low-frequency rTMS ($\leq$1 Hz) will reduce the cortical brain excitability, whereas high-frequency rTMS ($>$5 Hz) will enhance it. Design developments have made it possible to apply multiple stimuli at higher frequencies, such as in theta burst stimulation by which 3 to 5 pulses at more than 50 Hz are repeated every 200 ms (Huang et al., 2005). This frequency of 5 Hz falls within the theta band of the EEG, explaining the name.

1.2.3 Neuronavigation

The TMS coil can be positioned manually above the head, based on external landmarks or a visible response, such as thumb twitches and the corresponding measurable motor-evoked potentials (MEPs). The variability between operators handling the coil and the accuracy with which they control it, but also the variability between brains and the anatomical structures (Bartley et al., 1997; Sporns et al., 2005) cause this way of working to be unspecific and poorly reproducible. Nowadays, many hospital and research centres possess neuronavigated TMS devices, as represented in Fig. 1.10, by which the coil is positioned based on individual MRI. First, the subject's MRI data is loaded into the computer. Subsequently this data is co-registered to the real head by specifying landmarks, typically the nose and ears, using a digitising pen, a track device that the subject is wearing and a stereotactic camera. Similar trackers are attached to the TMS coil, such that the coil position and orientation relative to the subject's head can continuously be monitored. Spherical head model solutions are used to approximate current and electric field distributions induced in the head. This simple but fast modelling method enables the operator to see in real-time a prediction of the stimulated location and thus to position the coil more specifically. Moreover, it makes TMS studies more reliable and reproducible.
Combining TMS with stereotactic navigation is much like a car driver using a

GPS navigation system. Although it is a major improvement on manual coil positioning, the applied electromagnetic calculations are performed on spherical head models, which lead to inaccurate results by ignoring the true interaction between TMS and the actual tissues and their geometry.

Figure 1.10: Nexstim is one of the leaders in neuronavigated TMS with their Navigated Brain Stimulation. Figure from the Nexstim Ltd. (Helsinki, Finland) website.

1.3. Brain structure and function

We first explain some conventions in Fig. 1.11, in order to visualise and clearly refer to the different planes and directions in the remaining part of the PhD. In this Section, we start from the nervous system and discuss the different structures towards the cerebral cortex (Brodal, 2004). More details on the neurophysiology at the level of the neurons can be found in Chapter 6.

1.3.1 Nervous System

The central nervous system (CNS) consists of the brain and the spinal cord and is connected to the rest of the body through the peripheral nervous system (PNS), see Fig. 1.12 (Kandel et al., 2000). Together they control our daily life. The PNS includes the nerves, which can be divided in two types. The sensory or afferent nerves conduct impulses from the receptors toward the CNS, whereas the motor or efferent nerves carry impulses from the CNS to our organs, glands and muscles. Besides these two somatic components providing voluntary control, the PNS has also an autonomic part which functions below

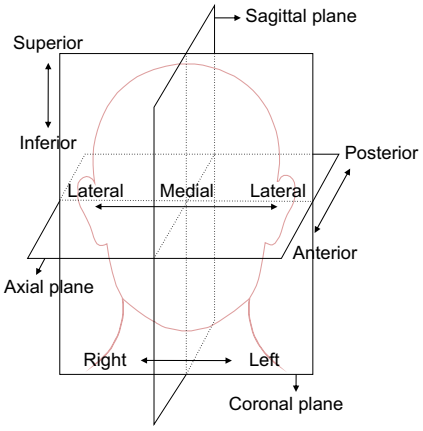

Figure 1.11: Anatomical directional terms and planes or sections of the human head. The sagittal plane is a vertical plane that divides the head into right and left regions. The coronal plane is a vertical plane that divides the head into front (anterior) and back (posterior) regions. The axial plane is a horizontal plane that divides the head into upper (superior) and lower (inferior) regions.

the level of consciousness. All these PNS nerves connect the various structures of the body with the brain, or directly , but mainly via the spinal cord, which is the highway for communication between the brain and the nerves throughout the body. Since the time-varying magnetic pulses of TMS are delivered to the brain, we will emphasise on this complex structure that serves as the centre of the nervous system.

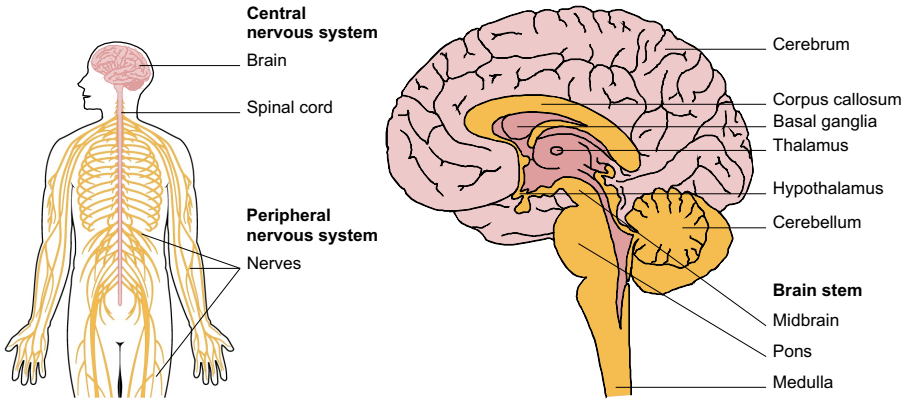

Figure 1.12: (Left) Construction of the nervous system. (Right) Medial view of sagittal brain section with the major structures.

1.3.2 Brain

At birth, the human brain weights on average 400 g. While the number of brain cells remains nearly constant, these cells become larger and they develop more interconnections during the first 6 years. At that age, the brain reaches its full size and weights almost 1.5 kg. There are about 86 billion neurons in the brain, but unlike most other cells, these basic units of the CNS cannot regrow after damage.

The brain consists of several major structures, illustrated in Fig. 1.12. The most rostral part of the brain is called the forebrain, which can be divided in the diencephalon and telencephalon. The first contains structures such as the thalamus and hypothalamus which are responsible for motor control, relaying sensory information and controlling autonomic functions. The telencephalon contains the cerebrum, the largest part of the brain (about two-thirds). It is divided into the right and the left hemisphere, both controlling the opposite (contralateral) side of the body. The outer portion of the cerebrum is a layer of grey matter, called the cerebral cortex, while the bulk of the deep parts is white matter. Grey matter contains dendrites and neural cell bodies, called soma, whereas white matter is composed of bundles of axons, which connect the various grey matter areas to each other. We will emphasise more on the neural structure in Section 6.1. The limbic system lies just beneath the cerebral cortex, on both sides of the thalamus. It is involved in many of our emotions and motivations. It is a complex set of structures such as the hippocampus and amygdala, both part of the cerebrum, and the hypothalamus, see Fig. 1.13. The basal ganglia, including the striatum (caudate nucleus and putamen) and substantia nigra, are intimately connected with the limbic system and the cortex. They are responsible for control of voluntary motor movements, cognition, emotion, routine behaviours and reward experiences. Tourette syndrome, obsessive-compulsive disorder, dystonia, Parkinson's and Huntington's diseases are all related to damage of the basal ganglia.

The brain stem is the posterior part of the brain, connecting it with the spinal cord, and includes the midbrain, pons and medulla. It manages our breathing, heart rate, temperature, sleep, attention and digestion. The brain stem maintains these essential functions autonomically. The cerebellum is a structure located in the back of the brain and is well known for its involvement in balance and coordination. While voluntary motion is managed in the motor cortex, the cerebellum takes over many learned skills, like bicycling or driving a car, and fine muscle control.

Cerebrospinal fluid (CSF) is a fluid, produced from arterial blood, that acts as a cushion to protect the brain from shocks and plays an important role in the autoregulation and metabolism of the CNS. With a total volume of about 200 ml it circulates along the spinal cord, the four interconnected brain cavities called ventricles, and the subarachnoid space between the brain and skull. The

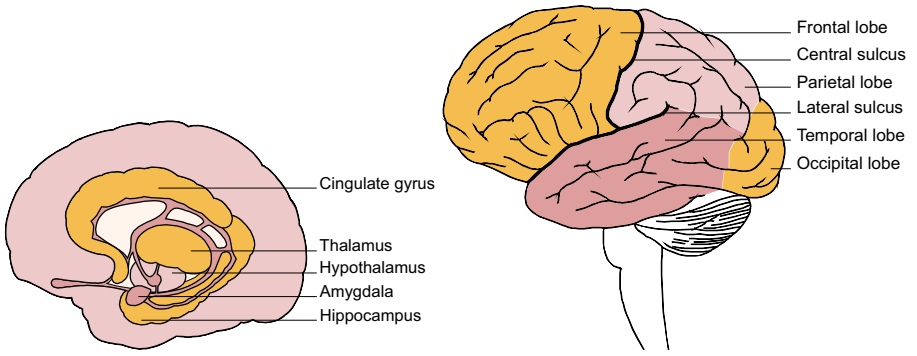

Figure 1.13: (Left) Structures in the limbic system, which controls many essential human behaviours. (Right) Lateral surface of the brain, with the cerebral cortex divided in four lobes by some major sulci.

lateral ventricles are the largest and located in both hemispheres. The third ventricle is in the diencephalon between the right and left thalamus and the fourth runs between the pons, medulla and cerebellum.
Since the electric fields evoked by TMS affect directly the cerebral cortex, we will zoom in on this structure and its different areas and corresponding functions.

1.3.3 Cerebral cortex

The cerebral cortex is an on average 2 to 4 mm thick, large surface of neural tissue that covers the brain. To fit within the constrains of the skull, it is extensively folded, resulting in cortical ridges, separated by grooves, called gyri and sulci respectively.
The cerebral cortex is conventionally divided in four lobes, as depicted in Fig. 1.13. The frontal lobe is located at the front of the brain and controls our memory, thinking, reasoning, movement and language production. This lobe is responsible for our personality and emotional traits, since it is well connected with the limbic system, where emotion is housed. The temporal lobe performs learning, hearing and speech perception. In about 90% and 70% of right- and left-handed individuals, respectively, the centres for language recognition and comprehension lie in the left temporal lobe. The parietal lobe monitors touch and sensation and body orientation. The occipital lobe controls our sight reception and interpretation, and is therefore often called the visual cortex.
The deep groove that separates the parietal and frontal lobes is the central sulcus. The lateral sulcus separates the parietal and temporal lobes. The cingulate gyrus lies just above the corpus callosum, close to the limbic system, and provides a pathway from the thalamus to the hippocampus.

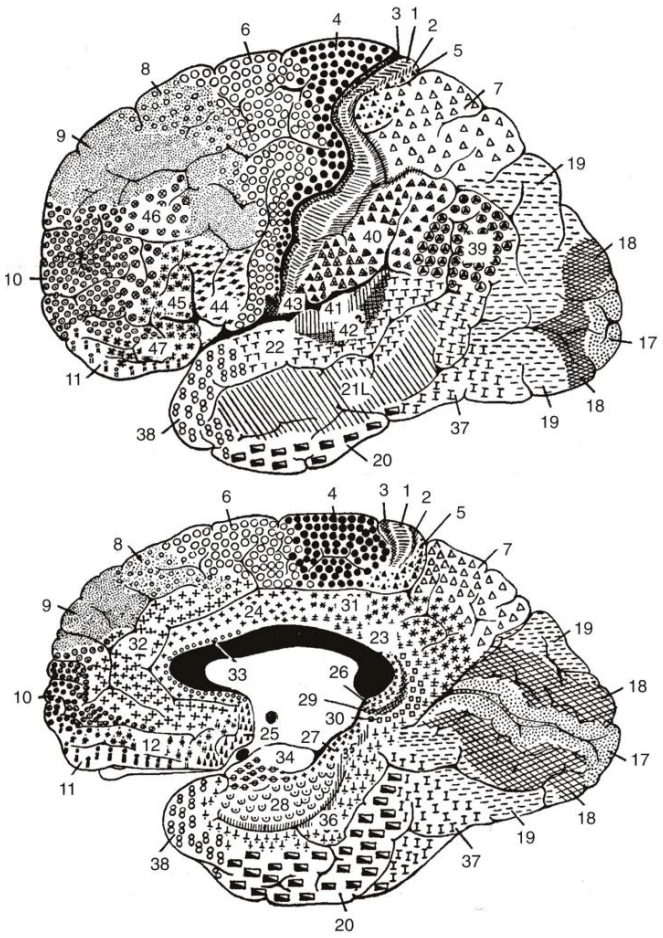

Figure 1.14: Lateral (left) and medial (right) surfaces of Brodmann's classification of the different areas of the cerebral cortex. Original figures from (Fuster, 2008).

The cerebral cortical cytoarchitecture was described by Brodmann (1909). He divided the cortex in 52 different Brodmann areas (BA), as shown on Fig. 1.14. BA 1, 2 and 3 form the postcentral gyrus, also known as primary somatosensory cortex (S1). BA 4 is the precentral gyrus, or primary motor cortex (M1). Along both sides of the central sulcus, one can represent the anatomical division, see Fig. 1.15. Larger areas for S1 or M1 are devoted to body regions characterised by great sensitivity and fine, complex movement, respectively. Besides M1, the motor cortex consists of the premotor cortex (PMC) and the supplementary motor area (SMA), together located in BA 6. BA 9 and 46 cover the dorsolateral prefrontal cortex (DLPFC). Other important areas are Wernicke, part of BA 22, where language is understood, and Broca, BA 44 and 45,

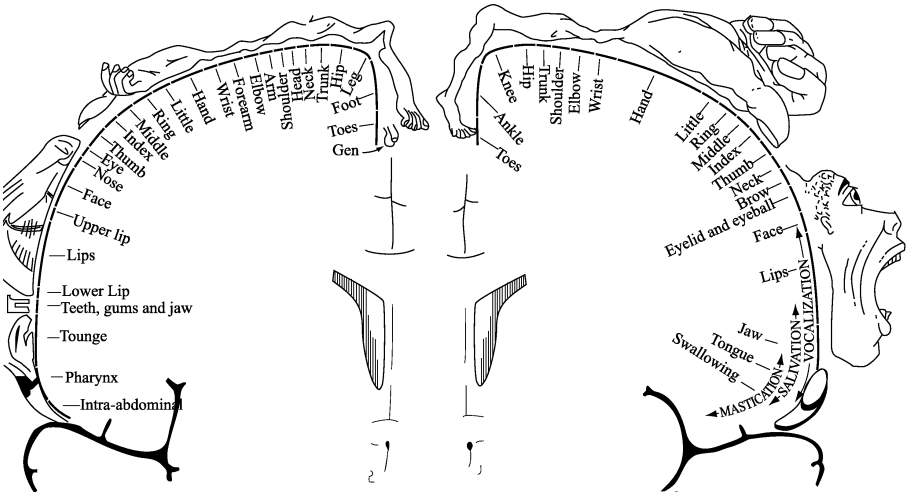

Figure 1.15: Organisation of the primary somatosensory cortex (S1) (left) and primary motor cortex (M1) (right). The hand and lip muscles are particularly well represented. Original figure from (Penfield and Rasmussen, 1950).

located at the junction of the temporal, parietal and occipital lobes, which is responsible for speech production. The anterior cingulate cortex (ACC) is the frontal part of the cingulate gyrus and consists of BA 24, 25, 32 and 33.
The cerebral cortex has six layers, from the most superficial layer I to the deep layer VI, and contains between 10 and 14 billion neurons of several types. The pyramidal neurons have a triangular-shaped soma, multiple dendrites and a single axon, for more details, see Fig. 6.1 of Section 6.1. They can be extremely large and both dendrites and axons branch extensively. Their axons extend through the white matter and project out of the brain region in which their soma or dendrites lie. Pyramidal neurons from layers II and III project to different cortical areas and from layers V and VI to subcortical areas. When the axons of these neurons form part of the pyramidal tracts leading to the spinal cord or brain stem, they are so-called pyramidal tract neurons (PTN), whereas neurons with their axons primarily sent to other cortical areas are pyramidal association fibres. Association fibre bundles may be short, connecting adjacent gyri, and are often referred to as U-fibres, or they may connect one lobe to another. For example, the arcuate fasciculus connects Broca's and Wernicke's areas and is an important neural tract for language function (Geschwind, 1970). Commissural fibres connect one hemisphere with the other. The largest commissural connection is the corpus callosum, which consists of about 300 000 fibres. In contrast to the pyramidal neurons, interneurons have short axons that do not leave the cortex and are limited to a single brain area. They are found in layer I, II, III and IV.

Neurotransmitters are chemicals released by neurons to send signals to other neurons, influencing them in either an inhibitory or excitatory way. Some neurons are coated, protected and insulated by a fatty material, called myelin, enabling them to quickly conduct these signals. The most common neurotransmitter in the brain (over 90% of the synapses) is the excitatory glutamate. The most important inhibitory neurotransmitter is γ-aminobutyric acid (GABA). Pyramidal neurons receive synaptic inputs from tens of thousands of excitatory neurotransmitters and several thousand inhibitory neurotransmitters. Therefore, they are mostly excitatory, whereas interneurons most often inhibit their targets.
The term "neuronal plasticity" refers to change or adaptation of neuronal function and structure dependent on activity (Holtmaat and Svoboda, 2009). For example, when some neurons are lost due to a stroke, reactivation of the function that was originally performed by the lost neurons is possible by plasticity of another group of neurons. Moreover, neuronal plasticity is the basis of learning. Every time a person learns something new, whether it is conscious or unconscious, that experience alters the structure of the brain. Thus, neurotransmission in itself not only contains current information but can also alter subsequent neurotransmission. Experiences that are noticeable enough to cause memory create new synaptic connections, strengthens or weakens existing ones, or even destroys old ones.

1.4. Head model

In this work, simple spherical head models are applied for the primary simulations, as illustration of the concepts of the presented method. The first model contains the layers scalp, skull and brain, with radii 9.2 cm, 8.6 cm and 8.0 cm respectively (Brody et al., 1973; Homma et al., 1995). Later on, when anisotropic material properties are included, this model is extended to five shells. The brain is then divided in grey matter, white matter and a central thalamus, with radii 8.0 cm, 7.0 cm and 2.0 cm respectively. In the white matter shell, fibre bundles are assumed to start from the thalamus and go in the radial direction to the grey matter shell.
For the more sophisticated simulations, accurate personalised head models are created from structural and diffusion-weighted MRI. They include realistic geometry, tissue anisotropy and traced neural fibre bundles connected with the targeted region. T1-weighted images were acquired from healthy volunteers on a 3 Tesla Philips Achieva MR scanner. They demonstrate differences in the T1 relaxation times of tissues (Bernstein et al., 2004; Haacke et al., 1999). Tissues that slowly realign their longitudinal magnetisation, have low signal and appear dark. Therefore, water-rich matter, such as cerebrospinal fluid, as well as dense bone and air appear dark, whereas fat, such as the lipids in the

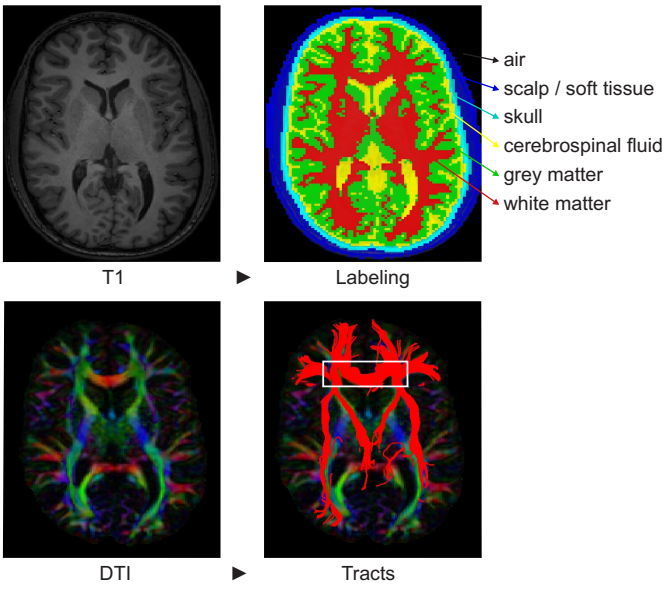

Figure 1.16: T1-weighted MRI is used to obtain the geometry and segmentation of the head model, and thus to assign to each voxel a certain label. DTI, on the other hand, is used for tissue anisotropy and to reconstruct the significant neural fibre bundles, in red, crossing a predefined region of interest, marked with a white frame. The DTI colours indicate the dominant direction of the diffusion tensor: red (right to left), green (posterior to anterior) and blue (inferior to superior). This way of working ensures a head model that is patient-specific.

myelinated white matter, appear bright. Statistical parametric mapping (SPM8 or SPM12) (Friston et al., 2007) is used to segment these T1 images into tissue probability maps. Based on these maps, the head models are constructed, surrounded with air and segmented into scalp, skull, CSF, grey and white matter, as illustrated in Fig. 1.16. White matter is known to be anisotropic due to the electrically insulating myelin sheaths. Since the transport of ions in conductivity and water molecules in diffusion are mainly constrained by the same extracellular space, a strong linear relationship between the eigenvalues of the conductivity and the self-diffusion tensors exists (Tuch et al., 2001). Therefore, in addition to the T1-weighted images, data sets of diffusion-weighted MRI, or better known as diffusion tensor images (DTI) (Basser et al., 1994b), of the same subjects were acquired. Anisotropic conductivity and permittivity tensors can then be computed from the diffusion tensors. This is discussed in more detail in Section 5.1.1. Based on the same DTI data sets, we generate anatomically plausible and reproducible reconstructions of fibre bundles in the brain, as depicted in Fig. 1.16. This relative new method is called tractography (Basser et al., 2000), and in this work, the graphical toolbox ExploreDTI

(Leemans et al., 2009) is used. For further information on tractography, we refer to Section 6.3.

1.5. Applications

1.5.1 Neurological and psychiatric disorders

In recent years, TMS has established itself as a promising diagnostic tool and alternative treatment for a broad range of neurological and psychiatric disorders (Ilmoniemi et al., 1999) including strokes (Di Pino et al., 2014; Wagner et al., 2006), Parkinson's disease (Fregni et al., 2005), tinnitus (Smith et al., 2007), epilepsy (Kimiskidis, 2010), phantom pain and depression (Padberg and George, 2009). After searching the scientific literature, Fox et al. (2014) identified 14 neurological and psychiatric diseases where improvement had been seen with TMS. They are listed in Table 1.2 with their corresponding most effective target brain region(s). Fox et al. found that these different stimulation target sites are often nodes along the same network. By using a data base of fMRI they looked for correlations in spontaneous brain activity, and consequently brain networks of functional connectivity. When one area is active and the activity in another area is also changed, this means they are functionally connected. They investigated the brain network spreading out from the sites stimulated by deep brain stimulation (DBS) for a certain disorder, and showed all of the connections reaching up to the surface of the brain are matching the corresponding TMS targets. So when treating diseases in the future, doctors may find the best site by first identifying the brain network (Fox et al., 2014) or the lesion (Di Pino et al., 2014).

1.5.2 Virtual brain lesion

Another useful property of either single pulse TMS and rTMS is their ability to temporarily disrupt the normal behaviour of a given cortical area, thus creating a 'virtual brain lesion' (Pascual-Leone et al., 2000). This effect of TMS can be thought of as inducing noise into neural processes. This enables investigators to establish the causal role and the timing of the contribution of a given cortical area to the behaviour or response under investigation. Since TMS has the ability to modify the brain state, it is a powerful tool to explore specific brain functions. Several research groups are applying TMS in their study of perception, attention, learning, plasticity, language and awareness. Unlike other techniques such as fMRI and EEG, TMS can assess whether a given brain area is necessary for a given function rather than it simply correlates with it.
It has been demonstrated that low-frequency (1 Hz) stimulation of the primary

Table 1.2: TMS as therapy for several neurological and psychiatric disorders with the corresponding target brain region(s). Italics indicate targets of *inhibitory* rather than excitatory stimulation. Table adapted from (Fox et al., 2014).

Therapy	Target brain region
Addiction	DLPFC (laterality unclear)
Alzheimer's disease	bilateral DLPFC
Anorexia	left DLPFC
Depression	left DLPFC, *right DLPFC*
Dystonia	*SMA/ACC*, *PMC*
Epilepsy	*active EEG focus*, cerebellum
Essential tremor	*cerebellum*, *M1*
Gait dysfunction	M1 (leg area)
Huntington's disease	*SMA*
Minimally consciousness	right DLPFC, M1
Obsessive compulsive disorder	*left orbitofrontal cortex*, *pre-SMA*
Pain	M1
Parkinson's disease	M1, *SMA*
Tourette syndrome	*SMA*

motor cortex (M1) produces inhibition of motor-evoked potentials (Chen et al., 1997), with reduced MEP amplitudes and longer cortical silent periods, while high-frequency M1 stimulation (above 5 Hz) produces significant changes in the opposite direction (Pascual-Leone et al., 1994). As explained by Kimiskidis (2010), the mechanisms of these persistent effects are similar to long-term depression (LTD) and long-term potentiation (LTP), two forms of synaptic plasticity elicited in neural structures by low- and high-frequency electrical stimulation, respectively. However, attempts to induce LTD and LTP with different frequencies of rTMS have mixed success, since the effects are weak and highly variable from one individual to another and across brain areas. Huang et al. (2005) were the first to show that TBS, illustrated in Fig. 1.8, produces long-lasting, consistent, sustained and controllable changes in cortical activity, providing a possible index for the underlying LTD and LTP processes.
When delivered over a specific cortical site, TMS can temporarily disrupt the ongoing process in that area. This allows for mapping motor and speech-related cortical areas (Krieg et al., 2014; Picht et al., 2013). Nowadays, the accurate mapping of critical regions of the cortex prior to neurosurgery, helps neurosurgeons to save these key areas. In 55% of the case studies with tumours in or near the motor cortex, this TMS mapping changed the surgical planning (Picht et al., 2012). Other applications in functional brain imaging are e.g. evaluating brain damage following stroke, and testing spinal cord integrity.

1.5.3 Safety

TMS is regarded as a safe brain stimulation technique, well tolerated and associated with very limited side effects. The most common side effect is mild headaches. Discomfort can occur due to the stimulation of muscles and nerves close to the coil, such as facial twitching. Since the coil produces an intense, but very brief clicking sound with each pulse, subjects normally wear earplugs during stimulation to prevent damage. The induction of epileptic seizures during rTMS studies is possible and counts as the most reported, though still rare, serious side effect. To prevent these undesirable effects, safety guidelines (Rossi et al., 2009; Wassermann, 1998) for the correct use of the technique were drawn, based on clinical experience and modelling. Single pulse TMS is considered as completely safe and for rTMS maximum stimuli intensity for various frequencies are prescribed, see Table 1.3. By this, also the coil temperature is limited, avoiding heating of the brain. Finally, the intense time-varying magnetic field generated by TMS can disrupt electrical devices such as pacemakers and is not compatible with metal objects implanted in or near the subject's head. In 2008, the US Food and Drug Administration (FDA) approved the first rTMS device for patients with major depression who do not respond to antidepressant medication. One year later, FDA clearance of navigated TMS was obtained for the assessment of the primary motor cortex for pre-procedural planning and in 2011 for neurosurgical planning. In 2013, the FDA allowed marketing of TMS devices to relieve pain caused by migraine headaches.

Table 1.3: Maximum safe duration (in s) of conventional rTMS trains and of individual trains within patterned rTMS, at different stimulus intensities. Numbers preceded by > denote the longest durations tested. A consensus has been reached for this table (Rossi et al., 2009).

Frequency (Hz)	**Intensity (% of motor threshold)**				
	90%	**100%**	**110%**	**120%**	**130%**
			conventional rTMS		
1	>1800	>1800	>1800	>360	>50
5	>10	>10	>10	>10	>10
10	>5	>5	>5	4.2	2.9
20	2.05	2.05	1.6	1.0	0.55
25	1.28	1.28	0.84	0.4	0.24
			patterned rTMS		
1		>270	>270	>180	50
5		10	10	10	10
10		5	5	3.2	2.2
20		1.5	1.2	0.8	0.4
25		1.0	0.7	0.3	0.2

1.5.4 Alternative stimulation techniques

Besides the non-invasive transcranial magnetic stimulation (TMS) discussed in this work, there are other techniques that activate the brain with electricity or implants to treat disorders.
Electroconvulsive therapy (ECT) is the most researched stimulation therapy and has the longest history of use (Abrams, 1992), as already described above in Section 1.1. When the patient is under general anaesthesia and has given a muscle relaxant, electrodes are carefully placed on the head. An electric current passes through the brain, causing a seizure. ECT is nowadays mainly used for medication-resistant major depression and schizophrenia. Despite its clinical efficacy, considerable side effects remain.
Transcranial electrical stimulation (tES) delivers a weak electrical current, usually in the order of several mA, via small electrodes placed on the scalp above the brain region of interest. The most common form of tES is transcranial direct current stimulation (tDCS) which uses a constant, low current (Nitsche and Paulus, 2000). Since tES only causes increased spontaneous cell firing, it has a smaller effect than TMS. It is not strong enough to generate action potentials, but causes more subtle changes by modifying the transmembrane resting potential. When tES is used according to the guidelines, it should not lead to any adverse side effects.
Deep brain stimulation (DBS) is a neurosurgical treatment in which a microelectrode is permanently implanted deep inside a patient's brain with a battery device implanted in the chest (Benabid et al., 2009). This invasive therapy stimulates the brain directly, much more focally and with a higher pulse frequency rate (up to more than 100 Hz) compared to TMS. DBS is mostly applied therapeutically for chronic movement disorders, such as Parkinson's disease, dystonia and tremor.
Vagus nerve stimulation (VNS) works through a device implanted under the skin in the chest that sends electrical pulses through the left vagus nerve, that runs from the medulla of the brain stem through the neck and down to the chest and abdomen (Groves and Brown, 2005). VNS is an indirect electrical stimulation of the brain and is an effective treatment for medication-resistant major depression and refractory epilepsy. Due to the invasiveness of DBS and VNS, there is the risk of bleeding and infection, unlike TMS. DBS and VNS, on the other hand, have the ability of sending continuously (24 hours a day, 7 days a week) stimulation pulses.

1.6. Aims of this PhD

Although during the last decade TMS has been frequently and widely used and its efficacy has already been shown, the underlying mechanisms remain

poorly understood (Hoogendam et al., 2010; Sack and Linden, 2003) and its working is hard to predict. Moreover, the treatment works well for some patients, for others only temporary, and for others not at all (Loo and Mitchell, 2005; Maeda et al., 2000). This variability restricts the many other potential applications and keeps neuroscientists from embracing TMS as a routine treatment method. To gain more insight, research is needed including bioelectromagnetic modelling that can accurately determine the impact of electromagnetic fields on the human brain both qualitatively and quantitatively. These simulations are crucial because *in vivo* measurements are typically expensive and large homogeneous patient groups are difficult to gather and restricted due to ethical issues (Rossi et al., 2009). Animal studies can provide a solution, but they benefit as well from modelling through prediction, better planning and control and consequently reduction of experiments.

This PhD has the aim to accurately capture the effects of TMS in the brain so to provide a numerical explanation for the widely observed variability of the working of TMS in clinical practice and psychological tests. This is achieved by detailed modelling of the macroscopic electric fields using realistic personalised head models, the relation of these fields to the stimulation mechanisms on the targeted fibre tracts and subsequently the membrane potentials on the neuronal level. We will investigate the observed variability of TMS (Casarotto et al., 2010; Lioumis et al., 2009) by comparing the influence of different TMS parameter changes, such as the coil position and orientation and the stimulation intensity. Moreover, we will elaborate on the effect of various geometrical and material properties in the head model, such as tissue anisotropy, the not well-known conductivity values and tract orientation. The validity of the developed numerical tools needs to be extensively tested with respect to accuracy, numerical convergence, etc.

In Part I we will emphasise on the electromagnetic phenomena caused by TMS and how the induced currents and electric field can be modelled. Since electromagnetism is inevitably coupled with Maxwell's equations, this will be discussed in detail in Chapter 2 together with the dielectric properties. With this knowledge, we will explain in Chapter 3 in more detail the working of TMS and how it can be modelled with the impedance method. Since the conventional method is suboptimal and ill conditioned due to the presence of dependent equations, we introduce the developed independent impedance method and its extension to anisotropic tissues. The impedance includes brain tissue properties, such as conductivity. Because these values are not well known, we will present in Chapter 4 the induced current MR phase imaging electrical impedance tomography, a possible technique to estimate these values as a function of frequency, using the independent impedance method. With the independent impedance method, the induced currents and electric field can be computed for TMS, as shown in Chapter 5.

Since the effects of TMS are not limited to these electromagnetic macroscopic fields in the brain, but interact with the neural system and may excite or inhibit certain neural pathways by altering their membrane potentials, we will emphasise on the neurophysiologic phenomena and thus the modelling of the membrane potentials on microscopic neuronal level in Part II. First we introduce the biophysics in Chapter 6. Chapter 7 builds a bridge between the two phenomena by explaining how the induced effective electric field leads to stimulation mechanisms along neural fibre bundles that can possibly result in stimulation. In Chapter 8 we discuss the resulting spatio-temporal variation of the membrane potentials along these fibre bundles. In Appendix B the results of a TMS experiment are studied in order to numerically explain the observed variability of the responses.
Last, but not least, we summarise the methodology and findings of this PhD and give some general conclusions. Since research never runs to its end, we finalise by discussing the perspectives.

PART I

Modelling the TMS physics

If you can't explain it simply, you don't understand it well enough.

Albert Einstein

2

Electromagnetic theory of TMS

The electromagnetic theory of TMS begins with Maxwell's equations. The excitation current flowing through the TMS coil causes a time-varying magnetic field, described by Biot-Savart's law. The effect of this generated magnetic field on the brain depends on the dielectric properties of the head materials.
In this chapter, Maxwell's equations are first explained in a general way, next to the dielectric properties of biological tissues. The application on TMS is finally elaborated.

2.1. Maxwell's equations

Electromagnetic phenomena are modelled by the electric and magnetic fields **E** and **H**, and by the electric and magnetic flux densities **D** and **B**. Their relationship is expressed by Maxwell's equations and constitutive laws (Maxwell, 1865).

The Maxwell's equations can be expressed in the following differential form:

$$\nabla \times \mathbf{E} = -\frac{\partial \mathbf{B}}{\partial t} \tag{2.1}$$

$$\nabla \times \mathbf{H} = \mathbf{J}_\mathrm{f} + \frac{\partial \mathbf{D}}{\partial t} \tag{2.2}$$

$$\nabla \cdot \mathbf{D} = \rho_\mathrm{f} \tag{2.3}$$

$$\nabla \cdot \mathbf{B} = 0 \tag{2.4}$$

The first equation is derived from Faraday's law and denotes that the time variation of a magnetic flux density induces an electric field. The second equation is the completion of Ampère's law, by adding the displacement current density $\partial \mathbf{D}/\partial t$ to the free current density $\mathbf{J}_\mathrm{f}$ as a source inducing a magnetic field. The third and fourth equations are derived from Gauss' law for an electric and magnetic field, respectively, with ρ_f the free charge density.

The boundary conditions for the electromagnetic fields and inductions across material boundaries are:

$$\mathbf{n} \times (\mathbf{E}_1 - \mathbf{E}_2) = 0 \tag{2.5}$$

$$\mathbf{n} \times (\mathbf{H}_1 - \mathbf{H}_2) = \mathbf{J}_\mathrm{fs} \tag{2.6}$$

$$\mathbf{n} \cdot (\mathbf{D}_1 - \mathbf{D}_2) = \rho_\mathrm{fs} \tag{2.7}$$

$$\mathbf{n} \cdot (\mathbf{B}_1 - \mathbf{B}_2) = 0 \tag{2.8}$$

$\mathbf{n}$ is the unit vector normal to the boundary pointing from material 2 into material 1 and subscript $_\mathrm{fs}$ refers to surface density of free sources along the boundary. The tangential components of the electric field are continuous across the boundary. The difference of the tangential components of the magnetic field are equal to the surface current density. The difference of the normal components of the electric flux density are equal to the free charge surface density and the normal components of the magnetic flux density are continuous across the boundary between the two materials.

There are two fundamental constitutive relationships that describe the behaviour of the material:

$$\mathbf{D} = \varepsilon \mathbf{E} \tag{2.9}$$

$$\mathbf{B} = \mu \mathbf{H} \tag{2.10}$$

with ε the electric permittivity and μ the magnetic permeability. They are related to the electric and magnetic susceptibilities, χ_e and χ_m, of the material.

$$\varepsilon = \varepsilon_0 \varepsilon_\mathrm{r} = \varepsilon_0 (1 + \chi_\mathrm{e}) \tag{2.11}$$

$$\mu = \mu_0 \mu_\mathrm{r} = \mu_0 (1 + \chi_\mathrm{m}) \tag{2.12}$$

Subscript $_0$ refers to the properties in vacuum, $\varepsilon_0 = (1/36\pi)10^{-9}$ F/m and $\mu_0 = 4\pi 10^{-7}$ H/m, whereas subscript $_\mathrm{r}$ refers to the dimensionless relative values of the material. Equations (2.9) and (2.10) can now be written as follow:

$$\mathbf{D} = \varepsilon_0 (1 + \chi_\mathrm{e}) \mathbf{E} = \varepsilon_0 \mathbf{E} + \mathbf{P} \tag{2.13}$$

$$\mathbf{B} = \mu_0 (1 + \chi_\mathrm{m}) \mathbf{H} = \mu_0 (\mathbf{H} + \mathbf{M}) \tag{2.14}$$

with **P** the dielectric polarisation and **M** the magnetisation of the material. In this work, only non-magnetic materials are considered, for which μ equals μ_0 or $\chi_\mathrm{m} = 0$. The relationship between magnetic field and magnetic induction is therefore linear with the factor μ_0.

Besides the electric permittivity and the magnetic permeability, there is a third constitutive parameter: the electric conductivity σ. Ohm's law describes how an electric field generates a conduction current density $\mathbf{J}_\mathrm{c}$:

$$\mathbf{J}_\mathrm{c} = \sigma \mathbf{E} \tag{2.15}$$

The free current consists of a source current $\mathbf{J}_\mathrm{s}$, which is usually a known externally applied source, and a conduction current density, which is generated by the electric field itself. In both free electric charge movement is involved.

$$\mathbf{J}_\mathrm{f} = \mathbf{J}_\mathrm{s} + \mathbf{J}_\mathrm{c} \tag{2.16}$$

More generally, these three material parameters can be inhomogeneous, anisotropic, nonlinear, time-invariant, frequency-dependent, or all of the above. In inhomogeneous materials, they depend on the location **r** within the material. In anisotropic materials, they depend on the x-, y- and z-direction of **E** or **H** propagation and become tensors instead of scalars. In nonlinear materials, the material parameters depend on the magnitude of the applied field. Materials with a frequency-dependent material parameter are referred to as dispersive. The frequency dependence of the dielectric properties comes into play when a time-varying electric field is applied.

2.2. Dielectric properties of biological tissues

The electric and magnetic fields and sources are position **r** and time t dependent. When the sources vary sinusoidally in time, their harmonic time dependence gives rise to sinusoidal fields. At least they do in linear material and when the fields have reached their steady state. Moreover, Maxwell's equations simplify considerably in the case of harmonic time dependence. Through the inverse Fourier transform, general solutions can be built as linear combinations of single-frequency solutions. When assuming that the fields have a

time dependence $e^{j\omega t}$, we have:

$$\mathbf{E}(\mathbf{r},t) = \hat{\mathbf{E}}(\mathbf{r})e^{j\omega t} \tag{2.17}$$
$$\mathbf{H}(\mathbf{r},t) = \hat{\mathbf{H}}(\mathbf{r})e^{j\omega t} \tag{2.18}$$

with $j = \sqrt{-1}$ the imaginary number, $\omega = 2\pi f$ the angular frequency, and $\hat{\mathbf{E}}(\mathbf{r})$ and $\hat{\mathbf{H}}(\mathbf{r})$ complex numbers. The accent circonflexe ˆ refers to the fact that the fields are phasors in the frequency domain. Throughout this work, we will not explicitly indicate the arguments of the magnitudes in order to make the notation more concise, unless to emphasise the dependence on any of the variables.

The time-harmonic version of Maxwell's equations (2.1-2.4) becomes:

$$\nabla \times \hat{\mathbf{E}} = -j\omega\hat{\mathbf{B}} \tag{2.19}$$
$$\nabla \times \hat{\mathbf{H}} = \hat{\mathbf{J}}_{\mathrm{f}} + j\omega\hat{\mathbf{D}} \tag{2.20}$$
$$\nabla \cdot \hat{\mathbf{D}} = \hat{\rho}_{\mathrm{f}} \tag{2.21}$$
$$\nabla \cdot \hat{\mathbf{B}} = 0 \tag{2.22}$$

Based on the constitutive relations (2.9) and equation (2.16), equation (2.20) can be rewritten as:

$$\nabla \times \hat{\mathbf{H}} = \hat{\mathbf{J}}_{\mathrm{s}} + \sigma\hat{\mathbf{E}} + j\omega\varepsilon\hat{\mathbf{E}} \tag{2.23}$$

The sum of the last two terms, the conduction and displacement current, is called the total induced current $\hat{\mathbf{J}}_{\mathrm{tot}}$. This total induced electric current is also referred to as the term eddy current.

$$\hat{\mathbf{J}}_{\mathrm{tot}} = \sigma\hat{\mathbf{E}} + j\omega\varepsilon\hat{\mathbf{E}} \tag{2.24}$$

Biological material has both dielectric and conductive properties and is therefore a lossy material. As mentioned before, it is non-magnetic. In the response of biological material to an electromagnetic field, there appear damping forces that give rise to a delay between the polarisation vector $\hat{\mathbf{P}}$ and the electric field $\hat{\mathbf{E}}$, and consequently a phase shift between $\hat{\mathbf{E}}$ and $\hat{\mathbf{D}}$, and to an electromagnetic energy loss as heat in overcoming these damping forces. At the macroscopic level this effect is expressed by means of a complex permittivity ε. By convention and as a result of the energy balance, the imaginary part is defined with a negative sign.

$$\varepsilon = \varepsilon' - j\varepsilon'' \tag{2.25}$$

where ε' is the real permittivity of the material, a measure of the charge displacement and consequent energy stored in the material, and ε'' the out-of-phase loss factor, a measure of the energy dissipated. The total induced current intensity of equation (2.24) can then be rewritten as the sum of a real part in

phase with the electric field, the so-called dissipative (lossy) component, and an imaginary part in phase quadrature with the electric field, the so-called reactive (lossless) component, illustrated in Fig. 2.1.

$$\hat{\mathbf{J}}_{\text{tot}} = \sigma\hat{\mathbf{E}} + j\omega\left(\varepsilon' - j\varepsilon''\right)\hat{\mathbf{E}} = \left(\sigma + \omega\varepsilon''\right)\hat{\mathbf{E}} + j\omega\varepsilon'\hat{\mathbf{E}} \tag{2.26}$$

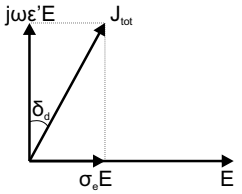

Figure 2.1: Total induced current density in the complex plane.

The dissipative current accounts for the conducting losses due to σ, i.e. the conduction current, and the damping losses due to $\omega\varepsilon''$, i.e. the displacement (polarisation) current. This way, we obtain the total effective conductivity σ_{e} of the material, which is a real number:

$$\sigma_{\text{e}} = \sigma + \omega\varepsilon''. \tag{2.27}$$

In addition, the total effective permittivity ε_{e} can be defined,

$$\varepsilon_{\text{e}} = \varepsilon' - j\frac{\sigma_{\text{e}}}{\omega} \tag{2.28}$$

such that

$$\sigma_{\text{e}} = -\omega\text{Im}(\varepsilon_{\text{e}}) \tag{2.29}$$

and the total induced current equals $j\omega\varepsilon_{\text{e}}\hat{\mathbf{E}}$. The dissipation of electromagnetic energy can be parametrised in terms of a loss angle δ_{d} between the induced and reactive current, as indicated on Fig. 2.1, or the corresponding loss tangent.

$$\tan(\delta_{\text{d}}) = \frac{\sigma_{\text{e}}}{\omega\varepsilon'} \tag{2.30}$$

2.2.1 4-Cole-Cole model

The dielectric properties have been experimentally characterised in the frequency range 10 Hz to 20 GHz for different biological tissues (Gabriel et al., 1996a,b) and a parametric model was developed to describe their variation as a function of frequency (Gabriel et al., 1996c). The 4-Cole-Cole model (Cole and Cole, 1941), expresses the frequency-dependent complex total effective

permittivity

$$\varepsilon_{\mathrm{e}}(\omega) = \varepsilon_{\infty} + \sum_{n=1}^{4} \frac{\triangle\varepsilon_n}{1 + (j\omega\tau_n)^{1-\alpha_n}} + \frac{\sigma_{\mathrm{i}}}{j\omega} \tag{2.31}$$

of which the real part is the permittivity ε' and the imaginary part can be used to compute the conductivity σ_{e}, according to equation (2.29). The dielectric spectrum of biological tissue is characterised by three main relaxation regions α, β and γ at low (n = 4), medium (n = 3) and high (n=2) frequencies respectively, and another minor δ dispersion (n=1) (Gabriel et al., 1996a). The low-frequency α dispersion, in the Hz to kHz range, is associated with ionic diffusion processes at the site of the cellular membrane. The β dispersion, in the 100 kHz region, is due to the polarisation of cellular membranes, protein and other organic macromolecules. The γ dispersion, in the GHz region, is due to the polarisation of water molecules. At last, the tissue also includes a contribution from a frequency-independent ionic conductivity σ_{i}. This static ionic conductivity, the permittivity in the high-frequency limit ε_{∞} and the parameter $\triangle\varepsilon_n$, relaxation time τ_n and distribution parameter α_n, with $n = 1,2,3,4$ corresponding to the different main relaxation regions, were obtained by fitting experimental measurements to equation (2.31) for each tissue (Gabriel et al., 1996c).

Table 2.1: 4-Cole-Cole model parameters of equation (2.31) for the considered tissues. Table adapted from (Gabriel et al., 1996c).

Tissue	**Skin**	**Bone**	**CSF**	**GM**	**WM**
ε_{∞} [F/m]	$4.0\varepsilon_0$	$2.5\varepsilon_0$	$4.0\varepsilon_0$	$4.0\varepsilon_0$	$4.0\varepsilon_0$
σ_{i} [S/m]	0.0004	0.02	2.0	0.02	0.02
$\triangle\varepsilon_1$ [F/m]	$39.0\varepsilon_0$	$10.0\varepsilon_0$	$65.0\varepsilon_0$	$45.0\varepsilon_0$	$32.0\varepsilon_0$
τ_1 [ps]	7.96	13.26	7.96	7.96	7.96
α_1 [-]	0.10	0.20	0.10	0.10	0.10
$\triangle\varepsilon_2$ [F/m]	$280\varepsilon_0$	$180\varepsilon_0$	$40\varepsilon_0$	$400\varepsilon_0$	$100\varepsilon_0$
τ_2 [ns]	79.58	79.58	1.59	15.92	7.96
α_2 [-]	0.00	0.20	0.0	0.15	0.10
$\triangle\varepsilon_3$ [F/m]	$3.0{\cdot}10^4\ \varepsilon_0$	$5.0{\cdot}10^3\ \varepsilon_0$	0.0	$2.0{\cdot}10^5\ \varepsilon_0$	$4.0{\cdot}10^4\ \varepsilon_0$
τ_3 [μs]	1.59	159.15	-	106.10	53.05
α_3 [-]	0.16	0.20	-	0.22	0.30
$\triangle\varepsilon_4$ [F/m]	$3.0{\cdot}10^4\ \varepsilon_0$	$1.0{\cdot}10^5\ \varepsilon_0$	0.0	$4.5{\cdot}10^7\ \varepsilon_0$	$3.5{\cdot}10^7\ \varepsilon_0$
τ_4 [ms]	1.59	15.92	-	5.30	7.96
α_4 [-]	0.20	0.00	-	0.00	0.02

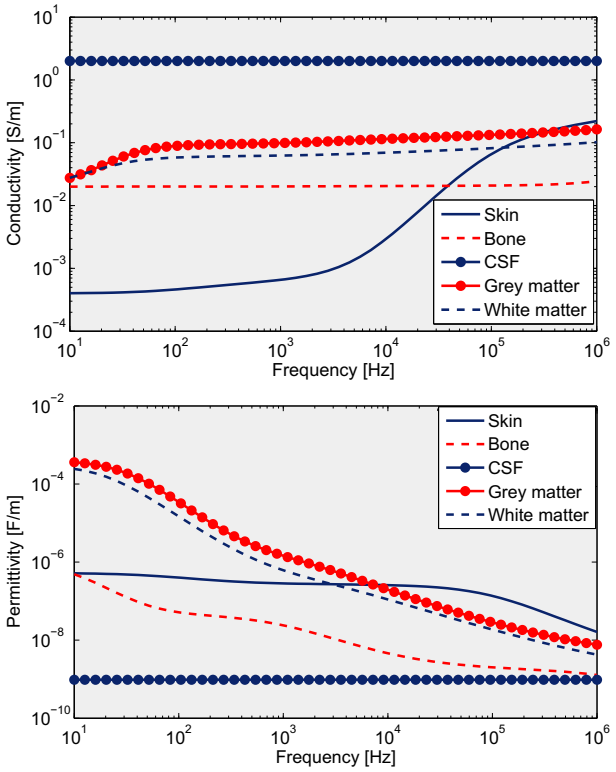

Figure 2.2: The dissipative conductivity σ_e and reactive permittivity ε' values according to the 4-Cole-Cole model for the relevant tissues of this work.

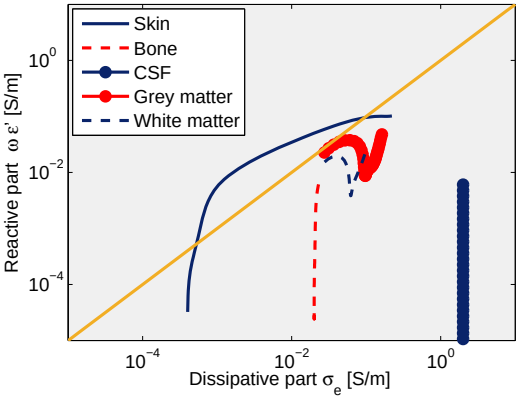

Figure 2.3: The ratio between the dissipative and reactive components of equation (2.26). The yellow line defines the one-to-one matching, illustrating that the dissipation of electromagnetic energy and corresponding loss tangent (2.30) cannot be neglected in this work.

The dielectric property values for the head tissues (wet) skin, (cortical) bone, cerebrospinal fluid (CSF), grey matter (GM) and white matter (WM), thus obtained and used in this work in the frequency range from 10 to 10^6 Hz are plotted in Fig. 2.2 and their parameters are listed in Table 2.1. Electrical properties of biological tissues are often approximated by a constant frequency-independent value, whereas, in reality, they vary naturally with frequency. The conductivity of grey matter, for example, changes from 0.02 S/m (order of Hz) to 0.10 S/m (kHz) and 0.16 S/m (MHz). In our opinion, this change cannot be neglected. Therefore, we will calculate for every simulation the dielectric property values of the head model tissues using this frequency-dependent 4-Cole-Cole model, corresponding with the applied stimulation frequency.
We stated before that biological tissues are lossy materials. Indeed, when plotting both the dissipative σ_e and reactive $\omega\varepsilon'$ components in Fig. 2.3, it is clear that the considered tissues have both dielectric and conductivity properties, neither of which can be neglected in the relevant frequency range.

2.3. Biot-Savart's law

An electric current source generates a magnetic flux density, as described by Biot-Savart's law.

$$\hat{\mathbf{B}}(\mathbf{r}) = \frac{\mu_0}{4\pi} \iiint_{\text{volume}} \frac{\hat{\mathbf{J}}_{\text{coil}}(\mathbf{r'}) \times (\mathbf{r} - \mathbf{r'})}{\|\mathbf{r} - \mathbf{r'}\|^3} \mathrm{d}\mathbf{v'} \tag{2.32}$$

where $\mathrm{d}\mathbf{v'}$ is the differential element of volume and $\hat{\mathbf{J}}_{\text{coil}}$ is the current density vector in that volume. In the case of TMS, the integral is over the entire volume of the coil, as illustrated in Fig. 2.4, with $\mathbf{r'}$ being one point of this coil volume.
We will now explain in detail how to calculate the magnetic flux density vector $\hat{\mathbf{B}}$, i.e. $[\hat{B}_x, \hat{B}_y, \hat{B}_z]$, in an arbitrary point $\mathbf{r} = [x, y, z]$, due to the current flow density $\hat{\mathbf{J}}_{\text{coil}} = [\hat{J}_x, \hat{J}_y, \hat{J}_z]$ in all points $\mathbf{r'} = [x', y', z']$ of a circular coil with radius R, that is positioned in the xy-plane, centred around the z-axis. The winding of the coil has a cross-sectional area A. Fig. 2.5 clarifies this considered situation.

$$\begin{bmatrix} \hat{B}_x(\mathbf{r}) \\ \hat{B}_y(\mathbf{r}) \\ \hat{B}_z(\mathbf{r}) \end{bmatrix} = \frac{\mu_0}{4\pi} A \int_0^{2\pi} \frac{\begin{bmatrix} \hat{J}_y(\mathbf{r'})(z - z') - \hat{J}_z(\mathbf{r'})(y - y') \\ \hat{J}_z(\mathbf{r'})(x - x') - \hat{J}_x(\mathbf{r'})(z - z') \\ \hat{J}_x(\mathbf{r'})(y - y') - \hat{J}_y(\mathbf{r'})(x - x') \end{bmatrix}}{((x - x')^2 + (y - y')^2 + (z - z')^2)^{\frac{3}{2}}} \mathrm{d}\psi \tag{2.33}$$

with

$$\begin{bmatrix} \hat{J}_x(\mathbf{r'}) \\ \hat{J}_y(\mathbf{r'}) \\ \hat{J}_z(\mathbf{r'}) \end{bmatrix} = \begin{bmatrix} -\hat{J}_{\text{coil}} \sin(\psi) \\ \hat{J}_{\text{coil}} \cos(\psi) \\ 0 \end{bmatrix} \tag{2.34}$$

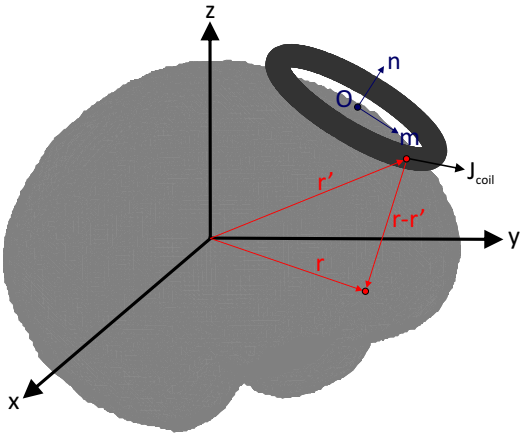

Figure 2.4: In every point **r**, one can calculate the magnetic field generated by the excitation current $\hat{\mathbf{J}}_{\text{coil}}$ flowing through each point **r'** of the coil.

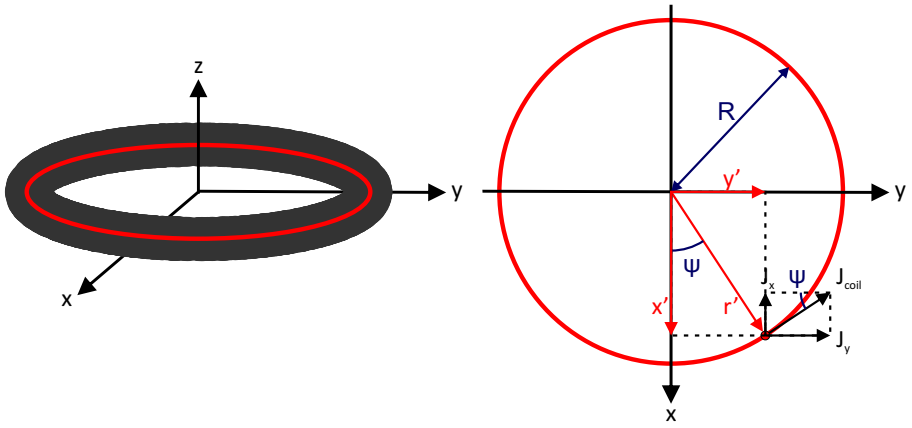

Figure 2.5: For this simple case, in which the coil is positioned in the xy-plane and centred around the z-axis, Biot-Savart's law is explained in detail.

and

$$\begin{bmatrix} x' \\ y' \\ z' \end{bmatrix} = \begin{bmatrix} R\cos(\psi) \\ R\sin(\psi) \\ 0 \end{bmatrix}. \tag{2.35}$$

2.3.1 General coil positioning

However, one should be able to position the TMS coil arbitrarily in space. Therefore, we extend the above equations to a general coil location and ori-

entation. As illustrated in Figs. 2.4 and 2.6, the coordinates of the centre of the coil **O** are (O_x, O_y, O_z), the unit vector normal to the plane of the coil and directed away from the subject's head is $\mathbf{n} = [n_x, n_y, n_z]$ and the unit vector in the direction of maximal induced currents (in homogeneous material) is $\mathbf{m} = [m_x, m_y, m_z]$. The latter vector becomes important in the implementation of figure-of-eight coils.

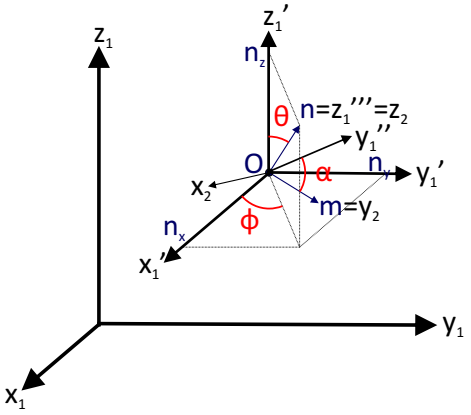

Figure 2.6: With one translation to the centre of the coil and three rotations over the angles ϕ, θ and α we can transform the previous simple case of a centralised coil to a general coil location and orientation.

First, we apply a translation of the origin to point (O_x, O_y, O_z).

$$\begin{bmatrix} x_1 \\ y_1 \\ z_1 \end{bmatrix} = \begin{bmatrix} O_x \\ O_y \\ O_z \end{bmatrix} + \begin{bmatrix} x_1' \\ y_1' \\ z_1' \end{bmatrix} \tag{2.36}$$

Then, we rotate around the z_1'-axis over the angle ϕ, in the interval $[0, 2\pi]$ radians:

$$\tan(\phi) = \frac{n_y}{n_x} \tag{2.37}$$

$$\begin{bmatrix} x_1' \\ y_1' \\ z_1' \end{bmatrix} = \begin{bmatrix} \cos(\phi) & -\sin(\phi) & 0 \\ \sin(\phi) & \cos(\phi) & 0 \\ 0 & 0 & 1 \end{bmatrix} \begin{bmatrix} x_1'' \\ y_1'' \\ z_1'' \end{bmatrix} \tag{2.38}$$

Subsequently, we rotate around the y_1''-axis over the angle θ, in the interval $[0, \pi]$ radians:

$$\tan(\theta) = \frac{\sqrt{n_x^2 + n_y^2}}{n_z} \tag{2.39}$$

$$\begin{bmatrix} x_1'' \\ y_1'' \\ z_1'' \end{bmatrix} = \begin{bmatrix} \cos(\theta) & 0 & \sin(\theta) \\ 0 & 1 & 0 \\ -\sin(\theta) & 0 & \cos(\theta) \end{bmatrix} \begin{bmatrix} x_1''' \\ y_1''' \\ z_1''' \end{bmatrix} \tag{2.40}$$

Finally, we rotate around the z_1'''-axis over the angle α, in the interval $[0, 2\pi]$ radians:

$$\cos(\alpha) = -m_x \sin(\phi) + m_y \cos(\phi) \tag{2.41}$$

$$\sin(\alpha) = \frac{m_z}{\sin(\theta)} \tag{2.42}$$

Since θ variates between 0 and π radians, $\sin(\theta)$ will always be positive, and therefore $\sin(\alpha)$ will have the same sign as m_z.

$$\begin{bmatrix} x_1''' \\ y_1''' \\ z_1''' \end{bmatrix} = \begin{bmatrix} \cos(\alpha) & -\sin(\alpha) & 0 \\ \sin(\alpha) & \cos(\alpha) & 0 \\ 0 & 0 & 1 \end{bmatrix} \begin{bmatrix} x_2 \\ y_2 \\ z_2 \end{bmatrix} \tag{2.43}$$

The complete transformation is illustrated in Fig. 2.6 and can be calculated as follows, with the sine and cosine of a certain angle α abbreviated by s_α and c_α, respectively, in order to simplify notation:

$$\begin{bmatrix} x_1 \\ y_1 \\ z_1 \end{bmatrix} = \begin{bmatrix} O_x \\ O_y \\ O_z \end{bmatrix} + \begin{bmatrix} c_\phi c_\theta c_\alpha - s_\phi s_\alpha & -c_\phi c_\theta s_\alpha - s_\phi c_\alpha & c_\phi s_\theta \\ s_\phi c_\theta c_\alpha + c_\phi s_\alpha & -s_\phi c_\theta s_\alpha + c_\phi c_\alpha & s_\phi s_\theta \\ -s_\theta c_\alpha & s_\theta s_\alpha & c_\theta \end{bmatrix} \begin{bmatrix} x_2 \\ y_2 \\ z_2 \end{bmatrix} \tag{2.44}$$

.

Notice that equations (2.41) and (2.42) are derived by e.g. submitting the points $(x_1, y_1, z_1) = (m_x, m_y, m_z)$ and $(x_2, y_2, z_2) = (0, 1, 0)$ in equation (2.44).

$$m_x = -\cos(\phi)\cos(\theta)\sin(\alpha) - \sin(\phi)\cos(\alpha) \tag{2.45}$$

$$m_y = -\sin(\phi)\cos(\theta)\sin(\alpha) + \cos(\phi)\cos(\alpha) \tag{2.46}$$

$$m_z = \sin(\theta)\sin(\alpha) \tag{2.47}$$

After multiplying the first equation by $-\sin(\phi)$ and the second by $\cos(\phi)$ and adding both, equation (2.41) is derived.

2.4. Conclusion

Through the law of Biot-Savart (2.32) the generated magnetic flux density can be calculated for every possible TMS stimulation case, i.e. for every coil shape, position and orientation and every excitation current waveform. The time variation of this magnetic field induces an electric field, according to

Faraday's law (2.19). Since the material below the coil, i.e. biological tissue, is not only dielectric but also conductive, additional conduction currents are induced (2.15). The total induced current (2.26) is thus the sum of the displacement currents and these conduction currents, in which the dielectric properties are obtained by the 4-Cole-Cole model (2.31). In the following chapter, we will explain how we implement this theory practically in the developed independent impedance method.

In the remaining part of this PhD, the dielectric properties are considered to be σ_e and ε' values as a function of frequency, or tensors in case of anisotropy. They represent the dissipative and reactive term in equation (2.26) and will be further referred to as conductivity and permittivity, with the basic symbols σ and ε, respectively, for simplicity of notation.

You only have a problem, when you are doing nothing to solve it.

my dad, Geert De Geeter

3

Independent Impedance Method

When simulations need to be carried out in a complex geometry, such as a realistic head model, Maxwell's equations cannot be analytically solved and numerical techniques become unavoidable. In the literature, a variety of methods are used to model the eddy-current distribution in biological tissues, e.g. the finite-difference method (FDM) (Liu et al., 2003), the finite element method (FEM) (Sekino and Ueno, 2004; Wagner et al., 2004), the boundary element method (BEM) (Salinas et al., 2009) and the impedance method (IM) (Han et al., 2007; Lu et al., 2008; Nadeem et al., 2003). All have their advantages and disadvantages. We chose to employ IM, introduced by Gandhi et al. (1984) and Orcutt and Gandhi (1988), for the application of TMS for the following reasons. BEM is significantly less efficient for millimetre-resolution models because it gives rise to fully populated matrices. FDM and FEM have the disadvantage that the whole volume, including the coil configuration, needs to be discretised, leading to a large number of unknowns. IM, on the other hand, has an easy implementation and tackles the above-mentioned problems. It utilises a regular three-dimensional (3D) grid of cubic elements, so-called voxels, for the head model, directly extractable from the segmented MR images, which eliminates the gridding and meshing problems that are often associated with FEM and BEM.

The 3D impedance method discretises the geometry into voxels and assigns material properties, represented as impedances, to each voxel. This leads to a

3D network of impedances with the time-varying magnetic induction in each voxel as source model. This linear system of equations can be solved by state-of-the-art solvers. However, it can be significantly ill-conditioned, leading to a long convergence time, or in some situations to no solution at all (Wang et al., 2008). This ill-conditionality is the result of the available redundant equations in IM. Therefore, we introduce and apply in this chapter the independent impedance method (IIM) that identifies a set of independent equations by defining independent loops in the 3D circuit. It solves the computations with improvement of conditionality and speed-up of numerical convergence.
The independent impedance method enables accurate electromagnetic simulations of TMS in the brain. Isotropic and anisotropic volume conduction head models are considered, wherein eddy-current distributions are calculated. The validity of the developed numerical techniques are tested on simple spherical head models with respect to accuracy, numerical convergence, etc. In the later chapters, application is performed on patient-specific realistic head models.
Results from this chapter have been published in (De Geeter et al., 2011a,b) and presented at the International Magnetics Conference (INTERMAG) in 2011 in Taiwan.

3.1. Traditional Impedance Method

As mentioned before, the human head model is tessellated into a uniform 3D Cartesian grid with small cubic voxels. Each voxel is labelled with its node in the lower left hand rear corner. We assign to the cell edges, starting from this node, three branch currents and impedances and to the adjacent cell faces three loop voltages. This guarantees that each quantity is taken into account only once during discretisation. The sign of branch currents is positive in the direction of the corresponding axes and the sign of loop voltages is chosen using the right hand rule, with the defined (x,y,z)-axes as reference; examining the loop from the positive direction of the loop axes, the voltage is positive if it travels anticlockwise. Fig. 3.1 illustrates the branch currents $\hat{I}_\mathrm{x}$, $\hat{I}_\mathrm{y}$, $\hat{I}_\mathrm{z}$, the voltages $\hat{V}_\mathrm{x}$, $\hat{V}_\mathrm{y}$, $\hat{V}_\mathrm{z}$ and impedances Z_x, Z_y, Z_z corresponding with voxel (i,j,k).
The impedance method is derived from the integral form of Faraday's law (2.19) for the relation between a time-varying magnetic flux density $\mathbf{B}$ and the induced electric field $\mathbf{E}$. In order to avoid time-stepping, the method is described in the frequency domain.

$$\oint_{\text{loop}} \hat{\mathbf{E}}(\mathbf{r}) \cdot \mathrm{d}\mathbf{l} = -j\omega \iint_{\text{surface}} \hat{\mathbf{B}}(\mathbf{r}) \cdot \mathrm{d}\mathbf{s}. \tag{3.1}$$

Both variables are position $\mathbf{r}$ dependent. We have explained in detail in Section 2.2 how the total induced current density, also called eddy current, depends

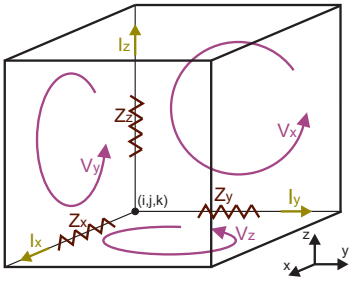

Figure 3.1: Voxel (i,j,k) with its corresponding branch currents $\hat{I}_x$, $\hat{I}_y$, $\hat{I}_z$, voltages $\hat{V}_x$, $\hat{V}_y$, $\hat{V}_z$ and impedances Z_x, Z_y, Z_z. Notice that this voxel is labelled with (i,j,k), referring to the coordinates of its lower left hand rear corner and not to those of its centre. The cell edges and faces that are not appointed belong to neighbouring voxels.

on the electric field via the constitutive relationships, see equation (2.26):

$$\hat{\mathbf{J}}_{\text{tot}} = (\sigma + j\omega\varepsilon)\hat{\mathbf{E}}. \tag{3.2}$$

Moreover, both conductivity and permittivity depend on the applied frequency through the used 4-Cole-Cole model (Cole and Cole, 1941; Gabriel et al., 1996c), see equation (2.31) and Fig. 2.2. We would like to repeat that σ and ε in fact refer to σ_e and ε', as pointed out in detail in Section 2.2. Consequently, we can write:

$$\oint_{\text{loop}} \frac{\hat{\mathbf{J}}_{\text{tot}}(\mathbf{r},\omega)}{\sigma(\omega) + j\omega\varepsilon(\omega)} \cdot \mathrm{d}\mathbf{l} = -j\omega \iint_{\text{surface}} \hat{\mathbf{B}}(\mathbf{r}) \cdot \mathrm{d}\mathbf{s} \tag{3.3}$$

in which the right-hand-side is the electromotive force $\hat{\mathbf{V}}_{\text{TMS}}$, the voltage in a closed loop due to a time-varying magnetic field. Equivalently, it is the voltage that would be measured by cutting the wire to create an open circuit and attaching a voltmeter to the leads. The latter equation (3.3) can also be seen as the Kirchhoff's voltage equation around each loop in the system, stating that the sum of all the voltages around the loop is equal to zero:

$$\sum_{\text{loop}} Z(\omega) \cdot \hat{\mathbf{I}}_{\text{tot}}(\mathbf{r},\omega) - \hat{\mathbf{V}}_{\text{TMS}}(\mathbf{r},\omega) = 0. \tag{3.4}$$

In case of isotropic materials, the lumped impedance Z is a scalar since both the conductivity and permittivity are scalars. To determine its value, we first rewrite equation (3.2) in x-, y- and z-components:

$$\begin{bmatrix} \hat{J}_{\text{tot,x}} \\ \hat{J}_{\text{tot,y}} \\ \hat{J}_{\text{tot,z}} \end{bmatrix} = \begin{bmatrix} (\sigma + j\omega\varepsilon)\hat{E}_x \\ (\sigma + j\omega\varepsilon)\hat{E}_y \\ (\sigma + j\omega\varepsilon)\hat{E}_z \end{bmatrix}. \tag{3.5}$$

Define Δx, Δy, and Δz as the x-, y-, and z-discretisation of the voxels. The total eddy current of the x-directed branch becomes $\hat{I}_{\text{tot,x}} = \hat{J}_{\text{tot,x}} \cdot (\Delta y \Delta z)$ and the voltage drop across the branch impedance for this current becomes $\hat{V}_{\text{branch,x}} = \hat{E}_{\text{x}} \cdot \Delta x$. With similar relations for these quantities in the y- and z-direction, we can obtain:

$$\begin{bmatrix} \hat{V}_{\text{branch,x}} \\ \hat{V}_{\text{branch,y}} \\ \hat{V}_{\text{branch,z}} \end{bmatrix} = \begin{bmatrix} Z_x \hat{I}_{\text{tot,x}} \\ Z_y \hat{I}_{\text{tot,y}} \\ Z_z \hat{I}_{\text{tot,z}} \end{bmatrix} \tag{3.6}$$

in which Z_x located on the x-oriented branch can directly be calculated:

$$Z_x(\omega) = \frac{\Delta x}{(\sigma(\omega) + j\omega\varepsilon(\omega))\Delta y \Delta z} \tag{3.7}$$

Similar equations can be derived for the impedances Z_y and Z_z.

Kirchhoff's voltage law is in the traditional IM considered on each cell face of the voxels by which the loop passes through the four impedances of the four edges. Because of that, each branch current can be written as a sum of the four loop currents surrounding each edge. For instance, the equation for the x-directed loop in the voxel (i,j,k) becomes, according to Fig. 3.2, with $0 \leq i < N_{\text{x}}$, $0 \leq j < N_{\text{y}}$ and $0 \leq k < N_{\text{z}}$:

$$\begin{aligned} \hat{V}_{\text{x}}(i,j,k) \;=\; & Z_{\text{y}}(i,j,k) \cdot \hat{I}_{\text{y}}(i,j,k) \\ & + Z_{\text{z}}(i,j+1,k) \cdot \hat{I}_{\text{z}}(i,j+1,k) \\ & - Z_{\text{y}}(i,j,k+1) \cdot \hat{I}_{\text{y}}(i,j,k+1) \\ & - Z_{\text{z}}(i,j,k) \cdot \hat{I}_{\text{z}}(i,j,k) \end{aligned} \tag{3.8}$$

$$\begin{aligned} \hat{V}_{\text{x}}(i,j,k) \;=\; & Z_{\text{y}}(i,j,k) \cdot [\hat{L}_{\text{x}}(i,j,k) - \hat{L}_{\text{x}}(i,j,k-1) \\ & + \hat{L}_{\text{z}}(i-1,j,k) - \hat{L}_{\text{z}}(i,j,k)] \\ & + Z_{\text{z}}(i,j+1,k) \cdot [\hat{L}_{\text{x}}(i,j,k) - \hat{L}_{\text{x}}(i,j+1,k) \\ & + \hat{L}_{\text{y}}(i,j+1,k) - \hat{L}_{\text{y}}(i-1,j+1,k)] \\ & - Z_{\text{y}}(i,j,k+1) \cdot [-\hat{L}_{\text{x}}(i,j,k) + \hat{L}_{\text{x}}(i,j,k+1) \\ & - \hat{L}_{\text{z}}(i,j,k+1) + \hat{L}_{\text{z}}(i-1,j,k+1)] \\ & - Z_{\text{z}}(i,j,k) \cdot [-\hat{L}_{\text{x}}(i,j,k) + \hat{L}_{\text{x}}(i,j-1,k) \\ & - \hat{L}_{\text{y}}(i-1,j,k) + \hat{L}_{\text{y}}(i,j,k)] \end{aligned} \tag{3.9}$$

where instead of branch currents, loop currents $\hat{L}_{\text{x}}$, $\hat{L}_{\text{y}}$ and $\hat{L}_{\text{z}}$ are introduced. $\hat{\mathbf{V}}$ is the electromotive force or voltage in the closed loop of the cell face that is caused by the stimulation, i.e. $\hat{\mathbf{V}}_{\text{TMS}}$ or the right-hand-side of equation (3.3). For simplicity of notation, the frequency dependence as well as the indices

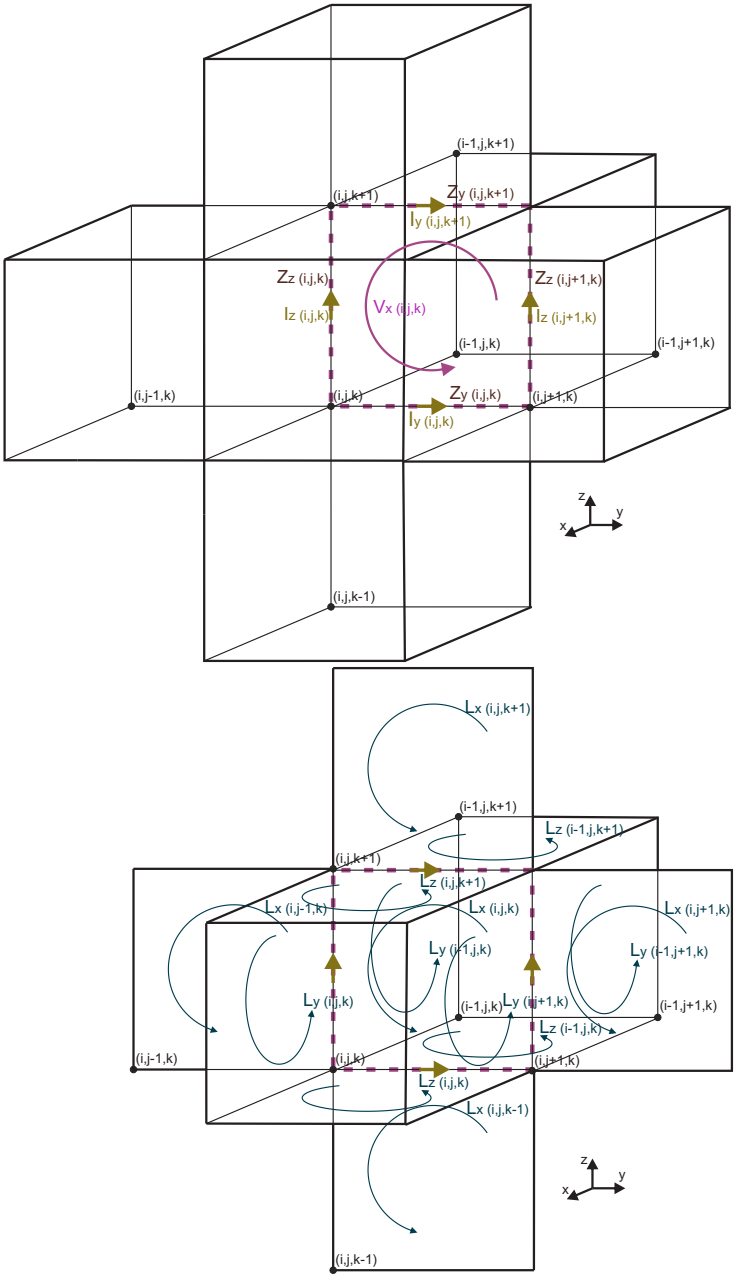

Figure 3.2: The x-directed loop in voxel (i,j,k) and corresponding (above) voltage $\hat{V}_x$, branch currents $\hat{I}$, impedances Z and (below) loop currents $\hat{L}$.

$_{\text{TMS}}$ and $_{\text{tot}}$ are omitted in the further descriptions. Similar sets of equations can be derived for y- and z-directed loops.

3.1.1 Practical implementation of IM

Assuming a $N_\text{x} \times N_\text{y} \times N_\text{z}$ discretised head model, the impedance method generates $3N_\text{x}N_\text{y}N_\text{z}$ equations, because of the x-, y- and z-component in (3.4). In matrix notation this becomes:

$$\mathcal{Z} \cdot \mathcal{I} = \mathcal{V} \tag{3.10}$$

with $\mathcal{I}$ the unknown $3N_\text{x}N_\text{y}N_\text{z} \times 1$ vector of branch currents and $\mathcal{V}$ the $3N_\text{x}N_\text{y}N_\text{z} \times 1$ vector of voltages. Each branch current can be written as a sum of loop currents $\mathcal{L}$ surrounding the corresponding edge. This relation can be expressed by the transformation matrix $\mathcal{T}$.

$$\mathcal{I} = \mathcal{T} \cdot \mathcal{L} \tag{3.11}$$

By defining $\tilde{\mathcal{Z}}$ as the $3N_\text{x}N_\text{y}N_\text{z} \times 3N_\text{x}N_\text{y}N_\text{z}$ coefficient matrix of the impedance network, the aforementioned equations lead to:

$$\tilde{\mathcal{Z}} = \mathcal{Z} \cdot \mathcal{T} \tag{3.12}$$

$$\tilde{\mathcal{Z}} \cdot \mathcal{L} = \mathcal{V} \tag{3.13}$$

$\mathcal{Z}$ and $\mathcal{T}$ are both determined by the choice of the loops. Here, each voxel with coordinates (i,j,k) is indexed as $i \cdot N_\text{y}N_\text{z} + j \cdot N_\text{z} + k$, hence the x-, y- and z-components of a value belonging to voxel (i,j,k) are at row $3(iN_\text{y}N_\text{z} + jN_\text{z} + k) + c$ with $c = 1,2,3$ respectively. For example, similar as in equation (3.8), the elements in matrix $\tilde{\mathcal{Z}}$ on row $rx = 3(iN_\text{y}N_\text{z} + jN_\text{z} + k) + 1$ for the x-directed loop in the voxel (i,j,k) become:

$$\begin{aligned}
\tilde{\mathcal{Z}}_{(rx,3((i-1)N_\text{y}N_\text{z}+jN_\text{z}+k)+2)} &= Z_\text{z}(i,j,k) \\
\tilde{\mathcal{Z}}_{(rx,3((i-1)N_\text{y}N_\text{z}+jN_\text{z}+k)+3)} &= Z_\text{y}(i,j,k) \\
\tilde{\mathcal{Z}}_{(rx,3((i-1)N_\text{y}N_\text{z}+jN_\text{z}+(k+1))+3)} &= -Z_\text{y}(i,j,k+1) \\
\tilde{\mathcal{Z}}_{(rx,3((i-1)N_\text{y}N_\text{z}+(j+1)N_\text{z}+k)+2)} &= -Z_\text{z}(i,j+1,k) \\
\tilde{\mathcal{Z}}_{(rx,3(iN_\text{y}N_\text{z}+(j-1)N_\text{z}+k)+1)} &= -Z_\text{z}(i,j,k) \\
\tilde{\mathcal{Z}}_{(rx,3(iN_\text{y}N_\text{z}+jN_\text{z}+(k-1))+1)} &= -Z_\text{y}(i,j,k) \\
\tilde{\mathcal{Z}}_{(rx,3(iN_\text{y}N_\text{z}+jN_\text{z}+k)+1)} &= Z_\text{y}(i,j,k) + Z_\text{z}(i,j+1,k) \\
&\quad + Z_\text{y}(i,j,k+1) + Z_\text{z}(i,j,k)
\end{aligned}$$

$$
\begin{aligned}
\tilde{\mathcal{Z}}_{(rx,3(iN_yN_z+jN_z+k)+2)} &= -Z_z(i,j,k) \\
\tilde{\mathcal{Z}}_{(rx,3(iN_yN_z+jN_z+k)+3)} &= -Z_y(i,j,k) \\
\tilde{\mathcal{Z}}_{(rx,3(iN_yN_z+jN_z+(k+1))+1)} &= -Z_y(i,j,k+1) \\
\tilde{\mathcal{Z}}_{(rx,3(iN_yN_z+jN_z+(k+1))+3)} &= Z_y(i,j,k+1) \\
\tilde{\mathcal{Z}}_{(rx,3(iN_yN_z+(j+1)N_z+k)+1)} &= -Z_z(i,j+1,k) \\
\tilde{\mathcal{Z}}_{(rx,3(iN_yN_z+(j+1)N_z+k)+2)} &= Z_z(i,j+1,k). \qquad (3.14)
\end{aligned}
$$

One can conclude that every row of the coefficient matrix $\tilde{\mathcal{Z}}$ contains at most 13 non-zero elements, namely 13 complex impedances or sum of impedances. It is wasteful to reserve storage for zero elements. This is the reason why we practically use a compressed column storage mode, sometimes called the Harwell-Boeing format (Press et al., 2007), for the sparse matrix $\tilde{\mathcal{Z}}$ while saving computation time and memory space. To store one complex number there are 16 bytes needed. Therefore, $\tilde{\mathcal{Z}}$ has a storage area smaller than $13 \cdot (3N_xN_yN_z) \cdot 16$ bytes.

This system of equations is solved numerically using a standard iterative method. Once we have obtained the loop currents $\mathcal{L}$, we can calculate the branch currents $\mathcal{I}$ along the edges of each cell by adding the values of their neighbouring four loop currents as in equation (3.11).

The system of equations seems to be however ill-conditioned. The iterative method has difficulties solving it and results in poor convergence, i.e. an increased number of iterations is required and a limited accuracy to which a solution can be obtained, and therefore a long computing time or possibly no solution. See also the results reported in (Wang et al., 2008). This is the reason why we introduced the independent impedance method, elaborated in the next Section.

3.2. Independent Impedance Method

The conventional IM is suboptimal and the main reason for the ill-conditionality is the presence of dependent equations. Appendix A verifies the existence of dependent loops in a simple $2 \times 2 \times 2$ circuit using IM. For a general case with problem scale $N_x \times N_y \times N_z$ we introduce graph theory to demonstrate these statements.

One voxel is represented by one node and the equations in (3.13) belonging to the voxel are constructed, considering three branches and three faces, as one can see in Fig. 3.1. There are $N = N_xN_yN_z$ nodes, $B = 3N_xN_yN_z$ branches and $F = 3N_xN_yN_z$ faces considered for the equations in total. In the traditional IM, Kirchhoff's voltage law is considered on the three cell faces of each voxel, resulting in $3N_xN_yN_z$ loops and therefore $3N_xN_yN_z$ equations. How-

ever, by considering the voxel network as a connected graph with N nodes and B branches, a spanning tree can be defined, i.e. a connected subset of the graph that contains all nodes, but not any loop. There exist more than one spanning tree for the given graph, but they all contain the same number of edges, namely $N-1$ edges. The graph theory now states that the number of independent loops is equal to $B-(N-1)$. This is illustrated in Fig. 3.3. For our problem, this means $3N_xN_yN_z-(N_xN_yN_z-1)$ independent loops, which is approximately a factor $1/3$ less than the considered total loops in the traditional method. This explains the ill-conditionality of IM, namely the existence of dependent loops and consequently dependent equations.

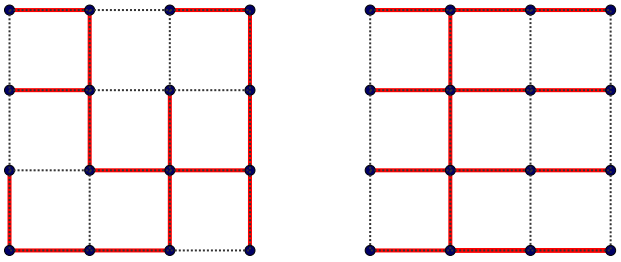

Figure 3.3: Possible spanning trees of the graph with N=16 nodes and B=24 branches. Many other trees are possible. This simple 2D example can easily be extended to 3D.

Based on graph theory we introduce the independent impedance method by determining a spanning tree and consequently obtaining a new set of independent equations. The chosen spanning tree meets some pre-defined criteria. The obtained loops have to contain as few branches as possible so as to reduce the memory storage, while the constructed tree has to preserve some regularity so that an easy implementation remains possible. Fig. 3.4 illustrates the choice of the tree, used in this PhD. It consists of all x-directed edges, for $x=u$ all y-directed edges and for $x=u$ and $y=v$ all z-directed edges. u and v are chosen as centralised as possible, to limit the dimension of the loops. We remark that alternative graph-trees are possible.

For adding every edge, which is not in the tree, we obtain a loop. We name the loop after the replenished branch and take its sign positive in the direction of that branch, see Fig. 3.4. All these loops form a maximal set of independent loops, for which we have to express Kirchhoff's voltage law. The number of equations in IIM that have to be solved is significantly reduced in comparison with IM, to the benefit of the computation time. IIM has the additional advantage that the coefficient matrix $\tilde{\mathcal{Z}}$ becomes now well-conditioned. Appendix A illustrates the independence of IIM by a simple example.

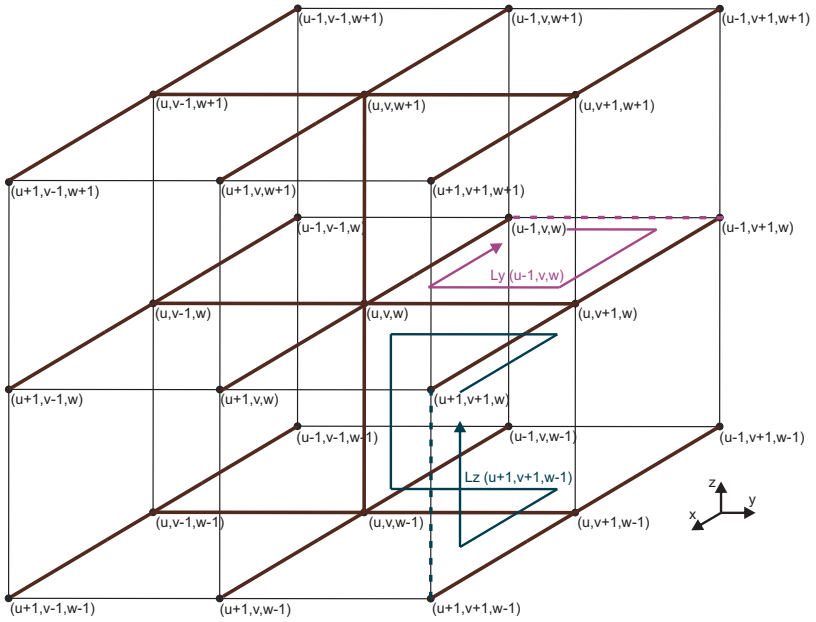

Figure 3.4: The chosen spanning tree for a $2 \times 2 \times 2$ cube, containing all edges in the x-direction, for $x = u$ all edges in the y-direction and for $x = u$ and $y = v$ all edges in the z-direction. The loop $\hat{L}_y(u-1,v,w)$ is obtained by adding the y-directed branch $(u-1,v,w)$ and the loop $\hat{L}_z(u+1,v+1,w-1)$ is obtained by adding the z-directed branch $(u+1,v+1,w-1)$.

3.2.1 Practical implementation of IIM

We solve the linear system (3.13), $\tilde{\mathcal{Z}} \cdot \mathcal{L} = \mathcal{V}$, for the loop currents $\mathcal{L}$, using the iterative preconditioned biconjugate gradient stabilised method (PBiCGSTAB) (Freund et al., 1992; Van der Vorst, 1992). Other iterative solvers such as multigrid are possible. Unlike the conjugate gradient method, the biconjugate gradient algorithm (BiCG) does not require a self-adjoint coefficient matrix, i.e. a square matrix that is equal to its own Hermitian transpose. Instead, they reference the matrix $\tilde{\mathcal{Z}}$ only through its multiplication by a vector $\mathbf{v}$ or the multiplication of its Hermitian transpose and a vector $\mathbf{v}$ (Press et al., 2007; Shewchuk, 1994). This way the method is very attractive for solving large sparse systems of equations. For coefficient matrices that are close to the identity matrix, the ordinary BiCG converges in a fast way. This suggests a technique called preconditioning (PBiCG), in which equation (3.13) can be solved indirectly through the use of the preconditioned form of it:

$$(\tilde{\mathcal{Z}}_{\mathrm{p}}^{-1} \cdot \tilde{\mathcal{Z}}) \cdot \mathcal{L} = \tilde{\mathcal{Z}}_{\mathrm{p}}^{-1} \cdot \mathcal{V} \tag{3.15}$$

The preconditioner matrix $\tilde{\mathcal{Z}}_{\mathrm{p}}$ is a matrix that approximates $\tilde{\mathcal{Z}}$, but is easier to invert. Here, we choose $\tilde{\mathcal{Z}}_{\mathrm{p}}$ equal to the diagonal part of $\tilde{\mathcal{Z}}$. Because $\tilde{\mathcal{Z}}_{\mathrm{p}}^{-1} \cdot \tilde{\mathcal{Z}} \approx \mathbb{1}$, the preconditioner allows the algorithm to converge in fewer steps. The stabilised PBiCGSTAB is a faster and more stable method than its ancestor PBiCG. From $\mathcal{L}$, the induced branch currents $\mathcal{I}$ can be calculated using equation (3.11).

As mentioned before in equation (3.12), matrix $\tilde{\mathcal{Z}}$ is the multiplication of the impedance matrix $\mathcal{Z}$ and the transformation matrix $\mathcal{T}$. $\mathcal{Z}$ and $\mathcal{T}$ are constructed similarly, because they are both determined by the choice of the loops (a simple example is illustrated in Appendix A). The smallest loop consists of only four edges, the biggest one of $N_{\mathrm{x}} + N_{\mathrm{y}} + 2$ edges. Every time a loop, indexed as m, passes through a c-directed edge (i,j,k), with $c = 1,2,3$, it corresponds with a non-zero value on row m and column $3(iN_{\mathrm{y}}N_{\mathrm{z}} + jN_{\mathrm{z}} + k) + c$ in matrix $\mathcal{Z}$ and a non-zero value on row $3(iN_{\mathrm{y}}N_{\mathrm{z}} + jN_{\mathrm{z}} + k) + c$ and column m in matrix $\mathcal{T}$. We will use this property in combination with PBiCGSTAB as the advantage that $\tilde{\mathcal{Z}}$ does not have to be stored in the memory explicitly. The p-th diagonal element of the preconditioner matrix becomes:

$$\begin{aligned} \tilde{\mathcal{Z}}_{\mathrm{p}(p,p)} &= \mathrm{diag}(\mathcal{Z} \cdot \mathcal{T})_{(p,p)} \\ &= \sum_{q} (\mathcal{Z}_{(p,q)} \cdot \mathcal{T}_{(q,p)}) \end{aligned} \tag{3.16}$$

Also for the used multiplications with vector $\mathbf{v}$ in PBiCGSTAB it suffices to store the sparse matrices $\mathcal{Z}$ and $\mathcal{T}$:

$$\tilde{\mathcal{Z}} \cdot \mathbf{v} = \mathcal{Z} \cdot (\mathcal{T} \cdot \mathbf{v}) \tag{3.17}$$

$$\tilde{\mathcal{Z}}^{\mathrm{H}} \cdot \mathbf{v} = \mathcal{T}^{\mathrm{H}} \cdot (\mathcal{Z}^{\mathrm{H}} \cdot \mathbf{v}) \tag{3.18}$$

The boundary conditions are that the human head model is situated in air. The branch currents corresponding to border voxels, i.e. the branch currents at the upper, right and front side of the domain, can be assumed zero due to the zero conductivity of air. Kirchhoff's current law states that at any node in an electrical network, the sum of currents flowing into that node is equal to the sum of currents flowing out of the node. Considering this, the boundary conditions are:

$$\hat{I}_{\mathrm{x}}(N_{\mathrm{x}},j,k) = 0 \tag{3.19}$$

$$\hat{I}_{\mathrm{y}}(i,N_{\mathrm{y}},k) = 0 \tag{3.20}$$

$$\hat{I}_{\mathrm{z}}(i,j,N_{\mathrm{z}}) = 0 \tag{3.21}$$

for every value of i, j and k. The number of branch currents RB that need to be found decreases consequently to $3N_{\mathrm{x}}N_{\mathrm{y}}N_{\mathrm{z}} - N_{\mathrm{x}}N_{\mathrm{y}} - N_{\mathrm{x}}N_{\mathrm{z}} - N_{\mathrm{y}}N_{\mathrm{z}}$.

Analogously, the number of loop currents RL that is necessary to solve equation (3.11) reduces with $N_xN_y + N_xN_z + N_yN_z$. As verified before, there are $3N_xN_yN_z - (N_xN_yN_z - 1)$ independent loops, leading to a $RL \times 1 = (2N_xN_yN_z - N_xN_y - N_xN_z - N_yN_z + 1) \times 1$ vector $\mathcal{L}$. $\mathcal{Z}$ becomes the $RL \times RB$ impedance matrix and $\mathcal{T}$ the $RB \times RL$ transformation matrix.
A flowchart of the 3D eddy-current solver IIM for the specific problem of TMS is shown in Fig. 3.5. Starting from the geometry and the material properties of the human head and the TMS coil configuration, the impedance, transformation and voltage matrices $\mathcal{Z}$, $\mathcal{T}$ and $\mathcal{V}$ respectively, can be obtained. The unknown eddy currents $\mathcal{I}$ can be calculated by solving equations (3.11) and (3.13).

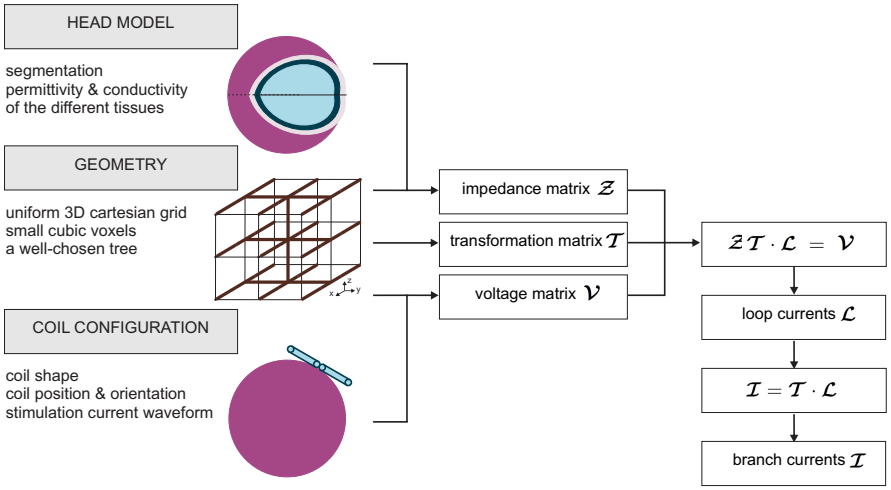

Figure 3.5: Flowchart of the 3D eddy-current solver using IIM

3.2.2 Simulations on a spherical head model

For the first electromagnetic calculations of TMS, a simple concentric three-layered spherical head model is considered. It contains the layers brain, skull and scalp, with radii 8.0 cm, 8.6 cm and 9.2 cm respectively (Brody et al., 1973; Homma et al., 1995). It is centralised in a cubic box of 20 cm $\times$ 20 cm $\times$ 20 cm and is surrounded by air. A TMS circular coil, consisting of just one turn, with an inner radius of 2.0 cm and outer radius of 2.5 cm is positioned 1.8 cm above the head model. The current through the coil is a sine wave with amplitude 7.66 kA and working frequency 3.6 kHz, which fits within the typical ranges of Table 1.1. A list of the assigned dielectric property values, according

to the 4-Cole-Cole model (2.31) and equation (2.29) for the applied frequency, is provided in Table 3.1. The inner layer brain is considered as grey matter.

Table 3.1: The relative permittivity (relative to the permittivity of vacuum ε_0) and conductivity values for the stimulation frequency of 3.6 kHz.

Tissue	$\varepsilon_\mathbf{r}$ **[-]**	σ **[S/m]**
Air	1.0005	0.0
Skin	30373.7	0.0011
Bone	1080.3	0.0203
CSF	109.0	2.0
Grey matter	56950.1	0.1069
White matter	26487.8	0.0655

The simulations are done with a discretisation of $N_\mathrm{x} = N_\mathrm{y} = N_\mathrm{z} = 100$ corresponding with a resolution of 2 mm of the spherical head model. The PBiCGSTAB based IIM needed 8.4 Gbytes and 2.3 h for calculating the eddy currents [f1]. 966 iterations were needed for reaching a normalised error less than a tolerance EPS of 2.0%.

$$\frac{\|\tilde{\mathcal{Z}} \cdot \mathcal{L} - \mathcal{V}\|}{\|\mathcal{V}\|} < \mathrm{EPS} \tag{3.22}$$

Figs. 3.6 and 3.7 illustrate the induced current density distribution, obtained with IIM, on cross sections and along three z-directed lines, respectively. In Section 1.2.2, we showed in Fig. 1.6 that the electric field in air, induced by a circular coil, is the strongest just below the coil and decreases with increasing distance from the coil. A similar pattern can be observed for the induced eddy currents. However, whereas the electric field in air drops to zero in the middle of the coil, the induced currents along that line (x=0.0 cm and y=0.0 cm) are small, but different from zero. This is due to the tissue properties of the head model. One can see the effect of the different conductivities on the eddy-current amplitude within the three layers, i.e. relatively lower amplitude for layers with lower conductivity.
Table 3.2 illustrates the convergence performance, i.e. the computing time (time) and the number of iterations (iter) of the IIM simulations required for reaching an error less than a desired tolerance EPS. When decreasing the tolerance, the accuracy of the results increases as well as the computational burden. A compromise has to be made. We can consider the numerical results with a normalised error, as defined in (3.22), less than a tolerance EPS of 0.1% as the correct solution $\hat{\mathbf{J}}_\mathrm{ref}$. The average error of the eddy-current density distribution

[1] 2 dual core Intel Xuon of 2.0 GHz with 16 Gb RAM memory on a 64 bit platform

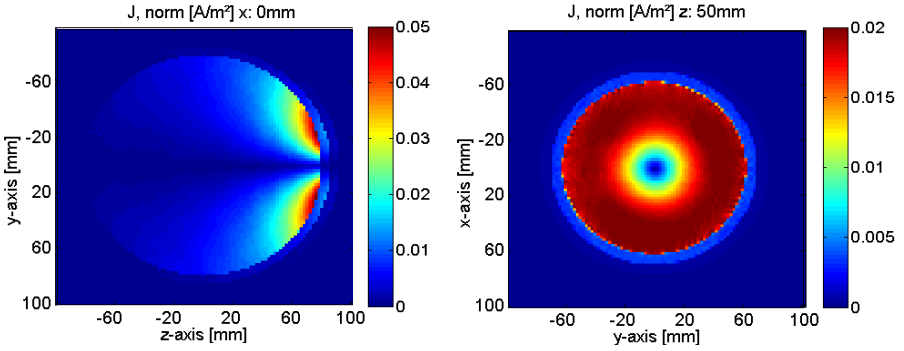

Figure 3.6: Distribution of the induced current density amplitude (in A/m^2) obtained with IIM in the spherical head model, on cross sections x=0.0 cm (left) and z=5.0 cm (right).

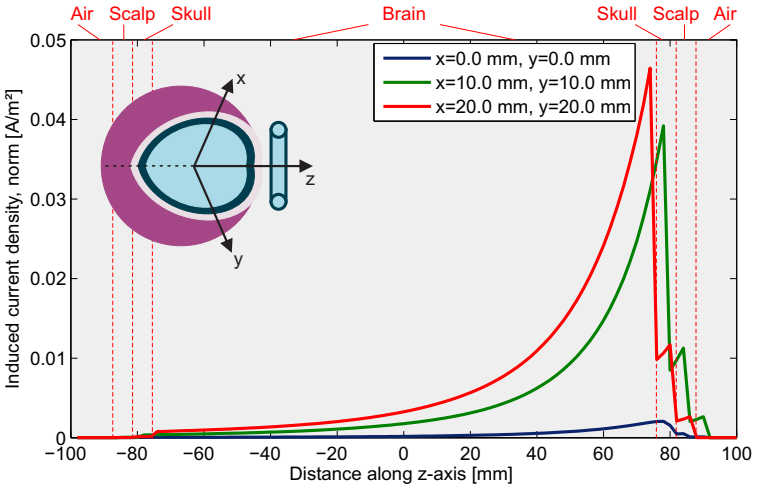

Figure 3.7: Induced current density amplitude (in A/m^2) along three z-directed lines. The first line is located at x=0.0 cm and y=0.0 cm, the second line at x=1.0 cm and y=1.0 cm and the third line at x=2.0 cm and y=2.0 cm. Corresponding with the last one, the interfaces of the different layers are indicated by vertical lines.

for a specific tolerance $\hat{\mathbf{J}}_{\text{tol}}$ can be described by:

$$\frac{1}{3N}\sum_{c=x,y,z}\sum_{\forall(i,j,k)}\frac{\left|\hat{J}_{\text{ref c}}(i,j,k)-\hat{J}_{\text{tol c}}(i,j,k)\right|}{\|\hat{J}_{\text{ref c}}(i,j,k)\|} \tag{3.23}$$

Fig. 3.8 shows this error together with the maximum and minimum error for a resolution of 5 mm. A tolerance of 2.0% is a good compromise.

Table 3.2: Convergence performance for different tolerances.

Tolerance EPS	Problem resolution 1 cm		5 mm		2 mm	
	iter	**time**	**iter**	**time**	**iter**	**time**
$1 \cdot 10^{-1}$	26	0.4s	72	16.4s	380	54.0min
$5 \cdot 10^{-2}$	35	0.5s	103	23.2s	730	1.7h
$2 \cdot 10^{-2}$	977	13.5s	243	54.5s	966	2.3h
$1 \cdot 10^{-2}$	985	13.6s	1131	4.2min	2299	5.4h
$5 \cdot 10^{-3}$	1036	14.2s	2216	8.2min	25472	2d 9h
$2 \cdot 10^{-3}$	2770	38.0s	6308	23.3min	27103	2d 13h
$1 \cdot 10^{-3}$	2975	40.8s	16070	59.8min	30518	2d 21h

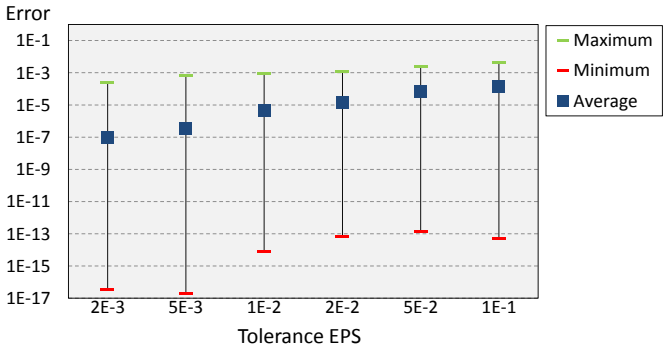

Figure 3.8: The error of the simulation results for a specific tolerance $\hat{\mathbf{J}}_{\text{tol}}$ relative to $\hat{\mathbf{J}}_{\text{ref}}$ for a resolution of 5 mm.

3.2.3 Comparison between IM and IIM

When comparing the independent impedance method with the traditional method, one can notice important differences. The number of equations and the number of unknowns reduce significantly for IIM. This advantage leads to a smaller dimension of the system matrix and consequently to a reduced memory allocation. The number of rows of both matrices $\mathcal{Z}$ corresponds with the number of defined loops and decreases from $3N_xN_yN_z$ for IM to $2N_xN_yN_z - N_xN_y - N_xN_z - N_yN_z + 1$ independent loops for IIM. The number of columns of the matrices $\mathcal{Z}$ corresponds with the number of branch currents that have to be found and decreases from $3N_xN_yN_z$ to $3N_xN_yN_z - N_xN_y - N_xN_z - N_yN_z$ due to the boundary conditions (3.19, 3.20, 3.21).
However, with increasing problem scale the obtained loops will contain more branches, resulting in an increasing number of non-zero values for each equation in matrices $\mathcal{Z}$ and $\mathcal{T}$ and consequently more memory storage. Fig. 3.9

illustrates the two opposite effects on the total number of non-zero elements in the matrices as a function of the problem scale. For small 3D circuits the effect of the reduced number of equations dominates.

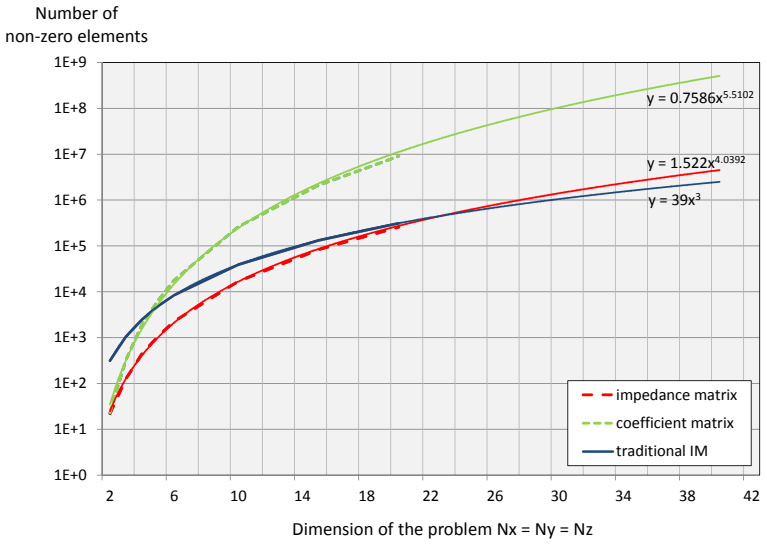

Figure 3.9: Number of non-zero elements in the stored matrices, namely the impedance matrix $\mathcal{Z}$, the coefficient matrix $\tilde{\mathcal{Z}}$ and the matrix $\mathcal{Z}$ in traditional IM, for different problem scales. Equations of the form $y = ax^b$ are fitted to the data.

Take for example a $10\times10\times10$ discretised model. The original coefficient matrix $\tilde{\mathcal{Z}}$, used in IM, is a 3000×3000 sparse matrix, containing 37668 non-zero elements. To solve the same system of equations in IIM, we use a 1701×2700 sparse matrix $\mathcal{Z}$, containing 16902 non-zero elements. Besides the fact that the memory occupation for this problem scale is significantly reduced, the new impedance matrix becomes well-conditioned. This means that the linear equation solution will be more accurate and less sensitive to errors in the data. Fig. 3.9 also shows the benefit of storing the impedance matrix $\mathcal{Z}$ instead of the coefficient matrix $\tilde{\mathcal{Z}}$, as explained in Section 3.2.
Conventionally, the traditional impedance method relies on the successive over-relaxation (SOR) algorithm for solving the linear system of equations (3.13) $\tilde{\mathcal{Z}} \cdot \mathcal{L} = \mathcal{V}$. SOR is a variant of the Gauss-Seidel method. An overcorrection to the value of $\mathcal{L}^n_{(g,1)}$, on the g-th row and at the n-th stage of Gauss-Seidel iteration, is made, anticipating future corrections and consequently resulting in faster convergence. When solving the system, each solution element can be written as (Liu et al., 2003):

$$\mathcal{L}^n_{(g,1)} = \mathcal{L}^{n-1}_{(g,1)} + \kappa\left(\mathcal{L}^{GS}_{(g,1)} - \mathcal{L}^{n-1}_{(g,1)}\right) \tag{3.24}$$

with κ the over-relaxation parameter. The method is convergent only for $0 < \kappa < 2$. $\mathcal{L}^{GS}_{(g,1)}$ is the Gauss-Seidel iterate:

$$\mathcal{L}^{GS}_{(g,1)} = \mathcal{V}_{(g,1)} - \sum_{h=1}^{g-1} \tilde{\mathcal{Z}}_{(g,h)} \cdot \mathcal{L}^{n}_{(h,1)} - \sum_{h=g+1}^{3N} \tilde{\mathcal{Z}}_{(g,h)} \cdot \mathcal{L}^{n-1}_{(h,1)} \tag{3.25}$$

However, when using the traditional method the equation system can become significantly ill-conditioned, as in (Wang et al., 2008). This results in long convergence time and even in some situations where the solution will not converge at all. This is the main reason why we have introduced the independent impedance method. IIM eliminates the dependent components by the use of graphs. We have determined a well-chosen spanning tree and confirmed the independence of the obtained loops using IIM. This independence improves the condition of the coefficient matrix $\tilde{\mathcal{Z}}$ and the convergence rate of the method. The linear system of equations can easily be solved now.
Table 3.3 illustrates the performance results for IM and IIM applied to the simulation of TMS in the implemented spherical head model. According to the computing time (time) and the number of iterations (iter) required for reaching an error less than a tolerance of 10%, IIM solved with the PBiCGSTAB algorithm clearly outperforms the SOR-based solutions of IM. However, the memory consumption (mem) was higher than for the conventional method, as explained before in this Section, see Fig. 3.9. Compared to the traditional IM, the proposed IIM achieves superior time efficiency and is therefore a useful tool for accurate, fast and numerical converging TMS simulations.

Table 3.3: Comparison of the performance results for IM and IIM.

Iterative method	**Problem resolution**					
	1 cm			**5 mm**		
	iter	**time**	**mem**	**iter**	**time**	**mem**
IM SOR	65	15.1min	22Mb	178	10.3h	179Mb
IIM SOR	27	9.0min	21Mb	93	2.8h	258Mb
IIM PBiCGSTAB	26	0.4s	21Mb	72	16.4s	258Mb

3.2.4 Validation of IIM

We validate the IIM method by comparing the obtained eddy-current simulations on the spherical model with the analytical solutions. The mathematical method for computing the current densities induced by a current flow in a coil, is based on (Eaton, 1992) and extended for computations inside the three-layered spherical head model due to the coil centralised in x=0.0 cm, y=0.0

cm and z=11.0 cm. Fig. 3.10 shows the analytical results for the same two-dimensional (2D) cross sections of the head model as in Fig. 3.6. Both results correspond well with each other qualitatively as well as quantitatively, as can be seen from the difference plots.

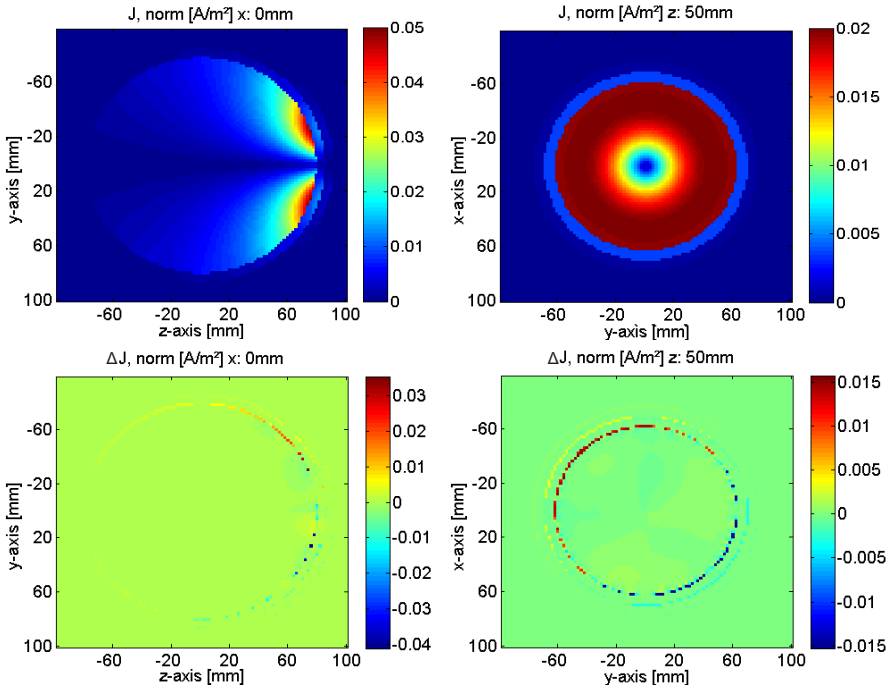

Figure 3.10: (Above) Analytical solution of the induced current density distribution on cross sections x=0.0 cm (left) and z=5.0 cm (right). (Below) Difference between the IIM and mathematical results.

We also performed similar simulations with COMSOL Multi-physics ® (COMSOL Inc., Los Angeles, California USA), a commercial FEM software package, as shown in Fig. 3.11. The comparison between IIM and FEM is difficult to make and therefore we only want to validate the presented IIM rather than to show the superiority of one method compared to another.
Finally, the independent impedance method is also validated against traditional method solutions. As illustrated in Fig. 3.12, a good agreement is obtained between IM and IIM, with an average difference of 6%.

3.3. Anisotropic Independent Impedance Method

Some biological tissues have anisotropic material properties. This means that the conductivity and permittivity are not equal in every direction and that

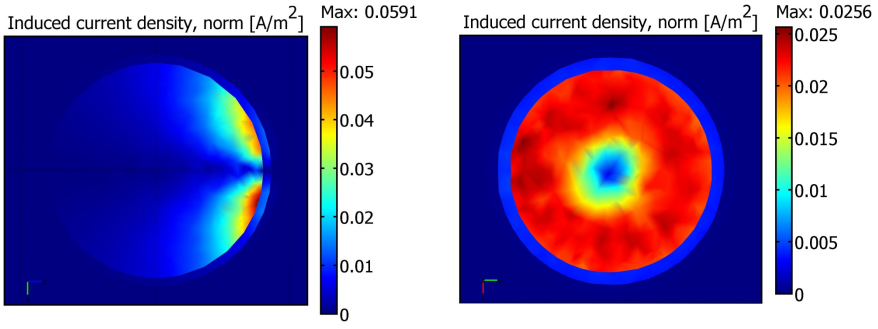

Figure 3.11: Finite element simulations of the induced current density distribution for the same set-up and on the same cross sections as in Fig. 3.10.

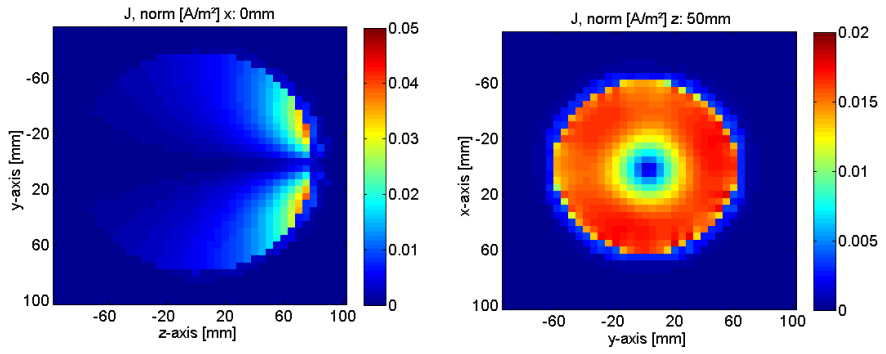

Figure 3.12: Conventional IM calculations of the induced current density distribution for the same set-up and on the same cross sections as in Fig. 3.10, with a resolution of 5 mm.

they can be written as position-dependent tensors. For example, the electrical properties of skull and white matter are known to be anisotropic (Wolters et al., 2006). The skull consists of a soft bone layer between two hard layers, resulting in a higher conductivity tangentially than radially to the skull surface (Rush and Driscoll, 1968). White matter consists of different nerve bundles connecting grey matter and has the highest conductivity parallel to the fibres and the smallest perpendicular to them due to insulating myelin sheaths (Nicholson, 1965).

Simulation studies have shown that electromagnetic fields can be highly sensitive to tissue anisotropy (Wolters et al., 2006). According to De Lucia et al. (2007), brain anisotropy has a non-negligible effect on the spatial distribution of the induced electric field during TMS. Consequently, it is necessary to include anisotropy in the eddy-current solver, which does not yet exist in the IM or IIM formulations, to our knowledge.

3.3.1 Practical implementation of anisotropic IIM

In general, the conductivity σ and the permittivity ε are tensors and, analogous to equation (3.5), the total current density can be written as follows:

$$\begin{bmatrix} \hat{J}_{\mathrm{tot,x}} \\ \hat{J}_{\mathrm{tot,y}} \\ \hat{J}_{\mathrm{tot,z}} \end{bmatrix} = \begin{bmatrix} A_{\mathrm{xx}} & A_{\mathrm{xy}} & A_{\mathrm{xz}} \\ A_{\mathrm{xy}} & A_{\mathrm{yy}} & A_{\mathrm{yz}} \\ A_{\mathrm{xz}} & A_{\mathrm{yz}} & A_{\mathrm{zz}} \end{bmatrix} \begin{bmatrix} \hat{E}_{\mathrm{x}} \\ \hat{E}_{\mathrm{y}} \\ \hat{E}_{\mathrm{z}} \end{bmatrix}. \tag{3.26}$$

For simplicity of notation, matrix $\mathcal{A}$ is defined as $A_{pq} = \sigma_{pq} + j\omega\varepsilon_{pq}$ for $p,q = \mathrm{x,y,z}$ and the position as well as the frequency dependence are omitted. Note that $\mathcal{A}$ is symmetric because biological tissues are reciprocal media. However, the presented method is not restricted to such media.

In case of isotropic materials, both the conductivity and permittivity are scalars. Consequently, the scalar impedances Z_{x}, Z_{y} and Z_{z} located on the x-, y- and z-oriented branches can directly be calculated for each voxel as in equation (3.7). Kirchhoff's voltage law for the x-directed loop in the voxel (i,j,k) in the traditional impedance method is written down in equation (3.8), but repeated here for clarity reasons:

$$\begin{aligned} \hat{V}_{\mathrm{x}}(i,j,k) \;=\; & Z_{\mathrm{y}}(i,j,k) \cdot \hat{I}_{\mathrm{y}}(i,j,k) \\ & + Z_{\mathrm{z}}(i,j+1,k) \cdot \hat{I}_{\mathrm{z}}(i,j+1,k) \\ & - Z_{\mathrm{y}}(i,j,k+1) \cdot \hat{I}_{\mathrm{y}}(i,j,k+1) \\ & - Z_{\mathrm{z}}(i,j,k) \cdot \hat{I}_{\mathrm{z}}(i,j,k) \end{aligned} \tag{3.27}$$

A straightforward extension to anisotropic cases is only possible when $\mathcal{A}$ is a diagonal matrix with $\sigma_{\mathrm{xy}} = \sigma_{\mathrm{xz}} = \sigma_{\mathrm{yz}} = 0$ and $\varepsilon_{\mathrm{xy}} = \varepsilon_{\mathrm{xz}} = \varepsilon_{\mathrm{yz}} = 0$. For this specific case, the expression for the scalar impedance is still valid provided that the electrical properties are replaced by those in the x-, y- and z-direction, respectively, as in (Tachas et al., 2009).

In the general case of anisotropy, it is still possible to use a lumped network, though in which each limb is characterised by three impedances instead of one. For each voxel, these corresponding impedances can be calculated by inverting matrix $\mathcal{A}$, multiplied by the length of the edge and divided by the cross-sectional area of the voxel in the direction perpendicular to the edge. Based on equation (3.26) and analogous to equation (3.6), we can consider:

$$\begin{bmatrix} \hat{V}_{\mathrm{branch,x}} \\ \hat{V}_{\mathrm{branch,y}} \\ \hat{V}_{\mathrm{branch,z}} \end{bmatrix} = \begin{bmatrix} Z_{\mathrm{xx}} & Z_{\mathrm{xy}} & Z_{\mathrm{xz}} \\ Z_{\mathrm{xy}} & Z_{\mathrm{yy}} & Z_{\mathrm{yz}} \\ Z_{\mathrm{xz}} & Z_{\mathrm{yz}} & Z_{\mathrm{zz}} \end{bmatrix} \begin{bmatrix} \hat{I}_{\mathrm{tot,x}} \\ \hat{I}_{\mathrm{tot,y}} \\ \hat{I}_{\mathrm{tot,z}} \end{bmatrix} \tag{3.28}$$

with the total eddy current of the x-directed branch $\hat{I}_{\mathrm{tot,x}} = \hat{J}_{\mathrm{tot,x}} \cdot (\Delta y \Delta z)$, the voltage drop across the total branch impedance for this current $\hat{V}_{\mathrm{branch,x}} =$

$\hat{E}_{\mathrm{x}} \cdot \Delta x$ and similar relations for these quantities in the y- and z-direction. Z_{pq} ($p,q = \mathrm{x},\mathrm{y},\mathrm{z}$) can be calculated using $\mathcal{A}^{-1}$ and the discretisations of the voxels. To demonstrate the effect of including anisotropy on IM, Kirchhoff's voltage law is written out in detail for the anisotropic case in the same x-directed loop as in equation (3.27):

$$\begin{aligned}
\hat{V}_{\mathrm{x}}(i,j,k) \;=\; & [Z_{\mathrm{xy}}(i,j,k) \cdot \hat{I}_{\mathrm{tot,x}}(i,j,k) + \\
& Z_{\mathrm{yy}}(i,j,k) \cdot \hat{I}_{\mathrm{tot,y}}(i,j,k) + \\
& Z_{\mathrm{yz}}(i,j,k) \cdot \hat{I}_{\mathrm{tot,z}}(i,j,k)] \\
+\; & [Z_{\mathrm{xz}}(i,j+1,k) \cdot \hat{I}_{\mathrm{tot,x}}(i,j+1,k) + \\
& Z_{\mathrm{yz}}(i,j+1,k) \cdot \hat{I}_{\mathrm{tot,y}}(i,j+1,k) + \\
& Z_{\mathrm{zz}}(i,j+1,k) \cdot \hat{I}_{\mathrm{tot,z}}(i,j+1,k)] \\
-\; & [Z_{\mathrm{xy}}(i,j,k+1) \cdot \hat{I}_{\mathrm{tot,x}}(i,j,k+1) + \\
& Z_{\mathrm{yy}}(i,j,k+1) \cdot \hat{I}_{\mathrm{tot,y}}(i,j,k+1) + \\
& Z_{\mathrm{yz}}(i,j,k+1) \cdot \hat{I}_{\mathrm{tot,z}}(i,j,k+1)] \\
-\; & [Z_{\mathrm{xz}}(i,j,k) \cdot \hat{I}_{\mathrm{tot,x}}(i,j,k) + \\
& Z_{\mathrm{yz}}(i,j,k) \cdot \hat{I}_{\mathrm{tot,y}}(i,j,k) + \\
& Z_{\mathrm{zz}}(i,j,k) \cdot \hat{I}_{\mathrm{tot,z}}(i,j,k)]. \qquad (3.29)
\end{aligned}$$

This loop is also illustrated in Fig. 3.13. Each voxel is defined by three cell faces and three cell edges, to which loop voltages respectively branch currents and impedances are assigned. Traditionally, Kirchhoff's voltage law is considered on each cell face of the voxels, by which the loop passes through four edges. In the isotropic case, one impedance is assigned to each cell edge, resulting in a contribution of four impedances to the loop, as in equation (3.27). In the case of anisotropy, on the contrary, each cell edge is characterised by three impedances of which two are meant as current-controlled voltage sources. When the loop passes through the z-directed edge of voxel (*i*,*j*,*k*), the potential difference measured over the impedance $Z_{\mathrm{zz}}(i,j,k)$ through which the current $\hat{I}_{\mathrm{tot,z}}(i,j,k)$ runs as well as the current-controlled voltage sources $Z_{\mathrm{xz}}(i,j,k) \cdot \hat{I}_{\mathrm{tot,x}}(i,j,k)$ and $Z_{\mathrm{yz}}(i,j,k) \cdot \hat{I}_{\mathrm{tot,y}}(i,j,k)$ contribute to the voltage drop. This results in a total of twelve contributing impedances associated to the aforementioned loop, as can be seen in equation (3.29).

Similar sets of equations are derived as equations (3.11-3.13). The difference in the amount of contributing impedances between isotropy and anisotropy will influence the sparsity of matrices $\mathcal{Z}$, $\mathcal{T}$ and thus $\tilde{\mathcal{Z}}$. The extension to anisotropic tissues for IIM is exactly the same as described above. Because IM is suboptimal to IIM, we choose the anisotropic IIM for the applications and the validation of the extended method.

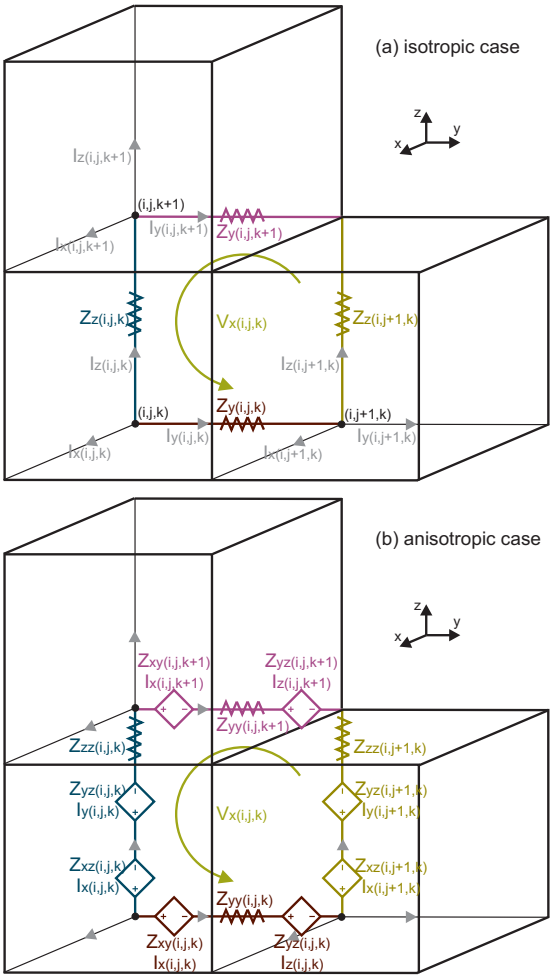

Figure 3.13: The contributing impedances and current-controlled voltage sources for an x-directed loop in voxel (i,j,k) and the corresponding voltage $\hat{V}_x$ in a) the isotropic and b) the extended anisotropic case.

3.3.2 Simulations on an anisotropic spherical head model

We apply the anisotropic IIM for the simulation of eddy currents in two different five shell spherical head models due to the same circular TMS coil as in Section 3.2.2, positioned 1.8 cm above the head models and supplied with a sinusoidal current (7.66 kA, 3.6 kHz). Both concentric head models contain the layers scalp, skull, grey matter, white matter and thalamus, with radii 9.2 cm, 8.6 cm, 8.0 cm, 7.0 cm and 2.0 cm respectively. In the first model, we assume that all tissues have isotropic material properties, whereas in the second one,

we assume anisotropic conductivity ratios for the skull (1:10 radially to tangentially to the skull surface) (Rush and Driscoll, 1968) and white matter (1:9 transversally to longitudinally along the nerve fibre) (Nicholson, 1965). In this white matter shell, the nerve bundles are assumed to start from the thalamus and go in the radial direction to the grey matter shell. The above ratios are an approximation of reality and are still not exactly known (Sadleir and Argibay, 2007). The isotropic tissue properties for the working frequency of 3.6 kHz are listed in Table 3.1. Thalamus is considered to have the same properties as grey matter. The tensors can be calculated from these isotropic values by imposing the volume constraint (Wolters et al., 2006), which states that the volume of the isotropic conducting sphere is equal to the anisotropic conducting ellipsoid. We use again the iterative preconditioned biconjugate gradient stabilised method (Van der Vorst, 1992) for solving the linear system (3.15). The induced eddy currents are then calculated from the known loop currents.
Although these spherical head models are a rough approximation of reality, they are very instructive since they can be solved analytically and easily be described in commercial FEM packages. This way, we can validate the proposed approach and use it in further research on more complex head models with realistic geometry. In reality, nerve bundles are not collinear in radial direction. Their trajectory can be reconstructed by diffusion tensor imaging and tractography, as will be explained in Section 6.3.

Fig. 3.14 compares the eddy-current distribution between the isotropic and anisotropic head models. The anisotropic conductivities cause an increased induction of currents in the scalp, skull, grey matter and thalamus. The maximum current density increases from $55.3{\cdot}10^{-3}$ A/m^2 to $60.8{\cdot}10^{-3}$ A/m^2 and is located 3.0 cm beneath the coil, corresponding with that part of the cortex that is the closest to the excitation coil. The difference between both simulations rises to $22.4{\cdot}10^{-3}$ A/m^2, which is about 40% of the maximum value, and is observed in the skull. However, for the application of TMS, especially the neurological system located in the brain is of interest. When focussing on these regions, the maximum current density difference becomes $10.5{\cdot}10^{-3}$ A/m^2, which is about 19% of the highest intensity, and is observed in grey matter. The inclusion of space-dependent anisotropic tissue properties seems essential. We strongly believe that the anisotropic behaviour of white matter in more sophisticated head models will even more affect the induced current distribution and that these results will lead to important new insights in the study of brain stimulation.

Table 3.4 summarises the performance and the required memory (mem) for both head models. The computing time (time) and the number of iterations (iter) of the IIM simulations required for reaching a normalised error, defined in equation (3.22), less than 2% are given for different resolutions. As illustrated in equations (3.27) and (3.29), more impedances contribute in the

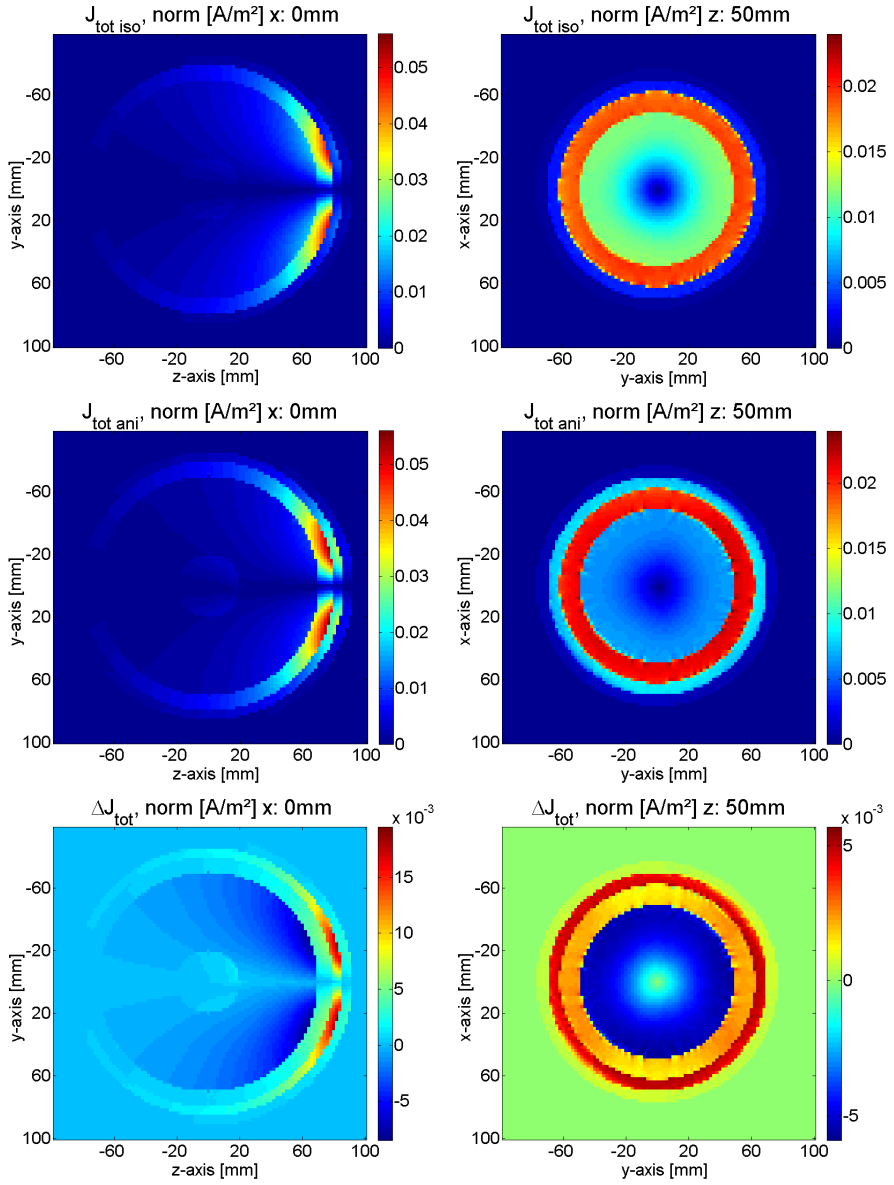

Figure 3.14: Comparison of the induced current density results obtained with IIM for a resolution of 2 mm in the isotropic head model (above), indicated with subscript iso, and those in the anisotropic head model (middle), indicated with subscript ani, on cross sections x=0.0 cm (left) and z=5.0 cm (right). At the bottom, the difference between both models is represented.

Table 3.4: Convergence performance and memory occupation.

	Isotropic model			Anisotropic model		
	iter	**time**	**mem**	**iter**	**time**	**mem**
10 mm	736	10.1 s	21 Mb	422	8.4 s	35 Mb
5 mm	231	51.9 s	258 Mb	273	1.4 min	470 Mb
2 mm	1522	3.5 h	8.4 Gb	1334	4.4 h	16 Gb

anisotropic case, which lead to a less sparse system matrix and consequently an increased computational burden.

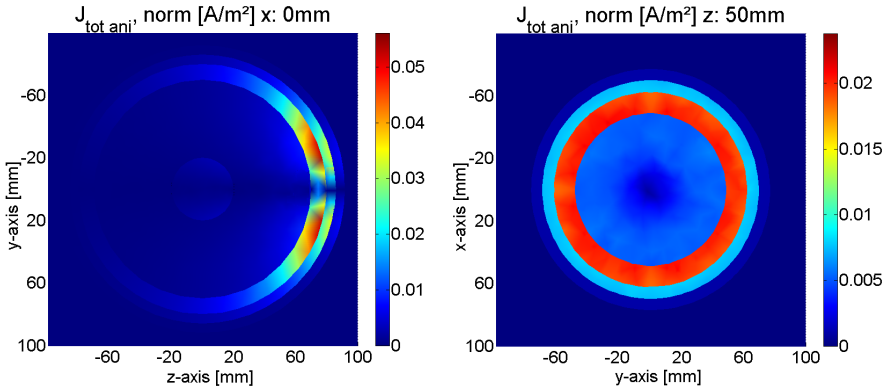

Figure 3.15: Finite element solutions obtained in the anisotropic head model, for the same set-up and on the same cross sections as in Fig. 3.14

.

We validate the numerical results of the extended anisotropic IIM by comparing the results with FEM solutions, obtained with the COMSOL software package. Fig. 3.15 shows the same cross sections of the head model as in Fig. 3.14 with the corresponding induced current density distributions. Both anisotropic IIM and FEM results correspond well with each other qualitatively as well as quantitatively. The FEM calculations have been implemented on a grid with a mesh element size between 8 mm in the scalp and skull and 13 mm in the brain. This resulted in a total of 461438 mesh elements and 29.9 min simulation time. Analogously as in the isotropic case, it is not our intention to compare the different methods, but to validate the obtained the results.

3.4. Discussion and assumptions

The independent impedance method is developed and explained in this chapter. It is based on the conventional impedance method (Section 3.1), but elim-

inates the dependent loops and consequently redundant equations in the linear system using graph theory. An appropriate spanning tree, i.e. a connected subset of the graph that contains all nodes but not any loop, is fitted to the 3D network. For adding every edge, which is not in the tree, we obtain a loop. All these loops form a maximal set of independent loops, for which we express Kirchhoff's voltage law. The number of equations in IIM that have to be solved is significantly reduced in comparison with IM, to the benefit of the computation time. It results as well in improved conditionality of the system. We implemented in this PhD a certain spanning tree, but the solution is independent of the tree choice.
Notice that we neglected the contribution of the eddy currents to the magnetic induction, as in (Nadeem et al., 2003) and (Wang et al., 2008).
The developed IIM has been tested with a standard problem being a stimulated spherical head model consisting of different tissues. It is compared to the IM solution and validated by comparison with analytical results and with simulations on a commercial FEM software package.
Since some biological tissues have anisotropic material properties, we extended our method such that for every voxel the conductivity and permittivity can be described by a full tensor. The anisotropic IIM is applied for the simulation of TMS on both isotropic and anisotropic spherical head models. The results showed that anisotropy had a non-negligible effect on the induced currents, yielding maximum differences of about 40% in the skull and 19% in grey matter. However, the impact of anisotropic tissues on TMS effects should be investigated on more realistic head models. The extended method is validated again by comparing the induced current distribution with FEM solutions.
The here elaborated and numerically validated electromagnetic solver is used throughout the PhD. It features computational efficiency and flexibility in execution for various head models encompassing different levels of fidelity.

Remember that all models are wrong; the practical question
is how wrong do they have to be to not be useful.

George Edward Pelham Box

4

Estimating conductivity

The head tissue conductivity values are up to now not well known. They are patient-specific and frequency-dependent. However, an accurate estimation of these values is important for the correct calculation of the induced currents originating from TMS. These accurate conductivity values associated to the various brain tissues need to be imported in the head model. This represents a next step towards accurate patient-specific TMS calculations. A precise tissue conductivity quantification will not only enhance the accuracy and fidelity of TMS modelling, but also the precision of source localisation using electroencephalography (EEG) (Crevecoeur et al., 2012) and the resolution of magnetoencephalography (MEG) for mapping brain activity. The localisation of neural sources starting from EEG data can contain errors of 3 up to 5 cm because of the uncertainty on conductivity values (Gaignaire et al., 2010), which is not acceptable.

Electrical impedance tomography (EIT) is a standard method for measuring the electrical conductivity (Cheney et al., 1999). After injecting currents into the patient using electrodes, the conductivity values are inferred from voltage measurements on the skin. EIT exhibits however a limited spatial resolution, since the surface measurements are less sensitive to conductivity changes in inner regions of the patient (Seagar et al., 1987). Recently, several hybrid tomography techniques have been developed, which are based on electric and magnetic fields (Gençer et al., 1994; Zlochiver et al., 2003), MR signals (Seo

and Woo, 2011) or acoustic modalities (Gebauer and Scherzer, 2008; Zhang and Wang, 2004). The frequency dependence is typically neglected since most devices operate at a fixed frequency. Moreover, when currents are injected through surface electrodes, problems such as the appearance of higher current densities near these conductors and susceptibility artefacts occur (Özparlak and Ïder, 2005).
In the induced current magnetic resonance electrical impedance tomography (ICMREIT) external coils induce currents inside the patient (Özparlak and Ïder, 2005). These currents create a secondary magnetic flux density in the brain, which is measured by the MR scanner and used to reconstruct the conductivity values. In some cases the reconstruction is done based on the measurement of the induced eddy-current distribution (Liu et al., 2009).
We propose in this chapter a novel ICMREIT-based technique for the non-invasive conductivity estimation in the low frequency domain. This new method, called induced current MR phase imaging EIT, makes use of the present gradient coils of the MR scanner to induce the eddy currents. The resulting secondary magnetic flux density causes variations of the phase image. The difference between two phase images obtained by gradient echo sequences with and without switching an eddy-current induction gradient is measured by the MR scanner and contains the information necessary to reconstruct the internal conductivity distribution. This necessitates solving an inverse problem, which consists of a large number of unknowns. Therefore, we use a segmented geometry, reducing the number of conductivity profiles that needs to be quantified from the number of voxels to the number of tissues. The independent impedance method (IIM), discussed in the previous Section 3.2, is applied for the eddy-current calculations and the parametrised frequency-dependent 4-Cole-Cole model, introduced in Section 2.2.1, is used as material model. First, we aim at recovering the required 4-Cole-Cole parameters for the tissues. Second, we modify the technique with multi gradient echo sequences by which only one parameter per tissue needs to be estimated, but with conservation of the frequency dependence of the conductivity values. Computer simulations are performed on spherical head models to evaluate the feasibility of the proposed conductivity estimation technique.
Results from this chapter have been presented at the International Conference of the IEEE Engineering in Medicine and Biology Society (EMBC) in 2010 in Argentina (De Geeter et al., 2010), the International Magnetics Conference (INTERMAG) in 2012 in Vancouver, the Workshop on Optimization and Inverse Problems in Electromagnetism (OIPE) in 2012 in Belgium and published in (De Geeter et al., 2013b).

4.1. Basic principles MR scanner

Magnetic resonance imaging (MRI) can produce high quality images of the inside of the human body by measuring the spatial distribution of nuclear spins in the body, usually those of protons. Human tissues consist typically of 60% to 80% water and each water molecule contains two hydrogen protons. When a hydrogen proton is placed in a homogeneous strong main magnetic DC field ($\mathbf{B}_{\mathrm{DC}}$), its magnetic dipole moment will precess around this field. Due to interactions with the surroundings, the magnetic dipole moment will rapidly (typically in 0.1 to 3 s) align with the main magnetic field. This process is called spin-lattice or T1 relaxation. When a radio-frequency (RF) pulse ($\mathbf{B}_{\mathrm{RF}}$) is sent at a specific frequency, called the Larmor frequency, the nucleus will be excited and the magnetic dipole moment is brought out of its equilibrium. It will precess around the main magnetic field and this precession results in an electromagnetic wave that is measured by the MR scanner and leads to a magnitude image and a phase image (Bernstein et al., 2004; Haacke et al., 1999). The Larmor frequency is given by

$$f_{\mathrm{L}} = \frac{\gamma_{\mathrm{g}}}{2\pi} B \tag{4.1}$$

with B the magnetic field strength at the nucleus and γ_{g} the gyromagnetic ratio, equal to $26.75 \cdot 10^7$ rad/sT for hydrogen protons.

The emitted MR signal decays with a time constant $\mathrm{T2}^*$, attributed to the presence of local magnetic field inhomogeneities. Since this wave itself carries no spatial information, gradient coils are provided. During the sequence of excitation and signal reception 3 different magnetic field gradients in the x-, y- and z-direction are applied to encode the MR signal spatially, more specific $\mathbf{G}_{\mathrm{x}}$ for frequency encoding, $\mathbf{G}_{\mathrm{y}}$ for phase encoding and $\mathbf{G}_{\mathrm{z}}$ for slice selection to connect the MR signal with its corresponding coordinates (x, y, z) (Bernstein et al., 2004). When the z-gradient is applied in combination with an RF excitation pulse, only one slice of magnetic dipole moments will be excited in the scanned subject. For example, consider a $\mathbf{B}_{\mathrm{DC}}$ of 1.0 T and a gradient $\mathbf{G}_{\mathrm{z}}$ of 0.01 T/m. The magnetic field strength for the slice at z = 0 cm is then 1.0 T and will be excited by a RF pulse at a Larmor frequency of 42.6 MHz. For the slice at z = 50 cm, however, the field is 1.005 T and utilisation of a RF pulse at 42.8 MHz, will selectively excite only the spins from this slice. Thus with the magnetic field strength being a function of z-location, the Larmor frequency also becomes a function of this location. When the y-gradient is applied after RF excitation but before signal reception, the magnetic dipole moments will precess at a different Larmor frequency depending on their position along the y-axis during the time this gradient is on. This leads to different phases in the y-direction after a phase encoding gradient is applied. When the x-gradient is

applied during signal acquisition, the magnetic dipole moments will precess at different Larmor frequencies depending on their x-position in the gradient. In this way, signals are obtained from a particular slice with phase encoded rows and frequency encoded columns. The recorded signals are digitised and stored in a matrix, the so-called k-space. After several spatially encoded MR signals are recorded, fast Fourier transform is applied on the k-space to reconstruct the MR image. The field-of-view (FOV) is the size of the total image. The image data is described by complex numbers and can be reconstructed as real and imaginary or as magnitude and phase images, see Fig. 4.1, depending on the clinical utility.

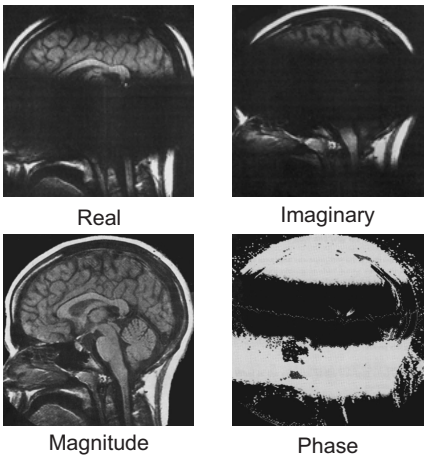

Figure 4.1: Real (Re), imaginary (Im), magnitude and phase images of the same MR signal. The magnitude and phase images can be calculated as $\sqrt{\mathrm{Re}^2 + \mathrm{Im}^2}$ and $\arctan(\mathrm{Im}/\mathrm{Re})$, respectively.

The decay of the MR signal can be recovered by applying a second RF pulse, more specifically a 180° refocusing pulse at TE/2 after the first RF pulse. After another TE/2, an echo signal is observed, hence the name echo time TE. The intensity of this echo signal decays with the time constant T2, typically 50 to 150 ms. Relaxation times T1, T2, and T2* are important tissue characteristics for imaging (Bernstein et al., 2004; Haacke et al., 1999). The sequence of an excitation RF pulse and a 180° refocussing pulse is called the spin-echo sequence. When the 180° RF pulse is replaced by rapidly reversing a magnetic gradient, it is called the field-echo or gradient-echo sequence. The gradient-echo sequence, illustrated in Fig. 4.2, is applied in this chapter to estimate the tissue conductivity values as further explained in Section 4.2.
The time between two successive excitation RF pulses is the repetition time TR, typically more than 1 s. In actual clinical settings, fast or turbo sequences

are performed to shorten the imaging time (TR = 10 to 100 ms) by using multiple reversal pulses or gradients. In this way, the decaying signal is continually refocussed such that multiple echo signals can be recorded from each excitation pulse. The turbo field-echo sequence is applied in this PhD to acquire the T1-weighted images.
Similar in concept to turbo spin-echo, is the echo planar imaging sequence. Rapid gradient reversal pulses of the readout gradient are utilised, resulting in multiple echo signals and reduction of fast dephasing or signal loss. The echo train technique can be pushed to the limit to fill the entire k-space with a single RF excitation pulse (TR is thus infinite). This so-called single-shot sequence requires the successive application of as many 180° pulses as there are k-space lines to fill. The single-shot spin-echo echo planar imaging sequence is applied in this PhD to acquire the DTI data sets. It is a very fast and efficient acquisition method, but has limited spatial resolution. The applied b-value identifies the measurement's sensitivity to diffusion and determines the strength and duration of the diffusion gradients. A b-value of zero delivers a T2-weighted EPI image for anatomical reference. The greater the b-value, the stronger the diffusion weighting, but the lower the signal quality.

4.2. Induced current MR phase imaging EIT

The measurements that are used for the conductivity estimation can be performed on a state-of-the-art MR scanner. The patient undergoes two times an MRI scan with gradient echo (GE) sequencing, as illustrated in Fig. 4.2. Recent studies (Seo and Woo, 2011; Van de Moortele et al., 2005) have shown the significant potential of phase images that hold information on the conductivity values of biological tissues. The GE sequence is executed twice and the difference of both phase images is recorded (De Deene et al., 2000). For the first image, only the essential components of a standard GE sequence are applied: the main uniform DC field ($\mathbf{B}_{\mathrm{DC}}$), 3 gradient fields for spatial localisation ($\mathbf{B}_{\mathrm{x}}$ + $\mathbf{B}_{\mathrm{y}}$ + $\mathbf{B}_{\mathrm{z}}$ = $\mathbf{G}_{\mathrm{x}}x$ + $\mathbf{G}_{\mathrm{y}}y$ + $\mathbf{G}_{\mathrm{z}}z$) and the RF field for excitation ($\mathbf{B}_{\mathrm{RF}}$). Moreover, the source current density in the excitation coil leads to a primary magnetic field ($\mathbf{B}_{\mathrm{p}}$).
For the second image, we switch an additional eddy-current induction (ECI) gradient ($\mathbf{B}_{\mathrm{ECI}}$) before the RF pulse. This gradient is switched on and off by the z-directed gradient coil, but all imaging directions and combinations of these are possible. It induces eddy currents into the patient, which, in turn, cause a secondary magnetic field ($\mathbf{B}_{\mathrm{s}}$) through Biot-Savart's law.

$$\hat{\mathbf{B}}_{\mathrm{s}}(\mathbf{r},\omega) = \frac{\mu_0}{4\pi} \iiint_{\mathrm{volume}} \frac{\hat{\mathbf{J}}_{\mathrm{eddy}}(\mathbf{r'},\omega) \times (\mathbf{r}-\mathbf{r'})}{\|\mathbf{r}-\mathbf{r'}\|^3} \mathrm{d}\mathbf{v'} \tag{4.2}$$

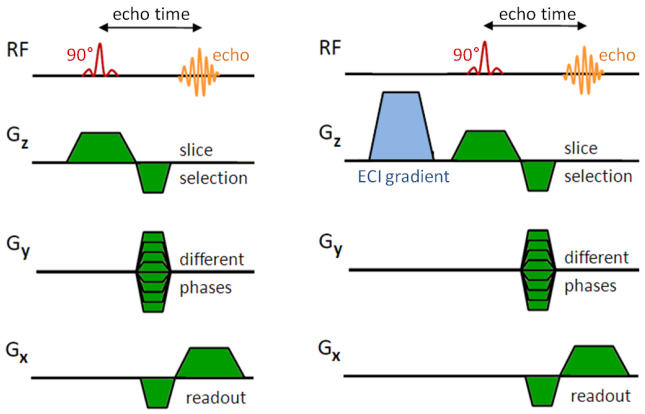

Figure 4.2: Pulse sequence diagrams illustrate in time the different steps that the sequence comprises. (Left) A standard GE sequence is applied a first time, with the 90° RF pulse for excitation, 3 trapezoidal field gradients for frequency encoding and readout ($\mathbf{G}_x$), phase encoding ($\mathbf{G}_y$) and slice selection ($\mathbf{G}_z$) and the echo resulting in the phase image ϕ_1. The hatched lines of $\mathbf{G}_y$ indicate that this amplitude is varied incrementally each time the sequence is executed. (Right) The same GE sequence is applied a second time, but with an additional z-directed ECI gradient for inducing extra eddy currents, resulting in the adjusted phase image ϕ_2.

where $\mathbf{r} = (x,y,z)$ and $\mathbf{r'} = (x',y',z')$ refer to field and source points respectively. The induced eddy currents $\mathbf{J}_{\text{eddy}}$ in (4.2) are calculated using the IIM of Section 3.2 and depend on the distribution of the conductivity in the patient. This way the secondary magnetic field contains the information necessary to reconstruct this conductivity distribution.

The phase obtained with a GE sequence can be calculated as the gyromagnetic ratio of hydrogen γ_g times the integration over the total magnetic field from time zero to the echo time TE being the time between the 90° RF pulse and (the centre of) the echo when the MR signal is measured. The phase difference $\Delta\phi = \phi_2 - \phi_1$ is defined as a point-wise subtraction of the phase image with and without ECI gradient. It is only related to the induced secondary field $\mathbf{B}_s$, because the other fields are cancelled out (Bernstein et al., 2004) and the images are acquired after the switching of the ECI gradient and therefore, $\mathbf{B}_{\text{ECI}}$ itself is not measured by the MR scanner:

$$\Delta\phi(\mathbf{r}) = \int_0^{\text{TE}} \gamma_g \mathbf{B}_s(\mathbf{r},t) \cdot \mathrm{d}t, \tag{4.3}$$

with $\mathbf{B}_s(\mathbf{r},t)$ being the secondary field in the time domain computed from phasor $\hat{\mathbf{B}}_s(\mathbf{r},\omega)$ (4.2).

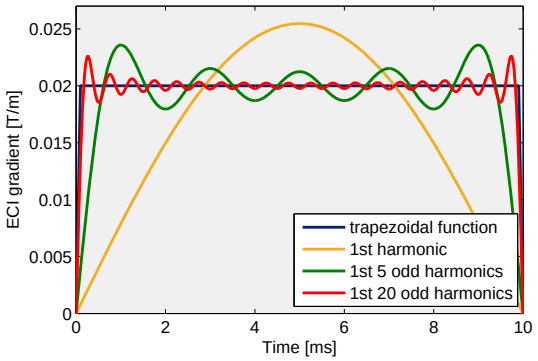

Figure 4.3: Decomposition of the trapezoidal ECI gradient with $A = 0.02$ T/m, $\tau = 0.1$ ms and $T = 20$ ms into the first 1, 5 and 20 odd Fourier harmonics.

Note that we combine an integration over time of $\mathbf{B}_s$ with the calculation of this field in the frequency domain with the time-varying magnetic field $\mathbf{B}_{\text{ECI}}$ and the frequency-dependent material properties as input. This necessitates Fourier and inverse Fourier transformations. The ECI gradient is a trapezoidal function and can be decomposed into Fourier harmonics:

$$\sum_{k=1}^{K} \frac{4A}{\omega_k \tau \pi (2k-1)} \sin(\omega_k \tau) \sin(\omega_k t) \tag{4.4}$$

with

$$\omega_k = \frac{2\pi(2k-1)}{T} \tag{4.5}$$

and A being the amplitude, T the period and τ the rise and fall time. Notice that only odd harmonics exist. The total number of odd harmonics K is optimally equal to ∞. The 3 curves in Fig. 4.3 show the first term, the first 5 terms and the first 20 terms in the Fourier expansion. As more terms are added, the superposition of sine waves better matches the trapezoidal curve, so that the accuracy of the results increases, but so will the computational burden. The first 10 odd harmonics (k = 1,2,...,10 corresponding with the 1st, 3th, ..., 19th harmonics) provide a reasonable approximation and will be applied in this work, unless otherwise specified. Since the period of the ECI gradient is typically between 0.1 and 100 ms, this reduces the frequency range of interest to 10^1-10^4 Hz. For each of these 10 odd harmonics and consequently for each of the corresponding angular frequencies ω_k, calculated with equation (4.5), the induced currents and secondary magnetic field are computed in the frequency domain. Subsequently, the secondary magnetic field as function of time can be

calculated:

$$\mathbf{B}_s(\mathbf{r},t) \approx 2\frac{1}{2\pi}\sum_{k=1}^{K}\mathrm{Re}\left(\hat{\mathbf{B}}_s(\mathbf{r},\omega_k)e^{j\omega_k t}\right) \tag{4.6}$$

Notice that it is multiplied with a factor 2, because the negative frequency spectrum is equal to the positive one.

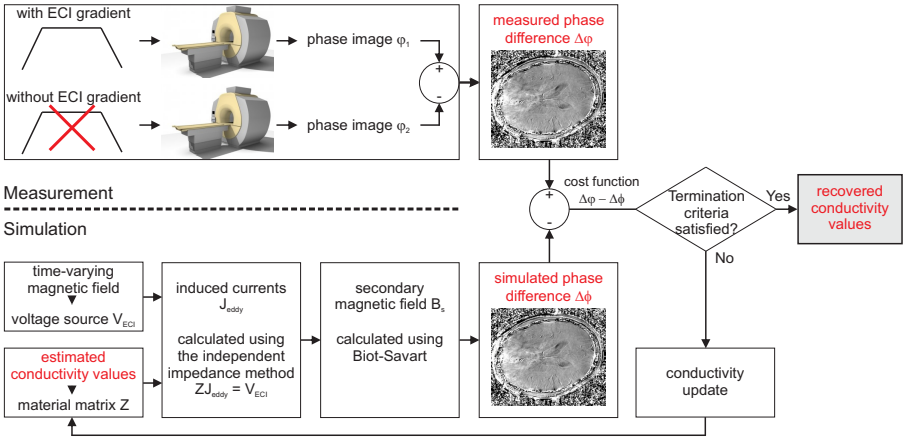

Figure 4.4: Flowchart of the proposed technique. In this numerical study, an artificial phase difference distribution is generated for a given applied ECI gradient on a segmented geometry with known material properties, and acts as 'measurement'.

The flowchart of the proposed method, the induced current MR phase imaging EIT, consisting of a measurement and a simulation part, is illustrated in Fig. 4.4. For a given applied ECI gradient on a segmented geometry with known material properties, an artificial phase difference distribution is generated which acts as 'measurement' in the numerical experiments. The inverse problem is then solved using an iterative optimisation algorithm where the difference between the 'measured' and simulated phase differences is minimised. We can numerically validate the proposed methodology by comparing the known conductivity values with the recovered ones.

4.2.1 Single GE sequence

First we perform a preliminary study on coarse spherical head models, in which the number of tissues are gradually increased. The 4-Cole-Cole material model (Cole and Cole, 1941; Gabriel et al., 1996c) describes the dielectric spectrum of biological tissues in terms of multiple dispersion regions, as explained in Section 2.2.1. With the parameters listed in Table 2.1, the conductivity values were obtained from equations (2.29) and (2.31) and plotted in Fig. 2.2. Since

the ECI gradient mainly consists of low frequencies, the frequency range of interest is reduced, corresponding with the α relaxation (n = 4) of this model. Moreover, the value of ε_∞ is fixed at 2.5 or 4 for low and high water-content tissues, respectively (Gabriel et al., 1996c). This results in four parameters ($\triangle\varepsilon_4$, τ_4, α_4 and σ_i) that need to be estimated per tissue.
We group these material parameters in the vector $\mathbf{p}$, characterised as $[\triangle\varepsilon_4, \tau_4, \alpha_4, \sigma_\mathrm{i}]$ for each tissue. The cost function is defined as:

$$K(\mathbf{p}) = \sum_{x,y,z} \|\Delta\varphi(x,y,z) - \Delta\phi(x,y,z,\mathbf{p})\| \tag{4.7}$$

with $\|\cdot\|$ the L_2-norm that measures the distance between the measured $\Delta\varphi(x,y,z)$ and simulated $\Delta\phi(x,y,z,\mathbf{p})$ phase differences for every voxel. A summation is made over all the voxels. The 4-Cole-Cole parameters are reconstructed by minimising this cost function:

$$\tilde{\mathbf{p}} = \arg\min_{\mathbf{p}\in P} K(\mathbf{p}). \tag{4.8}$$

P is the feasible domain of the material parameters in the frequency range of interest to limit the search space: $0 < \triangle\varepsilon_4 < 5 \cdot 10^7\varepsilon_0$, $10^{-3} < \tau_4 < 16 \cdot 10^{-3}$, $0 < \alpha_4 < 0.2$, $10^{-4} < \sigma_\mathrm{i} < 0.7$. For minimising the cost function, state-of-the-art iterative algorithms can be used, such as the non-gradient based Nelder-Mead simplex method (Nelder and Mead, 1965).
The simulations are performed on spherical head models with a coarse discretisation of 1 cm, as in (Özparlak and Ïder, 2005). An ECI gradient is applied with an amplitude A of 0.02 T/m, a rising time τ of 0.1 ms and a period T of 20 ms. 10 harmonics are considered for the Fourier transformation of the trapezoidal ECI gradient field. The echo time TE is 60 ms. These simulations are numerically validated in the following way. For the given ECI gradient and known material parameters $\check{\mathbf{p}}$, an artificial phase difference distribution $\Delta\phi$ can be generated. The defined low-parametric inverse problem is then solved towards the optimal reconstructed parameters $\tilde{\mathbf{p}}$, as in equation (4.8). The difference between $\|\check{\mathbf{p}} - \tilde{\mathbf{p}}\|$ expresses the accuracy of the methodology. The calculation time of one forward model evaluation is approximately 30 seconds[f2]. In this way, efficiency is obtained and solving the inverse problem, where this forward model is iteratively evaluated, becomes computationally feasible in time in comparison to traditional ICMREIT (Özparlak and Ïder, 2005).
In a first stage, we model the sphere as brain with $\check{\mathbf{p}} = [4.5 \cdot 10^7\varepsilon_0, 5.30 \cdot 10^{-3}, 0, 0.02]$ which correspond with the 4-Cole-Cole parameters for grey matter given in Table 2.1 (Gabriel et al., 1996c). Fig. 4.5 shows the evolution of the parameters $\mathbf{p}$ for which the phase difference is iteratively evaluated, and the

[2] 2 dual core intel Xuon of 2.0 GHz with 8 Gb RAM memory on a 64 bit platform

corresponding cost function. Convergence is obtained after approximately 50 evaluations in the forward solver, resulting in a total computational time of 1500 s or 25 min. Both the estimated and the actual 4-Cole-Cole conductivity profiles in the frequency domain are depicted in Fig. 4.6 and correspond well with each other. The estimated low frequency limit $\tilde{\sigma}_i = 2.06 \cdot 10^{-2}$ approximates well the actual value $\check{\sigma}_i = 0.02$.

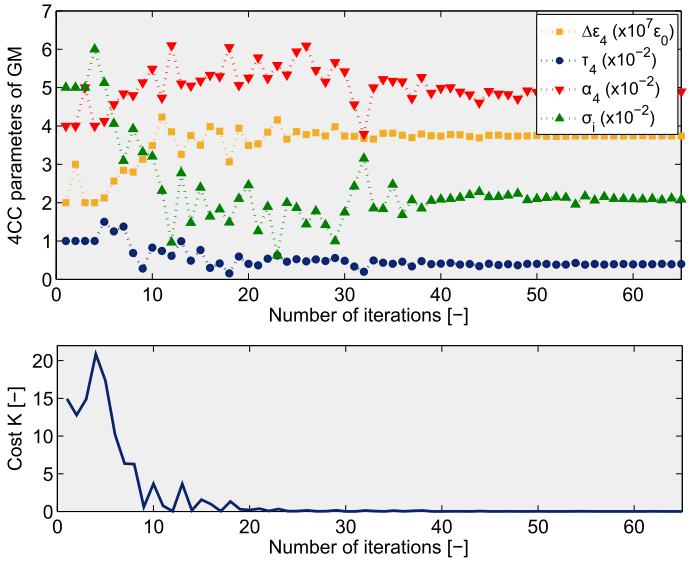

Figure 4.5: Evolution of the parameter values and cost function for the tissue grey matter. Notice that each parameter is divided by a certain factor, such that it has a value between 0.1 and 10. This facilitates the search process of the iterative algorithm.

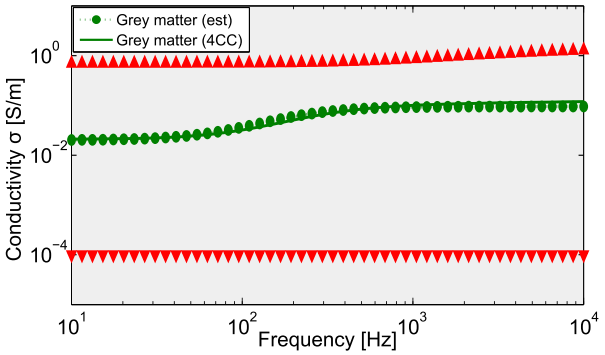

Figure 4.6: Estimated (est) conductivity profile of grey matter in comparison with the α relaxation of the 4-Cole-Cole model (4CC). The lower and upper bounds are indicated with marks.

In a second stage, we use a spherical model containing the layers brain and scalp, with $\check{\mathbf{p}}$=$[4.5 \cdot 10^7\varepsilon_0, 5.30 \cdot 10^{-2}, 0, 0.02,\ 3.0 \cdot 10^4\varepsilon_0, 1.59 \cdot 10^{-3}, 0.2, 0.0004]$ for the tissues grey matter and skin according to the 4-Cole-Cole model (Gabriel et al., 1996c), see Table 2.1. Fig. 4.7 illustrates the estimated conductivity profiles corresponding with a total cost K of $2.96 \cdot 10^{-5}$. However, these results are obtained with start values close to the actual values. Indeed, the cost function contains multiple local minima. This necessitates the use of a multi-start minimisation algorithm. This has the disadvantage that conductivity estimation becomes computationally slow, which can be partly resolved through the use of a parallel computing environment.

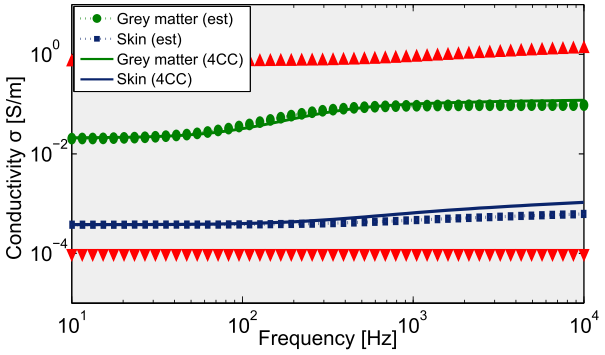

Figure 4.7: Estimated (est) conductivity profile of the tissues grey matter and skin in comparison with the α relaxation of the 4-Cole-Cole model (4CC). The lower and upper bounds are indicated with marks.

These preliminary simulations show that it is possible to estimate the conductivity values in the given frequency range in a feasible computational time. However, for an increasing number of tissues (> 2) the method is not converging well to the correct solution due to multiple local minima in the cost function. Therefore, we modify the technique with multi gradient echo sequences.

4.2.2 Multi GE sequences

Multiple gradient echo sequences are switched with distinct periods of the applied trapezoidal ECI gradient, as explained in Fig. 4.8. For each pulse sequence we fit a constant to the conductivities, so that a single parameter needs to be estimated per tissue. A large period means simulations in the low frequency domain, while small periods provide information about higher frequency domains. In this way, the frequency dependence of the electrical properties is maintained and a final curve can be constructed.
We carry out two GE sequences in total, by which the ECI gradient has an amplitude A of 0.02 T/m, a rising time τ of 0.1 ms and a period T that is changed

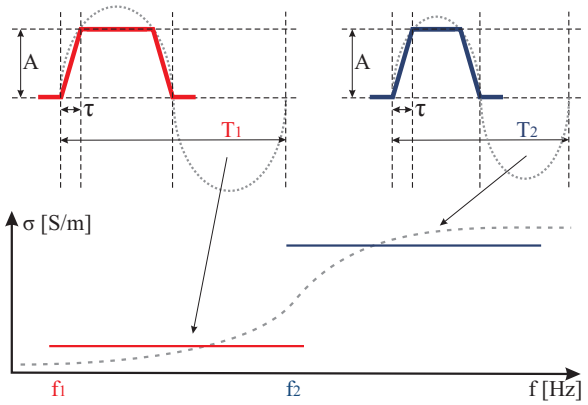

Figure 4.8: Principle of the multi GE sequences to reconstruct the frequency-dependent conductivities by estimating a single parameter per tissue for each trapezoidal ECI gradient.

from 20 ms to 2 ms. These periods correspond with the frequency ranges [50-950] Hz and [500-9500] Hz respectively, since the first 10 odd harmonics are used. The echo time is set to 60 ms, short enough since the eddy-current effect is averaged over this time interval, see equation (4.3). The proposed method is performed on a spherical head model segmented into the tissues skin, bone, grey matter and white matter. Initially, their conductivities are set to fixed values in the forward solver, grouped in vector $\mathbf{p}$. They are listed in Table 4.1 for the 2 mentioned frequency ranges and were chosen based on the 4-Cole-Cole model, which is plotted in Fig. 2.2.

Table 4.1: Fixed conductivity σ and permittivity ε values of the relevant tissues.

Tissue	Skin	Bone	Grey	White
		[50-950] Hz		
σ [S/m]	0.00055	0.02	0.095	0.06
ε [F/m]	$3.8 \cdot 10^4 \varepsilon_0$	$4.5 \cdot 10^3 \varepsilon_0$	$8.4 \cdot 10^5 \varepsilon_0$	$5.0 \cdot 10^5 \varepsilon_0$
		[500-9500] Hz		
σ [S/m]	0.001	0.02	0.11	0.065
ε [F/m]	$3.1 \cdot 10^4 \varepsilon_0$	$2.0 \cdot 10^3 \varepsilon_0$	$1.0 \cdot 10^5 \varepsilon_0$	$0.55 \cdot 10^5 \varepsilon_0$

The gradient based non-linear least squares method (Bates and Watts, 1988) is used to iteratively minimise the cost function, which is defined as the L_2-normalised difference between the 'measured' and simulated phase differ-

ence, divided by the L_2-norm of the 'measured' phase difference.

$$K_{\mathrm{n}}(\mathbf{p}) = \sum_{x,y,z} \frac{\|\Delta\varphi(x,y,z) - \Delta\phi(x,y,z,\mathbf{p})\|}{\|\Delta\varphi(x,y,z)\|}. \tag{4.9}$$

Notice that this is the same cost function as in equation (4.7), but normalised so that it has a value between 0 and 1.
In the inverse solver, the conductivities of the four human head tissues are set as the input parameters, listed in vector $\mathbf{p} = [\sigma_{\mathrm{skin}}, \sigma_{\mathrm{bone}}, \sigma_{\mathrm{grey}}, \sigma_{\mathrm{white}}]$, having each a starting value of 0.1 S/m. A lower and upper bound on these variables are defined, so that the solution remains in the range [0.0003 - 3.0] S/m. These bounds are chosen in such a way that the conductivities of the used tissues can have realistic values over the frequency range of interest and that the search space is not restricted too much. The minimum change in the variables for the finite-difference gradients is set to 0.01 S/m. The permittivity values of all tissues are fixed at $1.0 \cdot 10^5 \varepsilon_0$.
For the first pulse sequence with an ECI gradient period T of 20 ms, the termination tolerance of $1.0 \cdot 10^{-7}$ is obtained after 46 iterations by which the cost (4.9) decreased with 99.5%, as plotted in Fig. 4.9. Fig. 4.10 shows the convergence of the input parameters towards their recovered values, which are listed in Table 4.2 on line a) for the frequency range [50-950] Hz.
Similarly, for the second pulse sequence with an ECI gradient period T of 2 ms, four estimated conductivity values are obtained and can be found at line a) in Table 4.2 for the range [500-9500] Hz.

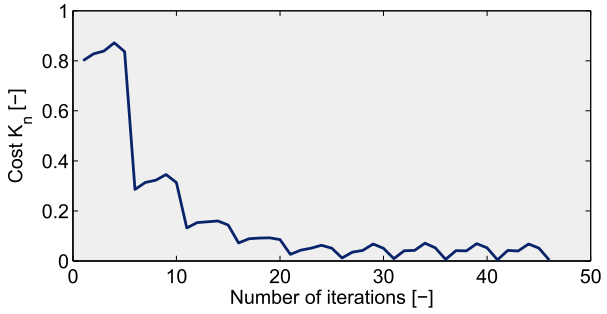

Figure 4.9: Evolution of the cost function for an ECI gradient with a period of 20 ms.

The reconstructed conductivity profiles are represented in Fig. 4.11 and agree well with the conductivity profiles of the 4-Cole-Cole model. This can also be observed when comparing Table 4.1 with line a) in Table 4.2. The reconstructed values for skin, bone, grey and white matter deviate [44%, −1.2%, 0.062%, 0.0017%] and [0.40%, 0.22%, 0.074%, −0.56%] respectively from the 4-Cole-Cole values.

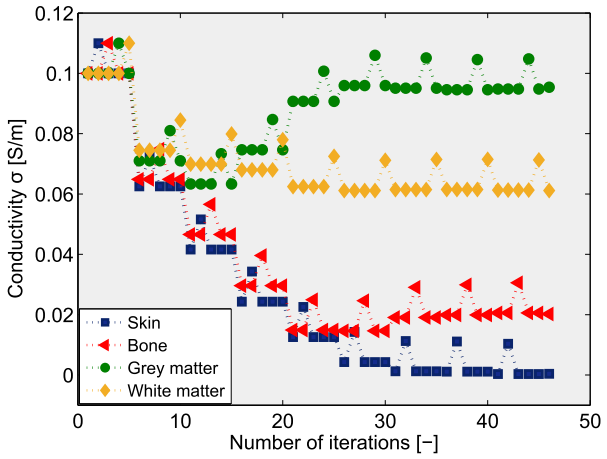

Figure 4.10: Conductivity parameters for an ECI gradient with a period of 20 ms are converging to their recovered values. The minimum change in the variables for the finite-difference gradients is set to 0.01 S/m, leading to sudden changes in the course of the curve.

Table 4.2: Reconstructed conductivity values σ, when the conductivities in the forward solver a) are set to fixed values (discussed here in Section 4.2.2) and b) are computed with the 4-Cole-Cole model (discussed in Section 4.2.4).

	Tissue	Skin	Bone	Grey	White
			[50-950] Hz		
a)	σ [S/m]	0.000310	0.020243	0.094941	0.059999
b)	σ [S/m]	0.000479	0.020213	0.095395	0.061166
			[500-9500] Hz		
a)	σ [S/m]	0.000996	0.019956	0.109919	0.065364
b)	σ [S/m]	0.002113	0.016495	0.096448	0.060703

4.2.3 Influence of number of harmonics

Since the trapezoidal ECI gradient is approximated by a finite superposition of sine waves, see equation (4.4), we find it important to investigate the sensitivity of the conductivity estimation towards the number of harmonics. Therefore, the first 20 odd harmonics are employed in the forward solver to accurately calculate the 'measured' phase difference. The inverse problem is subsequently solved for the first 1, 3, 5, 7, 10, 15 or 20 odd harmonics, as illustrated in the flowchart of Fig. 4.12. We assume here that no noise in present in the measurements (see further in Section 4.2.5). An ECI gradient with a period T of 20 ms is switched for these simulations. The higher the number of harmonics, the better the real applied trapezoidal ECI gradient is simulated, as can be seen in Fig. 4.3, and thus the more accurate the results will be.

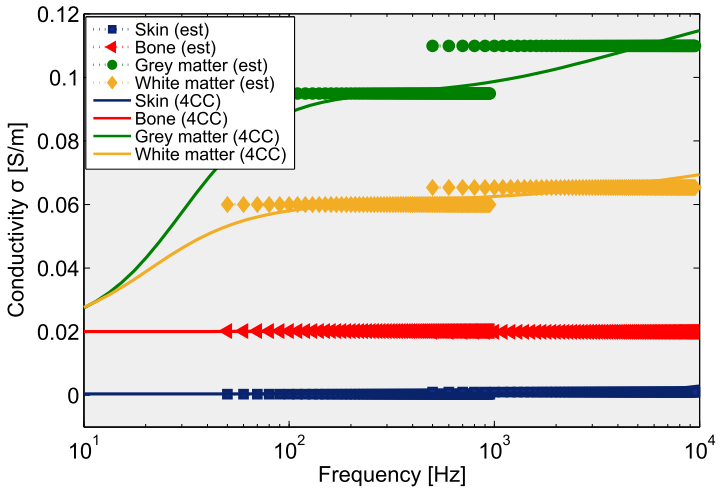

Figure 4.11: Reconstructed (est) profiles using constant material properties in the forward solver in comparison with the 4-Cole-Cole model (4CC).

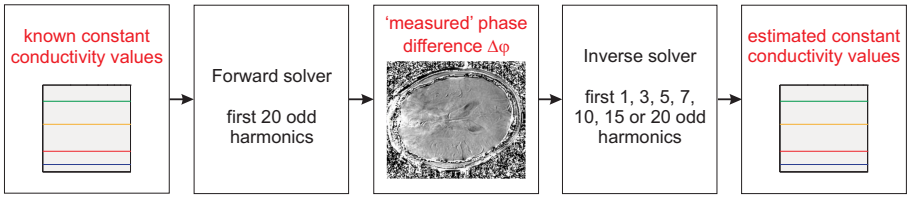

Figure 4.12: Flowcharts used to investigate the influence of the number of harmonics.

The logarithmic graph in Fig. 4.13 illustrates how the errors between the estimated and desired conductivity values decrease with increasing number of harmonics. When only the fundamental frequency of 50 Hz is considered, the resulting conductivities [0.59, 2.99, 3.00, 3.00] S/m are a wrong reconstruction. In general, the values are overestimated, but it is remarkable how, for each simulation, the more conductive tissues are properly related to the less conductive tissues. For an increasing number of harmonics, the resulting conductivity values decrease and improve till the best estimate of [0.000661, 0.019801, 0.095109, 0.060031] S/m is obtained for the first 20 odd harmonics.

4.2.4 Influence of material model

The electrical human head properties are frequency-dependent and the forward model needs to approximate the reality as close as possible. Therefore, we will include here in the 4-Cole-Cole model all parameters of Table 2.1 in the

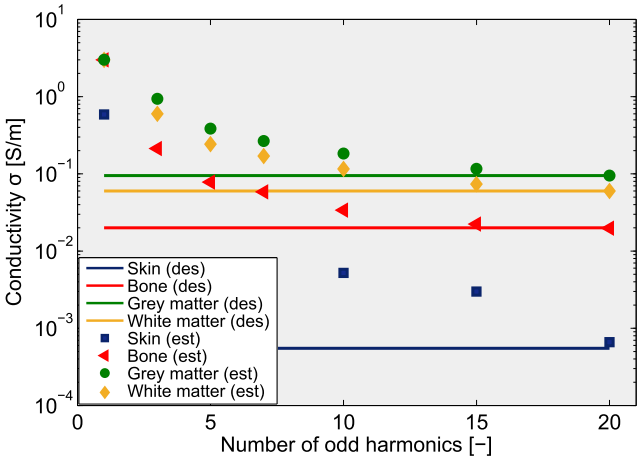

Figure 4.13: Convergence of the estimated conductivity values towards the desired values with increasing number of odd harmonics. The conductivity values are plotted on a logarithmic scale.

forward solver instead of the desired constant values of Table 4.1, as schematically shown in Fig. 4.14. In this way we study the influence of the material model.
Line b) of Table 4.2 lists the recovered values for the lower ([50-950] Hz) and higher ([500-9500] Hz) frequency domains. These values deviate [13%, −1.1%, −0.42%, −1.9%] and [−111%, 17%, 12%, 6.6%] respectively from the 4-Cole-Cole values. Whereas the first indicates an accurate conductivity estimation and the second is in itself also acceptable, the relation between both frequency domains is inadequate, as can be seen in Fig. 4.15. This is due to the fact that the input parameters are variable curves and the estimated output parameters are limited to constant values.

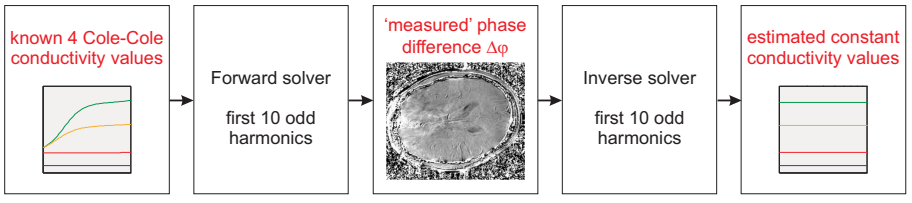

Figure 4.14: Flowchart used to investigate the influence of the material model.

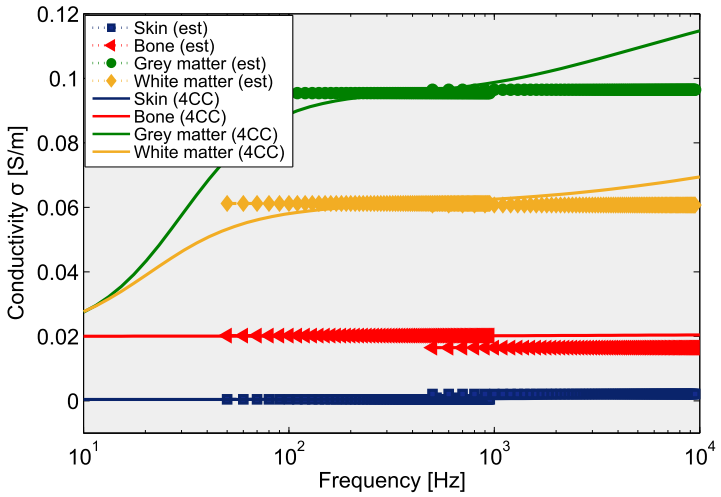

Figure 4.15: Reconstructed (est) conductivity profile using the 4-Cole-Cole material model in the forward solver in comparison with the 4-Cole-Cole model (4CC).

4.2.5 Influence of noise

The presence of noise in the signals of MRI is a key issue. The signal-to-noise ratio (SNR) is equal to the ratio of the average intensity of the signal to that of the noise, and is often used as a criteria for the image quality. Therefore, we evaluate the impact of SNR on the accuracy of the reconstructed parameters. The noise in MRI can be classified into three types; repetitive structured noise, non-repetitive structured noise and statistical noise (De Deene et al., 1998). Examples of repetitive structured noise are chemical shift artefacts, Gibbs ringing artefacts and field inhomogeneity artefacts. Motion artefacts are the main cause of non-repetitive structured noise (De Deene et al., 1998). Since we perform a point-wise subtraction of the phase images with and without ECI gradient, the repetitive noise is cancelled out. Moreover, different compensation methods for structured noise in general have been developed. The intrinsic part of statistical noise is called thermal noise and originates from the Brownian motion of electrons in both the subject and the scanner. This motion is random and therefore, thermal noise is characterised by a Gaussian amplitude distribution. Because it is very difficult to reduce statistical noise, we will numerically investigate the performance of the proposed technique in the presence of Gaussian noise.

We added subsequently 10%, 20%, 40% and 60% Gaussian noise to the phase difference for an ECI gradient with a period T of 20 ms. This 'measured' phase difference corresponds with a SNR of 10.05, 5.10, 2.70 and 1.95 respectively.

The noise **n** in every measuring point $i = 1,...,\mathrm{I}$ (here, I=24000) is defined as:

$$\mathrm{n}_i = N\sqrt{\frac{\sum_{i=1}^{\mathrm{I}} \mathrm{s}_i^2}{\mathrm{I}}} \cdot \mathrm{rand}(0,1) \tag{4.10}$$

with N the percentage of noise, **s** the signal without noise, i.e. the phase difference, and $\mathrm{rand}(0,1)$ a normally distributed random number with mean zero and standard deviation one. The corresponding signal-to-noise ratio is calculated as the ratio of the summed squared magnitude of the signal with noise **sn** to that of the noise **n**, and thus:

$$\mathrm{SNR} = \sqrt{\frac{\sum_{i=1}^{\mathrm{I}} \mathrm{sn}_i^2}{\sum_{i=1}^{\mathrm{I}} \mathrm{n}_i^2}}. \tag{4.11}$$

For each noise level, we obtained 100 artificial phase differences and estimated the conductivity values. The mean and standard deviation of these conductivity values are plotted as error bars in Fig. 4.16. The standard deviations increase to [1.8, 2.6, 1.4, 0.9] $\cdot 10^{-3}$ S/m for 60% Gaussian noise and their mean values differ up to [211%, −7.3%, 0.26%, 0.37%] from the 4-Cole-Cole values, listed in Table 4.1, respectively for the tissues skin, bone, grey and white matter. The discrepancy is largest in terms of percentage for skin due to its low conductivity value.

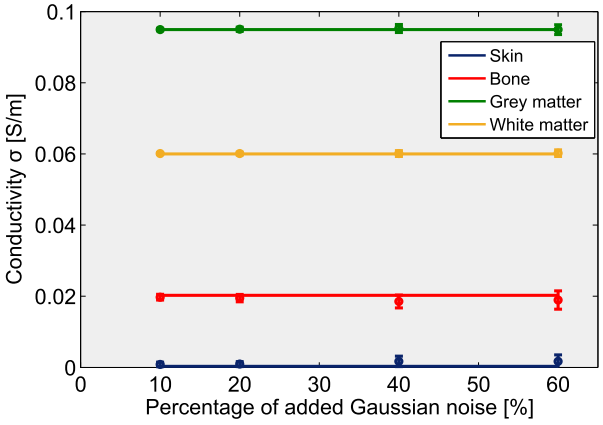

Figure 4.16: Error bars of the estimated conductivity values, calculated from artificial phase differences with added Gaussian noise. The mean values and standard deviations are plotted using markers and the solutions without noise are represented as solid lines.

4.3. Discussion, assumptions and future work

A novel version of the ICMREIT technique using phase images and multiple gradients is proposed for conductivity reconstruction of the human head in the low frequency domain. Numerical simulations have been performed on spherical head models, in which the number of tissues are gradually increased. We succeed in reconstructing the conductivity profiles of the tissues grey matter, skin, bone and white matter, confirming the potential and feasibility of the technique. Notice that we estimated the absolute conductivity values. For anisotropic tissues the conductivity tensors can be computed from these obtained isotropic values in combination with eigenvectors of the diffusion tensors, as will be explained in Section 5.1.1.
It seems that, in contrast to the conventional EIT method, the quality of estimation does not depend on the position of the tissue in the head. However, it does depend on the frequency, since the real part of the relative permittivity value is kept fixed at 1.0 and for lower (< 10 Hz) or higher ($> 10^4$ Hz) frequencies the actual value according to the 4-Cole-Cole model differs more for some tissues. We would like to emphasise that all performed simulations were able to make a correct distinction between the four tissues, i.e. the order of conductivity was maintained. Less conductive tissues were indeed reconstructed with lower conductivity values than the higher conductive tissues.

Two GE sequences are executed to demonstrate the principle, but for further research more sequences with different ECI gradient parameters are recommended to improve the frequency dependence of the conductivity profiles. Additional simulations on head models with realistic geometry and more tissues (e.g. CSF) are necessary. We predict that the inclusion of this high-conductive fluid will have a significant effect, since it also has a great influence on the EEG source localisation (Wolters, 2003). An error analysis should be done in case of incorrect segmentation of the head models. Additionally, the presented method should be tested on other conductivity models than the 4-Cole-Cole model.
Notice that the eddy-current effect is averaged over a certain time interval after the gradient switching, as can be seen in equation (4.3). To overcome this, the echo time is kept limited. Moreover, increasing the echo time in a GE sequence would lead to an exponential decrease in the signal-to-noise ratio.
The influence of the number of harmonics associated to the gradient and the material model is investigated. The latter underlines the need of experimental validation with measured MRI data, since the applied artificial phase difference is only an approximation of a real measurement. For example, a saline phantom with known conductivity values, determined by the salt concentration, would complete the proof of concept.
We evaluated the performance of the proposed technique in the presence of

Gaussian noise. Our results show that the numerically estimated values are robust to noise present in the phase difference signal. However, the feasibility and efficacy of the presented method will also depend on errors in acquisition such as phase wrapping errors and motion artefacts.
Overall, the induced current MR phase imaging EIT with multi GE sequences is promising. It can be used for increasing the accuracy of the computed macroscopic eddy-current distributions in TMS by importing recovered frequency-dependent conductivity values in the head models. Further research on the validity of the method in case of real clinical measurements is mandatory, taking into account practical constraints.

In science the credit goes to the man who convinces the world, not to the man to whom the idea first occurs.

Sir Francis Darwin

5

Macroscopic electric field distribution

Despite 30 years of research and the widespread use of TMS, most details of the underlying mechanisms remain unclear (Hoogendam et al., 2010; Sack and Linden, 2003). To gain a better understanding of the response to TMS, it is useful to model the electromagnetic effects of an excitation pulse on the human head through the use of accurate computer simulations. We detail in this chapter the macroscopic induced electric field distribution in the brain when TMS is applied.

Up to now, head models with simplified geometries such as half-planes or spherical shells (Davey et al., 2003; Deng et al., 2013; Miranda et al., 2003; Ravazzani et al., 1996) and realistic head models with isotropic material properties (Nadeem et al., 2003; Wagner et al., 2006) were used. Although spherical head models are instructive, they are a rough approximation of reality and the incorporation of realistic anatomical details is necessary. Moreover, as mentioned in Section 3.3 biological tissues, such as white matter (Wolters et al., 2006), have directionally dependent characteristics. Including these features is important, since De Lucia et al. (2007); Janssen et al. (2013) and Miranda et al. (2007, 2003) showed that even small geometrical alterations in the cortex as well as anisotropy and tissue heterogeneity can significantly alter the field distribution. However, the aforementioned anisotropic conductivity ratios, see Section 3.3.2, are an approximation of reality and are still not exactly known (Sadleir and Argibay, 2007). Therefore, more complex head

models are applied in the rest of this PhD with realistic geometry based on structural MRI and realistic anisotropic material parameters identified using DTI (Basser et al., 1994a,b; Tournier et al., 2011). DTI exploits the directional-dependent diffusion of water molecules in the brain, with the principal diffusion direction corresponding to the predominant orientation of fibre bundles (Jones and Leemans, 2011). This way, the measured diffusion tensors can be converted to conductivity and permittivity tensors. Combining T1-weighted with diffusion-weighted MRI of the same subject, leads to a detailed and precise head model reconstruction of reality.
Many articles (De Lucia et al., 2007; Haueisen et al., 1995; Salinas et al., 2009) use constant conductivity values for the scalp, skull, CSF, grey and white matter, that are compiled from the literature (Foster and Schwan, 1989; Geddes and Baker, 1967), though the electrical properties of biological tissues vary naturally with frequency. As before, we will obtain these values from the 4-Cole-Cole model (2.31) (Cole and Cole, 1941; Gabriel et al., 1996c). Also the displacement currents, due to non-zero permittivity values as can be seen from equation (2.9), are not neglected in this work. Calculations in isotropic head models (Wagner et al., 2004) have shown that it is necessary to take these currents into account for tissue permittivity values of the order 10^7 times the permittivity in vacuum.
In this chapter, TMS simulation are performed on patient-specific head models using the anisotropic independent impedance method. We compare the induced currents and electric fields in isotropic and DTI-based anisotropic head models, with or without neglecting the displacement currents for two different excitation waveforms, namely a sinusoidal and a damped sinusoidal current. A transient solution can be generated by successively plotting the frequency spectrum of the waveform, selecting a finite number of frequencies using the Gauss-Legendre quadrature rule (Press et al., 2007), calculating the induced currents for each frequency with the corresponding dispersive tissue properties and finally superposing the sinusoidal solutions. This approach is, to our knowledge, new for the simulation of TMS.
Results from this chapter have been published in (De Geeter et al., 2012).

5.1. Practical implementation

The time-varying magnetic field causes induced current densities $\hat{\mathbf{J}}_{\text{tot}}$ in the human head through Faraday's induction mechanism, which are calculated using the anisotropic IIM, explained in Chapter 3. This method assigns material properties, represented as impedances, to each limb of the voxels (Nadeem et al., 2003; Orcutt and Gandhi, 1988), which leads to a 3D lumped network of impedances. The magnetic induction, due to the excitation current in the coil, is calculated using Biot-Savart's law, resulting in voltage sources in the

IIM. Using Kirchhoff's voltage law, a linear system of current equations can be written for each loop in this network. Based on graph theory, we fitted an appropriate spanning tree, i.e. a connected subset of the graph that contains all nodes but not any loop, to the 3D network. By adding a limb, which is not in the tree, a loop is obtained. All these loops form a maximal set of independent loops, leading to a set of independent equations for the unknown eddy currents (Section 3.2). By using IIM instead of the conventional IM the conditionality is improved leading to an acceleration of the numerical convergence. Notice that we neglected the contribution of the magnetic induction originating from the induced eddy currents, since the order of magnitude of the induced currents density (10^{-2}-10^{2} A/m^2) is much smaller than the excitation current density through the coil (10^{8}-10^{9} A/m^2), as in (Nadeem et al., 2003; Wang et al., 2008). IIM was then formulated towards space-dependent anisotropic material properties (Section 3.3), which led to a more complex lumped network in which each limb is characterised by one impedance and two extra current controlled voltage sources.
When the total induced current densities $\hat{\mathbf{J}}_{\text{tot}}$ are obtained, the total induced electric fields $\hat{\mathbf{E}}_{\text{tot}}$ can be calculated:

$$\begin{bmatrix} \hat{E}_{\text{tot,x}} \\ \hat{E}_{\text{tot,y}} \\ \hat{E}_{\text{tot,z}} \end{bmatrix} = \begin{bmatrix} \sigma_{\text{xx}} + j\omega\varepsilon_{\text{xx}} & \sigma_{\text{xy}} + j\omega\varepsilon_{\text{xy}} & \sigma_{\text{xz}} + j\omega\varepsilon_{\text{xz}} \\ \sigma_{\text{xy}} + j\omega\varepsilon_{\text{xy}} & \sigma_{\text{yy}} + j\omega\varepsilon_{\text{yy}} & \sigma_{\text{yz}} + j\omega\varepsilon_{\text{yz}} \\ \sigma_{\text{xz}} + j\omega\varepsilon_{\text{xz}} & \sigma_{\text{yz}} + j\omega\varepsilon_{\text{yz}} & \sigma_{\text{zz}} + j\omega\varepsilon_{\text{zz}} \end{bmatrix}^{-1} \begin{bmatrix} \hat{J}_{\text{tot,x}} \\ \hat{J}_{\text{tot,y}} \\ \hat{J}_{\text{tot,z}} \end{bmatrix}. \tag{5.1}$$

We emphasise that there is a difference between the induced electric field $\hat{\mathbf{E}}$, used in the previous chapters 2-3 as the electric field induced in air, and the newly defined term $\hat{\mathbf{E}}_{\text{tot}}$, which represents the total induced electric field in the material, namely biological tissue, below the coil. This difference is demonstrated on a simple TMS example at the end of this chapter in Section 5.3.
In Section 5.2, the influence of changes in the modelled head is analysed. To compare the obtained results, the correlation coefficient between two sets of n data points, p_n and q_n, can be calculated as

$$\text{cc} = \frac{\sum_n (p_n - \bar{p})(q_n - \bar{q})}{\sqrt{\sum_n (p_n - \bar{p})^2 \cdot \sum_n (q_n - \bar{q})^2}} \tag{5.2}$$

with $\bar{p}$ and $\bar{q}$ the respective means. The more this coefficient approaches one, the more the resulting distributions of both head models match.

5.1.1 Tissue anisotropy based on DTI

The anisotropic material properties are derived from DTI data. DTI describes diffusive transport of water within tissues by an effective diffusion tensor $\mathcal{D}$. Since the transport of water molecules in diffusion and ions in conductivity

are mainly constrained by the same extracellular space, this tensor can characterise the anisotropy of the brain structure (Basser et al., 1994b). By construction, $\mathcal{D}$ is symmetric and positive definite. Therefore, it can be represented by an ellipsoid and can be written as follows:

$$\mathcal{D} = \begin{bmatrix} D_{xx} & D_{xy} & D_{xz} \\ D_{xy} & D_{yy} & D_{yz} \\ D_{xz} & D_{yz} & D_{zz} \end{bmatrix} = \mathcal{V} \cdot \begin{bmatrix} D_1 & 0 & 0 \\ 0 & D_2 & 0 \\ 0 & 0 & D_3 \end{bmatrix} \cdot \mathcal{V}^{-1} \tag{5.3}$$

where $\mathcal{V}$ is the orthogonal rotation matrix whose columns are the unit length eigenvectors $\mathbf{V}_i$ of the measured diffusion tensor and D_i the associated eigenvalues, with $i = 1,2,3$. The Jacobi method is applied in this PhD for the calculation of the eigenvalues and eigenvectors, since the diffusion tensors are real symmetric matrices (Press et al., 2007).

The conductivity tensor Σ is also symmetric and positive definite. Its eigenvalues are calculated by obeying the volume constraint (Wolters, 2003). If we denote the eigenvalues of Σ as σ_i and the isotropic conductivity value, obtained with the 4-Cole-Cole model (Cole and Cole, 1941; Gabriel et al., 1996c), as σ_{iso}, we can write

$$\frac{4}{3}\pi(\sigma_{\text{iso}})^3 = \frac{4}{3}\pi(\sigma_1\sigma_2\sigma_3). \tag{5.4}$$

These eigenvalues are also related to those of the diffusion tensor through a constant ratio (Tuch et al., 2001).

$$\frac{D_1}{\sigma_1} = \frac{D_2}{\sigma_2} = \frac{D_3}{\sigma_3} \tag{5.5}$$

Because the diffusion and conductivity tensors also share the same eigenvectors $\mathbf{V}_i$ (Tuch et al., 2001), Σ can be computed as follows:

$$\Sigma = \begin{bmatrix} \sigma_{xx} & \sigma_{xy} & \sigma_{xz} \\ \sigma_{xy} & \sigma_{yy} & \sigma_{yz} \\ \sigma_{xz} & \sigma_{yz} & \sigma_{zz} \end{bmatrix} = \mathcal{V} \cdot \begin{bmatrix} \sigma_1 & 0 & 0 \\ 0 & \sigma_2 & 0 \\ 0 & 0 & \sigma_3 \end{bmatrix} \cdot \mathcal{V}^{-1}. \tag{5.6}$$

Similar calculations can be carried out for constructing the permittivity tensor.

The fractional anisotropy (FA) (Basser and Pierpaoli, 1996) is a value between zero and one that describes the degree of tissue anisotropy, with zero indicating a completely isotropic tissue

$$FA = \sqrt{\frac{3}{2}\frac{\sum_{i=1}^{3}(D_i - \bar{D})^2}{\sum_{i=1}^{3} D_i^2}} \tag{5.7}$$

with $\bar{D}$ the mean diffusivity equal to $\frac{D_1+D_2+D_3}{3}$.

5.1.2 Damped sinusoidal excitation

Initially, we supply to the TMS coil a sinusoidal current

$$I_{\sin}(t) = A_{\mathrm{c}} \sin(\omega_{\mathrm{c}} t). \tag{5.8}$$

However, as explained in Section 1.2.2, the biphasic pulse that is produced by most commercially available TMS stimulators (such as Magstim Rapid^2) can be treated as a damped sinusoidal current, see equations (1.3-1.4) which are repeated here.

$$I_{\mathrm{dsin}}(t) = A_{\mathrm{c}}\, e^{-\alpha_{\mathrm{c}} t} \sin(\omega_{\mathrm{c}} t) \tag{5.9}$$

with

$$A_{\mathrm{c}} = \frac{V_{\mathrm{DC}}}{\omega_{\mathrm{c}} L},\ \alpha_{\mathrm{c}} = \frac{R}{2L},\ \omega_{\mathrm{c}} = \sqrt{\frac{1}{LC} - \alpha_{\mathrm{c}}^2}. \tag{5.10}$$

R, C and L are the total values of respectively the resistance, capacitance and inductance in the circuit and V_{DC} the initial voltage. The parameter ranges of typical TMS equipment are listed in Table 1.1.

Since the numerical method is formulated in the frequency domain, the Fourier transform of the applied currents is employed. The Fourier transform of the sine function (5.8) is a positive and negative complex delta function of amplitude $A_{\mathrm{c}}\pi$ at respectively the appropriate negative angular frequency $-\omega_{\mathrm{c}}$ and the positive angular frequency ω_{c}, whereas the Fourier transform of the damped sinusoidal function (5.9), with $\alpha_{\mathrm{c}} > 0$ and $t > 0$, is

$$I_{\mathrm{dsin}}(\omega) = \frac{A_{\mathrm{c}}\omega_{\mathrm{c}}}{-\omega^2 + 2j\alpha_{\mathrm{c}}\omega + \omega_{\mathrm{c}}^2 + \alpha_{\mathrm{c}}^2}. \tag{5.11}$$

To transform the resulting induced currents, indicated as $G(\omega)$, to its time domain representation $g(t)$, the inverse Fourier transform is applied:

$$g(t) = \frac{1}{2\pi} \int_{-\infty}^{+\infty} G(\omega) e^{j\omega t} \cdot \mathrm{d}\omega. \tag{5.12}$$

The sinusoidal excitation current corresponds with a single frequency, whereas the damped sinusoidal current has a continuous spectrum. Because it is impossible to compute the simulations for each frequency, we make use of the Gauss-Legendre quadrature rule (Press et al., 2007)

$$\int_a^b h(x) \cdot \mathrm{d}x \approx \frac{b-a}{2} \sum_{n=1}^{N} w_n\, h\left(\frac{b-a}{2} x_n + \frac{b+a}{2}\right). \tag{5.13}$$

This quadrature rule seeks to obtain the best numerical estimate of an integral by picking optimal points x_n and weights w_n, tabulated in (Stroud and Secrest,

1966). Equation (5.12) can then be written as follows:

$$g(t) \approx \frac{1}{2\pi} \frac{b-a}{2} \sum_{n=1}^{N} w_n \, G\left(\frac{b-a}{2} \omega_n + \frac{b+a}{2} \right) e^{j\left(\frac{b-a}{2}\omega_n + \frac{b+a}{2}\right)t}. \tag{5.14}$$

5.2. Simulations on a realistic head model

The geometry of the head model is constructed from structural MRI. A T1-weighted image was acquired from a healthy 25-year-old female volunteer on a 3 Tesla MR scanner (Philips Achieva 3.0T) at the University Medical Center Utrecht, the Netherlands, with a turbo field-echo sequence. The subject gave informed consent to participate in this study under a protocol approved by the University Medical Center Utrecht ethics board. The voxelsize equals $0.9 \times 0.9 \times 0.9$ mm^3 and the field-of-view (AP, RL, IS) is $230 \times 183 \times 140$ mm^3, which results in a $256 \times 204 \times 156$ matrix. The ratio between the repetition time TR, which is the time between 2 excitation pulses, and the echo time TE, which is the time between the 90° RF pulse and the MR signal sampling, TR/TE was 25 ms/4.5 ms. The flip angle was 30° and acquisition time 3.5 min. The segmentation into scalp, skull and the cerebral tissues CSF, grey and white matter is done using SPM8 (Friston et al., 2007). This yields an image of $84 \times 106 \times 83$ cubic elements of resolution $2.0 \times 2.0 \times 2.0$ mm^3.

In addition to the T1-weighted image, a DTI data set was acquired of the same subject, using an eight-channel head coil and a single-shot spin-echo echo planar imaging (EPI) sequence with the following parameters (Jones and Leemans, 2011): 60 diffusion-weighted images (b = 1200 s/mm^2) with the gradient directions uniformly distributed over the half sphere (Jones et al., 1999); 1 non-diffusion-weighted (b = 0 s/mm^2) image (6 excitations); 70 contiguous slices (no gap), slice thickness = 2 mm; acquisition matrix of 112×112, reconstructed to 128×128 matrix size with a field-of-view of 224×224 mm^2 (acquired voxelsize = $2.0 \times 2.0 \times 2.0$ mm^3, reconstructed voxelsize = $1.75 \times 1.75 \times 2$ mm^3); TR/TE = 10265 ms/107 ms; and acquisition time = 21.6 min.

Data preprocessing, such as diffusion tensor estimation, correction of subject motion and eddy-current induced geometric distortions, and co-registration of the DTI and T1 data to a common reference space were performed as described previously (Leemans and Jones, 2009; Vos et al., 2011). The used head model is visualised from different perspectives in Fig. 5.1.

The stimulation coil used for this Section is a single air-core coil with an inner and outer radius of respectively 3.0 cm and 3.5 cm that is positioned in the axial plane, symmetric to and 1.7 cm above the head models. An excitation current with parameter values V_{DC} = 1.4 kV, R = 50 mΩ, C = 100 μF and L = 10 μH is applied, as in (Wassermann et al., 2008), resulting in an amplitude A_{c}

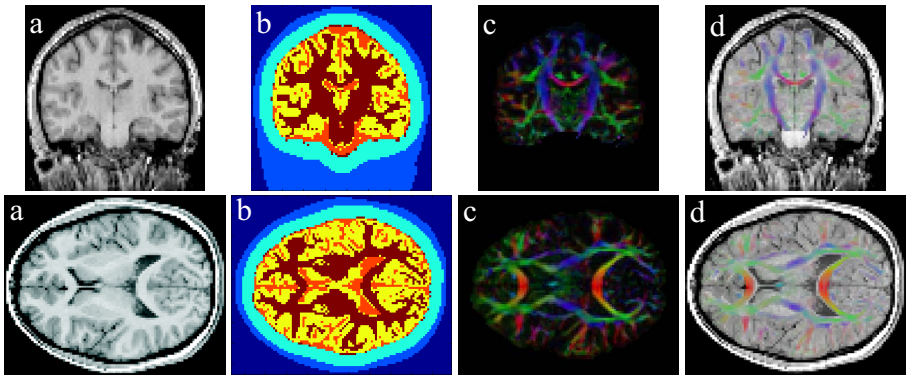

Figure 5.1: (Above) Coronal and (below) axial views of the (a) T1-weighted image; (b) segmentation into scalp (blue), skull (turquoise blue), CSF (orange), grey matter (yellow) and white matter (dark red) and surrounded by air (dark blue); (c) DTI colour map, indicating the dominant direction of the diffusion tensor: red (right-left), green (posterior-anterior) and blue (inferior-superior); (d) fusion of the DTI colour map with the structural MRI.

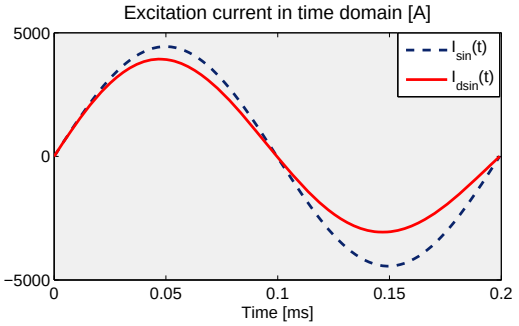

Figure 5.2: Sinusoidal and damped sinusoidal TMS excitation currents.

of 4.441 kA and a working frequency $\omega_c = 2\pi f_c$ with $f_c = 5.017$ kHz, as shown in Fig. 5.2. In this way, the calculations are in line with common stimulators. We take $a = \omega_c/2$, $b = 3\omega_c/2$ and $N = 30$ in equation (5.14) to obtain an acceptable approximation of the simulated damped sinusoidal current with the continuous function of (5.9) in an acceptable computational time. The linear system of equations is solved using the iterative preconditioned biconjugate gradient stabilised method (Press et al., 2007; Van der Vorst, 1992).
We will now investigate the influence of tissue anisotropy, displacement currents and the frequency dependence of the tissue parameters on the calculated induced currents and electric fields. The aim is to provide insights on the impact of possible assumptions and to provide an as realistic as possible TMS model. Sections 5.2.1 and 5.2.2 (Section 5.2.3) discuss the results in the frequency domain (time domain).

5.2.1 Influence of tissue anisotropy

We compare the calculated currents and fields in the isotropic head model where the material properties are obtained from the 4-Cole-Cole model with those in the DTI head model where the cerebral tissues CSF, grey and white matter are anisotropic. Figs. 5.3 and 5.4 show the same 2D cross sections as in Fig. 5.1 with the induced current density distributions and the difference between both models, respectively the induced electric field distributions.

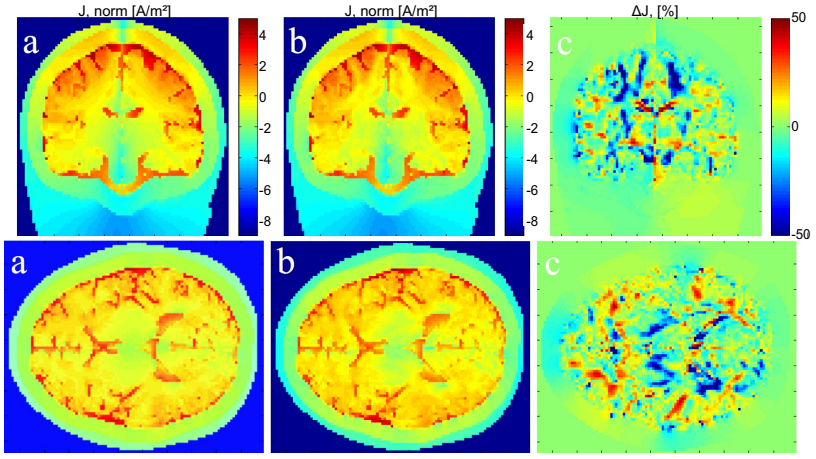

Figure 5.3: Induced current density amplitude $[A/m^2]$ in the (a) isotropic and (b) DTI head model on a natural logarithmic scale. (c) Difference between the induced current densities in the two models in terms of percentage (DTI minus isotropic, divided by DTI). The colour limits are set to specified minimum and maximum values for clarity reasons.

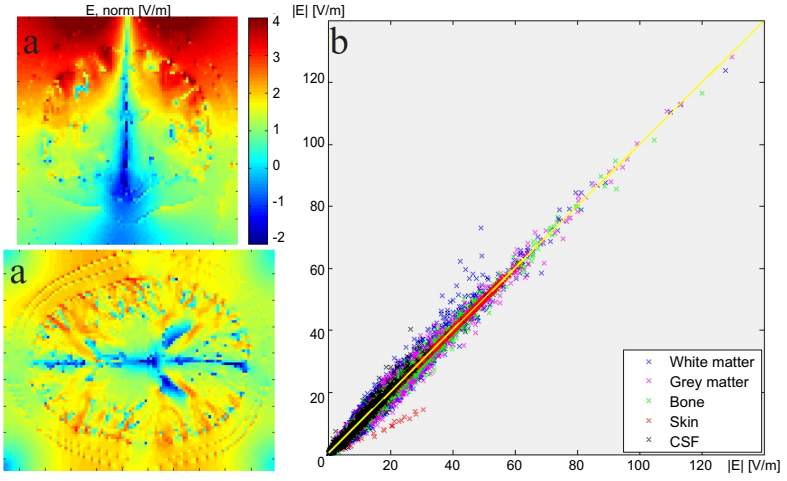

Figure 5.4: (a) Induced electric field amplitude [V/m] in the DTI head model on a natural logarithmic scale. (b) Induced electric field amplitudes of all voxels in the isotropic (x-axis) and DTI (y-axis) cases.

We can observe from Fig. 5.3 that for some voxels higher current densities are obtained in the isotropic model, with a maximum of 202.64 A/m^2, and for other voxels in the DTI model, with a maximum of 199.12 A/m^2. Both maxima are located at the same position, 5.1 cm beneath the centre of the coil and coinciding with CSF. In general as well, the main current densities are induced in this fluid, with a mean value of 12.5 A/m^2, due to its high conductivity value. The outer tissues scalp and skull, on the other hand, produce the lowest induced current densities, with mean values less than 0.5 A/m^2. The difference between both simulations rises to 63.72 A/m^2, which is about 92% of the value in the DTI model and 32% of the maximum value, and is observed in CSF, 12.3 cm beneath the coil and 8.4 cm from the maximum induced current density.
Table 5.1 lists the mean values, standard deviations, maxima of the induced currents in both head models, the correlation coefficient, see equation (5.2), between those induced currents and the mean fractional anisotropy (FA), see equation (5.7), in the DTI model for the five tissues. No big differences are observed related to the mean values and standard deviations between both models. As might be expected from the settings, the cerebral tissues, which are assumed anisotropic in the DTI model and have FA values different from zero, cause the lowest cc and consequently the highest differences. This effect is most profoundly visible in white matter, which is composed of nerve bundles surrounded by insulating myelin sheaths, resulting in a high FA of 0.7192. It is the myelin that enables neurons to quickly conduct impulses between the brain and different parts of the body.

Table 5.1: Statistic data: mean value (mean) [A/m^2], standard deviation (std) [A/m^2], maximum (max) [A/m^2] and correlation coefficient (cc) [-] of the induced current densities in the isotropic (iso) and DTI head models and the mean fractional anisotropy (FA) [-].

Tissue	Skin	Bone	CSF	Grey	White
mean iso	0.0499	0.3174	12.5197	1.2812	0.9178
mean DTI	0.0499	0.3176	12.3888	1.2927	0.9499
std iso	0.0740	0.3213	15.4088	1.2748	0.7826
std DTI	0.0740	0.3217	15.4635	1.2498	0.7858
max iso	0.56	4.89	202.64	28.43	17.03
max DTI	0.56	4.64	199.12	27.39	16.60
cc	0.9998	0.9992	0.9939	0.9920	0.9639
FA	0	0	0.1759	0.2805	0.7192

The electric field in the isotropic head model versus that in the DTI head model, calculated from the corresponding eddy currents, is plotted point by point in Fig. 5.4. Points situated on the yellow line display no difference between both models, whereas those above/below display an increased/decreased induction in the DTI model. When inspecting these electric fields, the maximum values are located in grey matter, 4.6 cm beneath the

centre of the coil, and equal 129.70 V/m and 128.29 V/m in the isotropic and DTI model respectively. The distribution of the electric field in the isotropic model is similar to that in the DTI model and is therefore not plotted. The voxels showing the highest differences up to 23.94 V/m, which is 19% of the maximum value, are situated in white matter, 5.9 cm beneath the coil and 3.9 cm from the maximum electric field. These findings are in agreement with (De Lucia et al., 2007), which reported that anisotropy has effect on the distribution of the induced electric field, yielding differences of the order of 10% of the maximum field, located in white matter.

In this Section, we emphasise the patient-specific character of the calculations due to a precise geometry and an accurate anisotropy distribution based on T1-weighted and diffusion-weighted MRI of the corresponding patient. Only the isotropic electrical properties are no personal values. They are obtained from the 4-Cole-Cole model, of which the parameters are determined to correspond to a close fit between the model and the most comprehensive human and ovine data set available for the particular tissue (Gabriel et al., 1996a,b,c). A possible technique to non-invasively assess these conductivity and permittivity values within the patient is the induced current MR phase imaging EIT that we presented in Chapter 4.

Because the electrical properties are not exactly known for a specific patient (Sadleir and Argibay, 2007), it is important to study how sensitive the calculated stimulation effects are to changes in the conductivity. Simulations were performed a second time, with the cerebral tissues conducting a factor 1.2 better, and the differentiation of the normalised electric field with respect to the normalised conductivity in terms of percentage was investigated

$$\mathrm{SA}_\sigma = 100 \frac{\left(E_{\sigma_2} - E_{\sigma_1}\right)/E_{\sigma_1}}{\left(\sigma_2 - \sigma_1\right)/\sigma_1} \tag{5.15}$$

with $\sigma_2 = 1.2\sigma_1$. This sensitivity is presented in the histogram of Fig. 5.5. The main part of the cerebral voxels shows a limited sensitivity, with a slightly positive mean value of 0.48%. This signifies that a change in conductivity of x leads to a change in the electric field of roughly 0.5% of x. In this specific case, E_{σ_2} is on average equal to $1.001E_{\sigma_1}$. The standard deviation is 11.51% and the 5th and 95th percentiles, describing the low and high ends of the distribution, are respectively -6.84% and 8.04%. This result agrees with Thielscher et al. (2011) who demonstrated that the increased field strengths caused by tissue boundaries is robust to changes in conductivity values.

5.2.2 Influence of displacement currents

Figs. 5.6 and 5.7 illustrate the effect of neglecting the displacement currents in the same 2D cross sections as in Fig. 5.1 by taking the permittivity zero. The

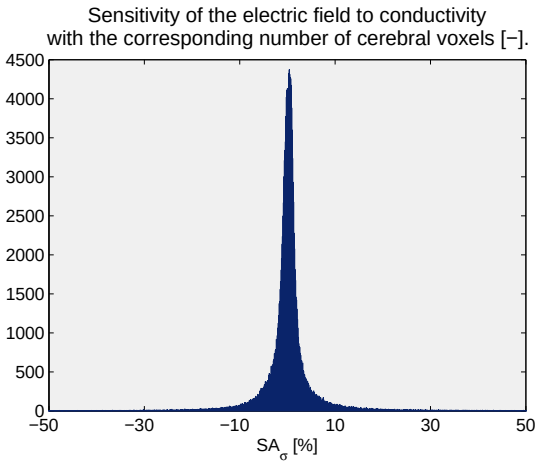

Figure 5.5: Sensitivity analysis when changing the conductivity.

model with ε obtained from the 4-Cole-Cole model is denoted as DTI, and the model with $\varepsilon = 0$ as DTI_0. Both positive and negative differences are observed between the induced current densities in both models. This can also be seen from the mean values, standard deviations and maxima, tabulated in table 5.2. On average the induced currents decreased in skin, whereas they increased in the other tissues. The greatest current changes are decreases up to 143.39 A/m^2, which is about 72% of the value in the DTI model and 72% of the maximum value, and is situated in CSF, 10.4 cm beneath the coil. Moreover, all voxels with a difference (decrease or increase) higher than 10.00 A/m^2 correspond with this highly conductive fluid, whereas its permittivity value is $1.09 \cdot 10^2$ times the permittivity in vacuum ε_0, as can be seen in Fig. 2.2 for the angular frequency ω_c equal to $37.83 \cdot 10^3$ rad/s. When studying the same differences in terms of percentage of the induced current densities in the DTI model, as presented in Fig. 5.6b, the major changes (>20%) are observed in CSF and skin. The simulations with neglected displacement currents resulted in on average 70% lower currents induced in skin, which has a permittivity value of $(2.98 \cdot 10^4)\varepsilon_0$. These results are contrary to the statement of Wagner et al. (2004) that it is only necessary to take the displacement currents into account for tissue permittivity values of the order $10^7\varepsilon_0$ for a source frequency of 5 kHz or more (here, f=5.017 kHz).

The distribution of the electric field induced in the DTI_0 head model is visualised in Fig. 5.7a and the amplitudes in both the DTI and DTI_0 models are plotted point by point in Fig. 5.7b. The highest induction in the DTI_0 model is observed in the same grey and white matter voxels as in the DTI model and amounts about 135 V/m up to a maximum of 180.08 V/m. The difference be-

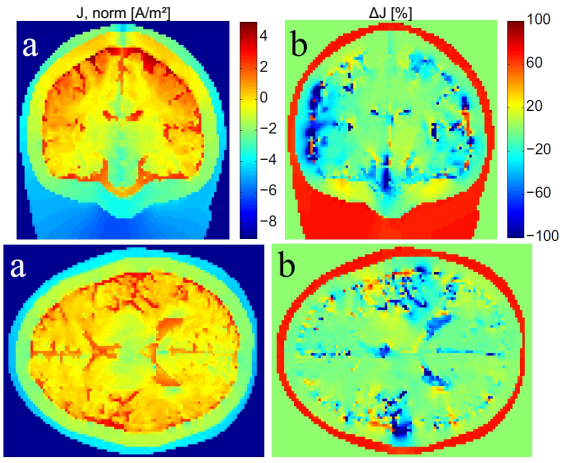

Figure 5.6: (a) Induced current density amplitude [A/m^2] in the DTI head model with neglected displacement currents (DTI_0) on a natural logarithmic scale. (b) Difference between the induced current densities in the two models in terms of percentage (DTI minus DTI_0, divided by DTI). The colour limits are set to specified minimum and maximum values for clarity reasons. Coronal and axial views respectively.

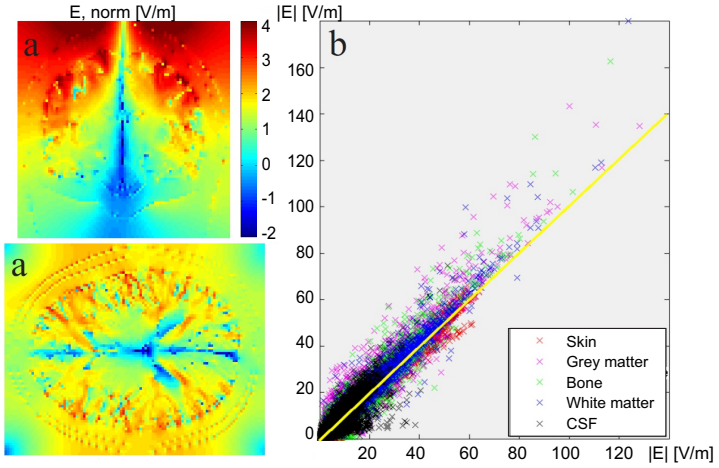

Figure 5.7: (a) Induced electric field amplitude [V/m] in the DTI_0 head model on a natural logarithmic scale. (b) Induced electric fields of all voxels in the DTI head models with ε obtained from the 4-Cole-Cole model (x-axis) and $\varepsilon = 0$ (y-axis).

tween both rises to 56.28 V/m, which is 44% of the maximum value, and is situated in grey matter, 6.4 cm beneath the coil and coinciding with the maximum field. Notice that the points are spread further away from the yellow line in comparison with Fig. 5.4b, displaying higher differences of the DTI_0 model than the isotropic one towards the DTI model. However, last decennia much

Table 5.2: Statistic data: mean value (mean) [A/m^2], standard deviation (std) [A/m^2], maximum (max) [A/m^2] and correlation coefficient (cc) [-] of the induced current densities in the DTI_0 head model.

Tissue	Skin	Bone	CSF	GM	WM
mean DTI_0	0.0155	0.3178	13.3523	1.3431	0.9749
std DTI_0	0.0229	0.3269	16.8883	1.3638	0.8406
max DTI_0	0.18	6.50	288.78	30.03	24.23
cc	0.9980	0.9911	0.9209	0.9657	0.9236

research has been dedicated to evaluate the relevance of tissue anisotropy on TMS, whereas, based on our simulations, the influence of neglecting the displacement currents seems more pronounced.

A sensitivity analysis when changing the permittivity was performed since these values are not well known, as discussed in the previous Section 5.2.1. Fig. 5.8 shows the histogram of the normalised changes in terms of percentage between the original electric field and those obtained with the permittivity values of the cerebral tissues multiplied with a factor 1.2, so to inspect the sensitivity.

$$\mathrm{SA}_\varepsilon = 100 \frac{(E_{\varepsilon_2} - E_{\varepsilon_1}) / E_{\varepsilon_1}}{(\varepsilon_2 - \varepsilon_1) / \varepsilon_1} \tag{5.16}$$

with $\varepsilon_2 = 1.2\varepsilon_1$. Again a moderate sensitivity is observed, with a mean value of 1.65%. This means that an increased permittivity of 20% leads to an increased electric field of 0.33%, namely E_{ε_2} equals on average $0.9967 E_{\varepsilon_1}$. The standard deviation amounts 20.60% and the 5th and 95th percentiles of the distribution are -17.72% and 22.65%, respectively.

5.2.3 Influence of frequency-dependent tissue properties

Up to now in the models, we stimulated the head with a sinusoidal excitation current (5.8). To study the influence of the frequency dependence of the tissue parameters on the calculated induced currents, we simulate the anisotropic DTI head model with permittivity values calculated using the 4-Cole-Cole model for an exponential decaying sinusoidal excitation (5.9), once with constant material parameters (calculated for $\omega = \omega_c$) (denoted as DTI_c) and once with frequency-dependent permittivity and conductivity values (DTI_v). The resulting eddy-current densities and the difference between both models can be viewed in Fig. 5.9 for the same coronal section as in Fig. 5.1. Fig. 5.10 shows the evolution of the induced eddy-current densities in time together with the applied excitation current. The waveform of the induced current densities

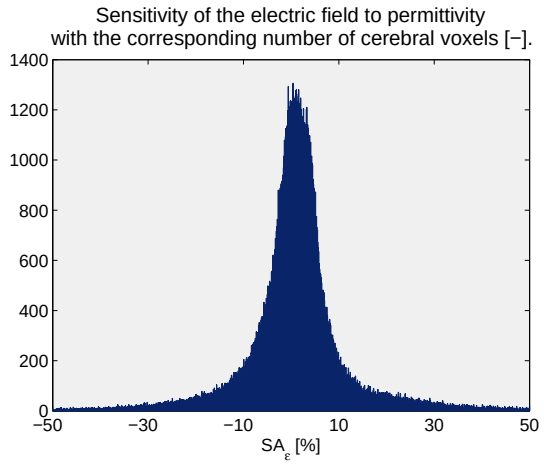

Figure 5.8: Sensitivity analysis introducing a perturbation on the permittivity.

varies as the first derivative of the decaying sine wave, as in (Wassermann et al., 2008).

The maximum induced current densities in this coronal section are 30.11 A/m^2 and 30.40 A/m^2 and are situated in CSF at time 0.096 ms for the DTI_v and DTI_c head models respectively. This voxel showed a higher density of 39.13 A/m^2 for the sinusoidal excitation with the same amplitude of 4.441 kA, due to the fact that the simulated damped sinusoidal excitation signal is an approximation of the function (5.9), by using the Gauss-Legendre quadrature rule, and consequently has a lower rate of change. The difference between the DTI_v and DTI_c models rises to 1.72 A/m^2 in the same voxel of CSF at time 0.236 ms, which is about 36% of the value in the DTI_v model and 6% of the maximum value, given that the current density amounts 4.79 A/m^2 in the DTI model with variable material parameters and 3.07 A/m^2 in the model with constant parameters.

Finally, we perform a sensitivity analysis to determine how sensitive the solution is to changes in the frequency. We stimulate the brain again with a sinusoidal excitation current, of which the frequency is multiplied with a factor 1.2, resulting in $\omega = 37.83 \cdot 10^3$ rad/s. Fig. 5.11 illustrates the differentiation of the normalised electric field with respect to the normalised frequency in terms of percentage

$$\mathrm{SA}_\omega = 100 \frac{(E_{\omega_2} - E_{\omega_1}) / E_{\omega_1}}{(\omega_2 - \omega_1) / \omega_1} \tag{5.17}$$

with $\omega_2 = 1.2\omega_1$. A high sensitivity is observed with a mean value of 100.18% and a standard deviation of 26.10%. This signifies that the electric field in-

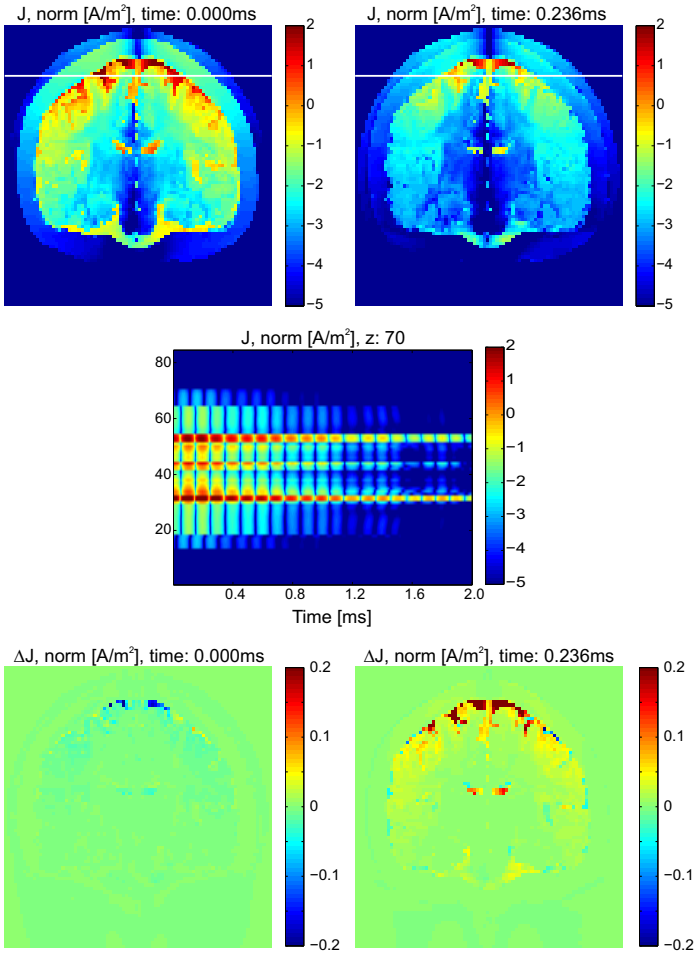

Figure 5.9: (Above) Coronal views of the resulting eddy-current density amplitudes [A/m^2] for the DTI$_v$ model at two different instants on a natural logarithmic scale. (Middle) These values on the marked white line, at z-voxel 70, as a function of time, also on a natural logarithmic scale. (Below) The difference between both models (DTI$_v$ - DTI$_c$) [A/m^2]. The single coil is still positioned in the axial plane, symmetric to and 1.7 cm above the head.

duced in the tissues varies approximately linear with frequency and in this case, E_{ω_2} equalises on average $1.2E_{\omega_2}$. This can be explained from the fact that the analysis starts from equation (3.1), where the magnetic flux density does not depend on the frequency. The 5th and 95th percentiles of the distribution are 84.21% and 115.33%.

The simulations can be improved by extending the interval [a,b] and by increasing the number of frequencies N, used in the Gauss-Legendre quadrature rule (5.13), so that the simulated excitation signal approximates better the function of (5.9). Nevertheless, this will also increase the computational time.

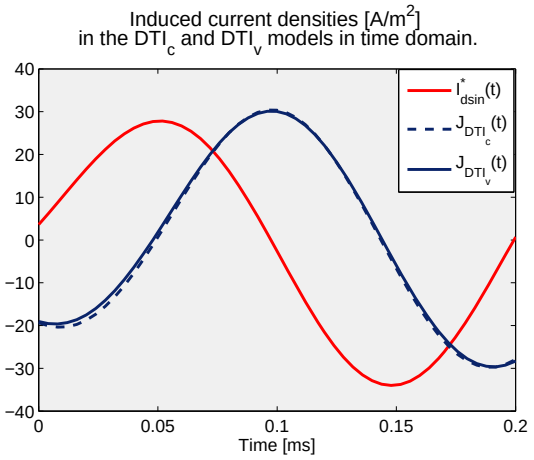

Figure 5.10: Waveforms of the simulated damped sinusoidal current [x100 A] and induced current densities [A/m^2] in one voxel of the DTI head model with constant material parameters (DTI$_c$) and with frequency-dependent material parameters (DTI$_v$). The simulations are performed with $a = \omega_c/2$, $b = 3\omega_c/2$ and $N = 30$ and the approximated excitation current is marked with *.

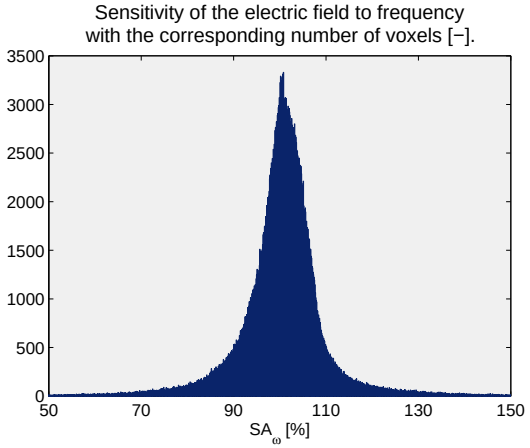

Figure 5.11: Sensitivity analysis when changing the frequency.

5.3. Discussion and assumptions

By applying the anisotropic IIM on head models with realistic geometry and realistic dispersive anisotropic tissue properties that are based on T1- and diffusion-weighted MRI, we were able to perform accurate and patient-specific simulations. The induction of the electric currents and electric fields in the isotropic head model for a sinusoidal excitation has been compared with

that in the DTI model where the cerebral tissues are taken anisotropic. Maximum induced currents of about 64 A/m^2 are observed in the highly conductive CSF for both models together with differences up to 32% of the maximum current. Differences up to 19% of the maximum induced field strength, on the other hand, are situated in white matter, corresponding with a high FA due to the insulating myelin. Neglecting the displacement currents, by taking the permittivity values not into account, is frequently done in the simulation of TMS. However, this assumption corresponds with a decrease of about 72% and 44% of the maximum induced current and field respectively which, to our opinion, cannot be disregarded. By stimulating the DTI head model with a damped sinusoidal current, we could study the influence of the frequency dependence of the tissues, leading to a difference of 6% of the maximum induced current densities. The induced electric field shows limited sensitivity to changes in conductivity and permittivity values, whereas it varies approximately linear with frequency. Model refinements and coupling to the neurophysiology will help to increase the knowledge and understanding of the electromagnetic response to TMS.

The head model constructed in this Section does not incorporate the skull anisotropy. In a first attempt to overcome this, one can assume an anisotropy ratio of 1:10 radially to tangentially to the skull surface (Rush and Driscoll, 1968; Wolters et al., 2006). Our model's level of detail can be further refined by taking more tissues and their specific electrical properties into account, as in (Nadeem et al., 2003). Moreover, as described before, these properties can be rendered patient-specific by using ICMREIT.

The induced electric field is assumed to be zero before and after the stimulation pulse. In reality, the switch in the stimulator circuit, see Section 1.2.1, enables the capacitor to discharge the high excitation current (2-10 kA) through the TMS coil in a short period of time (60-1000 μs). This very fast switching approves our approach, but including the transient effects in the future research would be interesting.

We would like to stress that the above described method for calculating the electric fields induced by TMS decouples a coupled equation. First, the magnetic flux density $\hat{\mathbf{B}}(\mathbf{r})$ is computed due to the excitation current density $\hat{\mathbf{J}}_{\text{coil}}$ through the coil, according to Biot-Savart's law (2.32), and leads to the electromotive force $\hat{\mathbf{V}}_{\text{TMS}}$. With Faraday's and Ampère's law (3.1-3.4) this results in the total induced currents $\hat{\mathbf{I}}_{\text{tot}}$. And based on this current, or current density $\hat{\mathbf{J}}_{\text{tot}}$, the total induced electric field $\hat{\mathbf{E}}_{\text{tot}}$ is calculated (5.1). Whereas, to be completely correct, the total magnetic field should be calculated due to both the excitation $\hat{\mathbf{J}}_{\text{coil}}$ and the induced current densities $\hat{\mathbf{J}}_{\text{tot}}$. Moreover, as mentioned before, the electric fields induced in the biological tissue $\hat{\mathbf{E}}_{\text{tot}}$ are different from $\hat{\mathbf{E}}$. We have checked this on a simple TMS example and compared the electric field induced in tissue to those induced in air, see Figs. 5.12 and 5.13.

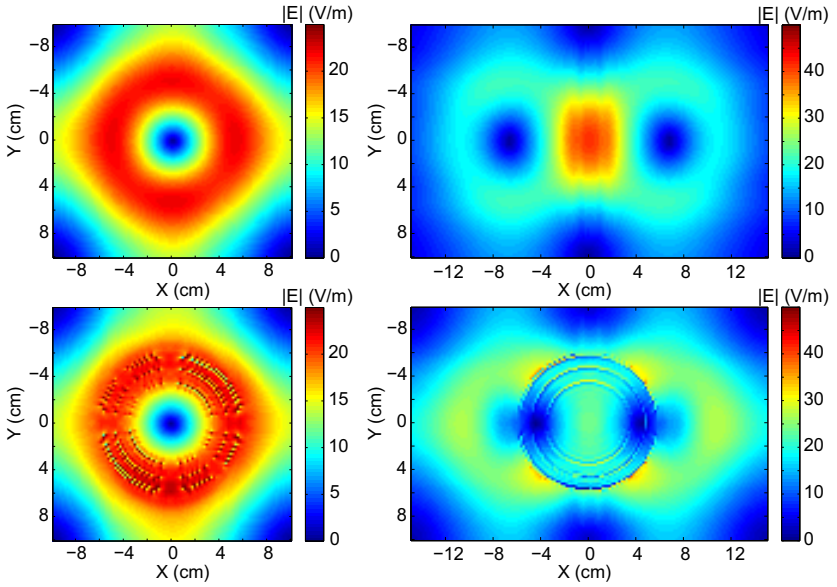

Figure 5.12: Tissue below the coil changes the induced electric field distribution. Similar coils are applied as in Fig. 1.6. The circular coil has a radius of 5 cm and 9 turns and the figure-of-8 coil consists of two such circular coils. A biphasic pulse of 640 A per loop with a pulse length of 230 μs is applied. The strength of the total electric field E_{tot} induced in a plane 3 cm below the coil is plotted (in V/m). (Above) There is only air below the coil and consequently E_{tot} equals E. (Below) A spherical head model, consisting of the tissues brain, skull and scalp, with radii 8.0 cm, 8.6 cm and 9.2 cm respectively, is considered as in Section 3.2.2. The coils are centrally positioned 1 cm above the scalp surface, causing the plotted planes intersecting this head model.

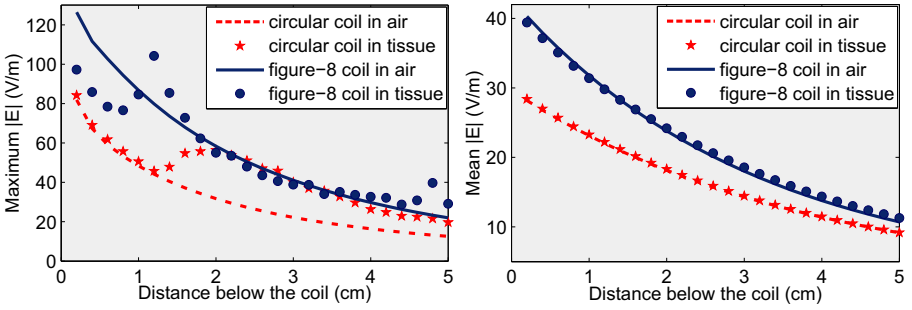

Figure 5.13: Similar to Fig. 1.7, (left) the maximum induced electric fields and (right) the average value over the 20×20 cm^2 area of both the circular and figure-of-8 coil are plotted as a function of the distance below the coil. This time, a distinction is made between the fields induced in air and those induced in the spherical head model.

The dielectric properties of biological tissue indeed deform the electric field distribution, not only in the voxels being tissue but also in the surrounding air

voxels. This effect is more pronounced for the figure-of-eight coil, due to the symmetry of the circular coil towards the spherical head model, and will be even higher for head models with realistic geometry.
The applied methodology, where DTI-based anisotropy, permittivity and the frequencies of the excitation are combined on a head model with an MRI-based geometry, can be used as the software in computer-assisted TMS. The advantage of such coupling of simulation software with coil hardware is that the brain stimulation can be planned, performed and monitored in a computer-controlled way. The information from the brain imaging techniques enables patient-specific simulations, in which the effects of gender, age, neurological condition, etc., are incorporated. Moreover, the location of the coil with the resulting electromagnetic effects can be displayed on the computer screen together with the anatomical MRI, providing a tool for online stimulus targeting. This will lead to a more optimal use of TMS in clinical practice.
Nevertheless, with these plans for the future in mind, we feel compelled to mention that recent papers (Forster et al., 2011; Picht et al., 2011) have compared peritumoural mapping of the motor cortex using presurgical navigated TMS, functional MRI (fMRI) and the gold standard of intraoperative direct cortical stimulation (DCS). They have reported a good match, even though these TMS studies were performed using spherical head models. For these cases, i.e. in the superficial cortex, it appeared that detailed complex models do not have a profound effect on the location of the maximum electric field in the superficial cortex.
The variability of the TMS effects, reported in many clinical and psychological studies (Casarotto et al., 2010; Hernandez-Pavon et al., 2014; Lioumis et al., 2009; Loo and Mitchell, 2005; Maeda et al., 2000), can however not be explained using such simplified models. Therefore, we believe electromagnetic modelling should be performed on realistic and personalised volume conduction head models. Moreover, they should be extended with a neurophysiological basis, which brings us to the next part of this PhD.

PART II

Modelling the TMS neurophysiology

You may call any brain scientist, with the simple question, "How does it work?" None of them will be able to explain completely. We already have a few insights, but no global theory. Everything you could proclaim broadly is doomed to be too simple.

Rik Achten, *in Modern Minds*

6

Introduction to neurophysiology and tractography

While applying transcranial magnetic stimulation, a change in brain activity is not only observed in cerebral areas nearby the TMS coil, but also in distant regions. Moreover, TMS can cause responses lasting longer than the duration of the stimulation itself. This indicates that we need to account for spatial and temporal effects of TMS on the brain. The brain consists of neurons. When applying an electric field on these neurons, the voltage across their plasma membrane, called membrane potential, is altered. If this change is high enough such that the potential exceeds its threshold, the neurons will communicate through the conduction of neural signals, called action potentials.
In this introducing chapter, we elaborate on these neurons (Brodal, 2004; Kandel et al., 2000) and how their response to TMS can be modelled, so to compute the spatio-temporal behaviour of the membrane potentials. Fibre tractography, which is applied to reconstruct the realistic 3D neural trajectories, is explained as well. This way, we will be able to compute the possible generation and propagation of action potentials along the targeted neural fibres due to TMS. Both the neurophysiological basics and tractography, introduced here, will be integrated in our TMS modelling studies of subsequent chapters.

6.1. Neuron structure and function

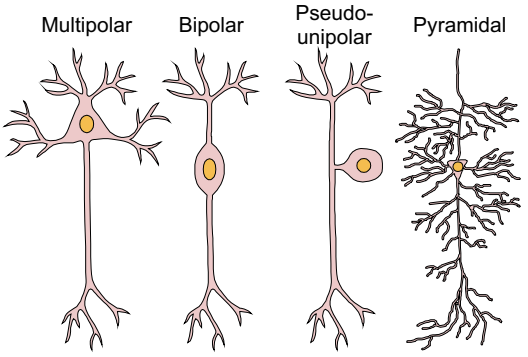

Figure 6.1: Basic neuron types, classified by the number of extensions from the cell body.

While there exist as many as 10 000 specific types of neurons in the human brain, one can generally differentiate some basic kinds, see Fig. 6.1. The motor neurons are multipolar and send signals to parts of the body, e.g. the muscles, for direct movement. The sensory neurons are pseudounipolar and transmit signals, e.g. touch and pain, from receptors of the body to the brain. Interneurons are multi- or bipolar and convey information between different types of neurons within the same region of the brain or spinal cord. They run for example through the cortical surface without crossing the grey matter - white matter (GM-WM) interface. The pyramidal neurons are multipolar and are involved in many areas of neuroplasticity and cognition.
Although there are different neuron types, they all contain the same structures, namely multiple dendrites, a cell body, an axon and axon terminals. These structures are illustrated in Fig. 6.2. The cell body or soma contains the nucleus and allows for synthesis of proteins and membranes to maintain the cell and keep the neuron functional. Most neurons have a single axon, whose morphology is highly variable (Holtmaat and Svoboda, 2009). Some axons extend locally (<1 mm long for some interneurons), whereas others may be as long as 1 m and more. The longest axons in the human body run from the spinal cord to the big toes. The axon diameter varies from less than a μm for the zebra fish, to several μm in certain nerves of the human brain, up to 1 mm in the giant fibre of the squid. Axons are specialised for the conduction of neural signals, called action potentials. They normally originate at the axon hillock, the junction of the cell body and axon, and are actively conducted down the axon into the axon terminals. These small branches of the axon form the synapses with other cells, which are the connections through which information flows from one neuron to another. When action potentials arrive at

a synapse, they cause a release of neurotransmitters that bind to receptors in the post-synaptic cell, as illustrated in Fig. 6.3. More specifically, the short and highly branched dendrites receive the chemical signals, convert them into electric impulses and transmit them to the cell body. Electric disturbances generated in the dendrites or cell body spread to the axon hillock. If the electric disturbance is large enough and exceeds the threshold, an action potential will again originate and be actively conducted down the axon to proceed the communication process.

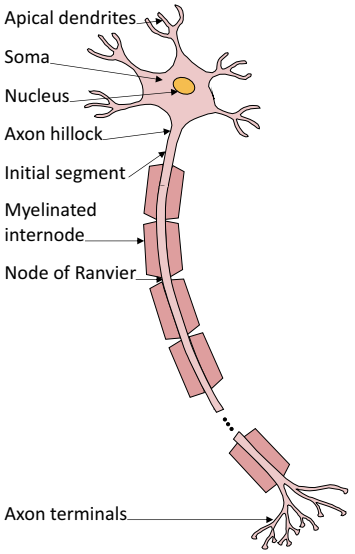

Figure 6.2: Compartmental model of the myelinated neuron, containing the apical dendrites, soma or cell body, axon hillock, initial segment and alternating myelinated internodes and nodes of Ranvier.

6.1.1 Myelinated neuron

Larger diameter axons tend to be myelinated. Since myelin has a high electrical resistance, it acts as an insulator and allows the axons to conduct action potentials with greater efficiency and velocity. Myelin sheaths are formed by oligodendrocytes in the central nervous system and consist of series of uniformly spaced segments, each extending about 1 mm along the outer surface of the axon. They are separated by small gaps, about 1.5 μm long, called nodes of Ranvier, as illustrated in Fig. 6.2. Since these nodes are not covered with a myelin sheath, they are directly exposed to the extracellular fluid, which contains ions necessary to regenerate an action potential. The layer of insulation created by the myelin coat inhibits current loss from the axon by blocking the

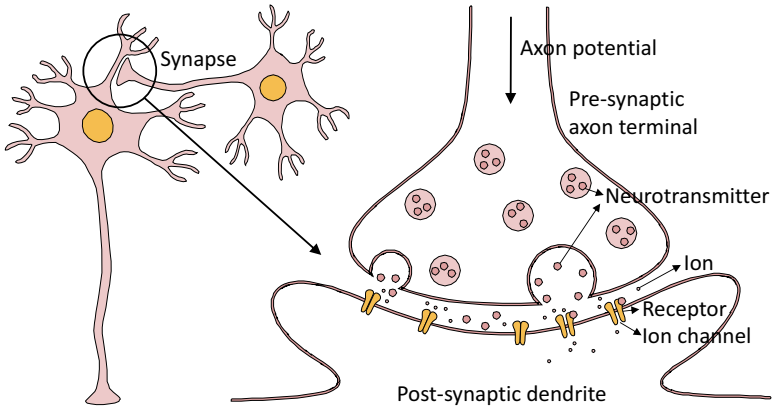

Figure 6.3: Mechanism of synapse. When an action potential reaches the axon terminals of pre-synaptic neuron, it triggers the release of neurotransmitters into the synapse. These neurotransmitters activate receptors on the dendrites of the post-synaptic neuron and open the ion channels, such that the ions can enter and trigger the propagation of the electric impulse.

movement of ions through the axon membrane. Therefore, ion channels in myelinated neurons are mostly concentrated in the nodes of Ranvier, which causes the electric impulses appear to travel from node to node, called saltatory conduction, with velocities up to 120 m/s (Kandel et al., 2000). In comparison, ion channels in unmyelinated neurons occur along the entire length of the axon, with impulse leakage through the membrane causing its spread to decay rapidly to an average speed of about 2 m/s.

6.1.2 Action potential

Most neurons communicate with each other by firing electric action potentials. An action potential is a series of sudden changes in the voltage across the plasma membrane. When axons are not conducting, they are said to be at rest. In this resting state, sodium (Na^+) and chloride (Cl^-) ions are mainly concentrated in the extracellular fluid, and potassium (K^+) ions and negatively charged proteins in the intracellular fluid, separated by the membrane, see Fig. 6.4. Slow pumps maintain this non-equilibrium state of ion concentrations, resulting in a membrane's resting potential of approximately -70 mV, meaning that the inside is negatively charged relative to the outside. When an impulse is sent, sodium channels open, Na^+ ions diffuse into the axon and the membrane depolarises rapidly. Once it reaches a certain threshold, an action potential will fire. At its peak, the membrane potential can be as much as +50 mV. This depolarisation of the membrane is followed by a rapid repolarisation and hyperpolarisation. Sodium channels become inactivated, potassium

channels open and K^+ ions exit the axon, gradually returning the membrane potential to its resting value.
If the initial depolarisation is not large enough, no action potential will be created. However, if depolarisation reaches the threshold voltage, a complete action potential occurs with the typical waveform as illustrated in Fig. 6.5. Moreover, if the threshold is surpassed, an additional increase in stimulus strength does not lead to higher voltages. This is referred to as the all-or-nothing law.
When the Na^+ channels are inactivated, they cannot be immediately opened again. Recovery from inactivation is a time- and voltage-dependent process. During the absolute refractory period, about 1 to 2 ms after the initiation of the first action potential, the initiation of another action potential is not possible, no matter how strong the stimulus is. However, a full recovery of the sodium channels usually takes about 4 to 5 ms until the membrane is completely repolarised. During this relative refractory period a stronger than normal stimulus is needed in order to elicit an action potential. It is followed by a brief hyperexcitability period of reduced threshold. After approximately 18 ms all influences of previous action potentials have faded out. Moreover, since the Na^+ channels are temporarily refractive, the electric impulse can only be transmitted to the next adjacent axon segment and not return to previous segments.

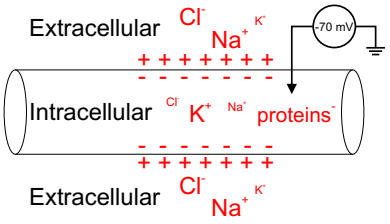

Figure 6.4: Under resting conditions, the membrane potential V, defined as the voltage across the cell membrane (inside versus outside) is approximately -70 mV. The size of the symbols reflects the proportion of the corresponding ion concentration.

6.2. Neuron response to stimulation

To model the excitability of neurons and the possible generation and propagation of action potentials, we consider the transmembrane potential, since it characterises the electrical state of a neuron. This electric state is an expression of the ion balance in the neuron. In the following, we present a passive and active model to predict the transmembrane potential responses to stimulation. This potential is calculated as a function of space and time. In the passive case, only subthreshold effects are described and, consequently, no action potentials will be generated. Since myelinated neurons contain dendrites, a soma,

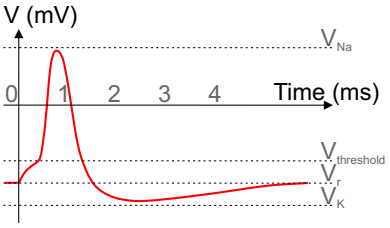

Figure 6.5: Typical waveform of an action potential. The membrane potential V starts at its resting value V_r. Once it exceeds a threshold, it depolarises towards the sodium Nernst potential V_Na, repolarises and hyperpolarises towards the potassium Nernst potential V_K and finally returns to its resting potential.

an axon hillock, an initial segment and alternating myelinated internodes and nodes of Ranvier, as shown in Fig. 6.2, we will simulate their response using a compartmental model where passive and active segments are combined. The dendrites, soma and myelinated internodes behave passively, while the axon hillock, initial segment and nodes of Ranvier behave actively.

6.2.1 Passive response

When a neuron is depolarised below its threshold for activation, the neuron returns to its resting state rather than to trigger. The subthreshold effect of stimulation by electromagnetic induction on the transmembrane potential V relative to its resting value was first described by Roth and Basser (1990). They employed the cable equation to model the passive properties of an infinitely long neural fibre.

$$\lambda^2 \frac{\partial^2 V}{\partial l^2} - (V - V_\mathrm{r}) = \tau \frac{\partial V}{\partial t} + \lambda^2 \frac{\partial E_l}{\partial l}. \tag{6.1}$$

λ is the space constant of the neural membrane, τ the time constant and $l = \|\mathbf{l}\|$ the local space parameter along the neural fibre. The last term is the activation function for stimulation (Rattay, 1986). In electromagnetic stimulation, such as TMS, an additional source of electric field is generated. The component of this induced electric field E tangent to the neural trajectory $\mathbf{l} = l\mathbf{1}_l$ effectively contributes to neuronal stimulation and is therefore called the effective electric field $E_l = \mathbf{E} \cdot \mathbf{1}_l$, see Fig. 6.6. Initially, the directional derivative of this effective electric field along the neural fibre $\partial E_l / \partial l$ was assumed to describe the effect of stimulation by electromagnetic induction on the transmembrane potential. Silva et al. (2008) later introduced two additional stimulation mechanisms, as will be explained in more detail in Section 7.1.
λ quantifies the length that a potential travels through the neuron, before it is

reduced to 37%, or $1/e$, of its initial magnitude. It is defined as

$$\lambda = \sqrt{\frac{r_{\mathrm{m}}}{r_{\mathrm{a}}}} \tag{6.2}$$

where r_{m} is the membrane's resistance times unit length and r_{a} the axial resistance per unit length at the intracellular space. The largest values of λ, some millimetres, are found in wide-diameter myelinated axons with a large r_{m} and small r_{a}. The smallest λ values, a fraction of a millimetre, occur in the thinnest unmyelinated axons.
The time constant τ is the time that it takes a potential to rise to 63%, or 1-$(1/e)$, of its final steady-state magnitude. It is defined as

$$\tau = r_{\mathrm{m}} c_{\mathrm{m}} \tag{6.3}$$

with c_{m} the membrane's capacitance per unit length.

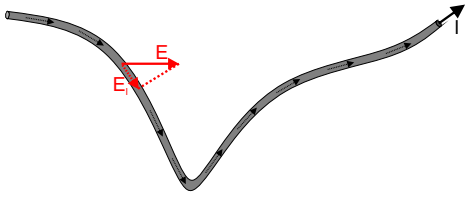

Figure 6.6: Axis l is defined along the neural trajectory and the effective electric field E_l is the component of the induced electric field E tangent to this axis.

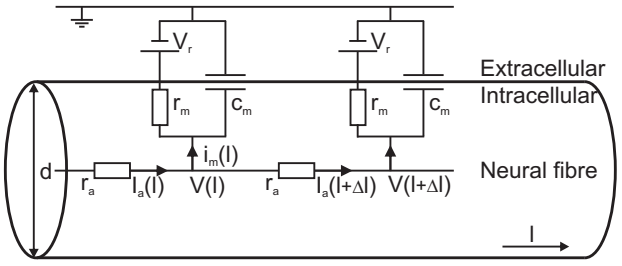

Figure 6.7: Electrical network representation of the passive neural fibre.

The equivalent network model of the passive neural fibre is shown in Fig. 6.7. In this model, the following assumptions are made. Neural segments are assumed to be cylindrical. The intracellular space is solely conductive and homogeneous and can thus be specified by a resistance r_{a}. The intracellular potential is only a function of l, the distance along the fibre. The extracellular

space is assumed to have zero resistivity and the extracellular potential produced by the fibre's own activity is thus negligible. This assumption is valid, because the extracellular potential produced by an action potential propagating along a single axon lying in a large extracellular volume conductor is less than 1 mV.
The axial current I_a at the intracellular space is given by Ohm's law, taking the component of the induced effective electric field into consideration:

$$I_\mathrm{a} = -\frac{1}{r_\mathrm{a}}\frac{\partial V}{\partial l} + \frac{1}{r_\mathrm{a}}E_l. \tag{6.4}$$

The difference between the axial current that goes in and out a segment must be equal to the current going through the membrane, which is the sum of a capacitive and resistive component. The membrane's current per unit length i_m can thus be expressed by:

$$i_\mathrm{m} = -\frac{\partial I_\mathrm{a}}{\partial l} \tag{6.5}$$

$$= c_\mathrm{m}\frac{\partial V}{\partial t} + \frac{V - V_\mathrm{r}}{r_\mathrm{m}} \tag{6.6}$$

with V_r the resting membrane potential. Combining equations (6.4-6.6) and introducing the space and time constants results in the passive cable equation (6.1).
We would like to emphasise that in order to attain stimulation, the rate of change of the electric field along the neuron's direction $\partial E_l/\partial l$ is of greater importance than the amplitude E_l. This can be deduced from equations (6.4) and (6.5), where the membrane's current is expressed. A positive current is outward the cell, see Fig. 6.7, and therefore making the voltage inside more negative; it hyperpolarises the cell. For depolarisation, a large negative membrane's current is required, corresponding with a large positive directional derivative of the axial current and thus of the effective electric field, see equation (6.4).

6.2.2 Active response

In order to study the activation and propagation of action potentials, we must consider the active properties of the neural fibre. In this PhD, an active model based on the Hodgkin-Huxley model is implemented.
First, the phenomenological model developed by Hodgkin and Huxley (1952) is discussed. Their empirical work of voltage-clamp experiments on the squid giant axon demonstrated how the macroscopic ionic current could be understood in terms of conductance changes in the membrane. This model has laid

the foundation to the mathematical description of the biophysical properties of neurons and their action potentials.

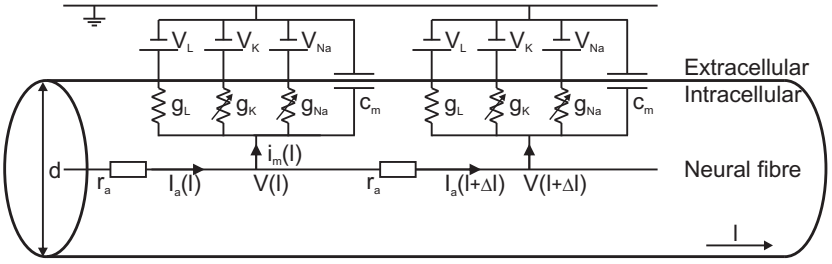

Figure 6.8: Electrical network representation of the active neural fibre.

As explained above, some membrane segments are active and contain selectively permeable ion channels which open and close depending on the voltage across the membrane. Particularly relevant are channels for sodium Na^+ and potassium K^+ ions and leakage L channels. The total current per unit length across the capacitive membrane consists of various ionic currents, see also the active network model of Fig. 6.8.

$$i_{\mathrm{m}} = c_{\mathrm{m}} \frac{\partial V}{\partial t} + i_{\mathrm{Na}} + i_{\mathrm{K}} + i_{\mathrm{L}}. \tag{6.7}$$

The sodium current per unit length is controlled by two types of fictional gates; one for activation m and one for inactivation h.

$$i_{\mathrm{Na}} = g_{\mathrm{Na}} m^3 h (V - V_{\mathrm{Na}}) \tag{6.8}$$

with V_{Na} the sodium Nernst potential. The activation gate m contribute to the fast opening of the sodium channel with increasing voltage, whereas h contribute to the relatively slow closing. The factor $m^3 h$ represents the probability that the sodium channel is open with a conductance per unit length g_{Na}. The temporal changes of these gates are described by

$$\frac{dm}{dt} = \alpha_m (1 - m) - \beta_m m \tag{6.9}$$

$$\frac{dh}{dt} = \alpha_h (1 - h) - \beta_h h \tag{6.10}$$

with the voltage-dependent transition rates α_m, β_m, α_h and β_h obtained by fitting to measurements:

$$\alpha_m = 100\frac{10^3V + 40}{1 - e^{-(10^3V+40)/10}} \tag{6.11}$$

$$\beta_m = 4 \cdot 10^3 e^{-(10^3V+65)/18} \tag{6.12}$$

$$\alpha_h = 70e^{-(10^3V+65)/20} \tag{6.13}$$

$$\beta_h = \frac{10^3}{1 + e^{-(10^3V+35)/10}}. \tag{6.14}$$

Because of the inactivation variable h the sodium current is transient. The channel opens ($m \to 1$) when the membrane depolarises, but closes after a while due to inactivation ($h \to 0$).
The potassium current per unit length is controlled by a single type of fictional gates; one for activation n. The gate has to be in an open configuration to allow an outward current of potassium ions.

$$i_K = g_K n^4 (V - V_K) \tag{6.15}$$

with V_K the potassium Nernst potential, g_K the maximal conductance per unit length of the channel and

$$\frac{dn}{dt} = \alpha_n(1 - n) - \beta_n n \tag{6.16}$$

with

$$\alpha_n = 10\frac{10^3V + 55}{1 - e^{-(10^3V+55)/10}} \tag{6.17}$$

$$\beta_n = 125e^{-(10^3V+65)/80}. \tag{6.18}$$

This potassium current is persistent and the channel remains open ($n \approx 1$) as long as the cell is depolarised.
If the membrane potential has a fixed value, the gates will reach steady-state values equal to $\alpha_i(V)/(\alpha_i(V) + \beta_i(V))$. The time courses for approaching these equilibrium values are described by simple exponentials with time constants $1/(\alpha_i(V) + \beta_i(V))$. Both parameters are depicted in Fig. 6.9 as a function of the transmembrane potential. Assuming that the resting potential is -65 mV, the initial values of the dimensionless gating variables are:

$$m_0 = 0.0529 \tag{6.19}$$

$$h_0 = 0.5961 \tag{6.20}$$

$$n_0 = 0.3177. \tag{6.21}$$

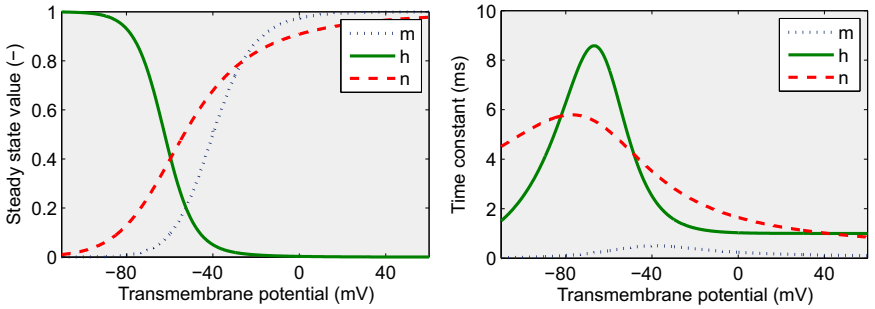

Figure 6.9: Voltage dependence of the gates. The steady-state sodium inactivation variable h decreases, while the sodium and potassium activation variables m and n increase with the transmembrane potential.

Finally, there is also a leakage current per unit length i_{L}. The active neural membrane contains a leak conductance g_{L}, which is voltage and time independent.

$$i_{\mathrm{L}} = g_{\mathrm{L}}(V - V_{\mathrm{L}}) \tag{6.22}$$

V_{L} is the leakage Nernst potential.

Equation (6.6) of the passive model has thus been replaced by the active and more complex expression (6.7) or, after substitution of the ionic currents, by

$$i_{\mathrm{m}} = c_{\mathrm{m}}\frac{\partial V}{\partial t} + g_{\mathrm{Na}}m^3h(V - V_{\mathrm{Na}}) + g_{\mathrm{K}}n^4(V - V_{\mathrm{K}}) + g_{\mathrm{L}}(V - V_{\mathrm{L}}), \tag{6.23}$$

while equations (6.4) and (6.5) remain valid. Analogous to the passive cable equation (6.1), the following is derived to model the active response:

$$\frac{1}{r_{\mathrm{a}}}\frac{\partial^2 V}{\partial l^2} - g_{\mathrm{Na}}m^3h(V - V_{\mathrm{Na}}) - g_{\mathrm{K}}n^4(V - V_{\mathrm{K}}) - g_{\mathrm{L}}(V - V_{\mathrm{L}}) = c_{\mathrm{m}}\frac{\partial V}{\partial t} + \frac{1}{r_{\mathrm{a}}}\frac{\partial E_l}{\partial l}. \tag{6.24}$$

As illustrated in Figs. 6.7 and 6.8, the neural fibre is divided into several cylindrical compartments or segments with diameter d and length Δl. The capacitance per unit area C_{m}, the resistivity of the axoplasm R_{a} and the conductances per unit area G_i (i =Na,K,L) are

$$C_{\mathrm{m}} = \frac{c_{\mathrm{m}}}{\pi d} \tag{6.25}$$

$$R_{\mathrm{a}} = \frac{\pi d^2 r_{\mathrm{a}}}{4} \tag{6.26}$$

$$G_i = \frac{g_i}{\pi d}. \tag{6.27}$$

The membrane's capacitance C_{m}^{*} and axial conductance G_{a}^{*} become:

$$C_{\mathrm{m}}^{*} = \pi d \Delta l C_{\mathrm{m}} = \Delta l c_{\mathrm{m}} \tag{6.28}$$

$$G_{\mathrm{a}}^{*} = \frac{\pi d^2}{4 \Delta l R_{\mathrm{a}}} = \frac{1}{\Delta l r_{\mathrm{a}}}. \tag{6.29}$$

The superscript * refers to the fact that the values are not per unit area. Combining equations (6.4-6.6) and (6.23) together with the newly introduced parameters, brings us to the compartmental cable equation. The axial current I_{a} between point l and $l + \Delta l$ is

$$I_{\mathrm{a}}(l + \Delta l) = G_{\mathrm{a}}^{*}\left(V(l) - V(l + \Delta l)\right) + G_{\mathrm{a}}^{*} \Delta l E_l(l). \tag{6.30}$$

and the current that goes through the membrane at point l is

$$I_{\mathrm{m}}(l) = I_{\mathrm{a}}(l) - I_{\mathrm{a}}(l + \Delta l) \tag{6.31}$$

$$= C_{\mathrm{m}}^{*} \frac{\partial V(l)}{\partial t} + \pi d \Delta l \Big(G_{\mathrm{Na}} m^3 h (V(l) - V_{\mathrm{Na}}) + G_{\mathrm{K}} n^4 (V(l) - V_{\mathrm{K}}) + G_{\mathrm{L}} (V(l) - V_{\mathrm{L}}) \Big). \tag{6.32}$$

6.2.3 Compartmental neurons

Since in reality the myelinated neural fibres contain passive dendrites, a passive soma, an active axon hillock, an active initial segment and alternating passive myelinated internodes and active Ranvier nodes, we will model them as compartmental neurons with passive and active membrane properties, as schematically represented in Fig. 6.10. Their behaviour can be computed with the following final compartmental cable equation:

$$C_{\mathrm{m}}^{*} \frac{\partial V(l)}{\partial t} + I_{\mathrm{ion}}(l) = G_{\mathrm{a}}^{*}\left(V(l - \Delta l) - 2V(l) + V(l + \Delta l)\right) + G_{\mathrm{a}}^{*} \Delta l E_l(l - \Delta l) - G_{\mathrm{a}}^{*} \Delta l E_l(l) \tag{6.33}$$

For the active components, the ionic current equals

$$I_{\mathrm{ion}}(l) = \pi d \Delta l \Big(G_{\mathrm{Na}} m^3 h (V(l) - V_{\mathrm{Na}}) + G_{\mathrm{K}} n^4 (V(l) - V_{\mathrm{K}}) + G_{\mathrm{L}} (V(l) - V_{\mathrm{L}}) \Big), \tag{6.34}$$

whereas it describes a more simple behaviour for the passive components

$$I_{\mathrm{ion}}(l) = \pi d \Delta l G_{\mathrm{m}} (V(l) - V_{\mathrm{r}}) \tag{6.35}$$

with G_{m} the conductance per unit area related to the membrane resistance r_{m}, namely $1/(\pi d r_{\mathrm{m}})$.

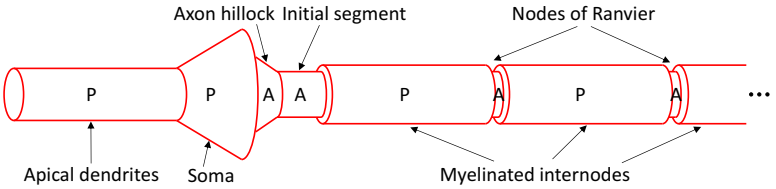

Figure 6.10: Schematic representation of the modelled myelinated neuron with the different compartments as in Fig. 6.2.

6.2.4 Practical implementation

In this work, we apply the Crank-Nicolson method to discretise the cable equation (6.33) in space and time with the grid steps Δl and Δt, respectively.

$$\begin{aligned}
&\tfrac{C_m^*}{\Delta t}\ (V(l,t+\Delta t)-V(l,t))+\frac{I_{\text{ion}}(l,t)+I_{\text{ion}}(l,t+\Delta t)}{2}\\
&=\ G_a^*\frac{V(l-\Delta l,t)+V(l-\Delta l,t+\Delta t)}{2}-2G_a^*\frac{V(l,t)+V(l,t+\Delta t)}{2}\\
&\quad +G_a^*\frac{V(l+\Delta l,t)+V(l+\Delta l,t+\Delta t)}{2}+G_a^*\Delta l\frac{E_l(l-\Delta l,t)+E_l(l-\Delta l,t+\Delta t)}{2}\\
&\quad -G_a^*\Delta l\frac{E_l(l,t)+E_l(l,t+\Delta t)}{2}
\end{aligned}\tag{6.36}$$

Let us now include a staggered time grid.

$$f(l,t+\frac{\Delta t}{2})=\frac{f(l,t)+f(l,t+\Delta t)}{2}\tag{6.37}$$

This brings equation (6.36) to the following expression:

$$\begin{aligned}
&2\tfrac{C_m^*}{\Delta t}\ (V(l,t+\frac{\Delta t}{2})-V(l,t))+I_{\text{ion}}(l,t+\frac{\Delta t}{2})\\
&=\ G_a^*V(l-\Delta l,t+\frac{\Delta t}{2})-2G_a^*V(l,t+\frac{\Delta t}{2})\\
&\quad +G_a^*V(l+\Delta l,t+\frac{\Delta t}{2})+G_a^*\Delta lE_l(l-\Delta l,t+\frac{\Delta t}{2})\\
&\quad -G_a^*\Delta lE_l(l,t+\frac{\Delta t}{2})
\end{aligned}\tag{6.38}$$

In matrix notation, we thus have:

$$\begin{bmatrix} 2(G_a^* + \frac{C_m^*}{\Delta t}) + G_m^* & -2G_a^* & 0 & 0 & ... & 0 \\ -G_a^* & 2(G_a^* + \frac{C_m^*}{\Delta t}) + G_m^* & -G_a^* & 0 & ... & 0 \\ ... & ... & ... & ... & ... & ... \\ 0 & ... & 0 & -G_a^* & 2(G_a^* + \frac{C_m^*}{\Delta t}) + G_m^* & -G_a^* \\ 0 & ... & 0 & 0 & -2G_a^* & 2(G_a^* + \frac{C_m^*}{\Delta t}) + G_m^* \end{bmatrix} \begin{bmatrix} ... \\ V(l-\Delta l, t+\frac{\Delta t}{2}) \\ V(l, t+\frac{\Delta t}{2}) \\ V(l+\Delta l, t+\frac{\Delta t}{2}) \\ ... \end{bmatrix}$$

$$= \begin{bmatrix} 2\frac{C_m^*}{\Delta t} & 0 & 0 & ... \\ 0 & 2\frac{C_m^*}{\Delta t} & 0 & ... \\ 0 & 0 & 2\frac{C_m^*}{\Delta t} & ... \\ ... & ... & ... & ... \end{bmatrix} \begin{bmatrix} ... \\ V(l-\Delta l, t) \\ V(l, t) \\ V(l+\Delta l, t) \\ ... \end{bmatrix} + \begin{bmatrix} G_a^* \Delta l & -G_a^* \Delta l & 0 & ... \\ G_a^* \Delta l & -G_a^* \Delta l & 0 & ... \\ 0 & G_a^* \Delta l & -G_a^* \Delta l & ... \\ ... & ... & ... & ... \end{bmatrix} \begin{bmatrix} ... \\ E_l(l-\Delta l, t+\frac{\Delta t}{2}) \\ E_l(l, t+\frac{\Delta t}{2}) \\ E_l(l+\Delta l, t+\frac{\Delta t}{2}) \\ ... \end{bmatrix} + \begin{bmatrix} ... \\ V^*(l-\Delta l, t+\frac{\Delta t}{2}) \\ V^*(l, t+\frac{\Delta t}{2}) \\ V^*(l+\Delta l, t+\frac{\Delta t}{2}) \\ ... \end{bmatrix} \quad (6.39)$$

Depending on the segment at location l, whether it is assigned to the dendrites, soma, axon hillock, initial segment, Ranvier nodes or myelinated internodes, and thus whether it has active or passive properties, the parameters values vary as follows:

$$G_m^* = \begin{cases} \pi d \Delta l G_m & \text{passive} \\ \pi d \Delta l (G_{Na} m^3 h + G_K n^4 + G_L) & \text{active} \end{cases} \quad (6.40)$$

$$V^* = \begin{cases} \pi d \Delta l G_m V_r & \text{passive} \\ \pi d \Delta l \left(G_{Na} m^3 h V_{Na} + G_K n^4 V_K + G_L V_L\right) & \text{active} \end{cases} \quad (6.41)$$

The passive and active membrane properties of the different segments, used in this work and similar to (Salvador, 2009), are presented in Table 6.1.

Table 6.1: Geometrical and electrical parameter values of the different neural segments, based on human sensory fibre data (Salvador, 2009; Wesselink et al., 1999).

Segment	Property	Value
General	Membrane's resting potential V_r	-84·10^{-3} V
	Sodium Nernst potential V_{Na}	43.7·10^{-3} V
	Potassium Nernst potential V_K	-84·10^{-3} V
	Leakage Nernst potential V_L	-84.14·10^{-3} V
	Sodium conductance per unit area G_{Na}	30000 S/m^2
	Potassium conductance per unit area G_K	300 S/m^2
	Leakage conductance per unit area G_L	600 S/m^2
	Resistivity of axoplasm R_a	0.33 Ωm
Dendrite (Passive)	Length L	1000 μm
	Diameter d	8 μm
	Capacitance per unit area C_m	0.028 F/m^2
	Conductance per unit area G_m	2.73 S/m^2
Soma (Passive)	Length L	80 μm
	Initial diameter d	8 μm
	Final diameter d	60 μm
	Capacitance per unit area C_m	0.028 F/m^2
	Conductance per unit area G_m	2.73 S/m^2
Axon hillock (Active)	Length L	10 μm
	Initial diameter d	12 μm
	Final diameter d	6 μm
	Capacitance per unit area C_m	0.028 F/m^2
Initial segment (Active)	Length L	20 μm
	Diameter d	6 μm
	Capacitance per unit area C_m	0.028 F/m^2
Myelinated internode (Passive)	Length L	$\pm$ 1000 μm [f3]
	Diameter d	10 μm
	Capacitance per unit area C_m	0.00005 F/m^2
	Conductance per unit area G_m	0.1 S/m^2
Ranvier node (Active)	Length L	1.5 μm
	Diameter d	6 μm
	Capacitance per unit area C_m	0.028 F/m^2

[3] depending on the length of the neural tract

Different neuron types have slightly different parameter values. This applies for the expressions of α_i and β_i as well, see equations (6.11-6.14) and (6.17-6.18), which were obtained by fitting to experiments of Hodgkin and Huxley (1952) on the squid giant axon. The used parameters are associated with the experimentally determined characteristics of human sensory fibres (Wesselink et al., 1999). They were adjusted from the original 20 °C to a body temperature of 37 °C. The corresponding voltage-dependent transition rates are

$$\alpha_m = 4.6 \cdot 10^6 \frac{18.4 \cdot 10^{-3} + V}{1 - e^{(-18.4 \cdot 10^{-3} - V)/10.3 \cdot 10^{-3}}} \tag{6.42}$$

$$\beta_m = 0.33 \cdot 10^6 \frac{-22.7 \cdot 10^{-3} - V}{1 - e^{(22.7 \cdot 10^{-3} + V)/9.16 \cdot 10^{-3}}} \tag{6.43}$$

$$\alpha_h = 0.21 \cdot 10^6 \frac{-111 \cdot 10^{-3} - V}{1 - e^{(111 \cdot 10^{-3} + V)/11 \cdot 10^{-3}}} \tag{6.44}$$

$$\beta_h = 14.1 \cdot 10^3 \frac{1}{1 + e^{(-28.8 \cdot 10^{-3} - V)/13.4 \cdot 10^{-3}}} \tag{6.45}$$

$$\alpha_n = 51.7 \cdot 10^3 \frac{93.2 \cdot 10^{-3} + V}{1 - e^{(-93.2 \cdot 10^{-3} - V)/1.1 \cdot 10^{-3}}} \tag{6.46}$$

$$\beta_n = 92 \cdot 10^3 \frac{-76 \cdot 10^{-3} - V}{1 - e^{(76 \cdot 10^{-3} + V)/10.5 \cdot 10^{-3}}} \tag{6.47}$$

and consequently, assuming the membrane is initially in rest with potential V_r, the initial gating variables have the following values:

$$m_0 = 0.02494 \tag{6.48}$$

$$h_0 = 0.7026 \tag{6.49}$$

$$n_0 = 0.2563. \tag{6.50}$$

With these values, m, h and n at the staggered grid can be calculated using the discretised equations (6.9,6.10,6.16). For example, for the activation gate m:

$$m(l, t + \frac{\Delta t}{2}) = \frac{\alpha_m(l,t) + \left(\frac{1}{\Delta t} - \frac{\alpha_m(l,t) + \beta_m(l,t)}{2}\right) m(l, t - \frac{\Delta t}{2})}{\frac{1}{\Delta t} + \frac{\alpha_m(l,t) + \beta_m(l,t)}{2}} \tag{6.51}$$

Subsequently, the parameters G^*_m and V^* can be computed and the compartmental cable matrix equation (6.39) solved for the membrane potentials V at time point $t + \frac{\Delta t}{2}$. Finally, these values can be converted back from the staggered to the normal grid $t + \Delta t$ using equation (6.37). This way of working produces a solution with an error of $O(\Delta t^2)$ while avoiding iteration of the equations (Salvador, 2009).

We stress that the parameters listed in Table 6.1 and the pre-factors of equations (6.42-6.47) are not the only possible values, but rather averaged values over different neuron types that approximate reality as close as possible. The internodal distances of a neural fibre is approximately 100 times larger than its diameter. Thus, the threshold for activation of large fibres are lower than for small fibres since the potential differences between nodes located far apart is generally larger than for nodes located closely together.
Moreover, a distinction can be made between fast and persistent sodium, and fast and slow potassium (McIntyre et al., 2002). Even more complex, morphologically realistic models with biophysical details exist such as the Purkinje cell (Jaeger et al., 1997) and the CA1 and CA3 pyramidal neurons (London and Husser, 2005; Traub et al., 1991) including the voltage-gated sodium, potassium and calcium channels and a large family of related ion channels.

As can be seen from the matrix notation (6.39), the first and last equations satisfy the Von Neumann boundary conditions. They specify the first spatial derivative of the solution at the first and last points of the discretised neuron. These conditions occur naturally in neuronal modelling, since $\partial V/\partial l$ is proportional to the axial current through the neuron. Often it is a good approximation to assume that no current is leaking out of the endpoints, thus stating Nagarajan et al. (1993).

$$\frac{\partial V}{\partial l}|_{l=0} = \frac{\partial V}{\partial l}|_{l=L_{\text{tot}}} = 0; \text{ for all t.} \tag{6.52}$$

L_{tot} is the total length of the neural fibre and so it determines the last point. They are often called sealed-end boundary conditions and guarantee that charge can accumulate at each end. These boundary conditions are implemented by setting

$$V|_{l=-1} = V|_{l=1} \text{ and } V|_{l=L_{\text{tot}}+1} = V|_{l=L_{\text{tot}}-1}; \text{ for all t,} \tag{6.53}$$

as can be seen in the first and last equation of (6.39) (Niebur and Niebur, 1991). The validity can be proven by expanding $V(l,t)$ in a Taylor series around the endpoints. For example, at $l = L_{\text{tot}}$,

$$V|_{l=L_{\text{tot}}+1} = V|_{l=L_{\text{tot}}} + \Delta l \frac{\partial V}{\partial l}|_{l=L_{\text{tot}}} + \frac{\Delta l^2}{2}\frac{\partial^2 V}{\partial l^2}|_{l=L_{\text{tot}}} + O(\Delta l^3). \tag{6.54}$$

Replacing $\partial^2 V/\partial l^2|_{l=L_{\text{tot}}}$ by $(V|_{l=L_{\text{tot}}+1} - 2V|_{l=L_{\text{tot}}} + V|_{l=L_{\text{tot}}-1})/\Delta l^2$ and using equation (6.52), gives $V|_{l=L_{\text{tot}}+1} = V|_{l=L_{\text{tot}}-1} + O(\Delta l^3)$. Therefore, the applied implementation (6.53) is correct to the second order in Δl.

6.3. Fibre tractography

For the proper modelling of the behaviour of the transmembrane potential along a neural fibre, information on the shape and direction of this fibre, i.e. the l-axis introduced in previous section, needs to be integrated. In this PhD, tractography is employed to reconstruct realistic 3D fibres in the white matter of the brain. This relatively new method is based on diffusion tensor imaging and produces anatomically plausible and reproducible reconstructions of neural fibres in the human brain *in vivo* as illustrated in Fig. 6.11. First, whole brain tractography is performed, using a deterministic streamline approach, to trace all neural fibre trajectories (Basser et al., 2000; Leemans et al., 2009). Close to the brain region that is targeted with the TMS coil, bundles of grouped neural fibres, called tracts, are selected, see also Fig. 1.16. Along each tract, the effective electric field E_l and its corresponding activation function for stimulation (Rattay, 1986) can then be computed, and with this input the spatio-temporal change of the transmembrane potential V follows from (6.39).

The graphical toolbox called ExploreDTI, developed by Leemans et al. (2009), written in Matlab (The Mathworks Inc., Natick, Massachusetts, USA) and shown in Fig. 6.12, is applied for the 3D reconstruction of the white matter fibres. It constructs a continuous and smooth diffusion tensor field from the discrete and noisy measured DTI data in order to ensure the reliability and robustness of the tractography. B-spline functions are fitted to the experimental data and interpolated (Basser et al., 2000). From the resulting diffusion tensors, individual fibre tracts are followed.

Suppose a fibre trajectory can be represented as a parametrised 3D space curve $\mathbf{r}(l)$ and $\mathbf{V}_{\max}$ is the normalised eigenvector associated with the greatest eigenvalue $D_{\max}$ of the diffusion tensor $\mathcal{D}$ at position $\mathbf{r}(l)$, see also (5.3). It is generally assumed (Basser et al., 2000) that this eigenvector lies parallel to the local fibre tract direction in coherently organised white matter:

$$\frac{d\mathbf{r}(l)}{dl} = \mathbf{V}_{\max}(\mathbf{r}(l)). \tag{6.55}$$

This Frenet equation, describing the evolution of a single fibre tract and illustrated in Fig. 6.13, is solved in ExploreDTI using Euler's method or the adaptive 4th-order Runge-Kutta method. The algorithm stops tracing the fibre when the tract reaches the boundaries of the image volume or a region with too low diffusion anisotropy or when the tract curvature becomes to high (Basser et al., 2000).

First, tracking is performed from all voxels inside the brain model, called whole brain tractography. Then, depending on the TMS case, specific regions of interest (ROIs) are defined. By using AND, OR/SEED and NOT operations, only those fibre tracts that do or do not penetrate these ROIs are selected.

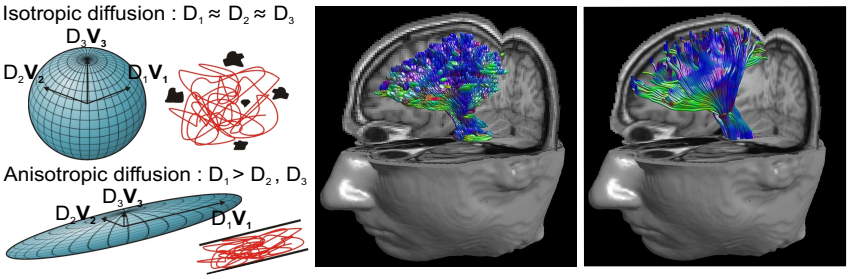

Figure 6.11: (Left) The diffusion in a single voxel can be represented by a sphere when water molecules are transported isotropically, or by an ellipsoid when transported anisotropically. (Middle) In myelinated white matter fibres the greatest diffusion is generally assumed to be parallel to the local direction of white matter, due to the myelin sheath surrounding the axons, resulting in ellipsoids of which the largest semi-axes are in the direction of the eigenvectors associated with the largest eigenvalues. (Right) Based on this diffusion data, the pathways of the myelinated white matter fibres can be reconstructed, a method called tractography. The last two images are originally from the ExploreDTI website.

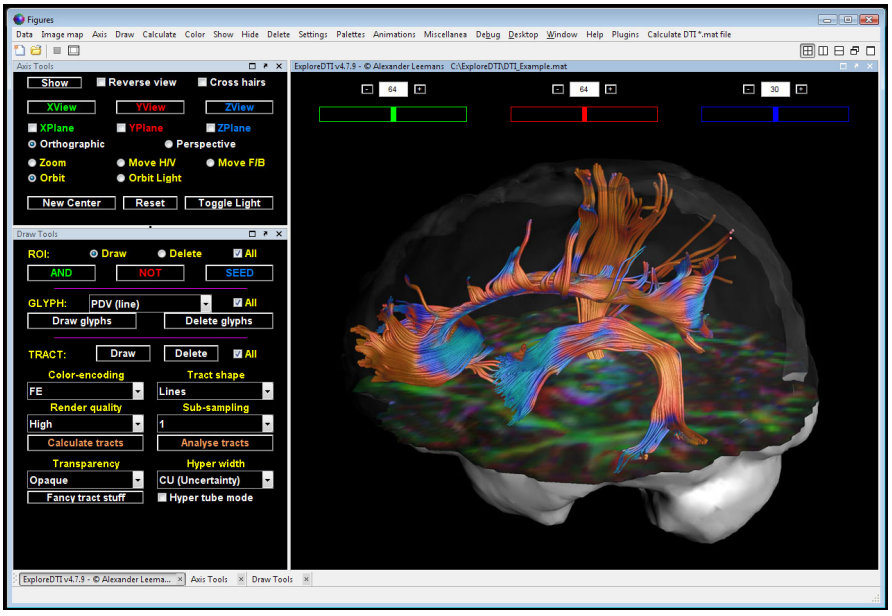

Figure 6.12: Screen shot of the graphical toolbox ExploreDTI (Leemans et al., 2009).

Since the diffusion tensor in a certain voxel used to compute the tract direction is averaged over that voxel, there are some limitations for non-uniform distribution of fibre directions within tractography. If the voxel contains highly curved fibres, reducing the voxelsize is advised. But for crossing, kissing,

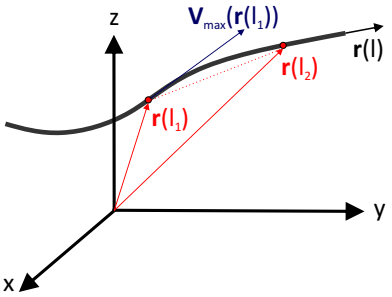

Figure 6.13: Representation of a fibre pathway as a space curve $\mathbf{r}(l)$. At position $\mathbf{r}(l_1)$, $\mathbf{V}_{\max}(\mathbf{r}(l_1))$ is the eigenvector corresponding to the largest eigenvalue. The Frenet equation (6.55) is valid, when $\Delta l = l_2 - l_1$ becomes small enough.

branching or merging fibres the method might fail to reconstruct the correct trajectories (Tournier et al., 2011). In these complex fibre configurations, the uncertainty of the dominant diffusion orientation is large, which makes it difficult to reliably reconstruct white matter fibre pathways (Jeurissen et al., 2013). Future research that can integrate such dispersion of pathway propagation during tractography is needed to tackle these limitations, for instance by resorting to probabilistic approaches (Behrens et al., 2007; Jeurissen et al., 2011).
Moreover, the tracts reconstructed with DTI-based tractography only represent anatomical or structural connectivity, and no functional nor effective connectivity is included. Functional connectivity may be estimated by measuring the correlation or covariance between brain areas using fMRI. The effective connectivity describes networks of causal effects of one neural element over another and thus the information flow. For further information, see the review of Friston (2011).

6.4. Conclusion

We introduced in this chapter the basic principles of neurophysiology and more specifically transmembrane and action potentials. The neuron response to stimulation is explained in Section 6.2. A passive and an active model are presented, together with a combined approach for compartmental neurons with both passive and active components. The spatio-temporal change of transmembrane potentials due to TMS can be calculated using a numerical time-stepping scheme. Section 6.3 explained fibre tractography extracted from DTI. In future chapters the transmembrane potentials are mapped on realistic head models with reconstructed neural fibre tracts and coupled to our developed electromagnetic solver from Part I.

You can't connect the dots looking forward; you can only connect them looking backwards. So you have to trust that the dots will somehow connect in your future. You have to trust in something - your gut, destiny, life, karma, whatever. This approach has never let me down, and it has made all the difference in my life.

Steve Jobs, *in his famous Stanford speech*

7

Effective electric field and stimulation mechanisms

Research in the field of TMS modelling has been conducted in various constructive phases. The magnetic field produced by the stimulation coil and the induced electric field were first calculated (Cohen et al., 1990; Salinas et al., 2007; Thielscher and Kammer, 2004). The induced eddy currents were further considered by Sekino and Ueno (2004); Wagner et al. (2004) to quantify the impact of TMS. Finally, the stimulation parameters which are related to the electric field along neural fibres were preliminary studied by Lu et al. (2008); Pashut et al. (2011); Salvador et al. (2011) and Opitz et al. (2011) among others. We believe that these latter electromagnetic computations need to be scrutinised and more accurately explored to fully understand and optimise the use of TMS.

An important issue in the application and research field of TMS is the variability of clinical results and psychological test outcomes towards the parameters in the TMS procedure such as the applied excitation current and the location and orientation of the coil. Efforts are dedicated in this PhD to open perspectives in understanding the effects of TMS and indicating the reasons for the widely observed variability of TMS.

To decrease the discrepancy between modelling and reality, we aim at a flexible and personalised TMS modelling method. First, the induced electric field distribution in the whole brain is calculated using the anisotropic IIM, as explained in Chapters 3 and 5. Realistic head models are used. They include patient-specific geometry and frequency-dependent anisotropic tissue properties, based on T1- and diffusion-weighted MRI. Secondly, this macroscopic electric field is mapped along the trajectories of the neural fibre tracts and serves as the input for the stimulation mechanisms. The coil configuration can be chosen freely in our computations and is specified by the coil shape, stimulation pulse and position relative to the head and the region of interest. In contrast to (Pashut et al., 2011), the trajectories of the investigated neural fibres are not limited to lie in a plane parallel to that of the coil. Another restriction in previously performed studies, is that a simplified geometry of the neural trajectories is considered and the respective electric field component along these bundles. In (Lu et al., 2008), the x-, y- and z-components of the electric field are computed and investigated for a non realistic straight test line within the brain. An artificial fibre mimicking a 2D axon reconstruction of the primary motor cortex based on macaque monkey data is considered in (Opitz et al., 2011). Salvador et al. (2011), on the other hand, modelled several types of neurons within a human folded cortical sheet to study the activation mechanisms with a 2D geometry of the trajectories. In contrast, we employ DTI-based tractography based on the diffusion tensor framework of the patient, to generate realistic 3D reconstructions of the neural fibres, as explained in Section 6.3. This approach clearly differs from previous studies.
Integrating DTI information in TMS is a relatively new concept. The diffusion tensor has mainly been used to derive realistic fibre anisotropy (De Lucia et al., 2007). In two recent studies of Opitz et al. (2011) and Nummenmaa et al. (2014) DTI-based tractography is applied to model the geometry of neural bundles. Opitz considered a small number (tens) of similarly oriented tracts close to each other, while Nummenmaa included about 750 detailed tracts. Both studies focussed on short (several mm) neural tracts localised near a single gyrus, whereas we study a substantially larger region of interest (several cm^3). Furthermore, the electric field distributions inside the skull are computed, using a simplified single-compartment boundary element model without incorporating anisotropic conductivities. Moreover, they investigated the absolute value of the induced electric field gradient, i.e. the derivative of the electric field component parallel to the tract. This term is only one of the three stimulation mechanisms as described in (Silva et al., 2008); and by neglecting the sign, distinction between depolarisation and hyperpolarisation cannot be made. In (Shahid et al., 2014), both tissue anisotropy and fibre tract information were subtracted from DTI to model the effects of transcranial direct current stimulation (tDCS).

The case study of this chapter focuses on the stimulation of the hand area of the left primary motor cortex (M1). We study the importance of implementing realistic 3D neural trajectories and the effect of small changes in orientation of the considered neural tracts on the stimulation mechanisms. We quantitatively investigate the impact of the poorly-known values of the tissue conductivities and neglecting their anisotropic properties. Moreover, the sensitivity of stimulation towards small adaptations in the coil configuration is examined.
Results from this chapter have been presented at the International Conference on Biomagnetism (BIOMAG) in 2014 in Halifax and published in (De Geeter et al., 2014).

7.1. Practical implementation

The first stimulation mechanism is defined as the directional derivative of the effective electric field along the neural fibre and equals

$$-\lambda^2 \frac{\partial E_l}{\partial l}. \tag{7.1}$$

This term was initially assumed to describe the effect of stimulation by electromagnetic induction on the membrane potential according to the classic cable theory (6.1) (Roth and Basser, 1990). This model was derived for long, straight and uniform fibres. However, neural fibres may be short, follow a curved path, terminate, branch or change in diameter. *In vitro* experiments revealed that excitation can take place even in the absence of effective electric field gradients. Maccabee et al. (1993) discovered that the threshold for activation is markedly reduced when the neural fibre is bent or when it is stimulated at its cut end. This is in agreement with simulation studies suggesting that excitation of short axons happens at terminations rather than at the directional derivative sites (Nagarajan et al., 1993). Therefore, a second mechanism is introduced, mainly occurring at terminations and sharp bends of the fibre (Roth, 1994)

$$-\lambda E_l. \tag{7.2}$$

Low-threshold excitation may also arise at inhomogeneities, leading to a third jump mechanism at the GM-WM interface due to the changing conductivity values (Miranda et al., 2007)

$$-\lambda \frac{\Delta E}{2}. \tag{7.3}$$

Fig. 7.1 schematically illustrates the three different stimulation mechanisms and the sites where they occur in the neural fibre bundle. These three mechanisms (7.1), (7.2) and (7.3) have been computed in a cortical sulcus by Silva et al. (2008) and were later tested on synthetic neural fibres by Salvador et al.

(2011). We will simulate them on realistic human fibre tracts. In order to incorporate all three mechanisms into the neurophysiological calculations, the two additional terms (7.2) and (7.3) are added as sources to the cable equations (6.1) and (6.24) for the passive and active response, respectively.

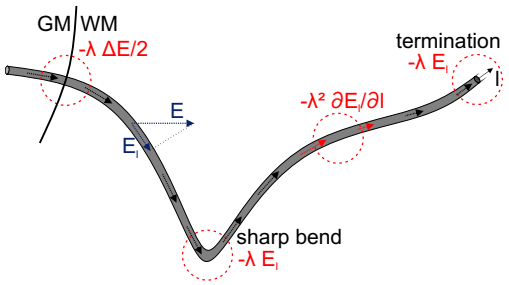

Figure 7.1: Neural fibre bundle along the l-axis and corresponding stimulation mechanisms. A first mechanism occurs when the effective electric field E_l changes its amplitude. A second mechanism occurs at terminations and sharp bends of the neuron where the effective electric field changes its direction. A third mechanism occurs when the neural fibre crosses a grey matter-white matter interface.

7.2. Simulations on a realistic head model and neural trajectories

An accurate personalised head model is created from structural and diffusion-weighted MRI. It includes realistic geometry, frequency-dependent electrical properties, i.e. conductivity and permittivity, tissue anisotropy and traced neural fibre bundles connected with the targeted region.

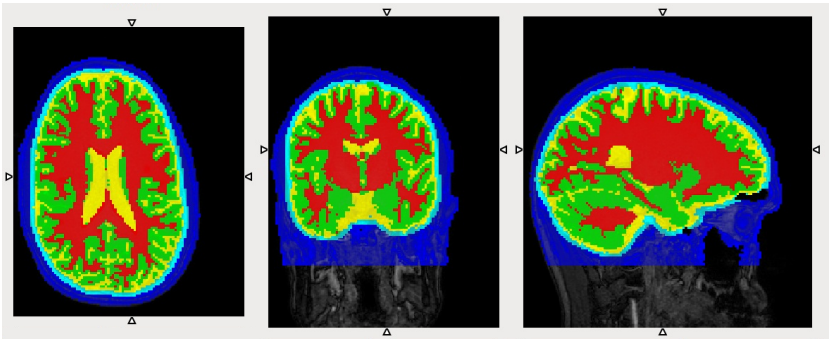

Figure 7.2: Segmentation based on T1-weighted MRI. Axial (left), coronal (middle) and sagittal (right) view of the constructed head model containing the tissues scalp (blue), skull (turquoise blue), cerebrospinal fluid (yellow), grey matter (green) and white matter (red) and surrounded by air (black). The original T1-weighted image is visualised on the background.

A T1-weighted image was acquired from a healthy 25-year-old female volunteer on a 3 Tesla MR scanner (Philips Achieva 3.0T) using a turbo field-echo sequence (TR/TE = 25 ms/4.5 ms, flip angle = 30°, field of view (FOV) $160\times240\times240$ mm^3 and matrix size $160\times256\times256$). The subject gave informed consent to participate in this study under a protocol approved by the University Medical Center Utrecht ethics board. SPM8 (Friston et al., 2007) was used to segment this image into tissue probability maps. Based on these maps, a head model is constructed (FOV $192\times236\times206$ mm^3 and matrix size $96\times126\times110$), surrounded with air and segmented into scalp, skull and the cerebral tissues cerebrospinal fluid, grey and white matter as visualised in Fig. 7.2. The electrical properties of these tissues vary naturally with frequency and their isotropic values are obtained from the 4-Cole-Cole model (Cole and Cole, 1941; Gabriel et al., 1996c).
In addition to the T1-weighted image, a DTI data set of the same subject was acquired using a single-shot spin-echo EPI sequence (FOV 224×224 mm^2 and matrix size 128×128, 60 diffusion-weighted images (b = 1200 s/mm^2) and 1 non-diffusion-weighted image (6 excitations)) (Jones and Leemans, 2011). The diffusion-weighted MRI data were corrected for (i) subject motion and eddy-current induced geometric distortions (Leemans and Jones, 2009) and (ii) EPI based deformations due to magnetic field inhomogeneities by non-rigidly warping the diffusion data to the T1-weighted image (Irfanoglu et al., 2012). The diffusion tensor was estimated using a robust outlier detection procedure (REKINDLE) with the iteratively reweighted linear least squares approach (Tax et al., 2015; Veraart et al., 2013). Anisotropic conductivity and permittivity tensors were computed from this diffusion tensor as explained in Section 5.1.1. It is important to incorporate these anatomical details, tissue heterogeneity and anisotropy, since they can significantly alter the induced electric field distribution (De Lucia et al., 2007; Miranda et al., 2007).

To reconstruct the fibre trajectories in the subject's brain, we use the graphical toolbox ExploreDTI (Leemans et al., 2009). First, whole brain tractography (Basser et al., 2000) is performed, in which a deterministic tracking algorithm estimates the principal diffusion orientation at each voxel, functioning as seed points, and propagates along this direction in steps of 1 mm. The seed fractional anisotropy measures the degree of preference for a single diffusion direction and its threshold is set to 0.2. The bending angle threshold is set to 30 degrees. Neural pathways between 5 and 25 cm are thus traced starting from each voxel until FA becomes smaller than 0.2 or the fibre direction changes more than 30 degrees.
Subsequently the region of interest method is applied to extract the relevant neural fibres. Since TMS targets in this study the left M1 hand area, this determines the central seed ROI, depicted as the blue dot in Fig. 7.3. Within its 15-mm range, a box is created. 12797 tracts that traverse this box are identified

from the whole-brain tractogram. Only those tracts whose first and last points are located more than 10 mm from another are kept, leading to 285 tracts. The subsequent selection criteria are that both end points should be connected to a GM-WM interface within their 5×5×5-voxel environment (2 voxels extra in each direction), and that no other tissue than white matter should be present along the tract between those two interfaces. This resulted in a total of 54 tracts, of which 5 have more than 50 representations. We will focus our study on these five most common and representative tracts. Another two are selected with trajectories similarly oriented to those of tract 1 and 2. All considered neural fibre tracts are represented as 3D space curves, i.e. x-, y- and z-coordinates, shown in Fig. 7.3 together with their position relative to the seed ROI.

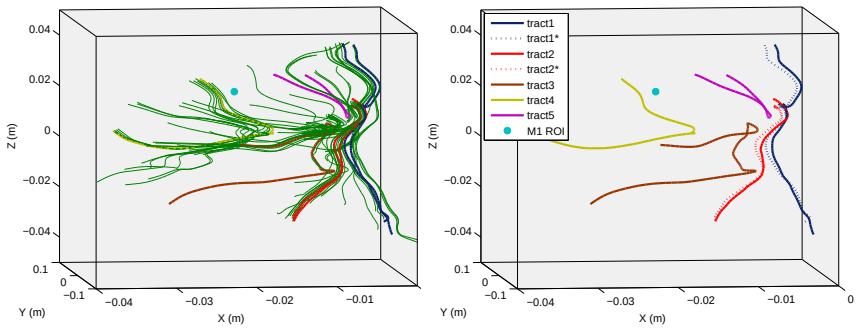

Figure 7.3: Selection of the five main neural fibre tracts from the group of 54 tracts near the left M1 hand area. Two extra fibres with similar oriented trajectories are selected, marked with an asterisk and indicated with dotted lines. The blue dot is the seed ROI centre.

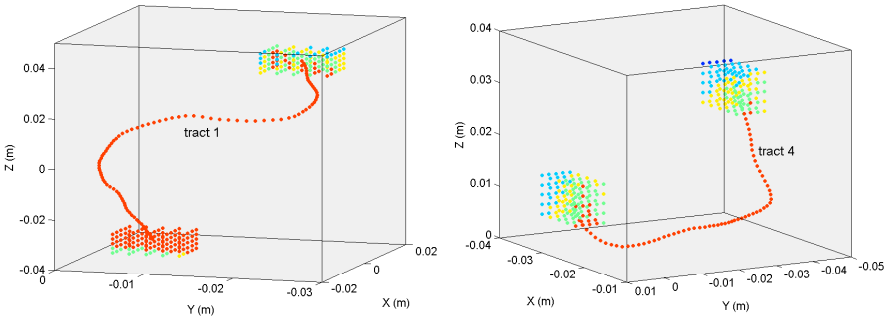

Figure 7.4: Fibre tracts connecting one GM-WM interface with another. (Left) Tract 1 and (right) tract 4 with the surrounding 5×5×5 voxels near their first and last points. The colours represent the corresponding tissue labels, analogously as in Fig. 7.2.

Since all tracts are considered as myelinated fibre bundles connecting one GM-WM interface with another, as illustrated in Fig. 7.4 for tract 1 and 4, these bundles mainly contain pyramidal neurons. Tract 1, 2, (1* and 2*) are pyramidal tract neurons (PTNs) whereas tract 3, 4 and 5 are association fibres. For more details on these different neuron types, we refer to Section 1.3.3. We make this distinction to investigate if we can draw similar conclusions as Salvador et al. (2011) concerning the activation mechanisms.
The TMS configuration can be characterised by the following parameters: the coil position, orientation and its design, the pulse waveform, duration and frequency and the stimulus amplitude. The presented method is developed in a flexible way so that all these parameters can be varied freely. The simulations are not restricted to coils placed parallel to the plane of the neural fibre bundle, as was the case in (Pashut et al., 2011). Remark that the considered neural bundles, depicted in Fig. 7.3-7.4, are three dimensional and thus not situated in a plane.
We modelled the response of a single biphasic pulse with a sinusoidal waveform (5.8) and a pulse width of 230 μs (ω_c=4.348 kHz), delivered to the hand area of the left primary motor cortex. The 70mm figure-of-eight Nexstim coil (Nexstim Ltd., Helsinki, Finland) is applied, with a mean winding diameter of 50 mm, and modelled as an air-core coil. During stimulation, it is placed tangentially to the scalp surface and the maximal induced current is directed anteriorly, as shown in Fig. 7.5. The stimulator output (peak excitation current time derivative) is set to 21.87 A/μs. The coil can be rotated and tilted to study the sensitivity of the stimulation mechanisms with respect to the coil's orientation.

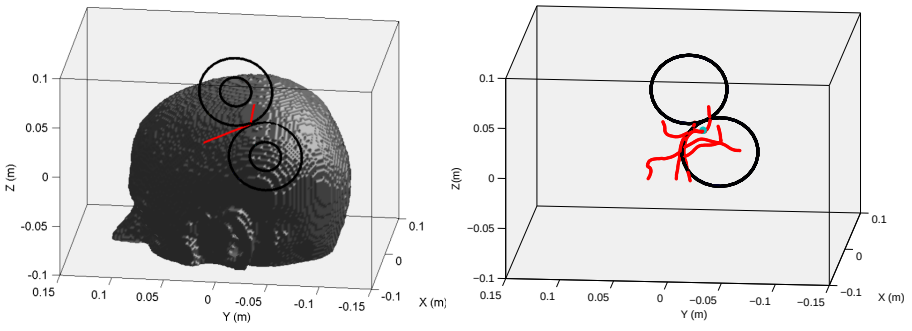

Figure 7.5: Coil location and orientation for TMS of the left M1 hand area. (Left) The coil position with respect to the head model. Both the inner and outer windings of the 70mm figure-of-eight biphasic Nexstim coil are visualised. The vectors illustrate the coil normal and the induced current direction. (Right) The coil position with respect to the selected neural fibre tracts and the seed ROI centre, respectively represented by lines and a dot. Only the outer windings of the coil are plotted.

A realistic personalised head model is thus reconstructed based on the patient's MRI. The DTI data set was co-registered to the T1-weighted data, leading to $160\times256\times256$ voxel matrices with voxelsize (1, 0.9375, 0.9375) mm^3. The coordinate system (x, y, z) is defined according to the neurological convention. The x-axis is oriented from left (L) to right (R), the y-axis from posterior (P) to anterior (A) and the z-axis from inferior (I) to superior (S), as can be seen in Fig. 7.5.
Since the coil is positioned above the left M1 hand area, we extended the matrices by adding 32 voxels air to the left of the head (neg x) and 20 voxels air superiorly (pos z), in order to reduce simulation inaccuracies. On the other hand, we cut off 4 voxels air anteriorly (pos y) and 56 voxels tissue below the nose (neg z), so to prevent unnecessary calculations in less interesting regions. This resulted in $192\times252\times220$ matrices, or FOV of $192\times236.25\times206.25$ mm^3, with the origin of the coordinate system (0, 0, 0) in the middle, or more specifically at the lower left hand rear corner of voxel (96, 126, 110). To reduce the computation time and memory of the electromagnetic solver, the voxelsize of the head model was doubled for the simulations, leading to induced electric field distributions with matrix size $96\times126\times110$.
Tractography is performed based on the 1-mm DTI. The ROI is defined as a $31\times31\times31$-voxel box (15 voxels extra in each direction) around the left M1 hand area, with coordinates (-0.0210, -0.0216, 0.0234) in m. The selected neural tracts are co-registered with the previously described reference space, as ExploreDTI applies the radiological (AP, RL, IS) coordinate system. Data from ExploreDTI was exported and post-processed in Matlab (R2013a, The Mathworks Inc. Natick, Massachusetts, USA).

7.2.1 Effective electric field

In summary, we model and simulate the effect of single pulse stimulation delivered to the left M1 hand area, with the coil positioned according to Fig. 7.5, using patient-specific MR data (Figs. 7.2-7.3). For this case study, the induced electric field is computed in the whole brain and the effective electric field is studied along the DTI-based realistic neural fibre trajectories, since this is the source term of the cable equation and the three stimulation mechanisms (7.1)-(7.3). All results are plotted at the time instant that the stimulation pulse begins, corresponding with maximum induced electric fields, see Fig. 1.8.
The anisotropic independent impedance method is used for performing the electromagnetic simulations. Since we are mainly interested in the induced electric field distribution within the cerebral tissues, only those voxels are imaged in Fig. 7.6.
The component of this electric field tangent to the trajectory l of each selected neural tract is then computed and depicted in Fig. 7.7. This term is called the

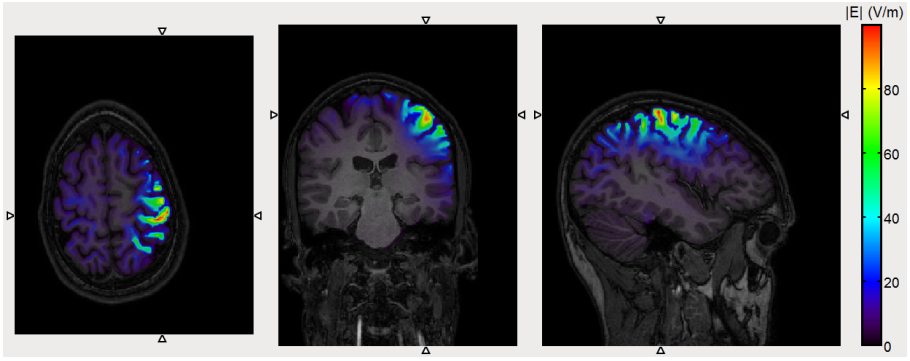

Figure 7.6: Induced electric field amplitude distribution (in V/m) due to TMS of the left M1 hand area. Only the values in the cerebral tissues are visualised for clarity reasons. Note that the views are different from those in Fig. 7.2.

effective electric field E_l, since it effectively contributes to neuronal stimulation, expressed in the three different stimulation mechanisms (Silva et al., 2008). Since only large tracts longer than 5 cm are considered here, the length constant λ is set to 2 mm (Silva et al., 2008), see also (6.2).

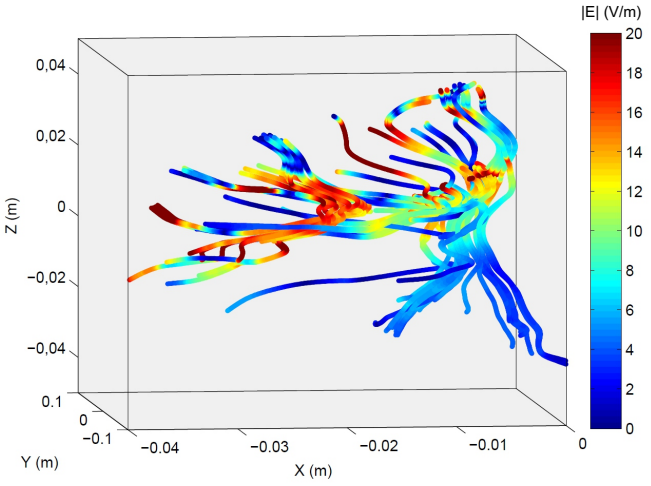

Figure 7.7: Induced effective electric field amplitude (in V/m) along all 54 neural fibre bundles due to TMS of the left M1 hand area, at the start of the stimulation pulse. The colour limit is set to 20 V/m for clarity reasons.

While the electric field in Fig. 7.6 remains mainly concentrated in the vicinity of the coil, its component parallel to the neuron's local orientation exhibits a larger and more irregular spatial spread, as can be seen from the $40\times20\times100$ mm^3 box in Fig. 7.7. This clarifies our decision to consider a substantially

larger area of interest than previous studies, namely all tracts traversing the 15-mm range around the left M1 hand hotspot. Not in all tract points near the coil, and thus near the M1 ROI, a large effective electric field is induced, and at the same time it is not limited to those points. This is illustrated more quantitatively in Fig. 7.8, in which the effective electric field of each point in the 54 neural tracts is plotted as a function of the distance between this point and the seed ROI centre. A strong and localised variation of the field can be observed. This is caused by the interplay of different factors such as the tract's position and orientation in relation to the TMS coil, the neural trajectory and its course along the white and grey matter interface. At a distance of 20 mm, the effective electric field can be near to zero or 25 V/m, illustrating the dependence on the above mentioned various factors. The same can be observed at 40 mm. Moreover, the average effective field is not continuously descending for increased distance: 14 mm away from the M1 hotspot, the field amounts on average 9.6 V/m, while at a double distance it is 12.9 V/m. At single tract points, this effect is even more pronounced, with effective field values up to 31.8 V/m at 27-mm distance and 17.1 V/m at 49 mm. The occurrence of the effective field amplitude at certain distance gives a trend of its spatial extent. The order of electric field magnitude decreased from 100 V/m (Fig. 7.6) to tens of V/m for its effective component (Figs. 7.7-7.8), which is consistent to literature for the applied stimulator output of 21.87 A/μs (Miranda et al., 2007; Salvador et al., 2011).

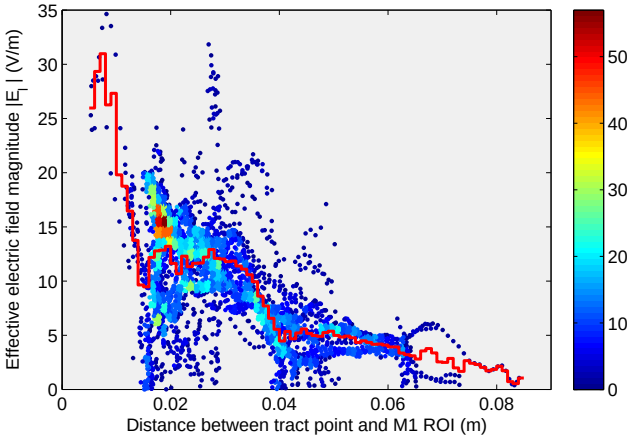

Figure 7.8: Strong and localised variation of the effective electric field. For each tract point, the effective field amplitude (in V/m) is plotted as a function of its distance from the M1 ROI centre (in m). The colours indicate the number of tract points out of in total 41664 points with those parameters. The averaged effective field over 1-mm intervals is represented by the red line.

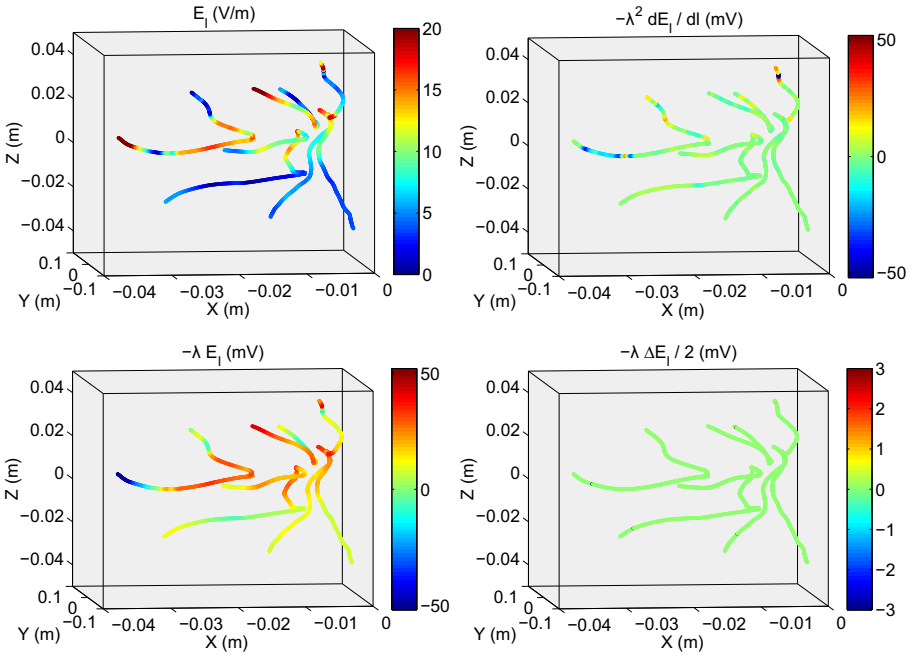

Figure 7.9: Modelling the impact of left M1 hand area TMS on the five considered neural fibre bundles. (Upper left) Induced effective electric field amplitude (in V/m). The colour limit is set to 20 V/m, similar as in Fig. 7.7. (Upper right) Directional derivative of the effective electric field along the neural fibres (in mV). (Lower left) Effective electric field term (in mV) which mainly reaches higher values at terminations and sharp bends. (Lower right) Electric field jump mechanism at the GM-WM interface (in mV). The colour range of the first two stimulation mechanisms is set to [-52, 52] mV, equally to the stimulation threshold proposed by Silva et al. (2008), the third one to [-3, 3] mV for clarity reasons. The length constant λ is equal to 2 mm. All plots are at the time instant when stimulation begins, corresponding with maximal induced electric field values as explained in Fig. 1.9. Consequently, the stimulation mechanisms are sinusoidal waves in phase. Large positive values cause depolarisation at this time moment, while large negative values cause hyperpolarisation now and depolarisation half a pulse width later.

In Fig. 7.9 we focus on the effective electric field amplitude along the five considered neural tracts and the corresponding 3 stimulation mechanisms. These mechanisms interact with the voltage-gated ion channels at the plasma membrane of the neurons, in accordance with the Hodgkin-Huxley dynamics (6.33) and alter the membrane potentials (Roth and Basser, 1990). Once they exceed a threshold, depolarisation occurs and an action potential is initiated resulting in an excited or inhibited neuron. Similar as in (Silva et al., 2008), we assume here stimulation will be achieved when one of the mechanisms reaches an magnitude higher than 52 mV. Remark no mechanism for the five selected tracts exceeds 52 mV and consequently no action potential will take place.

Nevertheless, these figures show relative results with respect to the stimulator output of this case study. When increasing the intensity of the stimulator, and thus the excitation current amplitude, the induced electric field increases proportionally such that the stimulation mechanisms exceed the stimulation threshold. We discuss this further in Section 8.3. The effective electric field term $-\lambda E_l$ is the most dominant mechanism. It reaches maximal values of 44.31 mV for tract 1, 34.43 mV for tract 2 and 41.89 mV for tract 5, all within the first 2.5 mm, and 33.04 and 33.10 mV for tract 3 and 4 at the place where they bend sharply. So this mechanism would exceed the 52 mV threshold in tract 1 for a peak excitation current time derivative higher than 25.67 A/μs. Remark, this output is a bit lower than the lowest stimulation thresholds for a biphasic pulse tabulated by Salvador et al. (2011). In Section 8.3 we will show a higher output is indeed needed to retrieve an action potential. The directional derivative term $-\lambda^2 \frac{\partial E_l}{\partial l}$ operates primarily in tract 1 and 4, with voltages up to 29.91 and 26.06 mV, due to the fast changing field at those points. The jump term $-\lambda \frac{\Delta E}{2}$ remains small (< 3 mV) for all tracts in this case study. In general, we can state that the stimulation mechanisms are the highest at neural terminations and bends; and that therefore activation mainly occurs at those sites.

These findings of strong variation and the preferred stimulations sites are consistent with those of Salvador et al. (2011). However, we find it hard to determine which mechanism dominates for which type of tract (PTNs 1, 1*, 2, 2*; association fibres 3, 4, 5) and even to dissociate these different types. This can be explained by the fact that in contrast to including predefined and simplified neural pathways, we received realistic, but irregular geometrical information from the DTI-based tractography.

7.2.2 Influence of neural tract orientation

In this subsection we assess the effect of differently oriented neural tracts on the effective electric field. As previously mentioned, alternative but closely located tracts were selected for tract 1 and 2 and marked with an asterisk (1* and 2*). Their effective electric fields are plotted in Fig. 7.10 as function of the distance along the neural pathway.

The distance l along neural tract 1 is measured from coordinate (-6.25, -24.52, 41.80) in mm towards (-1.00, -6.69, -34.50). The difference in effective electric field ΔE_l between this tract and its alternative has a mean of 0.52 V/m and reaches its maximum of 15.92 V/m for l equal to 4.4 mm. The point-wise difference Δl between the coordinates of both amounts to a minimum of 0.9 mm, a maximum of 3.7 mm and is on average 2.2 mm. The largest ΔE_l occur mainly in the first 5 mm of the tract, whereas Δl in this interval is limited to 2 mm and the angle between both tract orientations varies between 0.8 and 4 degrees.

This difference in effective field even causes the dominant stimulation mechanism to change from $-\lambda E_l$ for tract 1 to $-\lambda^2 \frac{\partial E_l}{\partial l}$ for tract 1*, both taking place at their beginning points. So a slightly different tract can give rise to the occurrence of distinct stimulation mechanisms.
For tract 2, the distance l is measured from coordinate (-6.11, -10.55, 19.57) towards (-13.00, 4.31, -29.50). A mean ΔE_l of 0.70 V/m is observed and a maximum of 2.70 V/m for l equal to 23.9 mm. Δl varies from 1.0 to 5.9 mm and is on average 2.8 mm. For both tracts, $-\lambda E_l$ is the dominant mechanism and activation will take place at the beginning of the neural fibres.
These results demonstrate the strong variability of the effective electric field among the tracts and confirm the need to model TMS effects for each case and each patient individually.

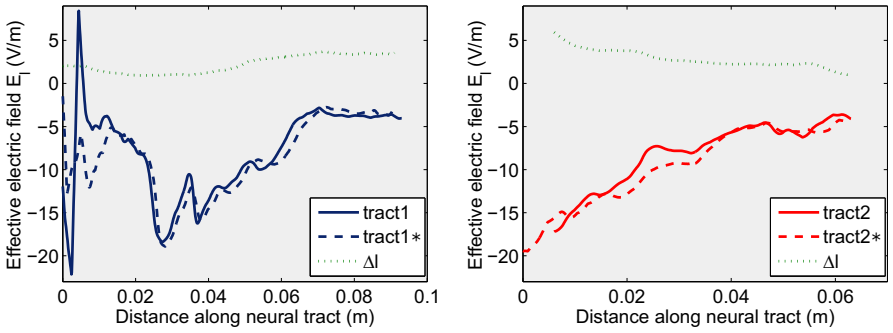

Figure 7.10: Effect of considering a slightly different oriented tract on the spatial variation of the effective electric field (in V/m). (Left) Tract 1 and (right) 2 with their corresponding similar tracts. Δl is the distance (in mm) between both neural tracts. The distance is measured starting from the point closest to the M1 ROI. The presented effective electric fields are at the moment that the stimulation pulse starts.

7.2.3 Influence of tissue anisotropy

When comparing the electric field of all cerebral tissues between the isotropic and DTI-based anisotropic head model, differences up to 38.89 V/m are observed. Fig. 7.11 depicts the effective electric field along the five selected tracts. At some tract points the field decreases with maximum 6.44 V/m and at others it increases with maximum 9.33 V/m, while the spatial field variation remains globally the same. To draw general conclusions, we computed the effective fields along all 54 tracts, resulting in a total of 41664 data points, and generated box plots for both the anisotropic and isotropic case and the difference between both ($\Delta E_{l,\text{iso}} = E_{l,\text{iso}} - E_l$), see Fig. 7.11. On each box, the central red mark is the median, the edges of the box are the 25th (Q1) and 75th

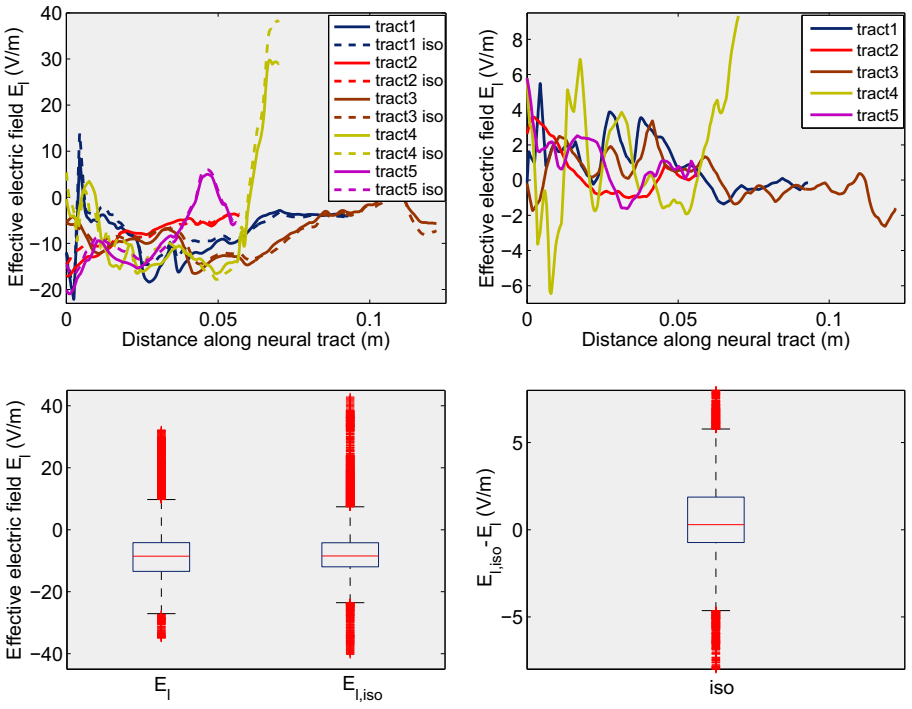

Figure 7.11: Effect of neglecting tissue anisotropy on the spatial variation of the effective electric field (in V/m). (Upper left) The anisotropic and isotropic results are indicated with solid and dotted lines, respectively. (Upper right) The difference between both. The distance is measured starting from the point closest to the M1 ROI. (Lower left) Box plots of the effective electric field for both cases (in V/m) for all 54 tracts. (Lower right) Box plot of the error $\Delta E_{l,\text{iso}}$ (in V/m) for all 54 tracts. All results are at the time that the stimulation pulse begins.

percentiles (Q3), the whiskers extend to extreme data points not considered outliers. Points are defined as outliers if they are smaller than Q1 - 1.5(Q3 - Q1) or larger than Q3 + 1.5(Q3 - Q1), and they are plotted individually.
Neglecting tissue anisotropy causes a moderated median increase of 0.29 V/m. 25% of all considered points show a decrease of more than 0.73 V/m and another 25% an increase of more than 1.87 V/m. More than 90% of the data points have a $\Delta E_{l,\text{iso}}$ between -4.64 and 5.78 V/m. The most extreme changes are -10.89 and 10.67 V/m. In general, a localised effective electric field increase is observed due to isotropic tissues. A correlation coefficient, see equation (5.2), of 0.9473 between both cases is obtained.

7.2.4 Influence of not well-known conductivity values

At low frequencies, where the conductivity values in literature are scarce and have larger than average uncertainties, the 4-Cole-Cole model should be used with caution in the knowledge that it provides a best estimate based on present data. For the applied fundamental frequency of 4.348 kHz, the conductivity values according to this model are 0.066 and 0.108 S/m for white and grey matter, respectively, see Section 2.2.1.

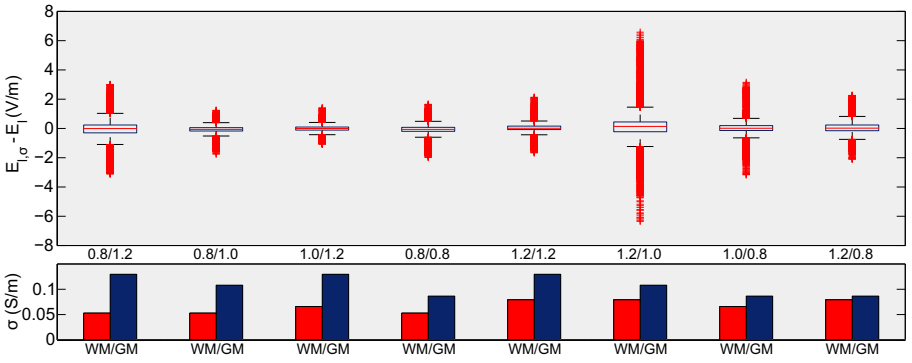

Figure 7.12: Effect of not well-known conductivity values on the effective electric field (in V/m). (Upper) Box plots of all 54 tracts of the difference $\Delta E_{l,\sigma}$ equal to $E_{l,\sigma} - E_l$ due to varying σ. They are arranged with an increasing WM/GM ratio and are labelled with the factors both conductivities $\sigma_{\mathrm{WM}}/\sigma_{\mathrm{GM}}$ are multiplied with. (Lower) For each case, the corresponding conductivity values (in S/m) of white and grey matter are indicated with red and blue bars, respectively.

To investigate the effect of these not well-known values, white matter conductivity was multiplied by 0.8, 1.0 and 1.2 and the same variation was applied for grey matter. For each combination, a box plot was generated of $\Delta E_{l,\sigma}$, defined as the effective electric field of the adapted minus standard case for all 54 tracts, and all plots are shown in Fig. 7.12. They are arranged according to an increasing WM/GM conductivity ratio from 0.41 to 0.92. At first glance, overall limited differences can be observed. More than 90% of the data points have a $\Delta E_{l,\sigma}$ between -0.66 and 0.67 V/m and a high correlation coefficient of 0.9981 between E_l and $E_{l,\sigma}$ is observed. The major changes take place when multiplying white matter conductivity by 1.2 and keeping grey matter conductivity unaltered, with a maximum effective field increase of 6.35 V/m and decrease of 6.57 V/m. When looking closer, it is remarkable how the median is always slightly negative (positive) and the 75th percentile is slightly lower (higher) than the 25th percentile in absolute value for reduced (raised) WM/GM conductivity ratios with respect to the original ratio of 0.61. This means that increasing the ratio resulted in an increased effective electric field and vice versa.

However, the impact remains limited and is not proportional for the left M1 hand area stimulation case study.

7.2.5 Influence of coil orientation

In this subsection, we study the influence of changes in the coil orientation to the effective electric field. First, the TMS coil is rotated about the normal vector (vector **n** in Section 2.3.1) by an angle α between -20 to +20 degrees, in steps of 10 degrees. Fig. 7.13 illustrates this coil rotation angle and the field changes $\Delta E_{l,\alpha}$ it causes. For α equal to -10 degrees, a moderate median increase of 0.25 V/m is observed. 25% of all tract points show a decrease of more than 0.42 V/m and another 25% an increase of more than 0.87 V/m. The most extreme changes are -7.78 and 11.75 V/m. Remark these values are relatively high compared to the effective electric field values which are mainly between -20 and 10 V/m as shown in Fig. 7.11. For α equal to +10 degrees, a moderate median increase of 0.12 V/m is observed. 25% of all points show a decrease of more than 0.67 V/m and another 25% an increase of more than 0.92 V/m. The most extreme changes are -12.12 and 6.55 V/m. When the coil is rotated by a larger angle, the differences in effective field obviously increase, leading to larger interquartile ranges and more extreme $\Delta E_{l,\alpha}$ up to 20.61 V/m for $\alpha = -20^\circ$ and -24.08 V/m for $\alpha = +20^\circ$, respectively. More than 90% of all data points have a $\Delta E_{l,\alpha}$ between -2.63 and 3.01 V/m for rotating the coil 10 degrees and the correlation coefficient amounts 0.9721. Rotating the coil 20 degrees reduces the latter to 0.8935.

Secondly, we tilted the TMS coil about the maximal induced current direction (vector **m** in Section 2.3.1) by an angle β, changing from -10 to +10 degrees, in steps of 5 degrees. When increasing the tilt angle even more, the coil crosses the modelled head surface, which is not relevant to simulate. The effect of this tilt angle on the effective electric field $\Delta E_{l,\beta}$, defined as $E_{l,\beta}$ minus standard E_l with $\beta = 0^\circ$, is presented in box plots in Fig. 7.14. A negative angle results in a moderate median decrease of 0.39 V/m (β=-10°) and 0.05 V/m (β=-5°), while a positive angle results on average in an increase of 0.29 V/m (β=+5°) and 1.00 V/m (β=+10°). Again, larger interquartile ranges and lower correlation coefficients (0.8956 versus 0.9795) are observed for larger tilt angles and more extreme differences up to 14.66 V/m and -38.59 V/m. More than 90% of the data points have a $\Delta E_{l,\beta}$ between -4.99 and 5.73 V/m for tilting the coil 10 degrees. Consequently, tilting causes almost twice greater changes in the effective electric field than coil rotation for this case study.

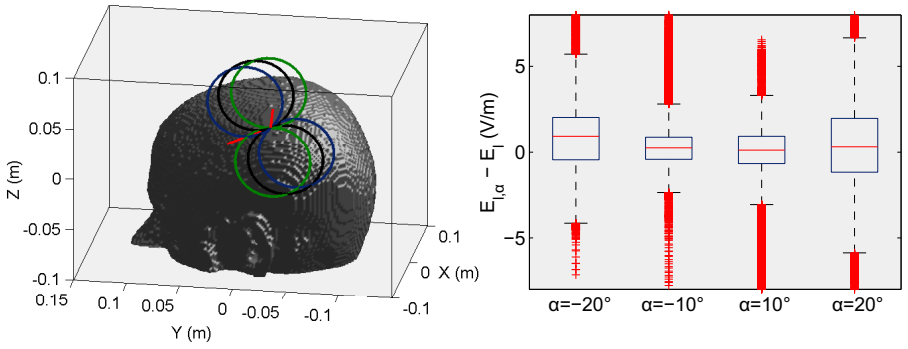

Figure 7.13: Effect of changing the coil rotation angle α. (Left) The red line illustrates the coil normal vector. Rotating the coil by a positive angle $\alpha = 20^\circ$ about this vector is shown in blue and by a negative angle $\alpha = -20^\circ$ in green. (Right) Box plots of all 54 tracts of the error $E_{l,\alpha} - E_l$ due to the different rotations.

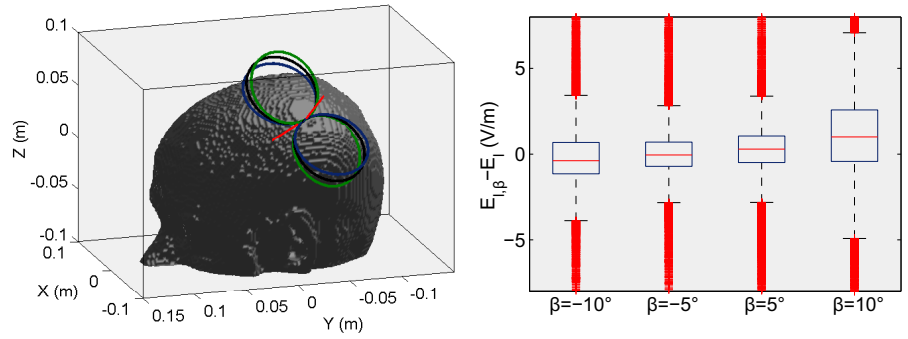

Figure 7.14: Effect of changing the coil tilt angle β. (Left) The red line illustrates the maximal induced current direction of the coil. Tilting the coil by a positive angle $\beta = 10^\circ$ about this vector is shown in blue and by a negative angle $\beta = -10^\circ$ in green. (Right) Box plots of all 54 tracts of the error $E_{l,\beta} - E_l$ due to tilting.

7.3. Discussion and assumptions

In Part I, a flexible solver has been developed for calculating the electromagnetic phenomena of TMS. Patient-specific results are preserved, since the head models include realistic geometry and tissue anisotropy based on the patient's MRI. In this chapter, the macroscopic induced electric field distribution is computed in the whole brain and its component parallel to the neurons' local orientation, the so-called effective electric field, is studied. Most models use 2D or simplified representations of the neural fibres with assumed geometries, whereas we embedded realistic 3D neural trajectories near the targeted region of interest reconstructed by DTI-based tractography. Moreover,

we investigated the stimulation mechanisms associated to terminations, sharp bends and GM-WM interface crossing of the fibre as well as the gradient of the effective electric field along the neural fibre tracts.

A large and irregular spatial spread of the effective electric field is observed. Up to 7-cm distance from the M1 ROI centre, fields of 6 V/m are induced at some points along the tracts (Fig. 7.8). Moreover, strong and localised field variations between the tracts themselves and along them are demonstrated. This is caused by the interplay of factors such as the tract's position and orientation in relation to the TMS coil, the neural trajectory and its course along the white and grey matter interface. The effective electric field term $-\lambda E_l$ proved to be the most dominant stimulation mechanism in the 5 main fibre bundles, occurring at neural terminations and bends (Fig. 7.9). The directional derivative term $-\lambda^2 \frac{\partial E_l}{\partial l}$ could compete at certain tract points, for example at the beginning points of tract 1* (Fig. 7.10), whereas the jump term $-\lambda \frac{\Delta E}{2}$ remained small ($<$ 3 mV) for all tracts.

However, the obtained findings should not be extrapolated without caution. It is not the aim of this study to draw general conclusions about which tracts or broader regions will be stimulated due to TMS and which stimulation mechanisms will cause the effect. All simulations of this chapter were performed for one specific healthy volunteer (female, 25 y), using her personal T1- and diffusion-weighted MRI, and with single pulse stimulation delivered to the left M1 hand area as case study. Nevertheless, we can make conclusions about the sensitivity of the model towards the investigated parameters.

Whereas it has been suggested that tissue anisotropy has only a modest effect on TMS modelling and consequently it can be ignored without major errors (Laakso et al., 2014; Nummenmaa et al., 2014; Opitz et al., 2011), our study indicates that these errors have the same order of magnitude as rotating the stimulation coil with 10 degrees, displayed in the box plots of Figs. 7.11 and 7.13-7.14 Therefore, we recommend the incorporation of realistic DTI-based anisotropy. The impact of including not-well known conductivity values, on the other hand, is limited, see Fig. 7.12, and hence justifies the use of the less accurate 4-Cole-Cole model for the kHz range.

Moreover, we observed that changing these different parameters affected the effective electric field and corresponding stimulation mechanisms in a non-trivial way. The interplay of their effects give rise to non-linear complex outcomes. It is therefore hard to draw general conclusions on the effects of parameters on the effective electric field. Furthermore, a strong variability can be observed. Consequently, predictions on stimulation results are difficult to make and case- and patient-specific simulations accommodating all parameters and respective effects are essential.

This study focussed on 54 selected neural fibre tracts, derived from 3D tractography reconstruction. One of the limitations is the missing interneurons,

which are assumed to be indirectly excited by TMS (Di Lazzaro and Ziemann, 2013). The effects of incorporating shorter tracts (<5 cm), applying tractography with lower FA threshold or higher bending angle threshold should be analysed, together with the impact of a higher stimulator output, in order to exceed the stimulation threshold of 52 mV (Silva et al., 2008).

All truths are easy to understand once they are discovered;
the point is to discover them.

Galileo Galilei

8

Spatio-temporal behaviour of membrane potentials

The effect of an applied electric field on a neuron, induced by TMS, corresponds in fact to a change of its transmembrane potential. Thus the next step in our computational model is the simulation of these transmembrane potentials. This chapter, extensively applies the independent impedance method for the electric field calculations and the cable equations, presented in Chapter 6, for the spatio-temporal behaviour of the membrane potentials on neural pathways, and this on various head models. Progressive steps are taken towards realistic and clinical relevant simulations, so to decrease the gap between modelling and reality in the application of TMS.

First, a preliminary study is performed on a simple rat head model represented by enclosed ellipsoids in which the neural fibres are considered as straight radially-oriented bundles. The passive cable equation, see Section 6.2.1, is applied to simulate the subthreshold response for different fibre orientations. These calculations show the potential of the developed methods to be applied for preclinical studies.

Furthermore, a realistic human head model with a single tract is considered. The neural trajectory is reconstructed with DTI-based tractography, as explained in Section 6.3. This tract is located near the left dorsolateral prefrontal

cortex, particularly targeted in the TMS treatment of medication-resistant depression (Pascual-Leone et al., 1996). Since the TMS coil is commonly positioned following an inaccurate standard procedure, we investigate its effect on the membrane potentials by looking at the number of initiated action potentials, using the active cable equation of Section 6.2.2.
Finally, the calculations are refined to a realistic head model enclosing multiple tracts nearby the targeted brain region of interest. This way, we demonstrate the flexibility of the developed methods and their applicability on various head models. The accuracy of the calculations depends on the chosen head model. In this last Section, the research from previous Chapter 7 is continued. The spatio-temporal variation of the membrane potentials is investigated for the same case study as in Section 7.2. All 54 tracts are segmented in dendrites, soma, axon hillock, initial segment and alternating Ranvier nodes and myelinated internodes, such that the complete compartmental cable equation, as explained in Section 6.2.3, can be applied. For the study in depth, we focus on a single tract. The influence of an increasing stimulator output is investigated, together with a sensitivity analysis of the not well-known neural parameter values on the stimulation threshold.
Results from this chapter have been presented at the International Conference on Biomagnetism (BIOMAG) in 2012 in France and the International IEEE EMBS Conference on Neural Engineering (NER) in 2013 in San Diego, USA (De Geeter et al., 2013a).

8.1. Preliminary study on a simple rat head model

As a preliminary study, we simulated the response to a 20mm figure-of-eight TMS coil delivered with a Rapid^2 stimulator (MagStim Inc., Whitland, United Kingdom) in a simple rat brain. The rat head is modelled as 6 concentric ellipsoids representing the tissues scalp, bone, CSF, grey matter, white matter and thalamus. The thalamus has a radius of 2 mm, the major and the two minor axes of the cortical layer are 28 mm and 14 mm long and the other layers are 2 mm and 1 mm thick near these major and minor axes respectively, similar to the rat's real dimensions (Paxinos and Watson, 2008). The neural fibres are considered as straight radially-oriented bundles located in white matter connecting the thalamus with grey matter. Each bundle is defined by two angles α and θ, as illustrated is Fig. 8.1, ranging from 0 to 180 degrees and from 0 to 360 degrees, respectively, in steps of 10 degrees.
The 20mm figure-of-eight coil is the smallest commercially available TMS coil and is positioned centrally over the rat head in the axial plane, perpendicular to the skull, see Fig. 8.1. It is modelled as two circular coils, located side-by-side, with 9 turns each and consists of copper wire with a rectangular cross section (0.80 mm $\times$ 5.50 mm). The inner and outer radii of one circular coil are

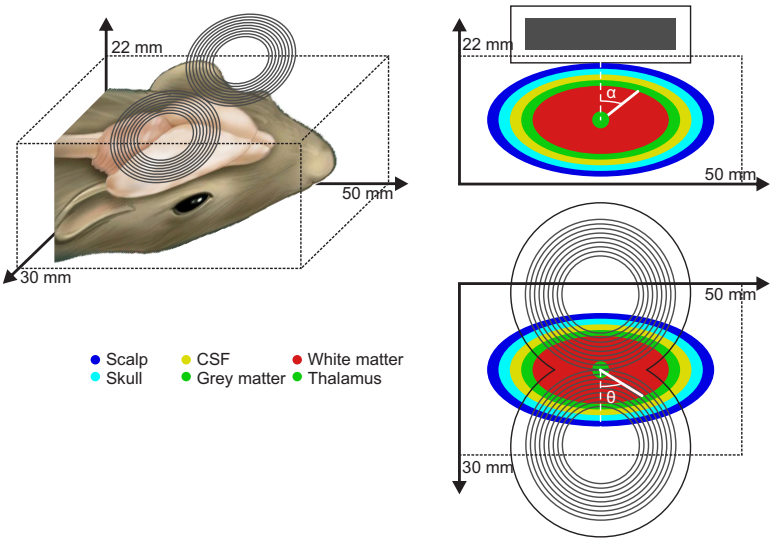

Figure 8.1: Axial and sagittal views of the modelled figure-of-eight TMS coil with coating and the rat head model.

4.35 mm and 13.15 mm respectively. We modelled the total excitation current at 50% output of the MagStim Rapid^2 stimulator (Whitland, United Kingdom) as a sine with peak amplitude of 1430 A in each wing, resulting in a current of 159 A and a current density of 36 A/mm^2 in each of the 9 turns. The applied pulse width is set to 1 ms. The isotropic material properties, corresponding to this 1 kHz frequency, are obtained from the 4-Cole-Cole model (2.31), similar to those of human tissues. The thalamus is considered to have the same properties as grey matter.

The induced electric field distribution is calculated using the isotropic independent impedance method, as explained in Chapters 3 and 5, for a field of interest of 30 mm $\times$ 50 mm $\times$ 22 mm with a resolution of 0.4 mm. Fig. 8.2 visualises this field and its component parallel to the neurons' local orientation, the so-called effective electric field, in the white matter.

This electric field affects the membrane potential of a neural fibre as described by the passive cable equation, see Section 6.2.1. Studies have shown that straight fibres are primarily activated by the gradient of the effective electric field along the neural fibres (Rattay, 1986), which is plotted in Fig. 8.3. Remark that this term needs to be multiplied with $-\lambda^2$ to obtain the first stimulation mechanism (7.1).

We simulated the variation of the membrane potentials along the fibre bundles due to a single biphasic TMS pulse according to the passive cable equation

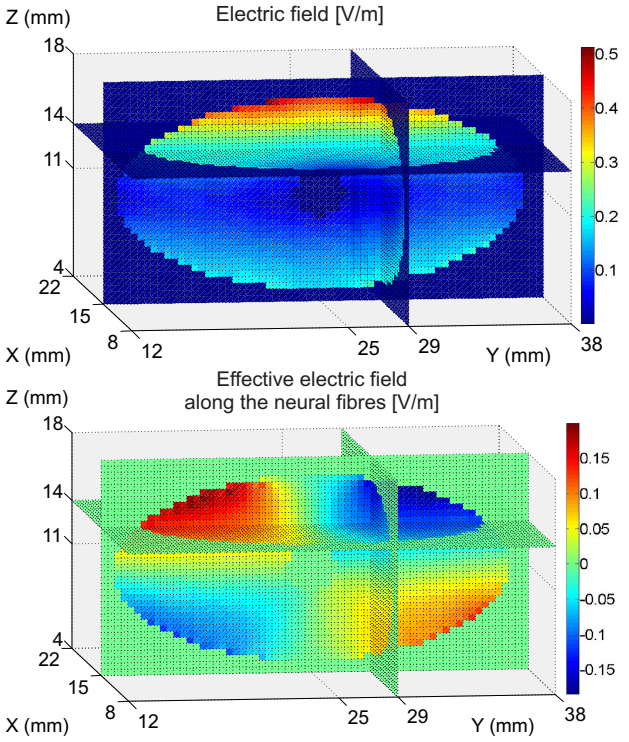

Figure 8.2: (Above) Induced electric field magnitude (in V/m) and (below) effective electric field (in V/m) in the rat head model. Voxels that do not belong to the white matter have been masked.

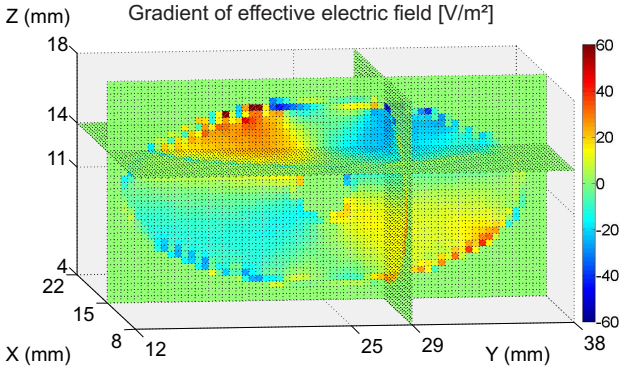

Figure 8.3: Directional derivative of the effective electric field along the neural fibres (in V/m^2). Voxels that do not belong to the white matter have been masked.

(6.1), which is repeated here for clarity reasons:

$$\lambda^2 \frac{\partial^2 V}{\partial l^2} - (V - V_\mathrm{r}) = \tau \frac{\partial V}{\partial t} + \lambda^2 \frac{\partial E_l}{\partial l}. \tag{8.1}$$

This equation is discretised using the Crank-Nicolson method, with Δt = 1 ms and Δl = 45 μm. The following parameter values were obtained from literature: the membrane capacitance per unit area C_m = 0.009 F/m^2 (Gentet et al., 2000), the membrane resistance R_m = 23 Ωm^2 and the axial resistivity R_a = 0.354 Ωm (Rosenthal and Bezanilla, 2000). When considering fibre bundles with a diameter d of 0.4 mm, the space and time constants become, based on equations (6.2-6.3) and (6.25-6.27) with $R_\mathrm{m} = 1/G_\mathrm{m}$:

$$\lambda = \sqrt{\frac{dR_\mathrm{m}}{4R_\mathrm{a}}} \tag{8.2}$$

$$\tau = R_\mathrm{m} C_\mathrm{m}, \tag{8.3}$$

equal to 0.0806 m and 0.207 s, respectively.

The resulting change of the membrane potential $\Delta V = V - V_\mathrm{r}$ for the neural fibre bundle, defined by the angles $\alpha = 40^\circ$ and $\theta = 90^\circ$, is plotted in red in Fig. 8.4 as a function of time. We can confirm the successive depolarisation, hyperpolarisation and once more depolarisation due to the induced (effective) electric field that is first highly positive, decreases to negative values and then turns positive again, as in Fig. 1.9. However, these potential changes remain limited and last as long as the period of stimulation, namely 1 ms. This subthreshold stimulation justifies the use of the passive cable theory, since no action potentials are generated.

When we take a neural fibre bundle in the opposite direction, namely $\alpha = 40^\circ$ and $\theta = 270^\circ$, the membrane potential changes reversely in time, see the blue curve in Fig. 8.4. This is due to the reversed sign of the effective electric field. We would observe a similar effect when rotating the coil 180 degrees, i.e. from posterior-to-anterior (PA) to anterior-to-posterior (AP), while considering the same fibre bundle as before.

Fig. 8.5 depicts the maximal membrane potential changes ΔV for different angle regions, which seem to be highly dependent on the fibre orientation. The highest values occur for $\alpha = 40 - 50^\circ$ and $\theta = 90^\circ$ and 270°, whereas the lowest values occur for $\alpha = 0 - 10^\circ$, $80 - 90^\circ$ and $170 - 180^\circ$ and $\theta = 0 - 20^\circ$, $160 - 200^\circ$ and $340 - 360^\circ$.

This study shows that neural fibres oriented perpendicular to the plane of the coil ($\alpha \approx k\pi$, $\forall\theta$), i.e. parallel to vector $\mathbf{n}$ of Section 2.3.1, are less accessible for stimulation. The effective electric field is limited in these fibres when compared to the amplitude of the electric field. On the other hand, we observed that for optimal stimulation the neural fibres should be oriented in the direc-

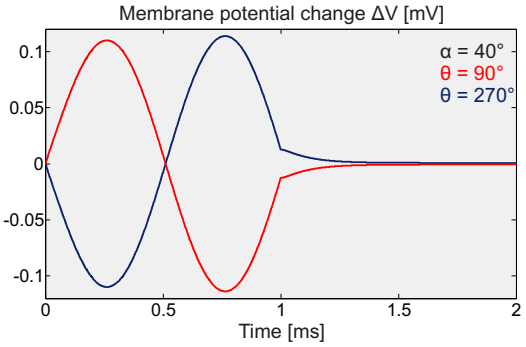

Figure 8.4: Temporal variation of the membrane potentials relative to the resting value (in mV) along the neural fibres, defined by the angles $\alpha = 40^\circ$ and $\theta = 90^\circ$ (in red) and 270° (in blue).

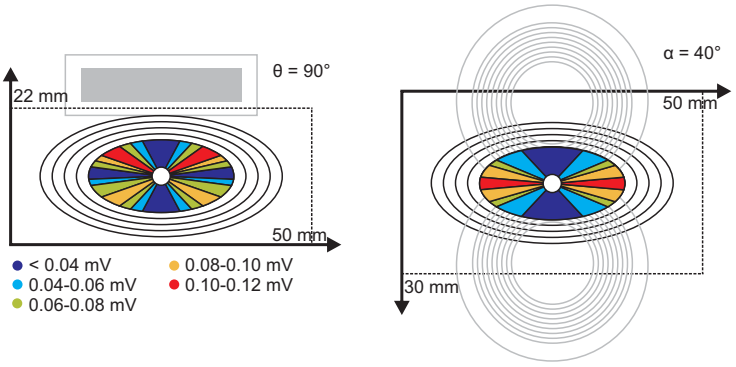

Figure 8.5: Maximal changes of the membrane potential relative to its resting value (in mV) for different angle ranges. The same axial and sagittal views as in Fig. 8.1 are plotted.

tion of the maximal induced currents ($\theta \approx \pi/2 + k\pi$), i.e. parallel to vector $\mathbf{m}$ of Section 2.3.1, and at an angle of 45 degrees relative to the normal vector $\mathbf{n}$ ($\alpha \approx \pi/4 + k\pi/2$). This is in correspondence with the fact that an externally applied electric field preferentially stimulates neural fibres which align parallel to it (Rushton, 1927).

However, this study is preliminary, since the TMS response is simulated on a simple ellipsoidal rat head model with straight radially-oriented neural fibres and isotropic tissue parameters. This simplicity leads to the loss of some valuable features, such as realistic brain geometry, cerebral tissue heterogeneity and neuronal structures. They have a significant effect on the spatial distributions of the induced electric field and its gradient along the fibre tracts, as shown in Fig. 7.8. The figure-of-eight coil was positioned centrally over the head model, whereas in most practical clinical applications, a certain degree of symmetry break is required (Roth et al., 2013). A symmetric stimula-

tion of the cortex is usually undesired, but instead a complex distribution that more likely reaches deeper regions. The coil position and orientation shapes strongly the distribution of the induced electric field, certainly in head models with realistic brain geometry and electrical properties. Only one of the three stimulation mechanisms, see Section 7.1, was taken into account. Moreover, the space constant λ ($\approx 8cm$) was taken in correspondence to the squid giant axon (Rosenthal and Bezanilla, 2000), but should be lowered. Indeed, values in the mm-order would be more suitable for mammals. We will include the above-mentioned features in the following sections.

8.2. Effect of inaccurate targeting of the left DLPFC

Repetitive TMS to the left dorsolateral prefrontal cortex (DLPFC) is clinically used for the non-invasive treatment of medication-resistant depression (George et al., 1995; O'Reardon et al., 2007; Padberg and George, 2009; Pascual-Leone et al., 1996). However, the pathophysiology of depression involves a wider cortical-subcortical network. The subgenual anterior cingulate cortex (sACC), corresponding to Brodmann area 25, shown in Fig. 1.14, and central to this limbic network, plays a role in the experience of negative mood states. It is successively targeted during chronic deep brain stimulation in depressed patients (Mayberg et al., 2005) by which electrodes are implanted in this region. Since TMS generates maximum electromagnetic fields in the cortical surface with a limited penetration into subcortical structures, its direct effect is restricted to more superficial targets. Therefore, the DLPFC, which corresponds roughly to Brodmann area 9 and 46 and has interconnections to the sACC (Carmichael and Price, 1995), was selected (George et al., 1995).
To target the left DLPFC, the TMS coil is commonly positioned following a standard procedure (George et al., 1995; Pascual-Leone et al., 1996), illustrated in Fig. 8.6, which is derived from the Talairach atlas (Talairach and Tournoux, 1988). First, the hand motor hotspot is identified by evoking a response of a hand muscle, usually the abductor pollicis brevis muscle. The coil is then moved 5 cm rostrally (i.e. towards the front) in a parasagittal plane, see Fig. 8.6. However, several studies have tested the reliability of this procedure and showed it was not precisely targeting the desired cortical region (Ahdab et al., 2010; Fitzgerald et al., 2009; Herwig et al., 2001; Nauczyciel et al., 2011; Peleman et al., 2010). Herwig et al. (2001) found that by applying this approach, approximately two-thirds of his subjects received stimulation over the premotor instead of the prefrontal cortex. The centre of the coil was thus located too dorsally (i.e. towards the back). These findings were worsened by more recent results (Nauczyciel et al., 2011) where the 5-cm distance was on average 17 mm too short. In contrast, another study found that the standard procedure resulted in targets 15 mm more rostral than the reference DLPFC (Peleman et al.,

2010). Nevertheless, they all demonstrate the large interindividual variability of brain size and morphology (Bartley et al., 1997; Rajkowska and Goldman-Rakic, 1995) and agree on the fact that the distance should be calculated or the target should be localised on the basis of patient-specific neuroanatomical data.

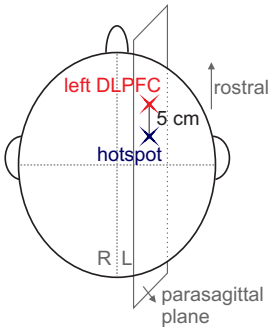

Figure 8.6: Standard procedure for targeting the left DLPFC. A parasagittal plane is a sagittal plane that divides the body into unequal right and left regions, see also Fig. 1.11.

To our knowledge, up to now only clinical trials have reported the effect of the inaccurate standard procedure, while simulations can provide added value by predicting the sensitivity of the TMS response to coil shifts. Therefore, in this Section we examine the electromagnetic and neurophysiologic changes due to parasagittal displacements of the stimulation coil with respect to the reference position. First, the induced electric field distribution in a realistic patient-specific head model is computed from which the activation function (Rattay, 1986) is calculated. Then one main neural bundle that is connected with the targeted left DLPFC is traced using tractography (Leemans et al., 2009). Finally, the spatial distribution of the membrane potentials along this bundle and its temporal dynamics are computed. Depending on the coil position, a number of action potentials are initiated in the cortical tissue and propagate along the fibre bundle towards deeper subcortical limbic regions.
We modulate the rTMS response in the prefrontal cortex of a human brain. The used head model includes realistic geometry, since it is constructed from a T1-weighted magnetic resonance image (MRI), and is segmented into the tissues scalp, skull, cerebrospinal fluid, grey matter and white matter. The frequency-dependent anisotropic tissue properties, i.e. conductivity σ and permittivity ε, are obtained from the 4-Cole-Cole model (Gabriel et al., 1996c). Their directional dependence is computed based on diffusion-tensor MRI of the same healthy subject. Also based on this DTI data set, the realistic oriented pathways of neural fibres are tracked located in the stimulated target by applying

MR tractography. As explained before in Section 6.3, the graphical toolbox ExploreDTI (Leemans et al., 2009) is used. Since the left DLPFC is targeted, this defines the first region of interest (George et al., 1995) and the sACC, part of the deeper limbic area, the second one ROI. The traced fibres are considered as one myelinated neural bundle, visualised in Fig. 8.7.

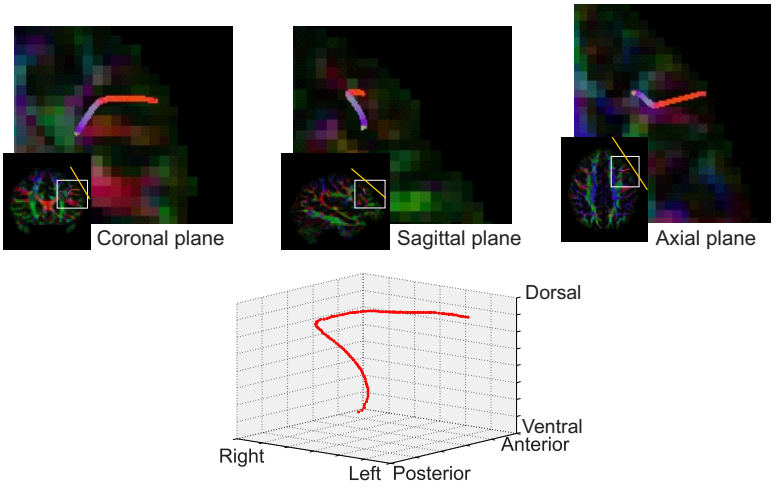

Figure 8.7: Orientation of the considered neural fibre bundle. The DTI colours indicate the dominant diffusion direction: red (right to left), green (posterior to anterior) and blue (ventral to dorsal). The yellow line shows the intersection of the figure-of-eight coil with the plane in question, and the white boxes the area which is zoomed in.

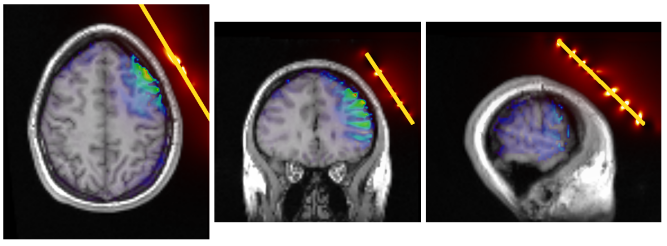

Figure 8.8: TMS to the left DLPFC. Axial, coronal and sagittal view of the T1-weighted MRI with the induced electric field distribution (in V/m). The colour limit of the electric field is set to the maximum value of 400 V/m. The yellow line shows the intersection of the figure-of-eight coil with the plane in question, similar as in Fig. 8.7.

As in clinical practice, a 70mm figure-of-eight TMS coil (MagStim Inc., Whitland, United Kingdom) (Salinas et al., 2007) is positioned above the left DLPFC, perpendicular to the skull, as can be seen in Fig. 8.8. For the purpose of this study, the coil is then shifted more towards the front or more towards

the back. To investigate the sensitivity of the results to these displacements, we simulated the effect of small shifts, namely 2-, 4-, 8- and 16-mm distances in both directions. We modelled the electromagnetic and neurophysiologic response of a multiphasic pulse stimulation, with a sinusoidal waveform and a pulse width of 250 μs, resulting in a frequency of 4.0 kHz, so as to mimic the MagStim Rapid^2 stimulator (Whitland, United Kingdom).

The induced eddy currents and electric field distributions are calculated using the anisotropic independent impedance method, presented in Chapter 3. The effective electric field along the neural fibres affects the membrane potentials and can cause a generation and propagation of action potentials. To describe this neurodynamic behaviour along the bundle we use the active Hodgkin-Huxley based model (6.33-6.34). These equations are repeated here, but for more details we refer to Section 6.2.2.

$$\begin{aligned} C_{\mathrm{m}}^{*}\frac{\partial V(l)}{\partial t}+I_{\mathrm{ion}}(l) \;=\; & G_{\mathrm{a}}^{*}\left(V(l-\Delta l)-2V(l)+V(l+\Delta l)\right) \\ & +G_{\mathrm{a}}^{*}\Delta l E_{l}(l-\Delta l)-G_{\mathrm{a}}^{*}\Delta l E_{l}(l) \end{aligned} \tag{8.4}$$

with the ionic current being the sum of sodium, potassium and leakage currents for the active components:

$$I_{\mathrm{ion}}(l)=\pi d\Delta l\left(G_{\mathrm{Na}}m^{3}h(V(l)-V_{\mathrm{Na}})+G_{\mathrm{K}}n^{4}(V(l)-V_{\mathrm{K}})+G_{\mathrm{L}}(V(l)-V_{\mathrm{L}})\right). \tag{8.5}$$

This equation is discretised using the Crank-Nicolson method, with Δt = 1 μs and Δl = 0.2 mm. The parameter values are obtained from the human fibre model of Wesselink et al. (1999), listed in Table 6.1. Active responses are taken into account by modelling the voltage-gated ion channels on the membrane at Ranvier nodes, see also the electrical network shown in Fig. 6.8. Remark that these nodes were the only neural segments implemented for these simulations and therefore, the interaction between these active components and the passive myelinated internodes was neglected, as well as the dendrite, soma, axon hillock and initial segment.

We investigate the electromagnetic and neurophysiologic differences between TMS to the reference DLPFC (case B) on the one hand and when the coil is shifted 8 mm more dorsally (Herwig et al., 2001; Nauczyciel et al., 2011) (case A) or rostrally (Peleman et al., 2010) (case C) on the other hand. Fig. 8.9 illustrates how the effective electric field along the neural fibre bundle changes as a function of the distance along this bundle. In all cases an action potential is initiated. The gradient of the electric field, which defines the activation function (Rattay, 1986), is the highest at 11.8 mm, namely where the tract bends. Neural bends are indeed crucial points for activation in accordance with literature (Maccabee et al., 1993). The amplitude of the electric field along the

bundle is the highest in Fig. 8.9A and the smallest in Fig. 8.9C. A spike can only be generated in case of a sufficient gradient of this electric field.

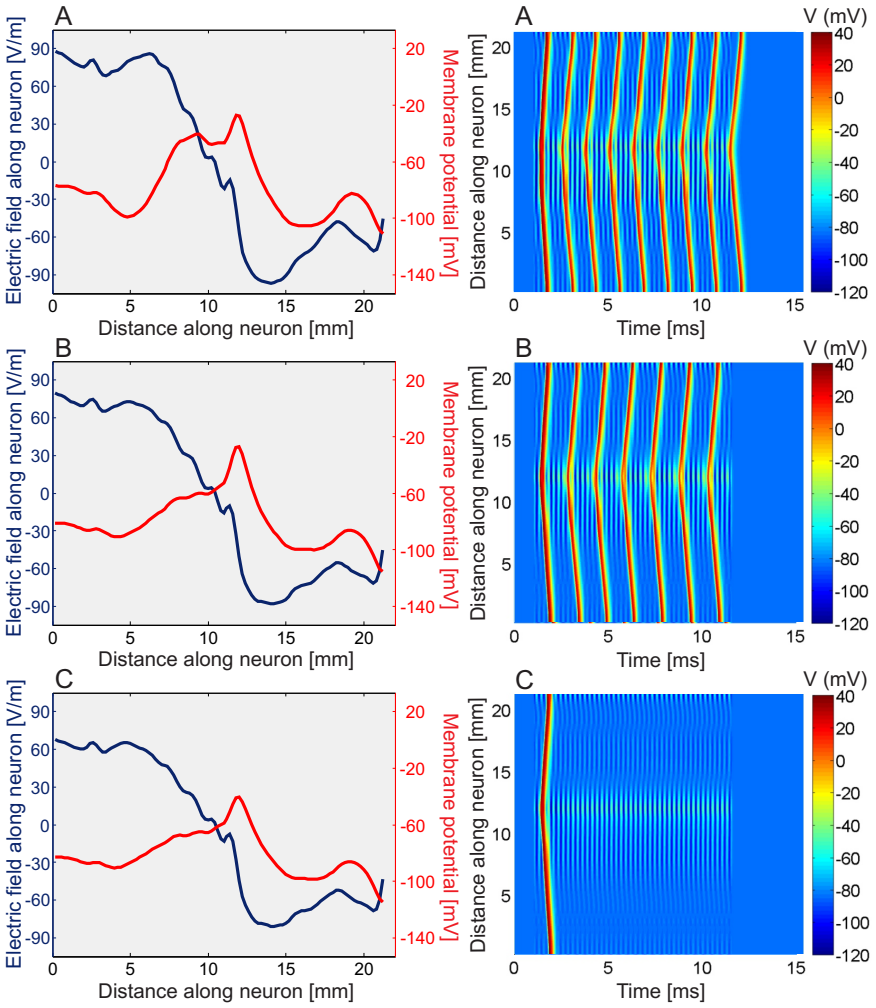

Figure 8.9: (Left) The electric fields along the tract and corresponding membrane potentials at the time of 1.290 ms, when the first action potential is initiated. This is thus 290 μs after the start of the multiphasic stimulation at time 1 ms. The neural bundle is oriented from the superficial cortex towards a more deeper subcortical region. (Right) Spatio-temporal distributions of the membrane potentials. (A) The coil is shifted 8 mm more dorsal, (B) reference position, (C) the coil is shifted 8 mm more rostral.

Also the simulated spatio-temporal distributions of the membrane potentials are depicted in Fig. 8.9. Initially, the membrane is in rest at -84 mV. After 1 ms a multiphasic pulse stimulation is applied that continues 10.45 ms. During this

period, 7 action potentials are initiated and are propagating in both directions of the tract, as simulated in case B. However, for a coil displacement of 8 mm more dorsal, case A, the simulations resulted in the generation of 9 spikes. For the 8-mm shift more rostral, Fig. 8.9C shows the generation of only one spike. Even though the electric field was moderately changed.
To investigate whether these findings can be generalised, i.e. increased (decreased) generation of action potentials in case of targeting more dorsal (rostral) stimulation regions, we simulated the effect of more shifts, namely 2, 4 and 16 mm in both directions. Fig. 8.10 depicts the number of generated action potentials, decreasing indeed from 11 to zero spikes with increasing coil displacements in the rostral direction.

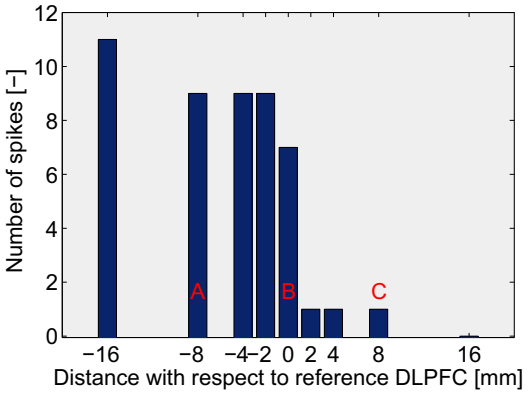

Figure 8.10: Impact of the coil displacement on the number of generated action potentials. Positive displacements are in the rostral direction (i.e. more towards the front of the head).

Remark that the applied simulations are based on the assumption that TMS effects originate from direct pyramidal axon stimulation. Moreover, the used neural model is a simplification, since it does only take nodes of Ranvier into consideration and not the heterogeneity of neural bundles, and it is limited to one bundle in a realistic volume conductor. In addition, the effect of only the first stimulation mechanism (7.1) is counted for. Generalisation of the obtained results is therefore difficult.

8.3. Simulations on a realistic head model and neural trajectories

Finally, we simulate the TMS response on the left M1 hand area of the same realistic head model as in Section 7.2. Whereas that section focused on the induced effective electric field and the three different stimulation mechanisms, we will now investigate their effects on the membrane potentials in time and space. The previous Sections 8.1 and 8.2 only modelled the passive and active

responses, respectively. We will now use the complete compartmental cable equation as explained in Section 6.2.4 including dendrites, soma, axon hillock, initial segment and alternating Ranvier nodes and myelinated internodes. Since there is a great difference between the lengths of the various segments, we implemented a variable space step, such that all segments are divided in 10 steps. For example, the length of one Ranvier node is approximately 1000 times smaller than that of one myelinated internode, see Table 6.1. Such a node of Ranvier will be discretised with a very fine space step Δl of 0.15 μm, while myelinated internodes have a spatial grid of about 100 μm, depending on the exact length of the neural tract. This way, memory problems are avoided. The time step Δt is 1 μs.

Table 8.1: Space step, space constant and time constant of the different neural segments, based on human sensory fibre data (Salvador, 2009; Wesselink et al., 1999).

Segment	Δl	λ	τ
Dendrite (Passive)	100 μm	1.49 mm	10.26 ms
Soma (Passive)	10 μm	[1.49 - 4.08] mm	10.26 ms
Axon hillock (Active)	1 μm	[123 - 87] μm	46.54 μs
Initial segment (Active)	2 μm	87 μm	46.54 μs
Myelinated internode (Passive)	$\pm$ 100 μm [f4]	8.70 mm	0.5 ms
Ranvier node (Active)	0.15 μm	87 μm	46.54 μs

Individual neurons, and even different patches of the membrane within a given neuron, can have different space constants because it depends upon the membrane resistance and the axial resistance (6.2). When the membrane resistance is low, and thus the conductance is high, ions (that cause the potential change) can leak through the membrane via open channels, resulting in a shorter space constant. When a neuron has a large diameter, the ions can flow easily along the axon and the axial resistance will be low, leading to a longer space constant. This explains the different λ values between active and passive segments and its range for those segments with variable diameter. The applied λ and τ values are calculated using equation (8.2). The conductance $(G_{\mathrm{Na}}m^3h + G_{\mathrm{K}}n^4 + G_{\mathrm{L}})$ of the active components is computed based on the initial values of the gates (6.48-6.50). As these gating variables change in time depending on the voltage, the conductance and consequently the space constant will also change. According to Rattay (1999), the compartment length should be smaller than $\lambda/4$ to obtain an error of the order of 1% compared to the solution of the continuous cable equation. Our values easily meet this requirement.

[4] depending on the length of the neural tract

The same 54 neural trajectories are considered as in Fig. 7.3. Trilinear interpolation is used to convert the fibre tracts from the 1-mm spatial grid to the more fine and variable mesh. We first focus on one tract, more specifically tract 5 of Fig. 7.3, which is an association fibre, plotted individually in Fig. 8.11 together with its corresponding segments.

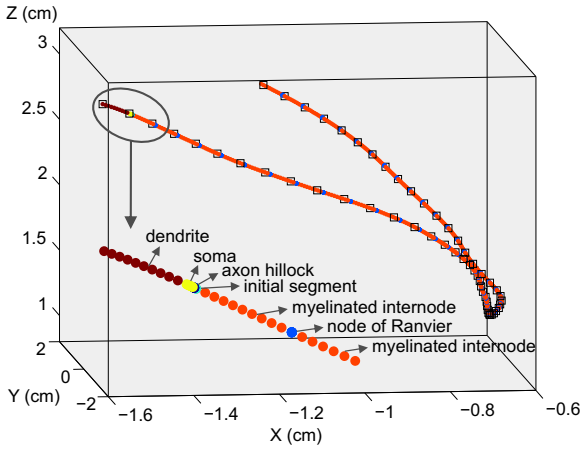

Figure 8.11: Orientation of tract 5 with its corresponding segments. The black squares indicate the original tract coordinates with 1-mm coarse step. Close-up from the first 65 tract points with variable fine step and their corresponding type of segment.

The membrane potential is assumed to be initially at rest, at its resting value V_r equal to -84 mV. After 20 μs, a single biphasic pulse with a pulse width of 230 μs is applied with a 70-mm figure-of-eight Nexstim coil (Nexstim Ltd., Helsinki, Finland). First, the peak excitation current time derivative is set to 21.87 A/μs, analogous to the TMS pulse simulated in Section 7.2. Back then, we hypothesised that this stimulator output is too small to generate action potentials. Therefore, it will be increased gradually. The resulting spatio-temporal distributions of the membrane potential are shown in Fig. 8.12. To facilitate the interpretation of these images, the horizontal white lines of Fig. 8.12A and B are depicted in Fig. 8.13 as a function of time and the vertical white lines of Fig. 8.12C are plotted in Fig. 8.14 as a function of space.
Case A of Fig. 8.13 confirms that a stimulator output of 21.87 A/μs, used in Section 7.2, is not high enough for the initiation of action potentials in the investigated tract 5. Only moderate changes of the membrane potential are observed for the duration of the stimulus. Fig. 8.13A focusses on the tract point at l=6.1 mm, indicated with a white horizontal line in Fig. 8.12A. It shows that the induced effective electric field yields a maximum value of 14.3 V/m. First a hyperpolarisation from -84 mV to -92.3 mV occurs, than a depolarisation to -73.1 mV, followed by a hyperpolarisation to -87.9 mV. This sequence is the result of the alternating sign of the effective electric field and the fact that $-\lambda E_l$

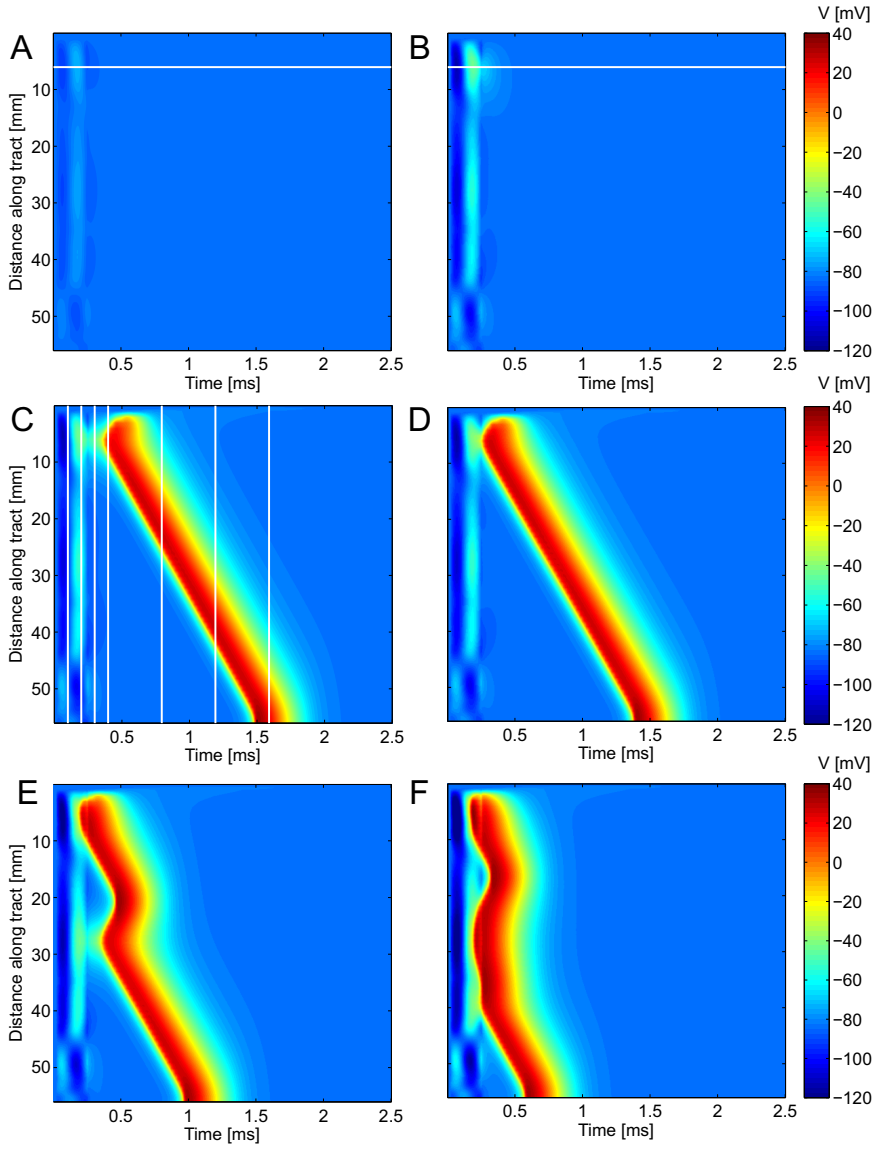

Figure 8.12: Variation of the membrane potential V (in mV) in time and distance along the neural tract for increasing stimulation intensity. (A) 21.87 A/μs, (B) 74.36 A/μs, (C) 75.90 A/μs, (D) 78.74 A/μs, (E) 96.24 A/μs and (F) 131.24 A/μs. To facilitate interpretation, the horizontal white lines of A and B are depicted in Fig. 8.13 as a function of time and the vertical white lines of C are plotted in Fig. 8.14 as a function of space.

is the dominant stimulation mechanism, see again Section 7.2. After the TMS pulse, at 250 μs, the membrane potential restores to its resting state.

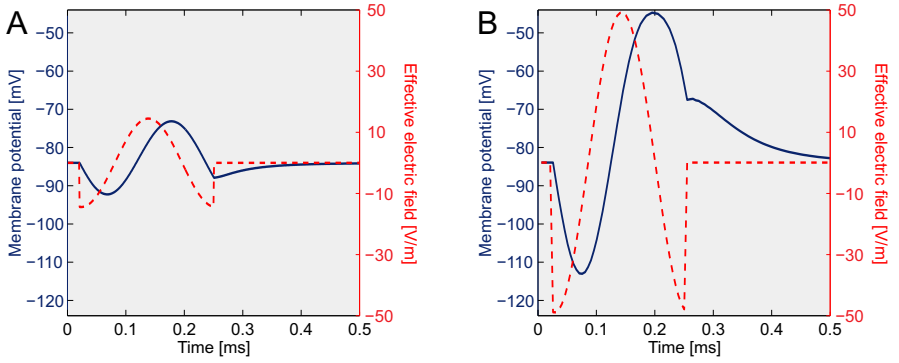

Figure 8.13: The effective electric fields and corresponding membrane potentials at point l=6.1 mm of tract 5, where the highest potentials are observed. The same information as the white horizontal lines of Fig. 8.12A and B is plotted as a function of time. These results are in agreement with the theoretical waveforms of Fig. 1.9, since $-\lambda E_1$ is the dominant stimulation mechanism.

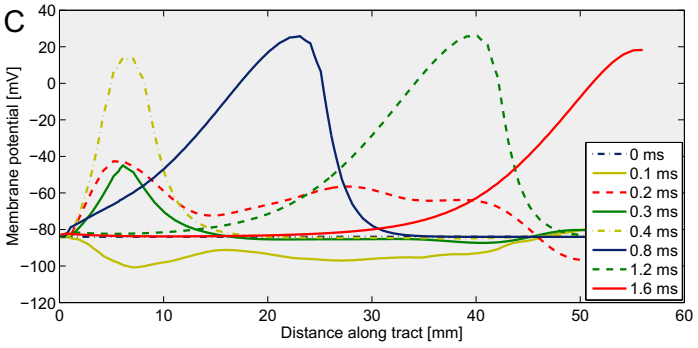

Figure 8.14: Membrane potential variation along the neural trajectory, for 7 different time points. The same information as the white vertical lines of Fig. 8.12C is plotted as a function of space.

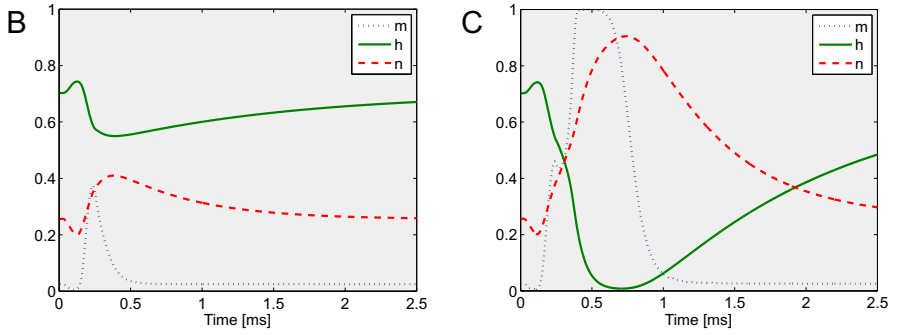

Figure 8.15: Variation of the dimensionless gating variables m, h and n at tract point l=6.1 mm for cases B and C of Fig. 8.12.

When increasing the stimulator output to 74.36 A/μs (case B), a similar wave pattern is produced, see Figs. 8.12B and 8.13B. The effective electric field rises to 48.4 V/m, resulting in a maximal membrane potential of -44.73 mV. After the TMS pulse, a higher and longer transient response is observed than for case A. Still, no action potential is generated. Fig. 8.15B displays the corresponding m, h and n values of the fictional gates as a function of time. The open probability of the activation gate for the sodium channel m starts increasing from 0.1 ms till 0.24 ms, whereas the sodium inactivation variable h decreases and the potassium activation variable n increases till 0.385 ms. It takes approximately 2.5 ms before they are all returned to their resting values. A stimulator output of 75.90 A/μs is required so that the depolarised membrane exceeds the threshold (case C). This stimulation threshold is comparable with the obtained values of Salvador et al. (2011). Fig. 8.12C shows that an action potential originates at position l=6.1 mm (at a node of Ranvier) and time t=0.38 ms and processes along the neural fibre till it reaches the end of the axon at l=56.1 mm and t=1.48 ms. The velocity of the signal can thus be approximated at 45 m/s. Remark that this action potential is initiated after the stimulation pulse, that ends at t=0.25 ms. Its progress is demonstrated in Fig. 8.14, which presents the white vertical lines of Fig. 8.12C and thus the membrane potential as a function of the distance along the tract, at different time points. During the stimulus, the membrane potential varies according to the expected pattern, i.e. mainly hyperpolarisation for negative effective electric fields and vice versa. At time 0.3 ms, this effect has faded out, except in the vicinity of l=6.1 mm where the membrane potential remains about -45 mV, see the green solid line. 100 μs later, this depolarisation has become even stronger, and values up to 20 mV are achieved. Once such an action potential arises, it is conducted unattenuated down the axon. Fig. 8.15C illustrates how open probability of the activation gate m increases to nearly 1 (0.9993) shortly after the stimulation pulse, opening the sodium channels such that Na^+ ions flow into the cell and raise the membrane potential further providing positive feedback. Then, the open probability of the inactivation gate h starts to decrease to nearly 0 (0.0081), turning off the Na^+ flow. This decreased flow is also due to a reduced driving force $(V - V_{\mathrm{Na}})$. Finally, the open probability of the activation gate n of the potassium channel increases slowly and K^+ ions flow out of the cell. This causes the membrane potential to return gradually to its resting value. It takes longer than 2.5 ms for the gating variables to return to their resting values.

When we increase the stimulator output from 75.90 A/μs to, for example, 78.74 A/μs, a similar response is observed, except that the action potential initiation occurs slightly faster, see case D of Fig. 8.12. Once initiated, it propagates at the same velocity. With further increase to 96.24 A/μs (case E), there arises a second action potential at l=27.5 mm. This signal is conducted in both

directions of the neural fibre and collides with the other one at l=20.5 mm. Because action potentials are followed by a refractory period, the membrane is extensively hyperpolarised and remains so until the ionic concentrations rebalance. As a consequence, two propagating action potentials that collide, annihilate. The main result of this increased stimulator output is faster communication. Due to the generation of multiple action potentials along the neural fibre, the electric signal reaches faster the end of the axon, ready for synaptic interaction with other neurons of the brain network. This is also demonstrated by the last case F of Fig. 8.12, in which the stimulator output is set to 131.24 A/μs. The action potential reaches the end of the axon at time t=0.58 ms.

To illustrate the influence of repeating single pulses shortly ($\leq$ 1 s) after each other, we simulated the effect of 4 stimulation pulses delivered at 1000 Hz. After 20 μs, the first biphasic pulse with a pulse width of 230 μs is applied over the left M1 hand area with a 70-mm figure-of-eight Nexstim coil (Nexstim Ltd., Helsinki, Finland), analogously as before. This biphasic pulse is repeated at the time points 1020, 2020 and 3020 μs. We still consider tract 5. Figs. 8.16 and 8.17 depict the obtained spatio-temporal variation of the membrane potential and corresponding values of the open probabilities of the activation and inactivation gates. For case A, the stimulation intensity is 78.74 A/μs. It has been shown in Fig. 8.12 that this intensity is sufficiently high in order to obtain an action potential. The first stimulation pulse triggers indeed an action potential, unlike the subsequent pulses. This is due to the recovery phenomena, which can be seen in Fig. 8.17A. The sodium channels are not recovered enough from inactivation and the membrane of tract 5 is in its refractory period. When increasing the stimulation intensity to 87.49 A/μs, case B, the third stimulation pulse triggers an action potential as well. Although the m, h and n values have not yet been returned to their resting values, an increased stimulus appears thus to trigger additional action potentials, indicating a relative instead of an absolute refractory period.
However, synapse is not included in the neurophysiological model, which makes it hard to accurately simulate the effects and certainly the long-term effects of rTMS.

The values of several parameters are not well known or may have a large inter- and/or intra-subject variability. In order to evaluate their influence on the predicted stimulation threshold, we perform a sensitivity analysis. This threshold is defined as the minimal peak excitation current time derivative needed to initiate an action potential at tract 5. The geometrical and electrical parameters are varied according to the values found in literature (Gentet et al., 2000; Manola et al., 2007; McIntyre et al., 2002; Rattay, 1999; Wesselink et al., 1999). The difference between the stimulation threshold, obtained with these extreme values, and the original threshold of 75.90 A/μs, corresponding with the parameter values of Table 6.1, are listed in terms of percentage in Table 8.2.

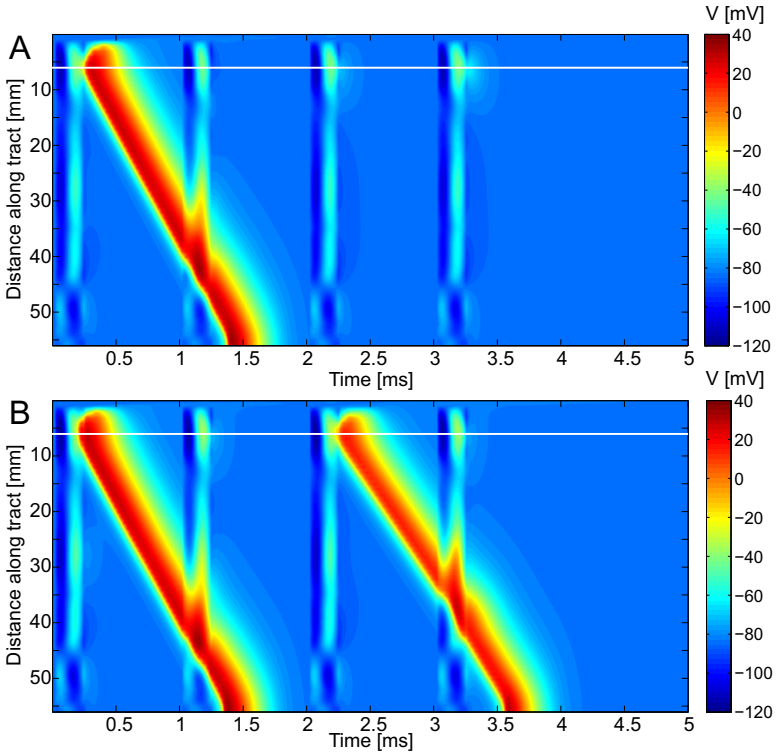

Figure 8.16: Variation of the membrane potential V (in mV) in time and distance along the neural tract for the stimulation intensities (A) 78.74 A/μs and (B) 87.49 A/μs. A total duration of 5 ms is investigated during which 4 stimulation pulses, with a pulse width of 230 μs, are delivered at 1000 Hz. The corresponding m, h and n values at the horizontal white lines are depicted in Fig. 8.17 as a function of time.

For example, Gentet et al. (2000) estimated the membrane capacitance per unit area C_m for all segments, except the myelinated internodes, of cortical pyramidal neurons to be 0.009 F/m^2, which decreases the stimulation threshold with 18.2% in comparison to the original used C_m of 0.028 F/m^2. The results of this Table 8.2 demonstrate that the stimulation threshold is highly sensitive to the intracellular resistivity R_a, with changes up to 75%, whereas it is less sensitive to changes in the lengths and diameters of the different segments. Also the initial state of the membrane potential is crucial. Assuming a lower V_0 of -120 mV, increases the threshold with 33.1% in comparison to the original -84 mV. When assuming an initial membrane potential of 40 mV, we were not able to generate an action potential, no matter how strong the stimulus is, due to the refractory period. The neuron cannot be activated again for some time since the inactivation variable h has not recovered yet. Unlike the other parameters, one extreme value does not correspond to a decrease, and the other with an

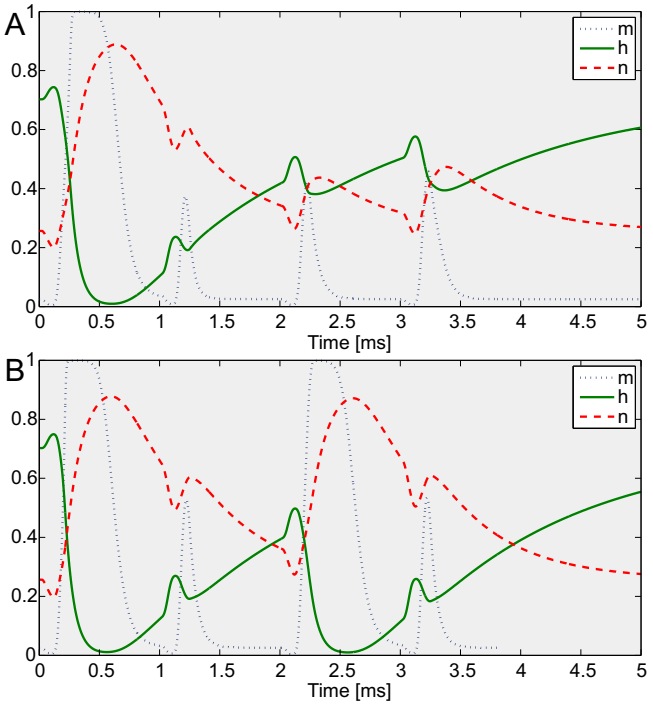

Figure 8.17: Variation of the dimensionless gating variables m, h and n at point l=6.1 mm of the considered tract 5 for cases A and B of Fig. 8.16.

increase of the obtained stimulation threshold. For example, an initial membrane potential of -70 mV results as well in an increase of 39.8%. The optimal value to start with is namely the resting potential V_r, equal to -84 mV. At last we remark the low sensitivity of the compartmental simulations to Δt, which can be taken up to 5 μs, instead of 1 μs. This would make the computational time five times shorter.

Up to now, we focussed on a single tract, namely tract 5. However, a group of 54 neural tracts near the stimulated left M1 hand area were selected in Section 7.2. Fig. 8.18 shows the simulated spatio-temporal variation of the membrane potentials for an applied stimulator output of 87.50 A/μs. Let us compare these images with Fig. 7.7, where the induced effective electric field is presented at the start of the stimulation pulse, t=20μs. Those neural fibres experiencing a large field will effectively generate more easily an action potential and conduct it unattenuated down their axons. Once more, these results confirm that it is not a sufficient condition for tracts to be close to the coil to be excited. It is an interplay of various factors, such as the position and orientation of the TMS coil, the applied excitation, the neural

Table 8.2: Sensitivity analysis of the neural parameter values on the stimulation threshold, defined as the minimal peak excitation current time derivative needed to initiate an action potential at tract 5. The changes are expressed in terms of percentage compared to the original threshold of 75.90 A/μs. The geometrical and electrical parameters were varied one at a time.

Parameter	Range	Change (%)
Initial membrane potential V_0 (mV)[f5]	-120 $\rightarrow$ 40	33.1 $\rightarrow$ /
Intracellular resistivity R_a (Ωm)	0.1 $\rightarrow$ 1	-38.6 $\rightarrow$ 75.2
Dendrite length (μm)	1000 $\rightarrow$ 2200	0 $\rightarrow$ 11.0
Dendrite diameter (μm)	2 $\rightarrow$ 32	0.1 $\rightarrow$ -1.4
Initial segment length (μm)	1.5 $\rightarrow$ 60	-0.6 $\rightarrow$ 1.4
Unmyelinated axon diameter (μm)[f6]	2.2 $\rightarrow$ 10.2	37.2 $\rightarrow$ -15.3
Myelinated internode capacitance (μF/m^2)	20 $\rightarrow$ 50	-30.5 $\rightarrow$ 0
Capacitance of other segments (F/m^2)	0.009 $\rightarrow$ 0.028	-18.2 $\rightarrow$ 0
Myelinated internode conductance (S/m^2)	0.1 $\rightarrow$ 0.2	0 $\rightarrow$ -16.7

trajectory in relation to this coil and its course along the white and grey matter interface. For the complete progress in time of the membrane potentials, we refer to a movie that is uploaded on the personal UGent website `http://users.ugent.be/~ndgeeter/research.htm`.

8.4. Discussion and assumptions

Numerical modelling of TMS has shown its added value in the determination of the effect of different stimulation parameters, such as the orientation of the neural fibres, the position of the coil, the stimulator output and the not well-known neural parameter values.

Neural fibres that are oriented perpendicular to the plane of the coil appear to be less accessible for stimulation, since they experience a small effective electric field. Optimal accessibility, on the other hand, is achieved for neural fibres that are oriented in the direction of the maximal induced currents and at an angle of 45 degrees relative to the normal vector of the coil.

We simulated the propagation of TMS effects in depression through anatomical connections to deeper limbic regions. We targeted the left DLPFC and shifted the coil up to 16 mm both in rostral and dorsal direction. The re-

[5] The initial m_0, h_0 and n_0 change with changing V_0, according to $\alpha_i(V_0)/(\alpha_i(V_0) + \beta_i(V_0))$. They equal $7.565{\cdot}10^{-4}$, 0.9954 and $8.846{\cdot}10^{-12}$ for -120 mV and 0.9999, $2.471{\cdot}10^{-6}$ and 0.999975 for 40 mV, respectively.

[6] This range is equivalent to the combination of an initial diameter of the axon hillock of 4.4 $\rightarrow$ 20.4 μm, a final diameter of the axon hillock of 2.2 $\rightarrow$ 10.2 μm, a diameter of the initial segment of 2.2 $\rightarrow$ 10.2 μm, a diameter of the myelinated internodes of 5.0 $\rightarrow$ 15.0 μm and a diameter of the nodes of Ranvier of 2.2 $\rightarrow$ 10.2 μm.

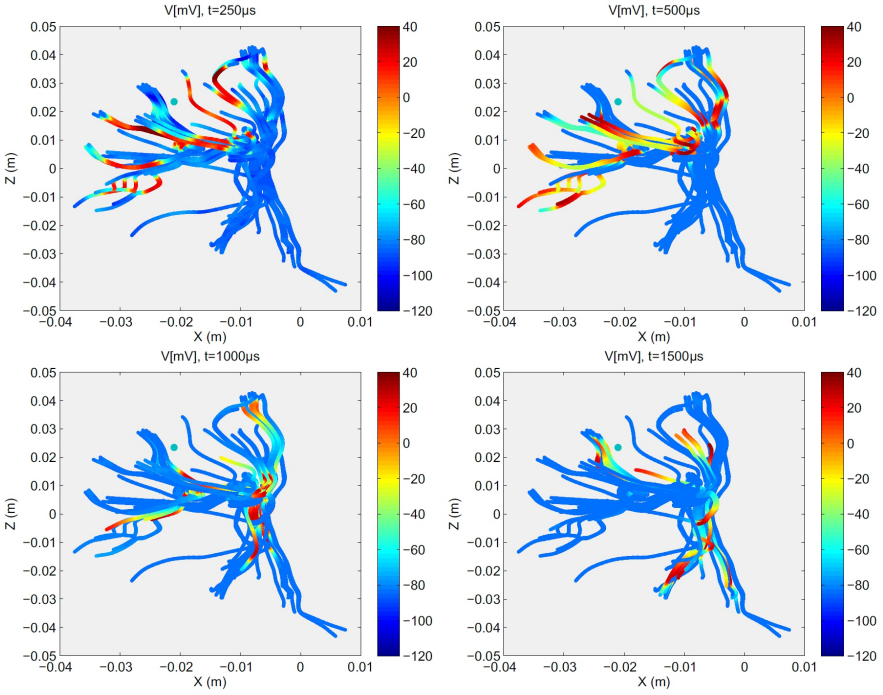

Figure 8.18: Temporal variation of the membrane potentials (in mV) in all 54 tracts as response to a biphasic TMS pulse to the left M1 hand area. The blue dot is the seed ROI centre.

sults indicate the high sensitivity of the neurophysiological response to TMS coil displacements, whereas the induced electric field variation is limited for small coil shifts. The spatial change of the electric field distribution causes the change in temporal excitation. But no generalised conclusion on the effect can be made, except for the fact that accurate positioning of the coil is crucial. This confirms that a patient-specific and accurate determination of the stimulation target in combination with a neuronavigation system is mandatory to perform reliable TMS studies, analogously as in (Casarotto et al., 2010; Lioumis et al., 2009).

Finally, we implemented the compartmental cable equation which combines the passive and active dynamics of the respective passive and active components. Close to a predefined region of interest, here the left M1 hand area, a group of neural fibres is reconstructed using tractography. Along these bundles the effective electric field and the three corresponding stimulation mechanisms were computed, together with the spatio-temporal variation of the membrane potentials. We believe that this is a good attempt of simulating the neural response to TMS in space and time as realistic as possible. Moreover,

the sensitivity of the stimulator threshold towards the not well-known and inter- and/or intra-subject variable neural parameters appeared to be acceptable.
However, this model still has some important assumptions, leaving room for improvement. All neural tracts used in the last section consist of a single apical dendrite, soma, axon hillock, initial segment and a myelinated axon. These segments are considered to be cylinders or truncated cones, as illustrated in Fig. 6.10. However, these are simplifications and in reality neurons have multiple dendrites, which on their turn can be branching expansively, see Fig. 6.1. Some neurons have multiple axons and one axon can change its diameter along its pathway. In the future, a distinction should be made between the different types of neurons, such as the pseudounipolar sensory neurons, the multi- or bipolar interneurons and multipolar pyramidal neurons. Salvador et al. (2011) makes a classification into pyramidal tract neurons (PTN), cortical interneurons, axon collaterals and association fibres and changes the morphological properties accordingly. Also the electrical properties should be adapted to the neuron type. Tsugorka et al. (2007) showed for example how the membrane potential for cortical interneurons behaves differently from PTNs.
The initial state of all neural fibres is assumed to be at rest, with a membrane potential V_r, whereas Table 8.2 demonstrated a high sensitivity of the stimulation threshold to this initial value. Moreover, no axonal terminations are implemented and, even more important, no synapse for further communication to other neurons in the connected brain network. This should be implemented in the future, to obtain a bigger picture of the neural response to TMS.

General conclusions and perspectives

One never notices what has been done; one can only see what remains to be done.

Marie Curie

9

General conclusions and perspectives

9.1. General conclusions

TMS has established itself as a promising non-invasive tool for exploring brain functions and for treating various neurological and psychiatric disorders, since it can modulate and modify the brain activity. However, there is limited knowledge concerning its physiological effects, which often makes the interpretation of its results ambiguous (Hoogendam et al., 2010; Sack and Linden, 2003). Moreover, a high variability of the TMS effect on brain functioning is repeatedly reported (Hernandez-Pavon et al., 2014; Lioumis et al., 2012; Loo and Mitchell, 2005; Maeda et al., 2000). This important shortcoming restricts the clinical use of TMS (Di Pino et al., 2014). To gain more insight, we developed a computational model for TMS that can accurately determine the impact of the induced electric fields on the human brain. By mapping these electric fields along neural fibres, reconstructed through tractography, we could acquire knowledge on the neuronal membrane potential behaviour. Moreover, the use of neuronavigated TMS and individual MRI allows to approach each case and each subject or patient individually. In this way, the gap between modelling and reality was decreased, increasing the fidelity of the developed model.

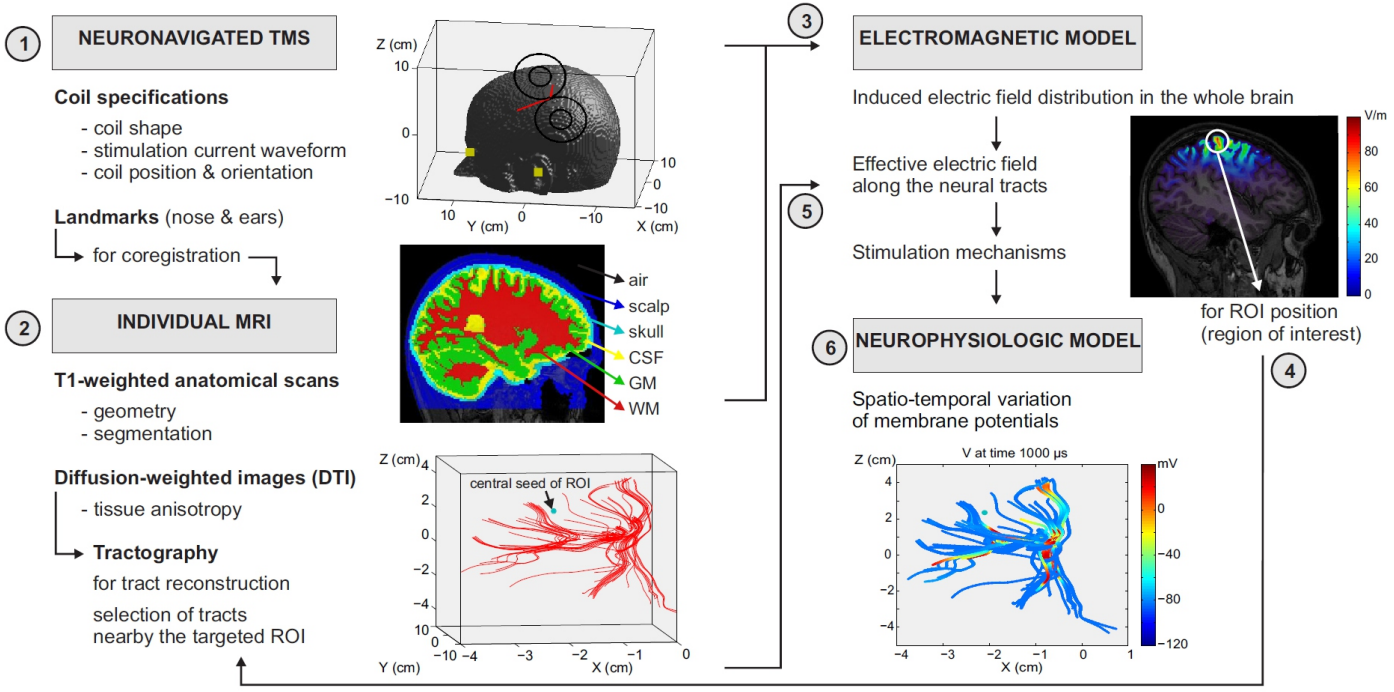

Figure 9.1: Flowchart of the presented computational model for TMS. The response to brain stimulation is calculated in a case- and subject-specific way from the macroscopic fields to the potentials on microscopic neuronal level.

Fig. 9.1 schematically shows how the different components elaborated in the PhD are linked and how they can be practically executed in an optimal TMS set-up. Prior to the stimulation session, two individual MRIs were acquired of the subject or patient; a T1-weighted image and a diffusion-weighted data set. A personalised head model is then constructed with realistic geometry and segmented into scalp, skull, cerebrospinal fluid, grey and white matter by applying statistical parametric mapping (SPM8 or SPM12) (Friston et al., 2007) on the structural T1 image. Anisotropic tissue properties, i.e. conductivity and permittivity, are included in the head model. Since the transport of ions in conductivity and water molecules in diffusion are mainly constrained by the same extracellular space, a strong linear relationship exists between the eigenvalues of the conductivity and the self-diffusion tensors (Tuch et al., 2001). Anisotropic conductivity and permittivity tensors can thus be computed from the diffusion tensors.
When neuronavigated TMS is applied, the neuronavigation system produces an output file with the coil specifications such as the coil type or shape, the applied stimulation pulse and the coil position and orientation. These specifications can be co-registered to the subject's MRI data by using the landmarks, typically the nose and ears, denoted by the digitising pen and saved as well in the output file.
The TMS excitation current produces a magnetic field, inducing eddy currents and an electric field in the brain. These can be calculated using the developed independent impedance method in case of a given isotropic or anisotropic volume conduction model. IIM is based on the conventional IM, but eliminates the dependent loops and consequently redundant equations (Wang et al., 2008) resulting in improved conditionality and speed-up of numerical convergence. A 3D network of impedances is generated and solved to determine the induced eddy currents. The electric field distribution in the whole brain can then be calculated.
Tractography is employed to reconstruct realistic 3D bundles of grouped neural fibres, called tracts, in the white matter of the brain. This method is applied on the diffusion tensor data set of the subject, preserving a personalised tractogram. Based on the weighted maxima of the induced electric field distribution, a region of interest (a box of one or several cm^3) is defined. Only those tracts that traverse this ROI are identified from the whole-brain tractogram. The induced electric field is mapped along the trajectories of these targeted tracts and serves as the input for the stimulation mechanisms (Silva et al., 2008).
Finally, the macroscopic electric fields lead to a change in the membrane potentials of the neural fibres and subsequently to depolarisation of the neurons. The distribution of the induced electric field is thus the key parameter of stimulation. In order to have a realistic and feasible coupling, accuracy is required

when solving the neurophysiological equations (Hodgkin and Huxley, 1952; Roth and Basser, 1990). The response of the stimulation mechanisms on the membrane potentials in the tracts are computed by a compartmental cable equation. All tracts are assumed to be myelinated neurons, containing sections representing dendrites, soma, axon hillock, initial segment and alternating Ranvier nodes and myelinated internodes, and are modelled with passive and active membrane properties. The spatio-temporal variation of the membrane potentials provides us information of when and where the stimulation occurred.
This flexible and personalised way of TMS modelling is, to our knowledge, innovative for the simulation of the response to TMS and represents a valuable step towards fully case- and patient-specific results. We investigated how TMS parameter changes, such as the coil position and orientation, affect the electric field distribution, stimulation mechanisms and membrane potentials. Variability was consequently observed in our simulation results, illustrating the need of high fidelity models for TMS.
The complete flowchart of Fig. 9.1 is followed step-by-step in Appendix B, where the variability of TMS is illustrated in a speech mapping case study.

9.2. Perspectives

Certainly all methods and models have their assumptions and, consequently, limitations. We enumerate all our concerns and possible extensions of the presented numerical model for future improvement.
There is limited literature on the stimulation parameters of the commercially available TMS devices. This makes it hard to simulate and compare research and clinical studies. For our simulations, the complete characterisation of the coil as well as the stimulus waveform is required. This includes the coil shape, inner and outer radii, wire dimensions, number of turns in each winding, coating dimensions, core dimensions and material. The stimulus waveform is characterised by the precise excitation pulse shape, amplitude, width and polarity, the pulse repetition frequency, duration of and interval between bursts or trains of pulses and the total number of pulses. Also the coil position and orientation on the scalp surface, relative to a reproducible reference frame needs to be known. Moreover, all these parameters are recommended to be reported for reproducing the research and clinical outcomes (Peterchev et al., 2012).
The coil position and orientation can be recorded by a neuronavigation system that monitors the TMS coil relative to the subject's head during the experiment. Another possible solution are moulds that fix the position of the coil in relation to the brain (Wyckhuys et al., 2013). However, neuronavigated TMS is preferred since it is more comfortable and it enables flexibility with respect

to coil location changes.
In order to confirm and verify the accuracy of the other specifications released by the manufacturers and to obtain more detailed information, we propose two possible measurements. First, X-rays of the coil can be taken, together with landmarks for calibrating the measurements, to model the 3D geometry as accurately as possible. Fig. 9.2 depicts the X-ray of the Magstim 20mm figure-of-eight coil (Whitland, United Kingdom). This was also done for other coil types by Salinas et al. (2007); Thielscher and Kammer (2004).

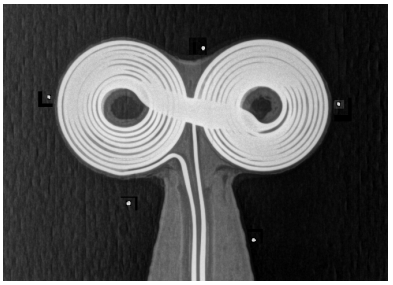

Figure 9.2: X-ray of the Magstim 20mm figure-of-eight coil. Based on this picture and the information of the manufacturer, we modelled this coil in Section 8.1 as two circular coils with 9 turns each, consisting of copper wire with a rectangular cross section of 0.80 mm $\times$ 5.50 mm, and with the inner and outer radii of one circular coil being 4.35 mm and 13.15 mm, respectively.

Secondly, we measured real current flowing through a TMS coil with a current clamp and an oscilloscope. Fig. 9.3 depicts the voltage in the Magstim 20mm figure-of-eight coil obtained at 1% power of the Rapid^2 stimulator (MagStim Inc., Whitland, United Kingdom). This reveals that the actual current shape differs significantly from the exponential damped sine, see equations (1.3-1.4), that is distributed publicly. It would be interesting to perform a Fourier analysis on this signal. Through the inverse Fourier transform (5.12), general solutions can be built as linear combinations of single-frequency solutions, analogous to the calculations in Section 5.1.2.
A peak amplitude of about 300 A is observed at 1% power of the stimulator device. For 50% power ($P \sim I^2$) the current will be $\sqrt{50}$ times bigger, in the order of 2 kA. This is of the same order of magnitude as the modelled 1.43 kA of the 20-mm figure-of-eight coil in Section 8.1. The measured signal of Fig. 9.3 has a pulse width of about 450 μs, corresponding to a frequency of 2.222 kHz. In our simulations 1 kHz was applied.
In addition, we investigated the penetration depth δ of the current in the copper coil wires.

$$\delta = \sqrt{\frac{2}{\sigma \mu 2\pi f}} \tag{9.1}$$

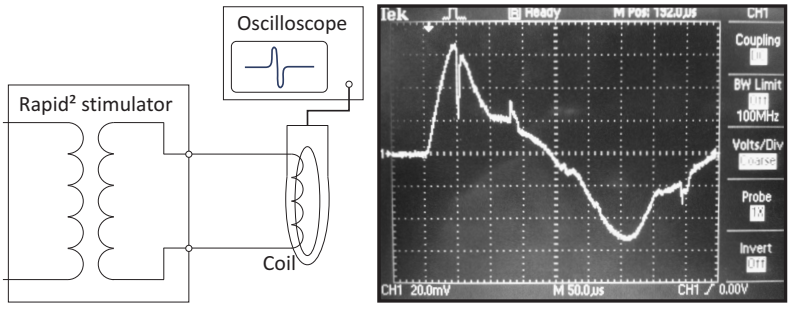

Figure 9.3: Real current waveform measurement with a current clamp and oscilloscope of the Magstim 20mm figure-of-eight TMS coil at 1% power of the Rapid^2 stimulator. The current clamp is positioned over one circular coil, and thus over 9 turns. The oscilloscope has a vertical voltage scale of 20.0 mV per division, which corresponds to 100 A per division due to the selected factor of 5 A/mV, and a horizontal time scale of 50 μs per division.

Copper has a conductivity σ of $5.96 \cdot 10^7$ S/m and a permeability μ of $1.256629 \cdot 10^{-7}$ H/m. Let us consider a stimulation frequency f of 2.222 kHz, as measured above for the 20mm figure-of-eight coil. The corresponding penetration depth is 1.38 mm. This means that the electric current flows through the entire rectangular cross section (0.80 mm $\times$ 5.50 mm, see Fig.9.2) of the wire of this coil. In general, rectangular conductor shapes are preferred, since they have the least skin effect and optimal surface area, in comparison to round and foil wires.

The dielectric properties, i.e. conductivity and permittivity values, of the considered tissues are obtained from the 4-Cole-Cole model corresponding to the applied stimulation frequency, see Section 2.2.1. However, the parameters listed in Table 2.1 are not well known. Particularly for the low-frequency range [Hz-kHz], which is the α dispersion, these values are more uncertain, and therefore the 4-Cole-Cole model should be used with caution. It might be interesting to consider other models or measurements for permittivity and conductivity values, such as the *in vivo* measurements of the cortical impedance spectrum in monkeys done by Logothetis et al. (2007).

In this PhD, the diffusion MRI analysis was based on DTI and the reconstructed neural fibre trajectories were derived with tractography using a deterministic streamline approach. With the current DTI resolution (≥ 1 mm), individual axons, neurons and synapses are not resolved, but the bulk-averaged tissue properties are taken in each voxel. During tractography, the dominant fibre orientation within each voxel is determined and successive discrete orientations provide an estimated tract reconstruction. This reconstruction is thus subject to noise contamination, which can lead to limited precision. Furthermore, DTI is not adequate to characterise complex fibre configurations, such as crossing and kissing fibres (Tournier et al., 2011). In these regions,

the uncertainty of the dominant diffusion orientation is large, which makes it difficult to reliably reconstruct white matter fibre pathways (Jeurissen et al., 2013). Future research that can integrate such dispersion of pathway propagation during tractography, for instance by resorting to probabilistic approaches (Behrens et al., 2007; Jeurissen et al., 2011), is needed to tackle these limitations.

Ruohonen et al. (1996) proposed that the component of the induced electric field perpendicular to the orientation of the neural fibre might be responsible for unexpected muscle responses, observed when magnetically stimulating peripheral nerves. This indicates there still might be other underlying TMS mechanisms that remain to be elucidated, besides the three discussed in Section 7.1 and implemented in this PhD.

The compartmental neuron model, explained in Section 6.2.3 for the simulation of the spatio-temporal variation of the membrane potentials, has some important assumptions as well. The neural tracts are segmented in a single apical dendrite, soma, axon hillock, initial segment and a myelinated axon. These segments are represented by cylinders or truncated cones, as illustrated in Fig. 6.10. A more accurate representation of the neuronal geometry that includes multiple dendrites and the main features of the axonal embranchment, see Fig. 6.1, is needed. Moreover, a distinction should be made between the different neuron types, such as the sensory neurons, interneurons and pyramidal neurons. The electrical parameters of the neural segments, listed in Table 6.1, are obtained for pyramidal tract neurons (PTNs) (Salvador et al., 2011; Wesselink et al., 1999) but will differ for other neuron types, especially for cortical interneurons (Tsugorka et al., 2007). Additionally, these parameter values are not well known and vary among literature (Gentet et al., 2000; Manola et al., 2007; McIntyre et al., 2002; Rattay, 1999; Wesselink et al., 1999). Recent research revealed that the axon morphology is even highly dynamic and experience dependent (Holtmaat and Svoboda, 2009). More accurate geometrical and morphological properties would lead to better estimates of the changes in membrane potentials due to stimulation.
The brain state is important to simulate the stimulation effects, since the initial membrane potentials affect the stimulation threshold, see Table 8.2. Perhaps they can be estimated with resting state fMRI. The brain activity at rest, i.e. when the subject is not performing an explicit task, is observed through changes in blood flow in the brain. fMRI most commonly uses the BOLD technique, which measures the blood oxygen level. Since the blood flow increases more than the oxygen extraction, blood becomes more oxygenated, resulting in an indirect measure of neural activity. The impact of this background activity should be investigated.
The voltage-dependent transition rates α and β for the sodium and potassium gates m, h and n, see equations (6.11-6.14) and (6.17-6.18), were obtained by fitting to measurements of Hodgkin and Huxley (1952) on the squid giant

axon performed at 20 °C. For human neural fibres at a body temperature of 37 °C, these rates were adjusted to equations (6.42-6.47). However, the applied neurophysiological model can be extended towards other temperatures, for example when the subject has a fever. For a temperature T_c in degrees Celsius, the rate factors α and β (6.42-6.47) should be multiplied with the following factor:

$$Q_{10}^{\frac{T_c-37}{10}} \tag{9.2}$$

with Q_{10} equal to 1.7, 2.9 and 3.0 for the rate factors of m, h and n, respectively, according to Wesselink et al. (1999).

The effect on synapses was not taken into account. Including this would allow us not only to investigate the individual behaviour of neural tracts, but also to predict the response on the whole brain network due to synaptic interactions between neurons. At this moment, our developed model can estimate how the brain activity, considered to be initially in the resting state, is altered due to a TMS pulse by studying the spatio-temporal change of the membrane potentials of the neural tracts of interest. This is only the very first step, which can also be noticed from the computed time span (a few ms). Once one or more action potentials are triggered, they may propagate along the considered neural fibre bundles. In reality, after being conducted down the axon they enter the axon terminals, which form the synapses with other neurons, see Fig. 6.3. When action potentials arrive at a pre-synaptic axon terminal, they cause a release of neurotransmitters into the synapse that bind to receptors in the post-synaptic neuron. New action potentials will be initiated, leading to further conduction of the neural signal, only if this post-synaptic neuron is excited sufficiently. This happens when multiple pre-synaptic neurons are triggered at the same time or when they release action potentials at a high frequency. A possible model for the diffusion and stochastic activation of synapses is the Monte Carlo-based method, called MCell (Stiles and Bartol, 2001).
In our model, a generated action potential is enabled to propagate in both directions of fibre tracts. The plasma membrane can indeed conduct the neural signals in both directions. However, synapse conducts the signal from the pre-synaptic axon terminal to the post-synaptic dendrite. Therefore, only those action potentials that are conducted down the axon into the terminal will contribute to further communication. This could be implemented in the future, by for example considering the neural tracts as diodes.
Along with synapse, the complete neural network of connections between the targeted and other brain regions should be included. More specifically, the targeted neural fibre bundles are connected with a network of other tracts to which they communicate. Based on DTI, subject-specific connectivity matrices can be obtained with the graphical toolbox ExploreDTI (Leemans et al., 2009), from which network properties such as efficiency, path length and con-

nectivity degree can be derived, as in (Caeyenberghs et al., 2013). In future work, implementing synapses and network interactions is essential so to obtain a bigger picture and better understanding of the neural response to TMS. Moreover, it is mandatory for the correct validation of the TMS solver with experimental measurements. Due to the absence of these synapses, our findings that are obtained for single pulse TMS should not be extrapolated to repetitive stimulation.
That further research on TMS modelling should focus on this connected brain network is emphasised by the theory of Fox et al. (2014): "Even though we are stimulating totally different sites for a given disease, we are stimulating the same networks (see Section 1.5.1). Our brain is an interconnected grid as complex, and often as confusing, as a map of criss-crossing streets in a large city. Just as a car accident might contribute to a traffic jam a few blocks away, stimulation can affect an area of the brain network that is not necessarily at the targeted site."

We want to stress that our findings are obtained for individual test subjects and should not be extrapolated to other healthy subjects or patiënts. The variability between brains and the anatomical structures (Bartley et al., 1997; Rajkowska and Goldman-Rakic, 1995) and the influence it has on the induced phenomena and corresponding simulation results may not be underestimated.

Validation of the obtained neurophysiological computational results with experiments remains difficult, since it is not evident to measure the membrane potential variation directly in the brain. We cannot easily construct a ground truth example resembling the complex biology of the human brain. Therefore, we are restricted to other, mostly indirect, measurements and observations.
Clinical comparison can be executed in a first stage with animal studies. For example, by means of micro single photon emission computed tomography (μSPECT), changes of the cerebral blood flow can be evaluated, which reflect changes in the neural activity (Wyckhuys et al., 2013). In a second stage these experiments can be translated towards human brain stimulation. The induced brain activity can be compared with other functional neuroimaging techniques, such as fMRI and positron emission tomography (PET). However, despite the relatively high spatial resolution (mm) of fMRI, its temporal resolution is low (100 ms - s). The blood oxygen level, measured during fMRI, remains an indirect measurement and peaks approximately 6s after neuronal activity. PET has an even lower temporal resolution (tens of seconds to minutes) and requires injection of a radioactive tracer. We suggest validation is feasible by comparing the obtained spatio-temporal variation of the membrane potentials within the brain network with measured TMS-evoked EEG responses. EEG can reveal with a high temporal resolution (ms) the spreading of neuronal activity. Its spatial resolution (cm) is, however, lower than that

of fMRI due to the volume conduction spread. Since we compute the membrane potentials along mm-long tracts instead of single neurons, this might not be a problem. Moreover, it would be interesting to investigate the activity changes in the whole brain network. We emphasise here the importance of well prepared and precisely executed experiments. TMS-compatible EEG systems should be applied, which suppress the huge electromagnetic artefacts in the EEG signal due to the electric field induced by the stimulus pulses (Ilmoniemi and Kičić, 2010). However, great challenges remain to avoid other artefacts, such as those originating from electrode movement, electrode polarisation, eye movement, muscle contraction activated by the pulse, or brain responses evoked by the coil click. Using high-resolution multichannel EEG is advised so to optimise the signal-to-noise ratio and spatial resolution. Careful post-processing of the data while reducing the artefacts by filtering will be important. For more information on how to measure TMS-evoked EEG responses, we refer to the guidelines of Ilmoniemi and Kičić (2010).

Optogenetics, a new technique in which light-sensitive proteins are used, might also offer a solution (Knöpfel and Boyden, 2012). Specific brain cells and circuits light up when they are active. The advantage of this promising technique is that it can monitor with a high spatial (10 μm) and temporal resolution (ms) the activity of individual neurons in living tissue, even within freely-moving animals. The major limitations are tissue absorption and tissue scattering.

Besides these neuroimaging techniques, *in-vitro* measurements using direct patch-clamp recordings are possible alternatives.

For completeness of this research we mention the existence of alternative software packages, such as the commercial finite element-based COMSOL Multi-physics ® (COMSOL Inc., Los Angeles, California USA) for field computations and NEURON `http://www.neuron.yale.edu/neuron` or GENESIS `http://www.genesis-sim.org/GENESIS` for neural simulations. However, during this PhD, we have chosen from the start to program own software in C++ language. This enabled us to model in complete freedom and with full flexibility the response to TMS from the macroscopic electric fields to the membrane potentials on microscopic neuronal level. Moreover, it allowed us to progress towards case- and patient-specific results by implementing the neuronavigation coil parameters and individual MRI, such as T1-weighted and diffusion-weighted images.

Appendices

A

Simple example of IM dependence and IIM independence

Consider a $2 \times 2 \times 2$ 3D network as in Fig. A.1. For simplicity of comparison between IM and IIM, we apply equations (3.19, 3.20, 3.21), resulting in the unknown matrix of branch currents $\mathcal{I}$:

$$\mathcal{I} = \begin{bmatrix} \hat{I}_x(1,1,1) \\ \hat{I}_y(1,1,1) \\ \hat{I}_z(1,1,1) \\ \hat{I}_x(1,1,2) \\ \hat{I}_y(1,1,2) \\ \hat{I}_x(1,2,1) \\ \hat{I}_z(1,2,1) \\ \hat{I}_x(1,2,2) \\ \hat{I}_y(2,1,1) \\ \hat{I}_z(2,1,1) \\ \hat{I}_y(2,1,2) \\ \hat{I}_z(2,2,1) \end{bmatrix} \tag{A.1}$$

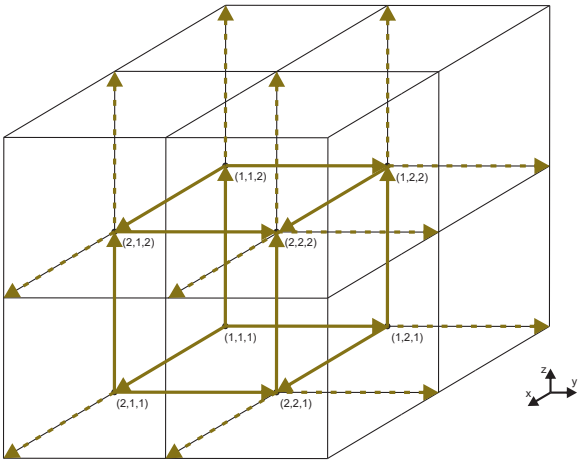

Figure A.1: $2 \times 2 \times 2$ 3D network with the corresponding branch currents.

The dependence of IM

In the traditional IM, Kirchhoff's voltage law $\mathcal{Z} \cdot \mathcal{I} = \mathcal{V}$ is considered on each cell face of the voxels, see Fig. A.2a. Therefore, each loop passes though the four impedances of the four edges of the face. The voltage matrix $\mathcal{V}$ and the impedance matrix $\mathcal{Z}$ become:

$$\mathcal{V} = \begin{bmatrix} \hat{V}_\mathrm{x}(1,1,1) \\ \hat{V}_\mathrm{y}(1,1,1) \\ \hat{V}_\mathrm{z}(1,1,1) \\ \hat{V}_\mathrm{z}(1,1,2) \\ \hat{V}_\mathrm{y}(1,2,1) \\ \hat{V}_\mathrm{x}(2,1,1) \end{bmatrix} \tag{A.2}$$

$$\mathcal{Z}^\mathrm{T} = \begin{bmatrix} 0 & -Z_\mathrm{x} & Z_\mathrm{x} & 0 & 0 & 0 \\ Z_\mathrm{y} & 0 & -Z_\mathrm{y} & 0 & 0 & 0 \\ -Z_\mathrm{z} & Z_\mathrm{z} & 0 & 0 & 0 & 0 \\ 0 & Z_\mathrm{x} & 0 & Z_\mathrm{x} & 0 & 0 \\ -Z_\mathrm{y} & 0 & 0 & -Z_\mathrm{y} & 0 & 0 \\ 0 & 0 & -Z_\mathrm{x} & 0 & -Z_\mathrm{x} & 0 \\ Z_\mathrm{z} & 0 & 0 & 0 & Z_\mathrm{z} & 0 \\ 0 & 0 & 0 & -Z_\mathrm{x} & Z_\mathrm{x} & 0 \\ 0 & 0 & Z_\mathrm{y} & 0 & 0 & Z_\mathrm{y} \\ 0 & -Z_\mathrm{z} & 0 & 0 & 0 & -Z_\mathrm{z} \\ 0 & 0 & 0 & Z_\mathrm{y} & 0 & -Z_\mathrm{y} \\ 0 & 0 & 0 & 0 & -Z_\mathrm{z} & Z_\mathrm{z} \end{bmatrix} \tag{A.3}$$

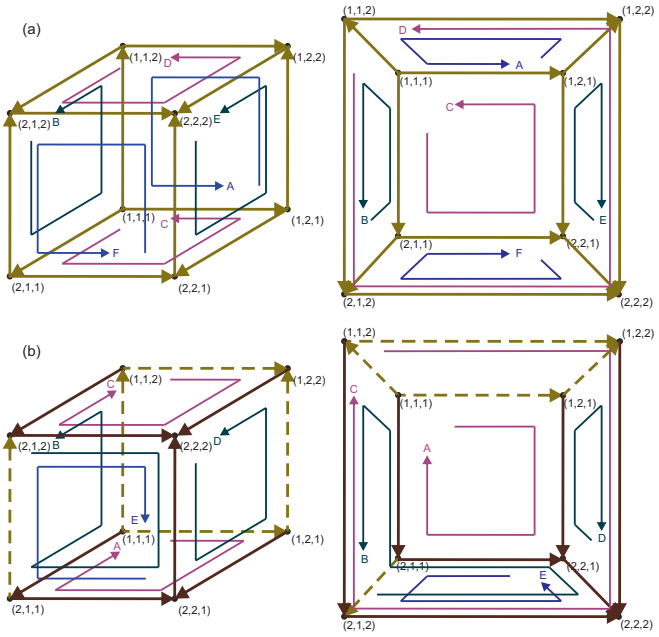

Figure A.2: (a) Definition of the loops for the conventional IM. (b) Definition of the loops for IIM.

The 6 rows of the impedance matrix correspond respectively to the loops A ($\hat{L}_x(1,1,1)$), B ($\hat{L}_y(1,1,1)$), C ($\hat{L}_z(1,1,1)$), D ($\hat{L}_z(1,1,2)$), E ($\hat{L}_y(1,2,1)$) and F ($\hat{L}_x(2,1,1)$), as illustrated in Fig. A.2a. It is important to notice that one of these loops can be written as a linear combination of the other loops. For instance, one can write:

$$D = A + B + C - E - F \tag{A.4}$$

From this simple example we can conclude that the traditional IM contains a set of dependent equations, causing the problem to be ill-conditioned.

The independence of IIM

For the developed independent impedance method, we first have to determine a well-chosen spanning tree. In Fig. A.2b this tree is indicated by the brown branches for a $2 \times 2 \times 2$ problem. The loops are obtained by adding the remaining branches, indicated by the dotted yellow lines. We then consider Kirchhoff's voltage law $\mathcal{Z} \cdot \mathcal{I} = \mathcal{V}$ over this set of loops. The voltage matrix $\mathcal{V}$, the impedance matrix $\mathcal{Z}$ and the transformation matrix $\mathcal{T}$ become:

$$\mathcal{V} = \begin{bmatrix} -\hat{V}_z(1,1,1) \\ \hat{V}_y(1,1,1) - \hat{V}_x(2,1,1) \\ -\hat{V}_z(1,1,2) \\ \hat{V}_y(1,2,1) \\ -\hat{V}_x(2,1,1) \end{bmatrix} \tag{A.5}$$

$$\mathcal{Z}^T = \begin{bmatrix} -Z_x & -Z_x & 0 & 0 & 0 \\ Z_y & 0 & 0 & 0 & 0 \\ 0 & Z_z & 0 & 0 & 0 \\ 0 & Z_x & -Z_x & 0 & 0 \\ 0 & 0 & Z_y & 0 & 0 \\ Z_x & 0 & 0 & -Z_x & 0 \\ 0 & 0 & 0 & Z_z & 0 \\ 0 & 0 & Z_x & Z_x & 0 \\ -Z_y & -Z_y & 0 & 0 & -Z_y \\ 0 & 0 & 0 & 0 & Z_z \\ 0 & Z_y & -Z_y & 0 & Z_y \\ 0 & -Z_z & 0 & -Z_z & -Z_z \end{bmatrix} \tag{A.6}$$

$$\mathcal{T} = \begin{bmatrix} -1 & -1 & 0 & 0 & 0 \\ 1 & 0 & 0 & 0 & 0 \\ 0 & 1 & 0 & 0 & 0 \\ 0 & 1 & -1 & 0 & 0 \\ 0 & 0 & 1 & 0 & 0 \\ 1 & 0 & 0 & -1 & 0 \\ 0 & 0 & 0 & 1 & 0 \\ 0 & 0 & 1 & 1 & 0 \\ -1 & -1 & 0 & 0 & -1 \\ 0 & 0 & 0 & 0 & 1 \\ 0 & 1 & -1 & 0 & 1 \\ 0 & -1 & 0 & -1 & -1 \end{bmatrix} \tag{A.7}$$

Remark that the number of loops are decreased from 6 (IM) to 5 (IIM) and that they are, according to the graph theory, constructed in such a way, that they are independent. Moreover, one can verify that the voltage matrix $\mathcal{V}$ and the coefficient matrix of the impedance network $\tilde{\mathcal{Z}} = \mathcal{Z} \cdot \mathcal{T}$ have both full rank and that this rank equals the number of variables, namely the 5 loop currents. Consequently, the solution of the system of linear equations $\tilde{\mathcal{Z}} \cdot \mathcal{L} = \mathcal{V}$ is unique.

B

Variability of TMS in a speech mapping case study

By studying the results of a speech mapping experiment, we aim to numerically explain the observed variability of TMS responses. We have chosen to investigate the effect of TMS on language because it is a complicated brain function, not corresponding to a single brain region but to a more complex neural network. We believe case- and subject- or patient-specific modelling is generally needed to accurately capture the electromagnetic and neurophysiologic phenomena triggered by TMS. Certainly when the stimulation interacts with such a complex neural network that can differ significantly from person to person (Sporns et al., 2005), thus affecting the stimulation outcome.

Introduction to speech mapping

During resective surgery, for example when removing a tumour or an epileptic zone, the patient may risk impairment of his functions (Pouratian and Bookheimer, 2010). Therefore, awake craniotomy is commonly used in combination with intraoperative functional mapping by direct cortical stimulation (DCS), especially when operating in the vicinity of motor or speech areas (Corina et al., 2010; Ojemann et al., 1988). This mapping is highly reliable, how-

ever, preoperative evaluation with TMS can be of great value (Krieg et al., 2014; Lioumis et al., 2012). TMS can create a 'virtual lesion' and temporarily disrupt the normal behaviour of the stimulated area. It may help in objective risk-benefit balancing of the planned surgery, and it may allow more targeted, smaller craniotomies, and faster and safer intraoperative mapping (Picht et al., 2013). Also for a patient that cannot undergo awake craniotomy, it may lead to safer surgery (Picht et al., 2013). It has been shown that navigated TMS can localise the cortical motor representations as accurately as DCS (Picht et al., 2011) and more accurately than fMRI (Forster et al., 2011) in tumour patients. Despite the good overall correlation between the speech-related regions identified with navigated TMS and DCS, low specificity in posterior language areas is observed (Picht et al., 2013). Where the motor skills are organised clearly and specifically in the primary motor cortex and therefore relatively easy to localise, see Fig. 1.15, language is derived from a complex and highly individualised network of cortical and subcortical connections (Catani et al., 2005). Amunts et al. (1999) studied Broca's area in ten post-mortem human brains and revealed significant variations in size as well as in the relation of this area to sulcal landmarks.

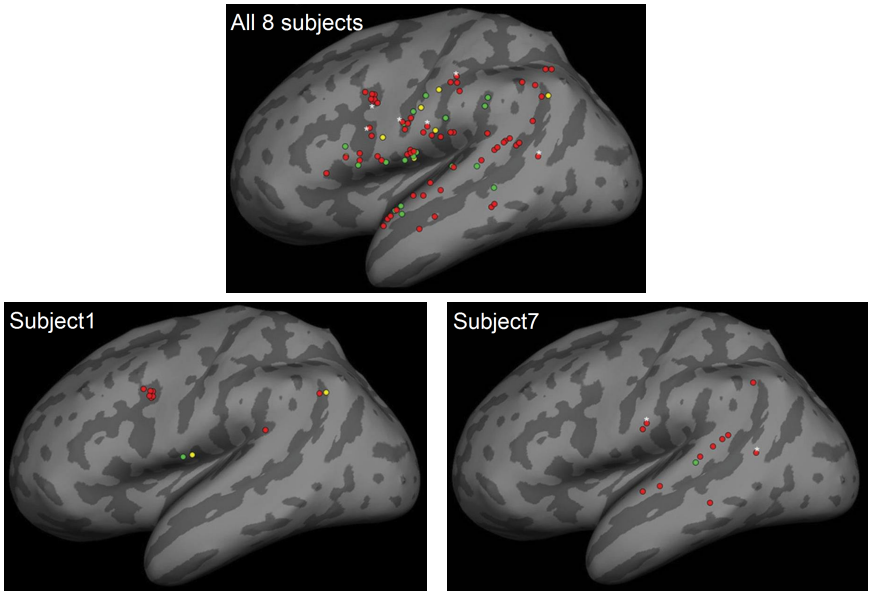

Figure B.1: Cortical sites that elicited TMS-induced object naming errors (above) for a total of 8 subjects, (bottom left) for one subject and (bottom right) for another subject. No-response errors, semantic and phonological paraphasias are indicated with dots. Original figures from (Hernandez-Pavon et al., 2014).

TMS has been used to affect speech performance during naming tasks. This way, one can non-invasively map the cortical speech-related areas as a preoperative evaluation. In contrast to TMS over the primary motor cortex, which is a small targeted area, speech mapping experiments reveal a large spread of the targeted cortical sites that lead to naming errors. The speech mapping studies of Lioumis et al. (2012) and Hernandez-Pavon et al. (2014), illustrated in Fig. B.1, demonstrated the high variability in number, type and location of the naming errors among their subjects.

Speech mapping case study

A speech mapping experiment was performed on a healthy, right-handed male subject at the Helsinki University Hospital, Finland, following the approach of Lioumis et al. (2012). Remember that in about 90% of right-handed individuals the language centres are situated in the left temporal lobe, see Section 1.3.3. During the first session, the baseline performance was measured of the subject who named images of simple objects as quickly and precisely as possible under normal conditions. The images were placed in random order. Those that were unfamiliar or named incorrectly were removed from the set. During the second session, the subject named these images again, while repetitive navigated brain stimulation was delivered to semi-random left-hemispheric areas. The eXimia Navigated Brain Stimulation (Nexstim Ltd., Helsinki, Finland) was used in combination with a biphasic 70mm figure-of-eight coil. The neuronavigation system monitored the coil position and orientation relative to the subject's head during this speech mapping experiment, which is of great value for our simulations. Every 2500 ms an object image was presented for 700 ms on the computer screen. During the second session, neuronavigated TMS was applied 300 ms after the image presentation onset. 5 pulses, with a pulse width of 230 μs, were delivered at 5 Hz spread over a total duration of 1000 ms. The performance of the subject, together with the TMS coil and object images were video-recorded, as in (Lioumis et al., 2012), so to analyse the results offline. The baseline responses were compared with those during TMS. A neurophysiologist categorised the naming errors induced by TMS by type and location. The different types are no-response error (anomic aphasia or anomia), phonologic paraphasia, semantic paraphasia and performance errors.

We selected four cases in which the coil was moved, rotated and tilted with limited deviations. One might assume that almost the same stimulation is performed. However, in one case, denoted as E_1, a naming error (more specifically a performance error) occurred, while in the other three cases, denoted as NE_{1a}, NE_{1b} and NE_{1c}, the subject appointed the object images smoothly as in the case without TMS. From the neuronavigation system we retrieved all

needed coil configuration parameters of these four cases, i.e. the coordinates of the centre of the coil **O**, the unit vector normal to the plane of the coil and directed away from the subject's head **n** and the unit vector in the direction of maximal induced currents (in homogeneous material) **m**. They are listed in Table B.1.

Table B.1: Coil specifications. Remark the positions are expressed according to the voxel sequence. To calculate the coordinates in meters relative to the centre, one must subtract ($N_x/2$, $N_y/2$, $N_z/2$) = (56,64,50) from it and multiply the result by the voxelsize of 2 mm.

Coil	Position O	Normal n	Direction m
$\mathbf{E}_1$	(14.08,76.28,45.02)	[0.972,-0.043,0.230]	[0.066,0.994,-0.091]
$\mathbf{NE}_{1a}$	(15.16,79.21,44.73)	[0.967,0.024,0.253]	[-0.016,0.999,-0.037]
$\mathbf{NE}_{1b}$	(14.36,77.00,44.64)	[0.975,-0.051,0.215]	[0.067,0.995,-0.070]
$\mathbf{NE}_{1c}$	(13.55,76.24,45.42)	[0.974,-0.102,0.203]	[0.115,0.992,-0.054]

T1-weighted and diffusion-weighted MRI were acquired from the subject. These data sets were post-processed using SPM12 (Friston et al., 2007) for the construction of a realistic 2-mm resolution anisotropic head model. This $112\times128\times100$ head model was segmented in the tissues scalp, skull, CSF, grey and white matter, with anisotropic tissue properties, based on the 4-Cole-Cole model (2.31). The nose, right and left ear of the subject were denoted by a digitising pen at the beginning of the TMS experiment and their positions were saved by the neuronavigation system. By using the coordinates of these landmarks, the coil specifications were co-registered to the head model.
The induced electric field distributions were computed for the four cases using the anisotropic independent impedance method, see Chapters 3 and 5. The results for cases E_1 and NE_{1a} are shown in Fig. B.2. At first sight, only minor differences can be noticed. Therefore, the distributions for the other two cases are not presented. Based on the electric field distribution, the centre of the region of interest (ROI) is defined. This is sometimes done by searching the overall maximum electric field value. Table B.2 indicates that these maxima (pos max) are located in the same voxel for the four cases. Another possible method is to search the first voxel in cerebral tissue which is situated in the extension of the coil normal vector (pos normal). Since the normal vectors are slightly different, see Table B.1, these voxels are scattered up to 5 mm (1 voxel = 2 mm) from each other. In this study, we have chosen the ROI centre using the position of the weighted mean. Within a sphere of radius 6 cm around the coil centre, the voxel positions are weighted by their electric field value, resulting in the positions listed in the last column of Table B.2. Consequently, we defined voxel (33,71,46) as the seed ROI centre, corresponding to coordinates (-0.046, 0.014, -0.008) in m. Within its 5-mm range, the full ROI box is created. Whole brain tractography is performed on the 1-mm DTI using the graphical

toolbox ExploreDTI (Leemans et al., 2009). The step size is set to 1 mm, the FA threshold to 0.2 and the bending angle threshold to 30 degrees. Although there is a user-defined influence, these main tractography parameters are in line with the conventional settings range in current literature. Those tracts that traverse the seed ROI box are identified. Only those tracts whose first and last points are located more than 5 mm from another are kept, reducing the number of tracts from 1239 to 35.

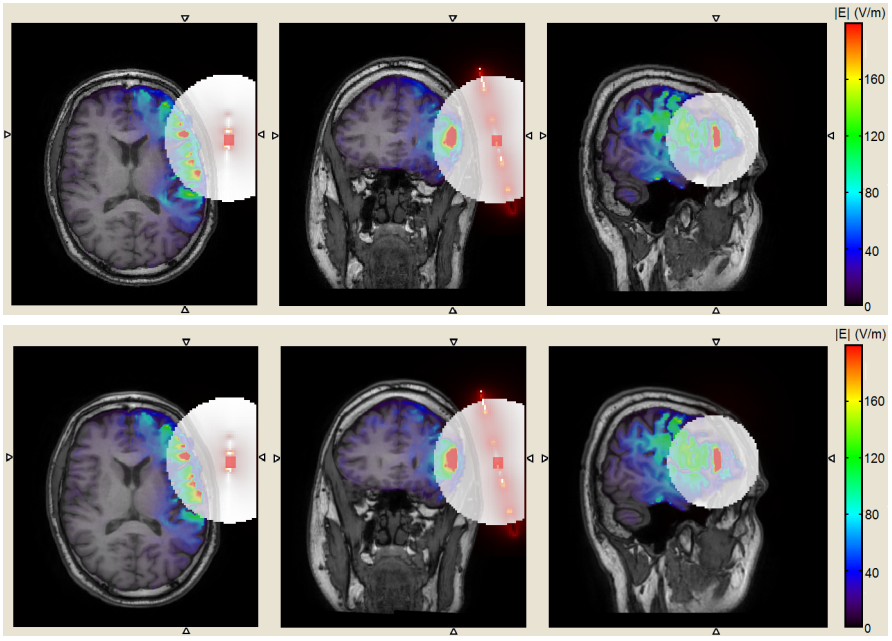

Figure B.2: (Left) Axial, (middle) coronal and (right) sagittal view of the induced electric field amplitude distribution (in V/m) due to (above) the E_1 stimulus and (below) the NE_{1a} stimulus. Only the values in the cerebral tissues are visualised for clarity reasons. The white mask indicates the sphere of radius 6 cm around the coil centre. The original T1-weighted image is visualised on the background.

Table B.2: Selection methods for the seed ROI centre. Remark the positions are expressed according to the voxel sequence. To calculate the coordinates in meters relative to the centre, one must subtract ($N_x/2$, $N_y/2$, $N_z/2$) = (56,64,50) from it and multiply the result by the voxelsize of 2 mm.

Coil	Pos max	Pos normal	Pos weighted
$\mathbf{E}_1$	(34,80,45)	(30,77,42)	(33,71,46)
$\mathbf{NE}_{1a}$	(34,80,45)	(31,79,41)	(34,74,46)
$\mathbf{NE}_{1b}$	(34,80,45)	(31,78,42)	(33,71,45)
$\mathbf{NE}_{1c}$	(34,80,45)	(30,78,43)	(32,71,46)

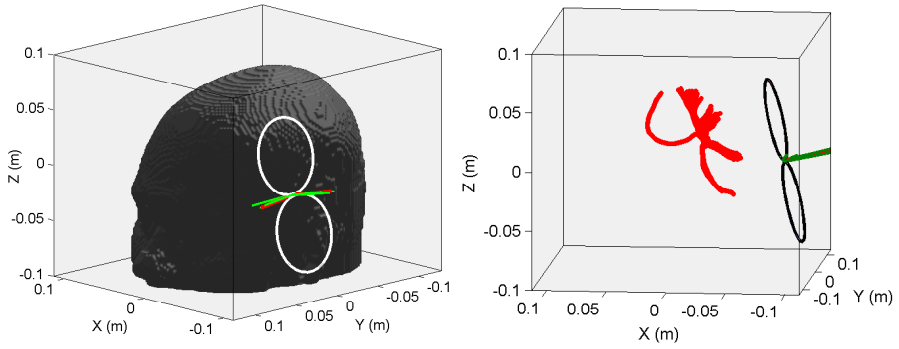

Figure B.3: (Left) The coil position with respect to the head model. The red and green lines represent the coil normal and the induced current direction for the cases that did (E_1) and did not (NE_{1a}, NE_{1b}, NE_{1c}) provoke a naming error, respectively. The outer windings of the 70mm figure-of-eight biphasic Nexstim coil are visualised for the error case. (Right) The coil position with respect to the 35 selected neural fibre tracts, represented by red lines.

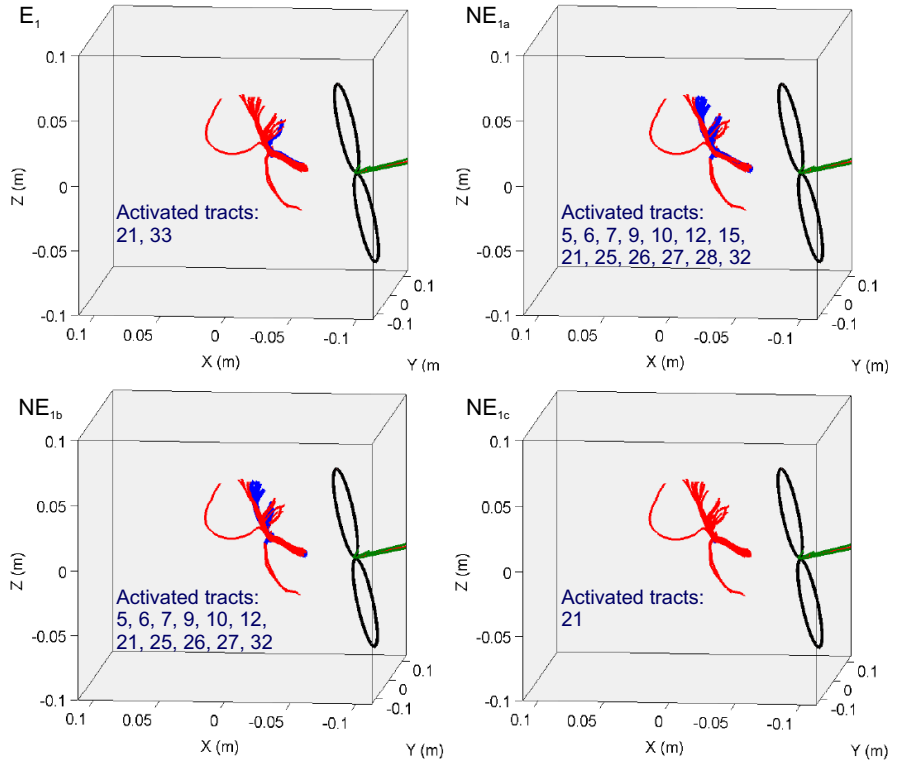

Figure B.4: The same figure as Fig. B.3 for the cases E_1, NE_{1a}, NE_{1b} and NE_{1c}. The tracts which are activated, i.e. when an action potential is conducted along them due to the stimulus, are coloured blue instead of red.

Fig. B.3 illustrates for the 4 cases how the coil is positioned and oriented relative to the head model. The two vectors **n** and **m** for the naming error case are indicated in red and for the non-error cases in green. Also the 35 considered tracts are visualised.
Finally, the spatio-temporal variation of the membrane potentials of all 35 neural fibre tracts are computed for the 4 cases. The compartmental cable equation, which combines passive and active neural components, is applied, as explained in Section 6.2.3, with the parameter values of Table 6.1. The blue-coloured tracts in Fig. B.4 show where activity is generated by the TMS pulse and reveal a large variability. One tract, more specifically tract 21, is activated for all coil positions. Another tract, tract 33, is only triggered for E_1, the case where a naming error is elicited. NE_{1a} induced action potentials in a total of 13 tracts, while NE_{1b} stimulated 11 tracts and NE_{1c} only one.
The calculated results using our developed methods are certainly sensitive to the coil specifications. In this way, we succeeded in numerically explaining the obtained variability in this speech mapping study. However, we could not justify why TMS for the case E_1 did elicit a naming error and did not for the other three cases. Even though there appeared one neural tract (tract 33) to be triggered only for the error case, we do not want to draw conclusions from this. Further research is needed, such as investigating the location and functional meaning of this tract in terms of the speech-related network, refining and optimising the neural model and its parameters, observing more neural tracts and including synapses and, consequently, the complete neural network of connections. For more details, we refer to our discussion on perspectives in Section 9.2.

Bibliography

Abrams, R. (1992). *Electroconvulsive therapy*. Oxford University Press, Oxford, United Kingdom.

Ahdab, R., Ayache, S., Brugières, P., Goujon, C., and Lefaucheur, J. (2010). Comparison of "standard" and "navigated" procedures of tms coil positioning over motor, premotor and prefrontal targets in patients with chronic pain and depression. *Neurophysiol. Clin.*, 40(1):27–36.

Amunts, K., Schleicher, A., Bürgel, U., Mohlberg, H., Uylings, H., and Zilles, K. (1999). Broca's region revisited: Cytoarchitecture and intersubject variability. *J. Comp. Neurol.*, 412(2):319–341.

Barker, A., Jalinous, R., and Freeston, I. (1985). Noninvasive magnetic stimulation of human motor cortex. *Lancet*, 2:1106–1107.

Bartley, A., Jones, D., and Weinberger, D. (1997). Genetic variability of human brain size and cortical gyral patterns. *Brain*, 120:257–269.

Basser, P., Mattiello, J., and Le Bihan, D. (1994a). Estimation of the effective self-diffusion tensor from the nmr spin echo. *J. Magn. Reson.*, 103:247–254.

Basser, P., Mattiello, J., and Le Bihan, D. (1994b). Mr diffusion tensor spectroscopy and imaging. *Biophys. J.*, 66:259–267.

Basser, P., Pajevic, S., Pierpaoli, C., Duda, J., and Aldroubi, A. (2000). In vivo fiber tractography using dt-mri data. *Magn. Reson. Med.*, 44:625–632.

Basser, P. and Pierpaoli, C. (1996). Microstructural and physiological features of tissues elucidated by quantitative-diffusion-tensor mri. *J. Magn. Reson. Ser. B*, 111:209–219.

Bates, D. and Watts, D. (1988). *Nonlinear regression analysis and its applications*. Wiley, New York, USA.

Behrens, T., Berg, H., Jbabdi, S., Rushworth, M., and Woolrich, M. (2007). Probabilistic diffusion tractography with multiple fibre orientations: What can we gain? *NeuroImage*, 34:144–155.

Benabid, A., Chabardes, S., Mitrofanis, J., and Pollak, P. (2009). Deep brain stimulation of the subthalamic nucleus for the treatment of parkinson's disease. *Lancet Neurol.*, 8(1):67–81.

Bernstein, M., King, K., and Zhou, X. (2004). *Handbook of MRI Pulse sequences*. Elsevier, Oxford, United Kingdom.

Brodal, P. (2004). *The central nervous system: structure and function*. Oxford University Press, Oxford, United Kingdom.

Brodmann, K. (1909). *Vergleichende Lokalisationslehre der Grohirnrinde des Menschen*. Barth, Leipzig, Germany.

Brody, D., Terry, F., and Ideker, R. (1973). Eccentric dipole in a spherical medium: generalized expression for surface potentials. *IEEE Trans. Biomed. Eng.*, 20(2):141–143.

Caeyenberghs, K., Leemans, A., Leunissen, I., Michiels, K., and Swinnen, S. (2013). Topological correlations of structural and functional networks in patients with traumatic brain injury. *Front. Hum. Neurosci.*, 7(726).

Carmichael, S. and Price, J. (1995). Limbic connections of the orbital and medial prefrontal cortex in macaque monkeys. *J. Comp. Neurol.*, 363(4):615–641.

Casarotto, S., Lauro, L., Bellina, V., Casali, A., Rosanova, M., Pigorini, A., Defendi, S., Mariotti, M., and Massimini, M. (2010). Eeg responses to tms are sensitive to changes in the perturbation parameters and repeatable over time. *PLoS one*, 5(4):e10281.

Catani, M., Jones, D., and Ffytche, D. (2005). Perisylvian language networks of the human brain. *Ann. Neurol.*, 57:8–16.

Chen, R., Classen, J., Gerloff, C., Celnik, P., Wassermann, E., Hallett, M., and Cohen, L. (1997). Depression of motor cortex excitability by low-frequency transcranial magnetic stimulation. *Neurology*, 48(5):1398–1403.

Cheney, M., Isaacson, D., and Newell, J. (1999). Electrical impedance tomography. *SIAM Rev.*, 41:85–101.

Cohen, L., Roth, B., Nilsson, J., Dang, N., Panizza, M., Bandinelli, S., Friauf, W., and Hallett, M. (1990). Effects of coil design on delivery of focal magnetic stimulation. technical considerations. *Electroencephalogr. Clin. Neurophysiol.*, 75:350–357.

Cole, K. and Cole, R. (1941). Dispersion and absorption in dielectrics: alternating current characteristics. *J. Chem. Phys.*, 9:341–351.

Corina, D., Loudermilk, B., Detwiler, L., Martin, R., Brinkley, J., and Ojemann, G. (2010). Analysis of naming errors during cortical stimulation mapping: implications for models of language representation. *Brain Lang.*, 115(2):101–112.

Crevecoeur, G., Restrepo, V., and Staelens, S. (2012). Subspace electrode selection methodology for the reduction of the effect of uncertain conductivity values in the eeg dipole localization: a simulation study using a patient-specific head model. *Phys. Med. Biol.*, 57:1963–1986.

Crowther, L., Marketos, P., Williams, P., Melikhov, Y., Jiles, D., and Starzewski, J. (2011). Transcranial magnetic stimulation: Improved coil design for deep brain investigation. *J. Appl. Phys.*, 109(7):07B314.

Davey, K. and Epstein, C. (2000). Magnetic stimulation coil and circuit design. *IEEE Trans. Biomed. Eng.*, 47(11):1493–1499.

Davey, K., Epstein, C., George, M., and Bohning, D. (2003). Modeling the effects of electrical conductivity of the head on the induced electric field in the brain during magnetic stimulation. *Clin. Neurophysiol.*, 114:2204–2209.

De Deene, Y., De Wagter, C., De Neve, W., and Achten, E. (1998). Mathematical analysis and experimental investigation of noise in quantitative magnetic resonance imaging applied in polymer gel dosimetry. *Signal Process.*, 70:85–101.

De Deene, Y., De Wagter, C., De Neve, W., and Achten, E. (2000). Artefacts in multi-echo t2 imaging for high-precision gel dosimetry: I. analysis and compensation of eddy currents. *Phys. Med. Biol.*, 45:1807–1823.

De Geeter, N., Crevecoeur, G., and Dupré, L. (2010). Low-parametric induced current - magnetic resonance electrical impedance tomography for quantitative conductivity estimation of brain tissues using a priori information: a simulation study. In *Proceedings of the 32nd Annual International Conference of the IEEE Engineering in Medicine and Biology Society (EMBC)*, Buenos Aires, Argentina.

De Geeter, N., Crevecoeur, G., and Dupré, L. (2011a). Eddy-current simulations using an independent impedance method in anisotropic biological tissues. *IEEE Trans. Magn.*, 47(10):3845–3848.

De Geeter, N., Crevecoeur, G., and Dupré, L. (2011b). An efficient 3d eddy-current solver using an independent impedance method for transcranial magnetic stimulation. *IEEE Trans. Biomed. Eng.*, 58(2):310–320.

De Geeter, N., Crevecoeur, G., and Dupré, L. (2013a). The effect of inaccurate targeting of the left dorsolateral prefrontal cortex on tms response. In *Proceedings of the 6th International IEEE EMBS Conference on Neural Engineering (NER)*, San Diego, California, USA.

De Geeter, N., Crevecoeur, G., and Dupré, L. (2013b). A numerical study on conductivity estimation of the human head in the low frequency domain using induced current mr phase imaging eit with multiple gradients. *IEEE Trans. Magn.*, 49(9):5004–5010.

De Geeter, N., Crevecoeur, G., Dupré, L., Van Hecke, W., and Leemans, A. (2012). A dti-based model for tms using the independent impedance method with frequency-dependent tissue parameters. *Phys. Med. Biol.*, 57(8):2169–2188.

De Geeter, N., Crevecoeur, G., Leemans, A., and Dupré, L. (2014). Effective electric fields along realistic dti-based neural trajectories for modelling the stimulation mechanisms of tms. *Phys. Med. Biol.*, 60(2):453–471.

De Lucia, M., Parker, G., Embleton, K., Newton, J., and Walsh, V. (2007). Diffusion tensor mri-based estimation of the influence of brain tissue anisotropy on the effect of transcranial magnetic stimulation. *NeuroImage*, 36(4):1159–1170.

Deng, Z., Lisanby, S., and Peterchev, A. (2013). Electric field depth-focality tradeoff in transcranial magnetic stimulation: simulation comparison of 50 coil designs. *Brain Stimul.*, 6(1):1–13.

Di Lazzaro, V. and Ziemann, U. (2013). The contribution of transcranial magnetic stimulation in the functional evaluation of microcircuits in human motor cortex. *Front. Neural Circuits*, 7(18).

Di Pino, G., Pellegrino, G., Assenza, G., Capone, F., Ferreri, F., Formica, D., Ranieri, F., Tombini, M., Ziemann, U., Rothwell, J., and Di Lazzaro, V. (2014). Modulation of brain plasticity in stroke: a novel model for neurorehabilitation. *Nat. Rev. Neurol.*, 10(10):597–608.

Eaton, H. (1992). Electric field induced in a spherical volume conductor from arbitrary coils: application to magnetic stimulation and meg. *Med. Biol. Eng. Comput.*, 30(4):433–440.

Fitzgerald, P., Hoy, K., McQueen, S., Maller, J., Herring, S., Segrave, R., Bailey, M., Been, G., Kulkarni, J., and Daskalakis, Z. (2009). A randomized trial of rtms targeted with mri based neuro-navigation in treatment-resistant depression. *Neuropsychopharmacol.*, 34(5):1255–1262.

Forster, M., Hattingen, E., Senft, C., Gasser, T., Seifert, V., and Szelényi, A. (2011). Navigated transcranial magnetic stimulation and functional magnetic resonance imaging: advanced adjuncts in preoperative planning for central region tumors. *Neurosurgery*, 68:1317–1324.

Foster, K. and Schwan, H. (1989). Dielectric properties of tissues and biological materials: a critical review. *Crit. Rev. Biomed. Eng.*, 17:25–104.

Fox, M., Buckner, R., Liu, H., Chakravarty, M., Lozano, A., and Pascual-Leone, A. (2014). Resting-state networks link invasive and noninvasive brain stimulation across diverse psychiatric and neurological diseases. *PNAS*, pages E4367–E4375.

Fregni, F., Simon, D., Wu, A., and Pascual-Leone, A. (2005). Non-invasive brain stimulation for parkinson's disease: a systematic review and meta-analysis of the literature. *J. Neurol. Neurosurg. Psychiatry*, 76:1614–1623.

Freund, R., Golub, G., and Nachtigal, N. (1992). *Iterative solution of linear systems*. Cambridge University Press, New York, USA.

Friston, K. (2011). Functional and effective connectivity: a review. *Brain Connect.*, 1(1):13–36.

Friston, K., Ashburner, J., Kiebel, S., Nichols, T., and Penny, W. (2007). *Statistical Parametric Mapping: The analysis of functional brain images*. Academic Press, San Diego, CA, USA.

Fuster, J. (2008). *The Prefrontal Cortex*. Academic Press, London, United Kingdom.

Gabriel, S., Lau, R., and Gabriel, C. (1996a). The dielectric properties of biological tissues: I. literature survey. *Phys. Med. Biol.*, 41:2231–2249.

Gabriel, S., Lau, R., and Gabriel, C. (1996b). The dielectric properties of biological tissues: Ii. measurement in the frequency range 10 hz to 20 ghz. *Phys. Med. Biol.*, 41:2251–2269.

Gabriel, S., Lau, R., and Gabriel, C. (1996c). The dielectric properties of biological tissues: Iii. parametric models for the dielectric spectrum of tissues. *Phys. Med. Biol.*, 41:2271–2293.

Gaignaire, R., Crevecoeur, G., Dupré, L., Sabariego, R., Dular, P., and Geuzaine, C. (2010). Stochastic uncertainty quantification of the conductivity in eeg source analysis by using polynomial chaos decomposition. *IEEE Trans. Magn.*, 46(8):3457–3460.

Gandhi, O., Deford, J., and Kanai, H. (1984). Impedance method for calculation of power deposition patterns in magnetically induced hyperthermia. *IEEE Trans. Biomed. Eng.*, 31:644–651.

Gebauer, A. and Scherzer, O. (2008). Impedance-acoustic tomography. *SIAM J. Appl. Math.*, 69(2):565–576.

Geddes, L. and Baker, L. (1967). The specific resistance of biological material a compendium of data for the biomedical engineer and physiologist. *Med. Biol. Eng.*, 5:271–293.

Gençer, N., Kuzuoglu, M., and İder, Y. (1994). Electrical impedance tomography using induced currents. *IEEE Trans. Med. Imag.*, 13:338–350.

Gentet, L., Stuart, G., and Clements, J. (2000). Direct measurement of specific membrane capacitance in neurons. *Biophys. J.*, 79(1):314–320.

George, M., Wassermann, E., Williams, W., Callahan, A., Ketter, T., Basser, P., Hallett, M., and Post, R. (1995). Daily repetitive transcranial magnetic stimulation (rtms) improves mood in depression. *Neuroreport*, 6(14):1853–1856.

Geschwind, N. (1970). The organization of language and the brain. *Science*, 170:940–944.

Groves, D. and Brown, V. (2005). Vagal nerve stimulation: a review of its applications and potential mechanisms that mediate its clinical effects. *Neurosci. Biobehav. R.*, 29(3):493–500.

Haacke, M., Brown, R., Thompson, M., and Venkatesan, R. (1999). *Magnetic Resonance Imaging: Physical Principles and Sequence Design*. John Wiley and Sons, Chichester, United Kingdom.

Han, Y., Lu, Y., and Zhang, H. (2007). A parallel 3-d impedance method to compute the induce current in human head by tms. In *IEEE/ICME International Conference on Complex Medical Engineering*, Beijing, China.

Haueisen, J., Ramon, C., and Czapski, P. (1995). On the influence of volume currents and extended sources on neuromagnetic fields: a simulation study. *Ann. Biomed. Eng.*, 23:728–739.

Heller, L. and van Hulsteyn, D. (1992). Brain stimulation using electromagnetic sources: theoretical aspects. *Biophys. J.*, 63:129–138.

Hernandez-Pavon, J., Mäkelä, N., Lehtinen, H., Lioumis, P., and Mäkelä, J. (2014). Effects of navigated tms on object and action naming. *Front. Hum. Neurosci.*, 8(660).

Herwig, U., Padberg, F., Unger, J., Spitzer, M., and Schonfeld-Lecuona, C. (2001). Transcranial magnetic stimulation in therapy studies: examination of the reliability of "standard" coil positioning by neuronavigation. *Biol. Psychiatry*, 50(1):58–61.

Hodgkin, A. and Huxley, A. (1952). A quantitative description of membrane current and its application to conduction and excitation in nerve. *J. Physiol.*, 117(4):500–544.

Holtmaat, A. and Svoboda, K. (2009). Experience-dependent structural synaptic plasticity in the mammalian brain. *Nat. Rev. Neurosci.*, 10:647–658.

Homma, S., Musha, T., Nakajima, Y., Okamoto, Y., Blom, S., Flink, R., and Hagbarth, K. (1995). Conductivity ratios of the scalp-skull-brain head model in estimating equivalent dipole sources in human brain. *Neurosci. Res.*, 22:51–55.

Hoogendam, J., Ramakers, G., and Di Lazzaro, V. (2010). Physiology of repetitive transcranial magnetic stimulation of the human brain. *Brain Stimul.*, 3:98–118.

Horvath, J., Perez, J., Forrow, L., Fregni, F., and Pascual-Leone, A. (2011). Transcranial magnetic stimulation: a historical evaluation and future prognosis of therapeutically relevant ethical concerns. *J. Med. Ethics*, 37(3):137–143.

Huang, Y., Edwards, M., Rounis, E., Bhatia, K., and Rothwell, J. (2005). Theta burst stimulation of the human motor cortex. *Neuron*, 45(2):201–206.

Ilmoniemi, R., Jarmo, R., and Jari, K. (1999). Transcranial magnetic stimulation-a new tool for functional imaging of the brain. *Crit. Rev. Biomed. Eng.*, 27(3-5):241–284.

Ilmoniemi, R. and Kičić, D. (2010). Methodology for combined tms and eeg. *Brain Topogr.*, 22(4):233–248.

Ilmoniemi, R., Virtanen, J., Ruohonen, J., Karhu, J., Aronen, H., and Katila, T. (1997). Neuronal responses to magnetic stimulation reveal cortical reactivity and connectivity. *Neuroreport*, 8(16):3537–3540.

Irfanoglu, M., Walker, L., Sarlls, J., Marenco, S., and Pierpaoli, C. (2012). Effects of image distortions originating from susceptibility variations and concomitant fields on diffusion mri tractography results. *NeuroImage*, 61:275–288.

Jaeger, D., De Schutter, E., and Bower, J. (1997). The role of synaptic and voltage-gated currents in the control of purkinje cell spiking: a modeling study. *J. Neurosci.*, 17(1):91–106.

Janssen, A., Rampersad, S., Lucka, F., Lanfer, B., Lew, S., Aydin, U., Wolters, C., Stegeman, D., and Oostendorp, T. (2013). The influence of sulcus width

on simulated electric fields induced by transcranial magnetic stimulation. *Phys. Med. Biol.*, 58:4881–4896.

Jeurissen, B., Leemans, A., Jones, D., Tournier, J., and Sijbers, J. (2011). Probabilistic fiber tracking using the residual bootstrap with constrained spherical deconvolution. *Hum. Brain Mapp.*, 32:461–479.

Jeurissen, B., Leemans, A., Tournier, J., Jones, D., and Sijbers, J. (2013). Investigating the prevalence of complex fiber configurations in white matter tissue with diffusion magnetic resonance imaging. *Hum. Brain Mapp.*, 34:2747–2766.

Jones, D., Horsfield, M., and Simmons, A. (1999). Optimal strategies for measuring diffusion in anisotropic systems by magnetic resonance imaging. *Magn. Reson. Med.*, 42:515–525.

Jones, D. and Leemans, A. (2011). Diffusion tensor imaging. *Methods Mol. Biol.*, 711:127–144.

Kandel, E., Schwartz, J., and Jessell, T. (2000). *Principles of neural science*. McGraw-Hill, New York, USA.

Kim, D., Georghiou, G., and Won, C. (2006). Improved field localization in transcranial magnetic stimulation of the brain with the utilization of a conductive shield plate in the stimulator. *IEEE Trans. Biomed. Eng.*, 53(4):720–725.

Kimiskidis, V. (2010). Transcranial magnetic stimulation for drug-resistant epilepsies: rationale and clinical experience. *Eur. Neurol.*, 63(4):205–210.

Knöpfel, T. and Boyden, E. (2012). *Optogenetics: Tools for controlling and monitoring neuronal activity*. Elsevier, Oxford, United Kingdom.

Krieg, S., Sabih, J., Bulubasova, L., Obermueller, T., Negwer, C., Janssen, I., Shiban, E., Meyer, B., and Ringel, F. (2014). Preoperative motor mapping by navigated transcranial magnetic brain stimulation improves outcome for motor eloquent lesions. *Neuro-oncology*, 16(9):1274–1282.

Laakso, I., Hirata, A., and Ugawa, Y. (2014). Effects of coil orientation on the electric field induced by tms over the hand motor area. *Phys. Med. Biol.*, 59:203–218.

Leemans, A., Jeurissen, B., Sijbers, J., and Jones, D. (2009). Exploredti: a graphical toolbox for processing, analyzing, and visualizing diffusion mr data. In *Proceedings of 17th Annual Meeting of Intl. Soc. Mag. Reson. Med.*, Hawaii, USA.

Leemans, A. and Jones, D. (2009). The b-matrix must be rotated when correcting for subject motion in dti data. *Magn. Reson. Med.*, 61:1336–1349.

Lioumis, P., Kičić, D., Savolainen, P., Mäkelä, J., and Kähkönen, S. (2009). Reproducibility of tms-evoked eeg responses. *Hum. Brain Mapp.*, 30(4):1387–1396.

Lioumis, P., Zhdanov, A., Mäkelä, N., Lehtinen, H., Wilenius, J., Neuvonen, T., Hannula, H., Deletis, V., Picht, T., and Mäkelä, J. (2012). A novel approach

for documenting naming errors induced by navigated transcranial magnetic stimulation. *J. Neurosci. Meth.*, 204(2):349–354.

Liu, F., Zhao, H., and Crozier, S. (2003). Calculation of electric fields induced by body and head motion in high-field mri. *J. Magn. Reson.*, 161(1):99–107.

Liu, Y., Zhu, S., and He, B. (2009). Induced current magnetic resonance electrical impedance tomography of brain tissues based on the j-substitution algorithm: a simulation study. *Phys. Med. Biol.*, 54:4561–4573.

Logothetis, N., Kayser, C., and Oeltermann, A. (2007). In vivo measurement of cortical impedance spectrum in monkeys: implications for signal propagation. *Neuron*, 55(5):809–823.

London, M. and Husser, M. (2005). Dendritic computation. *Annu. Rev. Neurosci.*, 28:503–532.

Loo, C. and Mitchell, P. (2005). A review of the efficacy of transcranial magnetic stimulation (tms) treatment for depression, and current and future strategies to optimize efficacy. *J. Affect. Disorders*, 3:255–267.

Lu, M., Ueno, S., Thorlin, T., and Persson, M. (2008). Calculating the activating function in the human brain by transcranial magnetic stimulation. *IEEE Trans. Magn.*, 44:1438–1441.

Maccabee, P., Amassian, V., Eberle, L., and Cracco, R. (1993). Magnetic coil stimulation of straight and bent amphibian and mammalian peripheral nerve in vitro: locus of excitation. *J. Physiol.*, 460(1):201–219.

Maeda, F., Keenan, J., Tormos, J., Topka, H., and Pascual-Leone, A. (2000). Interindividual variability of the modulatory effects of repetitive transcranial magnetic stimulation on cortical excitability. *Exp. Brain Res.*, 133(4):425–430.

Manola, L., Holsheimer, J., Veltink, P., and Buitenweg, J. (2007). Anodal vs cathodal stimulation of motor cortex: a modeling study. *Clin. Neurophysiol.*, 118:464–474.

Marcolin, M. and Padberg, F. (2007). Transcranial brain stimulation for treatment in mental disorders. *Adv. Biol. Psychiatr.*, 23:204–225.

Maxwell, J. (1865). A dynamical theory of the electromagnetic field. *Philos. Trans. R. Soc. Lond.*, 155:459–512.

Mayberg, H., Lozano, A., Voon, V., McNeely, H., Seminowicz, D., Hamani, C., Schwalb, J., and Kennedy, S. (2005). Deep brain stimulation for treatment-resistant depression. *Neuron*, 45(5):651–660.

McIntyre, C., Richardson, A., and Grill, W. (2002). Modeling the excitability of mammalian nerve fibers: influence of afterpotentials on the recovery cycle. *J. Neurophysiol.*, 87:995–1006.

Merton, P. and Morton, H. (1980). Stimulation of the cerebral cortex in the intact human subject. *Nature*, 285:227.

Miranda, P., Correia, L., Salvador, R., and Basser, P. (2007). Tissue heterogeneity as a mechanism for localized neural stimulation by applied electric fields. *Phys. Med. Biol.*, 52:5603–5617.

Miranda, P., Hallett, M., and Basser, P. (2003). The electric field induced in the brain by magnetic stimulation: a 3d finite-element analysis of the effect of tissue heterogeneity and anisotropy. *IEEE Trans. Biomed. Eng.*, 50:1074–1085.

Nadeem, M., Thorlin, T., Gandhi, O., and Persson, M. (2003). Computation of electric and magnetic stimulation in human head using the 3d impedance method. *IEEE Trans. Biomed. Eng.*, 50(7):900–907.

Nagarajan, S., Durand, M., and Warman, E. (1993). Effects of induced electric fields on finite neuronal structures: a simulation study. *IEEE Trans. Biomed. Eng.*, 40(11):1175–1188.

Nauczyciel, C., Hellier, P., Morandi, X., Blestel, S., Drapier, D., Ferre, J., Barillot, C., and Millet, B. (2011). Assessment of standard coil positioning in transcranial magnetic stimulation in depression. *Psychiatry Res.*, 186(2):232–238.

Nelder, J. and Mead, R. (1965). A simplex-method for function minimization. *Comput. J.*, 7:308–313.

Nicholson, P. (1965). Specific impedance of cerebral white matter. *Exp. Neurol.*, 13(4):384–401.

Niebur, E. and Niebur, D. (1991). Numerical implementation of sealed-end boundary conditions in cable theory. *IEEE Trans. Biomed. Eng.*, 38(12):1266–1271.

Nitsche, M. and Paulus, W. (2000). Excitability changes induced in the human motor cortex by weak transcranial direct current stimulation. *J. Physiol.*, 527(3):633–639.

Nummenmaa, A., McNab, J., Savadjiev, P., Okada, Y., Hmlinen, M., Wang, R., Wald, L., Pascual-Leone, A., Wedeen, V., and Raij, T. (2014). Targeting of white matter tracts with transcranial magnetic stimulation. *Brain Stimul.*, 7:80–84.

Ojemann, G., Creutzfeldt, O., Lettich, E., and Haglund, M. (1988). Neuronal activity in human lateral temporal cortex related to short-term verbal memory, naming and reading. *Brain*, 111(6):1383–1403.

Opitz, A., Windhoff, M., Heidemann, R., Turner, R., and Thielscher, A. (2011). How the brain tissue shapes the electric field induced by transcranial magnetic stimulation. *NeuroImage*, 58:849–859.

Orcutt, N. and Gandhi, O. (1988). A 3-d impedance method to calculate power deposition in biological bodies subjected to time varying magnetic fields. *IEEE Trans. Biomed. Eng.*, 35:577–583.

O'Reardon, J., Solvason, H., Janicak, P., Sampson, S., Isenberg, K., Nahas, Z., McDonald, W., Avery, D., Fitzgerald, P., Loo, C., Demitrack, M., George, M., and Sackeim, H. (2007). Efficacy and safety of transcranial magnetic stimulation in the acute treatment of major depression: a multisite randomized controlled trial. *Biol. Psychiatry*, 62(11):1208–1216.

Özparlak, L. and Ïder, Y. (2005). Induced current magnetic resonance - electrical impedance tomography. *Physiol. Meas.*, 26:S289– S308.

Padberg, F. and George, M. (2009). Repetitive transcranial magnetic stimulation of the prefrontal cortex in depression. *Exp. Neurol.*, 219:2–13.

Pascual-Leone, A., Rubio, B., Pallardó, F., and Catalá, M. (1996). Rapid-rate transcranial magnetic stimulation of left dorsolateral prefrontal cortex in drug-resistant depression. *Lancet*, 348(9022):233–237.

Pascual-Leone, A., Valls-Solé, J., Wassermann, E., and Hallett, M. (1994). Responses to rapid-rate transcranial magnetic stimulation of the human motor cortex. *Brain*, 117(4):847–858.

Pascual-Leone, A., Walsh, V., and Rothwell, J. (2000). Transcranial magnetic stimulation in cognitive neuroscience - virtual lesion, chronometry, and functional connectivity. *Curr. Opin. Neurobiol.*, 10:232–237.

Pashut, T., Wolfus, S., Friedman, A., Lavidor, M., Bar-Gad, I., Yeshurun, Y., and Korngreen, A. (2011). Mechanisms of magnetic stimulation of central nervous system neurons. *PLoS Comput. Biol.*, 7:e1002022.

Paxinos, G. and Watson, C. (2008). *The rat brain in stereotaxic coordinates*. Academic Press, San Diego, CA, USA.

Peleman, K., Van Schuerbeek, P., Luypaert, R., Stadnik, T., De Raedt, R., De Mey, J., Bossuyt, A., and Baeken, C. (2010). Using 3d-mri to localize the dorsolateral prefrontal cortex in tms research. *World J. Biol. Psychiatry*, 11(2_2):425–430.

Penfield, W. and Rasmussen, T. (1950). *The Cerebral Cortex of Man*. Macmillan, New York, USA.

Peterchev, A., Jalinous, R., and Lisanby, S. (2008). A transcranial magnetic stimulator inducing near-rectangular pulses with controllable pulse width (ctms). *IEEE Trans. Biomed. Eng.*, 55:257–266.

Peterchev, A., Wagner, T., Miranda, P., Nitsche, M., Paulus, W., Lisanby, S., Pascual-Leone, A., and Bikson, M. (2012). Fundamentals of transcranial electric and magnetic stimulation dose: definition, selection, and reporting practices. *Brain Stimul.*, 5(4):435–453.

Picht, T., Krieg, S., Sollmann, N., Rösler, J., Niraula, B., Neuvonen, T., Savolainen, P., Lioumis, P., Mäkelä, J., Deletis, V., Meyer, B., Vajkoczy, P., and Ringel, F. (2013). A comparison of language mapping by preoperative navigated transcranial magnetic stimulation and direct cortical stimulation during awake surgery. *Neurosurgery*, 72:808–819.

Picht, T., Schmidt, S., Brandt, S., Frey, D., Hannula, H., Neuvonen, T., Karhu, J., Vajkoczy, P., and Suess, O. (2011). Preoperative functional mapping for rolandic brain tumor surgery: comparison of navigated transcranial magnetic stimulation to direct cortical stimulation. *Neurosurgery*, 69:581–588.

Picht, T., Schulz, J., Hanna, M., Schmidt, S., Suess, O., and Vajkoczy, P. (2012). Assessment of the influence of navigated transcranial magnetic stimulation

on surgical planning for tumors in or near the motor cortex. *Neurosurgery*, 70(5):1248–1257.

Pouratian, N. and Bookheimer, S. (2010). The reliability of neuroanatomy as a predictor of eloquence: a review. *Neurosurg. Focus*, 28(2):E3.

Press, W., Teukolsky, S., Vetterling, W., and Flannery, B. (2007). *Numerical recipes: the art of scientific computing*. Cambridge University Press, New York, USA.

Rajkowska, G. and Goldman-Rakic, P. (1995). Cytoarchitectonic definition of prefrontal areas in the normal human cortex: Ii. variability in locations of areas 9 and 46 and relationship to the talairach coordinate system. *Cereb. Cortex*, 5(4):323–337.

Rattay, F. (1986). Analysis of models for external stimulation of axons. *IEEE Trans. Biomed. Eng.*, 10:974–977.

Rattay, F. (1999). The basic mechanism for the electrical stimulation of the nervous system. *Neuroscience*, 89(2):335–346.

Ravazzani, P., Ruohonen, J., Grandori, F., and Tognola, G. (1996). Magnetic stimulation of the nervous system: induced electric field in unbounded, semi-infinite, spherical and cylindrical media. *Ann. Biomed. Eng.*, 24:606–616.

Rosenthal, J. and Bezanilla, F. (2000). Seasonal variation in conduction velocity of action potentials in squid giant axons. *Biol. Bull.*, 199(2):135–143.

Rossi, S., Hallett, M., Rossini, P., and Pascual-Leone, A. (2009). Safety, ethical considerations, and application guidelines for the use of transcranial magnetic stimulation in clinical practice and research. *Clin. Neurophysiol.*, 120:2008–2039.

Roth, B. (1994). Mechanisms for electrical stimulation of excitable tissue. *Crit. Rev. Biomed. Eng.*, 22(3-4):253–305.

Roth, B. and Basser, P. (1990). A model of the stimulation of a nerve fiber by electromagnetic induction. *IEEE Trans. Biomed. Eng.*, 37:588–597.

Roth, Y., Pell, G., and Zangen, A. (2013). Commentary on: Deng et al., electric field depth-focality tradeoff in transcranial magnetic stimulation: simulation comparison of 50 coil designs. *Brain Stimul.*, 6:14–15.

Roth, Y., Zangen, A., and Hallett, M. (2002). A coil design for transcranial magnetic stimulation of deep brain regions. *J. Clin. Neurophysiol.*, 19(4):361–370.

Ruohonen, J., Panizza, M., Nilsson, J., Ravazzani, P., Grandori, F., and Tognola, G. (1996). Transverse-field activation mechanism in magnetic stimulation of peripheral nerves. *Electroencephalogr. Clin. Neurophysiol.*, 101(2):167–174.

Rush, S. and Driscoll, D. (1968). Current distribution in the brain from surface electrodes. *Anesth. Analg.*, 47(6):717–723.

Rushton, W. (1927). The effect upon the threshold for nervous excitation of the length of nerve exposed, and the angle between current and nerve. *J. Physiol.*, 63:357–377.

Sack, A. and Linden, D. (2003). Combining transcranial magnetic stimulation and functional imaging in cognitive brain research: possibilities and limitations. *Brain Res. Rev.*, 43:41–56.

Sadleir, R. and Argibay, A. (2007). Modeling skull electrical properties. *Ann. Biomed. Eng.*, 35(10):1699–1712.

Salinas, F., Lancaster, J., and Fox, P. (2007). Detailed 3d models of the induced electric field of transcranial magnetic stimulation coils. *Phys. Med. Biol.*, 52:2879–2892.

Salinas, F., Lancaster, J., and Fox, P. (2009). 3d modeling of the total electric field induced by transcranial magnetic stimulation using the boundary element method. *Phys. Med. Biol.*, 54:3631–3647.

Salvador, R. (2009). *Numerical modelling in transcranial magnetic stimulation*. PhD thesis, University of Lisbon, Portugal.

Salvador, R., Silva, S., Basser, P., and Miranda, P. (2011). Determining which mechanisms lead to activation in the motor cortex: A modeling study of transcranial magnetic stimulation using realistic stimulus waveforms and sulcal geometry. *Clin. Neurophysiol.*, 122:748–758.

Seagar, A., Barber, D., and Brown, B. (1987). Theoretical limits to sensitivity and resolution in impedance imaging. *Clin. Phys. Physiol. Meas.*, 8:A13–31.

Sekino, M. and Ueno, S. (2004). Fem-based determination of optimum current distribution in transcranial magnetic stimulation as an alternative to electroconvulsive therapy. *IEEE Trans. Magn.*, 40:2167–2169.

Seo, J. and Woo, E. (2011). Magnetic resonance electrical impedance tomography (mreit). *SIAM Rev.*, 53(1):40–68.

Shahid, S., Bikson, M., Salman, H., Wen, P., and Ahfock, T. (2014). The value and cost of complexity in predictive modelling: role of tissue anisotropic conductivity and fibre tracts in neuromodulation. *J. Neural Eng.*, 11:036002.

Shewchuk, J. (1994). *An introduction to the conjugate gradient method without the agonizing pain*. Carnegie Mellon University, Pittsburgh, PA, USA.

Silva, S., Basser, P., and Miranda, P. (2008). Elucidating the mechanisms and loci of neuronal excitation by transcranial magnetic stimulation using a finite element model of a cortical sulcus. *Clin. Neurophysiol.*, 119:2405–2413.

Smith, J., Mennemeier, M., Bartel, T., Chelette, K., Kimbrell, T., Triggs, W., and Dornhoffer, J. (2007). Repetitive transcranial magnetic stimulation for tinnitus: a pilot study. *Laryngoscope*, 117:529–534.

Sporns, O., Tononi, G., and Kötter, R. (2005). The human connectome: a structural description of the human brain. *PLoS Comput. Biol.*, 1(4):e42.

Stiles, J. and Bartol, T. (2001). *Monte Carlo methods for simulating realistic synaptic microphysiology using MCell. In: Computational neuroscience: realistic modeling for experimentalists*. CRC Press, Boca Raton, FL, USA.

Stroud, A. and Secrest, D. (1966). *Gaussian Quadrature Formulas*. Prentice-Hall, Englewood Cliffs, NJ, USA.

Tachas, N., Samaras, T., Baskourelos, K., and Sahalos, J. (2009). Effects of skeletal muscle anisotropy on induced currents from low-frequency magnetic fields. *Phys. Med. Biol.*, 54:N541–N547.

Talairach, J. and Tournoux, P. (1988). *Co-Planar Stereotaxic Atlas of the Human Brain*. Thieme Medical Publishers, New York, USA.

Tax, C., Otte, W., Viergever, M., Dijkhuizen, R., and Leemans, A. (2015). Rekindle: Robust extraction of kurtosis indices with linear estimation. *Magn. Reson. Med.*, 73(2):794–808.

Thielscher, A. and Kammer, T. (2004). Electric field properties of two commercial figure-8 coils in tms: calculation of focality and efficiency. *Clin. Neurophysiol.*, 115:1697–1708.

Thielscher, A., Opitz, A., and Windhoff, M. (2011). Impact of the gyral geometry on the electric field induced by transcranial magnetic stimulation. *NeuroImage*, 54:234–243.

Tournier, J., Mori, S., and Leemans, A. (2011). Diffusion tensor imaging and beyond. *Magn. Reson. Med.*, 65:1532–1556.

Traub, R., Wong, R., Miles, R., and Michelson, H. (1991). A model of a ca3 hippocampal pyramidal neuron incorporating voltage-clamp data on intrinsic conductances. *J. Neurophysiol.*, 66(2):635–650.

Tsugorka, T., Dovgan, O., Stepanyuk, A., and Cherkas, V. (2007). Variety of types of cortical interneurons. *Neurophysiology*, 39:227–236.

Tuch, D., Wedeen, V., Dale, A., George, J., and Belliveau, J. (2001). Conductivity tensor mapping of the human brain using diffusion tensor mri. *Proc. Natl. Acad. Sci. U.S.A.*, 98:11697–11701.

Ueno, S., Tashiro, T., and Harada, K. (1988). Localized stimulation of neural tissue in the brain by means of a paired configuration of time-varying magnetic fields. *J. Appl. Phys.*, 64:5862–5864.

Van de Moortele, P., Akgun, C., Adriany, G., Moeller, S., Ritter, J., Collins, C., Smith, M., Vaughan, J., and Uğurbil, K. (2005). B1 destructive interferences and spatial phase patterns at 7 t with a head transceiver array coil. *Magn. Reson. Med.*, 54:1503–1518.

Van der Vorst, H. (1992). Bi-cgstab: a fast and smoothly converging variant of bi-cg for the solution of nonsymmetric linear systems. *SIAM J. Sci. Statist. Comput.*, 13:631–644.

Veraart, J., Sijbers, J., Sunaert, S., Leemans, A., and Jeurissen, B. (2013). Weighted linear least squares estimation of diffusion mri parameters: strengths, limitations, and pitfalls. *NeuroImage*, 81:335–346.

Vos, S., Jones, D., Viergever, M., and Leemans, A. (2011). Partial volume effect as a hidden covariate in dti analyses. *NeuroImage*, 55:1566–1576.

Wagner, T., Fregni, F., Eden, U., Ramos-Estebanez, C., Grodzinsky, A., Zahn, M., and Pascual-Leone, A. (2006). Transcranial magnetic stimulation and stroke: A computer-based human model study. *NeuroImage*, 30:857–870.

Wagner, T., Zahn, M., Grodzinsky, A., and Pascual-Leone, A. (2004). Three-dimensional head model simulation of transcranial magnetic stimulation. *IEEE Trans. Biomed. Eng.*, 51:1586–1594.

Wang, H., Liu, F., Xia, L., and Crozier, S. (2008). An efficient impedance method for induced field evaluation based on a stabilized bi-conjugate gradient algorithm. *Phys. Med. Biol.*, 53:6363–6375.

Wassermann, E. (1998). Risk and safety of repetitive transcranial magnetic stimulation: report and suggested guidelines from the international workshop on the safety of repetitive transcranial magnetic stimulation, 1996. *Electroencephalogr. Clin. Neurophysiol.*, 108:1–16.

Wassermann, E., Epstein, C., Ziemann, U., Walsh, V., Paus, T., and Lisanby, S. (2008). *The Oxford Handbook of Transcranial Magnetic Stimulation*. Oxford University Press, Oxford, United Kingdom.

Wesselink, W., Holsheimer, J., and Boom, H. (1999). A model of the electrical behaviour of myelinated sensory nerve fibres based on human data. *Med. Biol. Eng. Comput.*, 37(2):228–235.

Wolters, C. (2003). *Influence of tissue conductivity inhomogeneity and anisotropy on EEG/MEG based source localization in the human brain*. PhD thesis, Max Planck Institute of Cognitive Neuroscience, Leipzig, Germany.

Wolters, C., Anwander, A., Tricoche, X., Weinstein, D., Koch, M., and MacLeod, R. (2006). Influence of tissue conductivity anisotropy on eeg/meg field and return current computation in a realistic head model: A simulation and visualization study using high-resolution finite element modeling. *NeuroImage*, 30:813–826.

Wyckhuys, T., De Geeter, N., Crevecoeur, G., Stroobants, S., and Staelens, S. (2013). Quantifying the effect of repetitive transcranial magnetic stimulation in the rat brain by spect cbf scans. *Brain Stimul.*, 6(4):554–562.

Zangen, A., Roth, Y., Voller, B., and Hallett, M. (2005). Transcranial magnetic stimulation of deep brain regions: evidence for efficacy of the h-coil. *Clin. Neurophysiol.*, 116(4):775–779.

Zhang, H. and Wang, L. (2004). Acousto-electric tomography. *Proc. SPIE*, 5320:145–149.

Zlochiver, S., Rosenfeld, M., and Abboud, S. (2003). Induced-current electrical impedance tomography: a 2-d theoretical simulation. *IEEE Trans. Med. Imag.*, 22:1550–1560.